LAL 11-119
Juin 2011

UNIVERSITÉ PARIS-SUD 11
École Doctorale de Physique de la Région Parisienne (ED 107)
Laboratoire de l'Accélérateur Linéaire

THÈSE

présentée pour obtenir le grade de

DOCTEUR EN SCIENCES PHYSIQUES
de l'Université Paris XI

Spécialité : Physique Théorique

par

Michał Wąs

Searching for gravitational waves associated with gamma-ray bursts in 2009-2010 LIGO-Virgo data

Soutenue le 27 juin 2011 devant la Commission d'Examen

MM.	A. Stocchi	Président
	E. Plagnol	Rapporteur
	P. Shawhan	Rapporteur
Mme	F. Marion	Examinateur
MM.	R. Mochkovich	Examinateur
	P. Hello	Directeur de thèse
	P. Sutton	Invité

Recherche d'ondes gravitationnelles associées aux sursauts gamma dans les données LIGO-Virgo de 2009-2010

Résumé

Cette thèse présente les résultats de la recherche de signaux impulsionnels d'ondes gravitationnelles associés aux sursauts gamma dans les données 2009-2010 des interféromètres LIGO-Virgo. L'étude approfondie des mécanismes d'émission d'ondes gravitationnelles par les progéniteurs de sursauts gamma, ainsi que des mécanismes d'émission de rayons gamma eux-mêmes, permet de déterminer les caractéristiques essentielles du signal à détecter : polarisation, délai temporel, etc ... Cette connaissance de l'émission conjointe permet alors de construire une méthode d'analyse qui inclut les a priori astrophysiques. Cette méthode est de plus robuste vis-à-vis des bruits transitoires présents dans les données. L'absence de détection nous permet de placer des limites observationnelles inédites sur la population des sursauts gamma.

Mots Clés : Rayonnement gravitationnel, Sursauts Gamma, Traitement du signal, Interférométrie

Abstract

In this thesis we present the results of the search for gravitational wave bursts associated with gamma-ray bursts in the 2009-2010 data from the LIGO-Virgo gravitational wave interferometer network. The study of gamma-ray bursts progenitors, both from the gamma-ray emission and the gravitational wave emission point of view, yields the characteristic of the sought signal: polarization, time delays, etc ... This knowledge allows the construction of a data analysis method which includes the astrophysical priors on joint gravitational wave and gamma-ray emission, and moreover which is robust to non-stationary transient noises, which are present in the data. The lack of detection in the analyzed data yields novel observational limits on the gamma-ray burst population.

Keywords: Gravitational waves, Gamma ray bursts, Signal processing, Interferometry

Disclaimer: The work presented in this thesis has not been reviewed by the LIGO Scientific Collaboration or the Virgo Collaboration. Therefore it should not be taken as representative of the scientific opinion of either collaboration. This document has been assigned Laboratoire de l'Accélérateur Linéaire number LAL 11-119, LIGO document number LIGO-T1100248, Virgo document number VIR-0347A-11.

Contents

Remerciements

Tout d'abord, je souhaiterais remercier Guy Wormser et Achille Stocchi de m'avoir accueilli au laboratoire, ainsi que les services administratifs du laboratoire qui mon permit de ne pas être distrait de mon travail de thèse. En particulier Annie Huguet, Isabelle Valeon et Sabine Rayaume du service mission (appelé par certain « service vacances »), pour l'assistance dans mes deux douzaines de missions, sans lesquelles cette thèse ne serait pas la même.

Je souhaiterais exprimer ma gratitude à Peter Shawhan et Eric Plagnol d'avoir accepté la lourde tache de rapporteur, à Achille Stocchi d'avoir pris en charge la présidence du jury, et à Frédérique Marion et Robert Mochkovich d'avoir évaluer mon travail.

Je suis reconnaissant à Patrice Hello de m'avoir encadré durant cette thèse. Il a toujours était prêt à répondre à mes questions ou à m'écouter expliquer une idée. Mais il m'a aussi laisser la liberté de poursuivre mes sujets de recherche.

Merci à l'ensemble du groupe Virgo à Orsay pour la magnifique ambiance dans l'extension à la dérive du bâtiment 208. En particulier, Nicolas pour les discussions dans le RER, Fabien pour les sous, et Arun, Florent, Miltos et Samuel pour m'avoir supporté dans leur bureau.

Je souhaiterais remercier mes collaborateurs : Patrick Sutton, Isabel Leonor et Gareth Jones ; sur le travail desquels je me suis reposer pour construire cette thèse. Et de manière plus générale les collaborations LIGO et Virgo pour les données collecté et les ressources mises à ma disposition.

Je remercie également ceux qui ont contribué à mon engagement dans cette direction. En particulier Patrick Sutton qui m'a fait découvrir le milieu des ondes gravitationnelles en stage, ainsi que plus en amont, Sławomir Brzezowski et Yann Brunel pour leurs ambitieux cours de physique.

Enfin, je suis redevable à tous ceux qui ont contribué à rendre ce manuscrit compréhensible en le corrigeant tant du point de vue du fond que de la forme. Merci Patrice, Marie-Anne, Nicolas, Fabien, Maman, Papa et Simon. Les fautes dans ces remerciements devrait vous donnez une idée du travail qu'ils ont eu à faire.

Synthèse

Les ondes gravitationnelles sont l'une des prédictions de la théorie de la Relativité Générale d'Einstein. Bien qu'elles aient été prédites depuis près d'un siècle, elles n'ont pas encore été observées directement. Pour le moment la seule confirmation observationnelle de l'existence d'ondes gravitationnelles est indirecte. Pour quelques systèmes d'étoiles à neutron double en orbite proche une diminution de la période orbitale a été observée grâce à l'analyse des impulsions radio émises par l'une des étoiles à neutron (qui est donc un pulsar). Cette décroissance de la période orbitale est expliquée par la perte d'énergie du système par rayonnement gravitationnel. Les observations sont effectuées pour certains systèmes depuis les années 70, et elles sont en parfait accord avec les prédictions de la Relativité Générale avec une précision de l'ordre du pour mille.

En parallèle un important effort expérimental a été entrepris depuis les années 60 afin d'observer directement les effets des ondes gravitationnelles sur Terre. Cette thèse s'inscrit dans cette effort en participant à l'analyse des données des détecteurs d'ondes gravitationnelles LIGO et Virgo qui sont les instruments les plus sensibles jusqu'à présent. En particulier nous nous intéressons à la détection d'ondes gravitationnelles qui pourraient être émises par les progéniteurs de sursauts gamma. Ces évènements catastrophiques sont détectés grâce à leur émission de photons gamma, mais ils pourraient être aussi à l'origine d'une importante émission d'ondes gravitationnelles.

Propriétés des ondes gravitationnelles

La théorie de la Relativité Générale décrit le mouvement d'objets sous l'influence de l'interaction gravitationnelle. Le cadre théorique est que l'espace temps est décrit par une variété pseudo-riemannienne et les masses tests se déplacent suivant les géodésiques de cette variété. La métrique de la variété est déterminée par la présence d'une distribution de masse-énergie dans l'univers. Ainsi la masse-énergie courbe l'espace et en retour la courbure de l'espace détermine comment les objets se déplacent. L'équation d'Einstein

$$G_{\mu\nu} = \frac{8\pi G}{c^4} T_{\mu\nu},$$

décrit la formation de cette courbure. Le tenseur d'Einstein $G_{\mu\nu}$ est seulement fonction de la métrique et de ses deux premières dérivées spatio-temporelles, alors que le tenseur énergie-impulsion $T_{\mu\nu}$ est le terme source et décrit la distribution de masse-énergie dans l'univers.

L'équation d'Einstein est non-linéaire et il est impossible de la résoudre analytiquement à part dans quelque cas simples. Néanmoins dans la limite où la courbure est faible ces équations peuvent être linéarisées, ce qui donne lieu à deux degrés de liberté dynamique de la courbure. L'évolution de ces deux degrés de liberté est décrite par de simples équations de propagation d'ondes avec une célérité égale à la vitesse de la lumière. Ces deux degrés de liberté représentent les deux polarisations des ondes gravitationnelles pouvant se propager dans une direction donnée.

Les deux degrés de liberté sont habituellement décrits par deux polarisations linéaires : « plus » et « croix », distinguées par leur effet sur un cercle de masses libres, le plan du cercle étant orthogonal à la direction de propagation. Une onde polarisée « plus » déforme le cercle de masse libre en une ellipse qui est alternativement écrasée et étirée suivant une direction donnée, alors qu'une onde polarisée « croix » a le même effet mais suivant une direction tournée de 45°. Bien sûr toutes les combinaisons linéaires de ces deux polarisations sont possibles. En particulier, si l'onde polarisée « plus » et « croix » sont d'amplitude égale et décalé d'un quart de période, l'onde totale est dite polarisée circulairement.

L'équation d'Einstein décrit aussi l'émission d'ondes gravitationnelles par des masses en mouvement. Dans ce cadre, la courbure n'est pas nécessairement faible, mais dans la limite où le mouvement de ces masses est lent par rapport à la vitesse de la lumière, l'émission des ondes gravitationnelles est bien décrite par l'évolution du moment quadrupolaire de ces masses.

Une discussion plus détaillée des propriétés des ondes gravitationnelles est données dans le chapitre 1.

Détecteurs d'ondes gravitationnelles

Les détecteurs d'ondes gravitationnelles LIGO et Virgo utilisent comme principe de détection l'effet des ondes gravitationnelles sur des masses libres. Le concept de base est celui de l'interféromètre de Michelson, la lumière transmise par cet interféromètre dépend de la différence de longueur entre les deux bras orthogonaux qui le composent. Les miroirs formant l'interféromètre étant suspendus, ils peuvent être considérés comme des masses libres dans le plan horizontal pour des ondes gravitationnelles de haute fréquence par rapport aux résonances des suspensions. Les fréquences de ces résonances sont en général inférieures à quelques hertz. Ainsi, une onde gravitationnelle se propageant orthogonalement au plan de l'interféromètre et d'axe de polarisation colinéaire à l'un des bras, alternativement allonge un

bras de l'interféromètre et raccourcit l'autre, ceci a pour effet de modifier la puissance transmise par l'interféromètre. La variation relative de la longueur des bras est égale à l'amplitude de l'onde gravitationnelle, et cet effet devrait permettre la détection du passage d'une onde gravitationnelle.

Néanmoins, les ondes gravitationnelles ne sont pas le seul phénomène physique induisant une fluctuation de la puissance transmise par l'interféromètre. La surface des miroirs formant l'interféromètre fluctue thermiquement et la position de ces miroirs est perturbée par les vibrations du sol transmises à travers le système de suspension. Aussi, la précision de la mesure de la puissance transmise par l'interféromètre n'est pas infinie, elle est entre autre limitée par les fluctuations quantiques du nombre de photons détecté par une photo-diode pour une puissance incidente donnée.

De nombreuses améliorations ont été apportées à ce concept de simple interféromètre de Michelson pour pallier aux bruits sismiques, thermiques et quantiques, mais aussi pour réduire de nombreuses autres sources de bruit que nous ne mentionneront pas ici. Au final une sensibilité suffisante a été obtenue pour espérer extraire du bruit des ondes avec une amplitude inférieure à 10^{-21} dans la bande de fréquence sensible des détecteurs, qui va de quelque hertz à quelque milliers de hertz.

Une discussion plus détaillée des détecteurs interféromètrique d'ondes gravitationnelles est donnée dans le chapitre 2

Sursauts gamma

Les sursauts gamma sont de brèves bouffées de photons gamma provenant de points particuliers dans le ciel. Ils ont été découverts dans les années 70. Leur durée typique est comprise entre $0.1 - 100\,\mathrm{s}$ et le spectre en énergie est piqué dans la gamme de $10 - 100\,\mathrm{keV}$. Les quarante années d'observation qui ont suivi la découverte des sursauts gamma ont permis d'avoir une certaine compréhension de leur origine.

La distribution de la durée des sursauts a une structure bimodale, avec des sursauts courts ($\lesssim 2\,\mathrm{s}$) et des sursauts longs ($\gtrsim 2\,\mathrm{s}$), néanmoins il n'y a pas de séparation nette entre ces deux familles. Ces sursauts sont distribués uniformément sur le ciel et leurs progéniteurs sont situés à des distance cosmologiques de l'ordre de $10\,\mathrm{Gpc}$. L'énergie émise par la source sous forme de photons gamma durant le sursaut est de l'ordre de $10^{-3}\,\mathrm{M}_\odot\mathrm{c}^2$ (où $M_\odot = 1$ masse solaire). Les sursauts courts sont le plus probablement dus à la coalescence d'une étoile à neutron avec une autre étoile à neutron ou un trou noir. Les sursauts longs sont, pour leur part, probablement produits par l'effondrement d'une étoile massive en rotation rapide, c'est-à-dire un cas extrême de supernova qui est appelé hypernova. Lors de cet effondrement un trou noir entouré d'un disque de matière nucléaire ou bien une étoile à neutron magnétisée et en rotation rapide est formée. Dans tous les cas de figure

un jet de matière se propageant à des vitesses relativistes est éjecté par l'événement cataclysmique. Ce jet émet du rayonnement gamma principalement suivant un cône autour de l'axe de rotation de symétrie du système. L'angle d'ouverture de ce cône est typiquement de l'ordre de 5° pour les sursauts longs et de l'ordre de 30° pour les sursauts courts, avec une grande dispersion dans les deux cas. Pour plus de détails sur la phénoménologie des sursauts gamma voir section 4.1.

Les sursauts gamma sont détectés par un réseau de satellites avec un taux de l'ordre de un par jour. La direction dans le ciel et le temps de début de l'émission gamma sont publiés par le réseau GCN (Gamma-ray burst Coordinates Network) avec un temps de latence de l'ordre de la minute.

Émission d'ondes gravitationnelles

Une émission d'ondes gravitationnelles par le cœur du progéniteur est attendue à la fois pour les sursauts courts et pour les sursauts longs

Pour le cas des sursauts courts le modèle de coalescence d'astres compacts doubles prédit une émission d'ondes gravitationnelles, dans la bande passante des détecteurs actuels, durant les quelques dizaines de secondes avant la coalescence. Étant donné que l'émission est due à la rotation orbitale du système binaire et que l'axe de rotation pointe approximativement vers l'observateur, l'onde reçue par l'observateur sera polarisée circulairement.

Pour le cas des sursauts longs la situation est moins claire, étant donné qu'il est très difficile de modéliser avec précision l'effondrement d'une étoile massive. Néanmoins les modèles qui prédisent une grande énergie émise sous forme d'ondes gravitationnelles correspondent à des instabilités rotationnelles du cœur de l'étoile. Dans le cas où le cœur est une étoile à neutron le principal cas de figure est la formation de mode barre (excès de densité ayant la forme d'une barre) dans l'étoile. Dans le cas où est un trou noir entouré d'un disque d'accrétion les principaux cas de figure sont la formation de mode barre dans le disque, ou bien la fragmentation du disque. Dans ce dernier cas le cœur s'apparente alors à un système binaire formé du trou noir et du fragment en question.

Ces instabilités rotationnelles se développent dans les quelques secondes qui suivent la formation des objets en question. Dans tous ces cas de figures la distribution de masse est approximativement en rotation rigide autour de l'axe pointant vers l'observateur, et les ondes gravitationnelles reçues par l'observateur serons donc aussi polarisées circulairement.

Dans le cadre de l'effondrement stellaire il existe de nombreux autres modèles d'émission qui ne donnent pas nécessairement lieu à une émission polarisée circulairement. Mais dans tous ces autre modèles, l'émission attendue provenant d'un progéniteur extra-galactique ne serait pas visible avec les détecteurs actuels. Nous ne prendrons donc pas en compte ces modèles dans la suite.

Nous discutons en détails l'émission par les coalescence d'astres compacts dans la section 3.3.2 et pour l'effondrement stellaire dans la section 3.3.3.

Coïncidence temporelle

Le cœur des progéniteurs de sursauts gamma émet potentiellement des ondes gravitationnelles, alors que les photons formant le sursaut lui même sont émis à une grande distance du cœur dans le jet relativiste. Ceci résulte en un décalage temporel entre l'arrivée des ondes gravitationnelles et des photons gamma, et ce décalage doit être pris en compte lors d'une analyse qui associe ces deux messagers.

Pour le cas des sursauts courts le jet relativiste est créé en moins de 1 seconde après la coalescence, et la propagation du jet entre sa création et l'émission de photon gamma prends au plus quelque secondes du point de vu de l'observateur. Cette durée courte s'explique par la contraction relativiste des distances dans le jet du point de vue de l'observateur, en réalité le temps de propagation est beaucoup plus long dans le référentiel du cœur du progéniteur. Il en résulte que les ondes gravitationnelles créées par une coalescence de binaire devraient arriver au plus tôt une minute avant, et au plus tard en même temps que les photons gamma.

Pour le cas des sursauts long la situation est encore une fois plus complexe. Le jet doit en premier percer l'enveloppe de l'étoile ce qu'il fait avec une vitesse non relativiste en un temps qui peut durer jusqu'à 100 s. Ensuite le temps de propagation du jet jusqu'à émission de photons gamma est plus long et peut durer jusqu'à 200 s dans le référentiel de l'observateur. De plus l'évolution du cœur du progéniteur peut se dérouler en deux étapes, avec en premier la formation d'une étoile à neutron puis celle d'un trou noir avec un disque d'accrétion dense. Ces deux évènements peuvent être séparés d'au plus 100 s avec une possible émission d'ondes gravitationnelles associée à chacun d'entre eux. Au final pour prendre en compte tout les cas possible nous faisons une recherche d'ondes gravitationnelles associées à un sursaut gamma dans les dix minutes précédant le début du sursaut et incluant toute la durée du sursaut. Ce choix de fenêtre d'analyse inclut automatiquement le cas des sursauts courts, nous le discutons de manière plus approfondie dans la section 4.3.

Analyse de donnée

Après étalonnage, les données récoltées par un détecteur interférometrique sont sous la forme d'une série temporelle

$$d(t) = \underbrace{F_+(\theta,\phi)h_+(t) + F_\times(\theta,\phi)h_\times(t)}_{s(t)} + n(t), \tag{1}$$

où $h_+(t)$ et $h_\times(t)$ sont les amplitudes des deux polarisations des ondes gravitationnelles traversant le détecteur, $F_+(\theta,\phi)$ et $F_\times(\theta,\phi)$ sont des facteurs géométriques dépendant de la direction de propagation (θ,ϕ) de l'onde, et $n(t)$ est la somme des bruits du détecteur. Le but premier de l'analyse de données des détecteurs d'ondes gravitationnelles est de déceler le signal $s(t)$ qui est éventuellement caché dans les données $d(t)$ par le bruit $n(t)$.

En règle générale ces analyses de données peuvent être répertoriées suivant deux critères : la connaissance nécessaire de la forme d'onde et la manière de combiner les données de plusieurs détecteurs. Pour le premier critère, si la forme attendue de l'onde gravitationnelle est bien connue et décrite par plusieurs paramètres une recherche par corrélation avec une famille de calques peut être effectuée ; dans le cas contraire une méthode plus générale de recherche d'excès de puissance dans le plan temps-fréquence des données doit être utilisée. Pour le second critère, le point de départ est que l'onde gravitationnelle $\big(h_+(t),\, h_\times(t)\big)$ qui traverse chaque détecteur est la même, au temps de propagation entre les détecteurs près. Deux approches sont utilisées pour prendre en compte cette propriété : rechercher le signal dans chaque détecteur de manière indépendante, le décrire avec plusieurs paramètres, et vérifier si le même signal est observé par plusieurs détecteurs ; ou bien combiner de manière cohérente les données des différents détecteur, c'est à dire construire de nouvelles séries temporelles à partir des données et rechercher un signal dans ces données combinées. La seconde approche est en principe plus sensible, mais n'est pas toujours réalisable à cause de sa complexité numérique, les combinaisons cohérente devant être créées séparément pour une grille fine de positions dans le ciel.

Pour la recherche d'ondes gravitationnelles associées aux sursauts gamma nous adoptons une méthode de recherche par excès de puissance dans des données combinées de manière cohérente. Les raisons de ce choix sont que pour le modèle d'effondrement d'étoile massive il n'y a pas de prédiction précise de la forme des ondes gravitationnelles émises, et que la connaissance de la position dans le ciel et du temps du sursaut simplifie grandement la méthode cohérente d'analyse. Une information cruciale apportée par les modèles du cœur des sursauts gamma est que les ondes gravitationnelles détectables sont polarisées circulairement, c'est à dire qu'il n'y a qu'un seul degré de liberté pour l'onde. Du fait de cette propriété le signal observé dans les détecteurs est corrélé même en utilisant seulement deux détecteurs. Sans cette contrainte au moins trois détecteurs seraient nécessaires pour obtenir une corrélation. Les corrélations des données entre détecteurs nous permettent de réaliser des combinaisons linéaires où le signal se combine de manière constructive ou bien destructive. La combinaison constructive est utilisé pour rechercher le signal de manière plus sensible, alors que les combinaisons destructives sont utilisées pour rejeter les coïncidences fortuites dues aux bruits des détecteurs qui restent présentes dans ces dernières. Au final, des candidats à une détection d'ondes gravitationnelles sont générés et

classés selon une statistique de détection, une quantité qui croît lorsque un candidat ressemble plus à un signal qu'à du bruit.

Une fois que la méthode d'analyse est déterminée, il est nécessaire de caractériser sa capacité à séparer le signal du bruit. La distribution de la statistique de détection due au seul bruit de détecteurs ne peut pas être déterminée *a priori* car les données des détecteurs contiennent de nombreux bruit transitoires qui ne sont pas modélisés (le bruit n'est pas gaussien). La distribution est donc obtenue en analysant les données des détecteurs après les avoir décalées en temps pour enlever les corrélations dues aux ondes gravitationnelles. Cette distribution permet de déterminer le seuil en statistique de détection nécessaire pour qu'un signal soit détecté avec une probabilité de fausse détection donnée, et donc de déclarer si parmi les évènements obtenus au cours de l'analyse un ou plusieurs candidats correspondent à des détections d'ondes gravitationnelles.

Ce seuil en statistique de détection est également nécessaire pour déterminer la sensibilité de l'analyse. Des signaux d'ondes gravitationnelles peuvent être aisément rajoutées aux données des détecteurs en s'inspirant de l'équation (1), ce qui permet de déterminer la valeur de la statistique de détection pour une amplitude d'onde gravitationnelle donnée, c'est-à-dire d'obtenir l'amplitude nécessaire pour détecter une onde gravitationnelle d'une forme donnée. En l'absence de détection d'un signal, la connaissance de la sensibilité permet d'exclure le passage d'ondes gravitationnelles de grande amplitude. Jusqu'à présent tout les résultats des détecteurs d'ondes gravitationnelles sont de ce type.

Pour une discussion abstraites des méthodes d'analyses de données des détecteurs d'ondes gravitationnelles voir chapitre 5, et pour une description de l'analyse utilisé pour obtenir les résultats ci-dessus voir section 7.2.

Résultats

Les détecteurs LIGO et Virgo ont collecté conjointement des données entre le 7 Juillet 2009 et le 20 Octobre 2010. Le détecteur Virgo est situé à Cascina en Italie, et les deux détecteurs LIGO sont situés aux États Unis, à Livingston en Louisianne et à Hanford dans l'état de Washington. Durant cette période les satellites gamma ont communiqué à travers le réseau GCN les informations sur la détection de 407 sursauts gamma. Étant donné que les détecteurs d'ondes gravitationnelles ne récoltent pas des données de qualité en permanence nous avons analysé les données de ces détecteurs en association avec seulement 153 sursauts gamma.

Nous avons analysé chacun des sursauts gamma séparément, pour chaque sursauts gamma nous avons ajusté par une procédure automatique les paramètres de l'analyse afin de séparer au mieux le bruit de fond des détecteurs au moment du sursaut d'un éventuel signal provenant de la direction dans

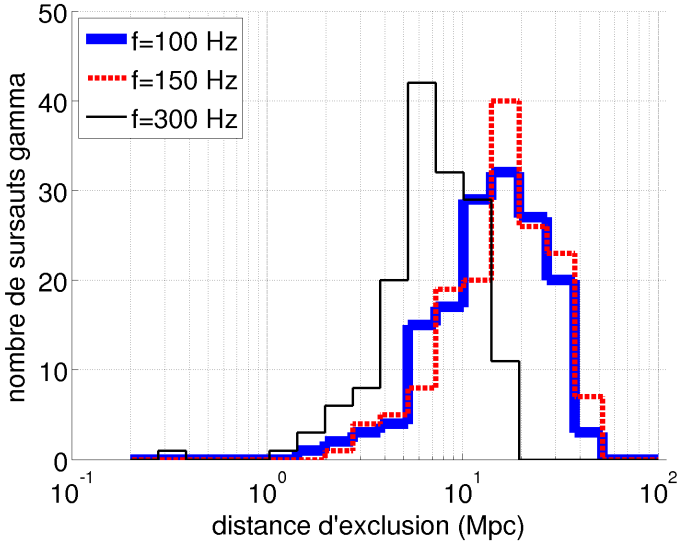

FIGURE 1 – Histogramme sur l'ensemble des 153 sursauts gamma analysés de la distance d'exclusion à 90% de confiance pour les 3 formes d'ondes gravitationelles correspondant au modèle d'effondrement stellaire. Les 3 fréquences des sinusoïdes avec enveloppe gaussienne sont : 100, 150 et 300 Hz. Pour chacune de ces formes d'ondes une émission d'une énergie de $10^{-2}\,M_{\odot}c^2$ sous forme d'ondes gravitationnelles est présupposée.

le ciel du sursaut. Nous avons aussi estimé le bruit de fond et la sensibilité de l'analyse pour chacun de ces sursauts.

L'ensemble des évènements trouvés pour ces 153 sursauts gamma est consistent avec la distribution de bruit de fond estimée, cet ensemble a une probabilité d'être due uniquement au bruit de fond de 25%. Étant donnée cette non détection nous avons établi des limites supérieures sur plusieurs modèles d'émission d'ondes gravitationnelles. En tout, nous avons considéré 5 familles de forme d'ondes : 2 correspondant à la coalescence d'astres compacts et 3 correspondant à l'effondrement d'étoiles massives en rotation.

Les deux familles de coalescence sont les binaires étoile à neutron - trou noir et les étoiles à neutron doubles. La distribution des masses des deux astres compacts utilisée pour chaque famille de binaire est représentative de notre connaissance sur la formation de ces systèmes binaires. Cette connaissance provient des observations radio et des simulations numériques de leur formation. La forme de l'onde est le résultat d'un développement perturbatif de la Relativité Générale.

Comme nous l'avons discuté précédemment, il n'existe pas de modèle précis de l'effondrement stellaire. Afin de caractériser d'une manière simple notre recherche d'ondes gravitationnelles, nous considérons une simple onde

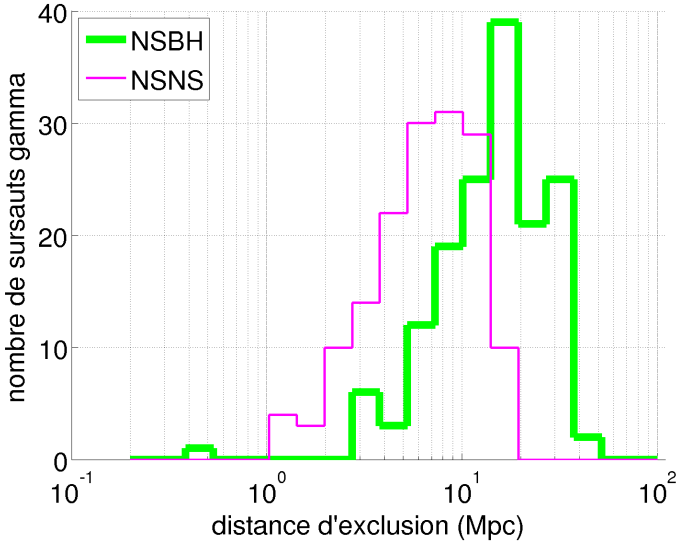

FIGURE 2 – Histogramme sur l'ensemble des 153 sursauts gamma analysés de la distance d'exclusion à 90% de confiance pour les 2 formes d'ondes correspondant au modèle de coalescence : coalescence de deux étoiles à neutrons (NSNS) et coalescence d'une étoile à neutron avec un trou noir (NSBH).

sinusoïdale polarisée circulairement avec une enveloppe gaussienne d'une dizaine de cycles. Cette forme devrait être caractéristique de l'émission par des instabilités rotationnelles, et nous choisissons l'amplitude de l'onde correspondante à la valeur haute de l'énergie gravitationnelles potentiellement émise, qui est de $E \sim 10^{-2}\,\mathrm{M}_\odot\mathrm{c}^2$. La bande de fréquence pour laquelle les détecteurs sont sensibles à des distances extra-galactiques est $60 - 500\,\mathrm{Hz}$, nous considérons donc 3 fréquence pour les sinusoïdes : 100, 150 et 300 Hz afin de couvrir cette bande.

Pour ces cinq familles les distributions des distances d'exclusions sur l'ensemble des sursauts gamma analysés sont montrées sur les figures 1 et 2. Typiquement nous obtenons que les sursauts sont à plus d'une dizaines de Mpc. Ces distances d'exclusions par sursauts peuvent être combinées en une exclusion sur des modèles de distribution en distance de la population de sursauts gamma.

Nous considérons un modèle simple de la population de sursauts gamma. Nous supposons que tous les sursauts gamma émettent une onde gravitationnelle sinusoïdale à 150 Hz avec une enveloppe gaussienne et une énergie émise de $10^{-2}\,\mathrm{M}_\odot\mathrm{c}^2$. Pour la distribution en distance nous considérons qu'une fraction f des sursauts est distribuée uniformément dans un volume de rayon R, le reste étant suffisamment loin pour pouvoir être considérer comme à l'infini. En combinant les courbes de sensibilités de chacun des sursauts nous

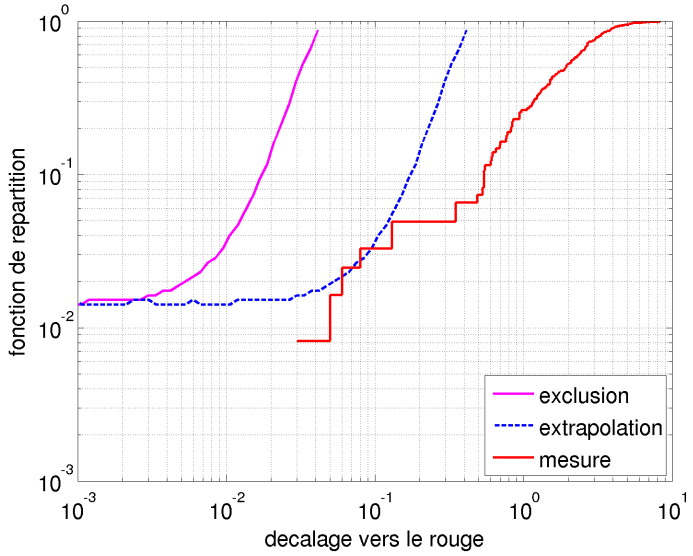

FIGURE 3 – Exclusion sur la fonction de répartition de la distance des sursauts gamma en supposant la forme d'onde sinusoïdale avec enveloppe gaussienne et une énergie émise de $10^{-2}\,M_\odot c^2$. L'espace des paramètres au dessus de la ligne violette est exclue avec 90% de confiance par la non observation d'ondes gravitationnelles associés aux 153 sursauts gamma analysés. La courbe rouge montre la distribution des décalages vers le rouge observée pour les sursauts gamma détectés par le satellite Swift entre le début de la mission (en 2005) et août 2010. La courbe pointillée bleue est l'extrapolation des résultats pour des détecteurs plus sensibles d'un facteur 10, qui est la sensibilité attendue pour les détecteurs de seconde génération.

obtenons une exclusion sur l'espace de paramètres (f, R). Cette exclusion est représentée sur la figure 3, avec la distance mesurée en terme de décalage vers le rouge. Pour référence, le décalage vers le rouge est proportionnel à la distance pour des distances inférieures à $\sim 1\,\mathrm{Gpc}$, et un décalage vers le rouge de 10^{-2} correspond à une distance de 40 Mpc. Cette exclusion se situe un facteur 10 en de ça des décalages vers le rouge mesurés pour les sursauts gamma, mais ce décalage n'est mesuré que pour $\sim 10\%$ des sursauts, donc pour la majorité des sursauts analysés il n'est pas connu.

Ce résultat montre qu'une détection d'ondes gravitationnelles associées aux sursauts gamma avec les données actuelles est peu probable. Néanmoins cette recherche était utile étant donné que la présence d'un sursaut gamma proche ($\lesssim 10\,\mathrm{Mpc}$) était possible (probabilité $\lesssim 1\%$). Nous avons aussi ouvert la route aux recherches futures qui devraient permettre de trouver des ondes gravitationnelles en utilisant les données des détecteurs d'ondes gravitationnelles de seconde génération. Ces détecteurs sont une amélioration

des détecteurs actuels, et ils devraient être mis en route à l'horizon 2015 avec une sensibilité améliorée d'un facteur 10, c'est-à-dire un nombre de détections attendues multiplié par un facteur[1] 1000. D'après la figure 3, la détection d'ondes gravitationnelles en coïncidence avec des sursauts gamma sera vraisemblable avec ces nouveaux détecteurs.

[1] Les détecteurs sont sensible à l'amplitude de l'onde une décroît proportionnellement à l'inverse de la distance.

Introduction

Gravitational waves are one of the early predictions of Einstein's theory of General Relativity which describes the gravitational interaction and the space-time structure. Nevertheless for the past 100 years gravitational waves have eluded any direct observations, and have only been seen as a missing energy in some close binary pulsar systems, which is with a precise agreement with General Relativity predictions. The main reason is that the gravitational interaction is very weak, and gravitational waves have only tiny effects on matter or any form of scientific apparatus.

However, this same property allows gravitational waves to be a direct messenger of the interior evolution of the most dense objects in the known Universe, as they are not obscured by the intervening matter between the object interior and the observer as other messengers such as photons and other particles are. Hence gravitational wave observations should open a new observational window on the Universe.

A particular example of systems which gravitational waves might probe are the progenitors of gamma-ray bursts, one of the most violent observed events. These progenitors convert a fraction of a solar mass directly into energy emitted under the form of a burst of photons that is a few seconds long. They are much brighter than for instance supernovae which emit the same amount of electromagnetic energy on a time scale of weeks. A gravitational wave observation associated to such an event should provide a definitive answer on the nature of the gamma-ray burst progenitors, which is a debated question in the community.

Different experiments aiming at detecting gravitational waves have been proposed and operated over the past 50 years. Currently the most sensitive detectors are Virgo and LIGO, and these detectors have jointly taken data in 2009-2010. In this thesis we present the results of a search for gravitational wave bursts associated with gamma-ray bursts in these data.

We begin in chapter 1 by a reminder on the main results of General Relativity concerning gravitational waves, especially on the properties of gravitational waves which are important for their detection. Afterwards, the detection principle of current interferometric gravitational wave detectors is exposed in chapter 2, along with the main sources of noise which limit the detectors sensitivity.

The next two chapters are devoted to astrophysical discussions. A rapid overview of the main expected gravitational wave sources is given in chapter 3, along with a more detailed discussion of the gravitational wave emission of potential gamma-ray bursts progenitors. The following chapter focuses on the process of gamma-ray bursts emission and how the electromagnetic observations motivate the particular gravitational wave parameter space over which we perform the search.

Afterwards follows a more technical discussion of gravitational wave data analysis. In chapter 5 we present the data analysis method used in the search for gravitational wave bursts associated with gamma-ray bursts. And in chapter 6 we discuss in detail the background estimation method for gravitational wave searches, a central element for defining the significance of a gravitational wave detection candidate.

In the last chapter we describe the analysis of the LIGO and Virgo data in a search for gravitational wave bursts associated with gamma-ray bursts. This description gives details about the used data set, the exact construction of the analysis pipeline and the obtained results which place some improved limits on the gamma-ray burst astrophysics.

Chapter 1

Gravitational Waves

Gravitational waves are one of the early predictions of Einstein's theory of General Relativity, a geometric framework which brings together special relativity and gravitation. Below we give a rapid overview of the parts of General relativity which are relevant to this thesis, mainly following the results given in Weinberg's "Gravitation and Cosmology" [1] with some inputs from other books [2, 3, 4, 5]. In the first three sections we sketch out the main steps of the derivation of gravitational waves from General Relativity without going into the details of how each step is actually performed, and in the last two sections we describe the properties of gravitational waves that are needed in the next chapters.

1.1 General Relativity

General Relativity describes space-time as a 4 dimensional manifold, with a pseudo-Riemannian metric. If one chooses a local coordinates system $\{x_\mu\}$, the infinitesimal length element $\mathrm{d}s$ is expressed as a function of the infinitesimal changes in coordinates $\mathrm{d}x^\mu$ and the metric tensor field $\underline{g}$ evaluated at the given point in space-time x

$$\mathrm{d}s^2(x) = g_{\mu\nu}(x)\mathrm{d}x^\mu \mathrm{d}x^\nu. \tag{1.1}$$

In this chapter we will denote by an underscore $\underline{X}$ tensors, by bold characters $\boldsymbol{X}$ 4-vectors and by normal characters with Greek subscripts $X_{\mu\nu\ldots}$ their components. For space only coordinates we use Latin subscripts, and for spatial 3-vectors the notation $\vec{X}$.

Properties of the gravitational field are encoded in the curvature of this metric, which for an infinite empty space without gravitation is the flat *Minkowski metric* $\underline{\eta}$, whose expression in the usual time-space (t, x, y, z)

Cartesian coordinate system is

$$\eta_{\mu\nu} = \begin{pmatrix} -1 & 0 & 0 & 0 \\ 0 & 1 & 0 & 0 \\ 0 & 0 & 1 & 0 \\ 0 & 0 & 0 & 1 \end{pmatrix}. \tag{1.2}$$

The force of gravitation is described by the metric, following the principle that free moving test masses follow geodesics, i.e. shortest paths according to the metric. The gravitational field is created by energy/mass present in space-time described by the energy-momentum tensor field $\underline{T}$ through the *Einstein equation*

$$G_{\mu\nu} = R_{\mu\nu} - \tfrac{1}{2} g_{\mu\nu} R = \frac{8\pi G}{c^4} T_{\mu\nu}, \tag{1.3}$$

where the left hand side of the equation is a second order differential operator of $\underline{g}$ which we detail below and the right hand side is the gravitational field source term. The constant in front of the energy-momentum tensor is chosen so that General Relativity yields the same results as Newtonian gravity in the slow moving, weak field regime. The expression of *Einstein tensor* $\underline{G}$ is more convolved to justify, however it can be shown that this is the only second order operator of $\underline{g}$ that is reasonable and that yields a flat metric in empty space [3].

To write explicitly the Einstein tensor in some coordinate system we introduce the *affine connexion*

$$\Gamma^{\sigma}_{\lambda\mu} = \tfrac{1}{2} g^{\nu\sigma} \left(\partial_\lambda g_{\mu\nu} + \partial_\mu g_{\lambda\nu} - \partial_\nu g_{\mu\lambda} \right). \tag{1.4}$$

It is not a tensor, but it arises naturally in the equation of motion of a test mass, and lets one to write compactly the *Riemann-Christoffel curvature tensor* as

$$R^{\lambda}{}_{\mu\nu\kappa} = \partial_\kappa \Gamma^{\lambda}_{\mu\nu} - \partial_\nu \Gamma^{\lambda}_{\mu\kappa} + \Gamma^{\eta}_{\mu\nu} \Gamma^{\lambda}_{\kappa\eta} - \Gamma^{\eta}_{\mu\kappa} \Gamma^{\lambda}_{\nu\eta}. \tag{1.5}$$

This tensor describes the parallel transport of a 4-vector around closed paths. It can also be shown [1] that all second order tensors that are linear in second derivative of the metric can be constructed from the Riemann tensor $R^{\lambda}{}_{\mu\nu\kappa}$ and lower order tensors. For instance, the expression of the Einstein tensor is

$$G_{\mu\nu} = R_{\mu\nu} - \tfrac{1}{2} g_{\mu\nu} R, \tag{1.6}$$

where the Ricci tensor $\underline{R}$ and the Ricci scalar R are defined by

$$R_{\mu\nu} = R^{\lambda}{}_{\mu\lambda\nu}, \tag{1.7a}$$

$$R = g^{\mu\nu} R_{\mu\nu}. \tag{1.7b}$$

For a better understanding of the Einstein equation, one can draw an analogy with the source equation of electrodynamics where a second order operator of the potential $\boldsymbol{A}$ is equal to the source current $\boldsymbol{J}$:

$$\partial_\mu \partial^\mu A^\nu - \partial_\mu \partial^\nu A^\mu = -\mu_0 J^\nu. \tag{1.8}$$

That is the relation between the field of the theory (respectively $\boldsymbol{A}$ and $\underline{g}$) and the source field (respectively $\boldsymbol{J}$ and $\underline{T}$) are analogous, and some results are similar. This analogy can be useful as many results such as the retarded potential solutions and gauge freedoms are similar in the two cases, but much simpler in the electrodynamics case.

1.2 Linearized General Relativity

The Einstein equation is non linear, however in the weak field limit, which is for instance a good approximation in Earth's neighborhood, the theory can be linearized, which greatly simplifies the description. In this section we will briefly derive the linearized theory of General Relativity.

The starting point of the linearized theory is to decompose the metric into the Minkowski metric and a weak deviation from it

$$g_{\mu\nu} = \eta_{\mu\nu} + h_{\mu\nu} \qquad \text{with} \quad |h_{\mu\nu}| \ll 1, \tag{1.9}$$

and then to keep only the terms linear in $h_{\mu\nu}$ while raising and lowering indices using $\eta_{\mu\nu}$. The linearized form of the Einstein equation is

$$\partial^\sigma \partial_\sigma h_{\mu\nu} - \partial_\lambda \partial_\mu h^\lambda{}_\nu - \partial_\lambda \partial_\nu h^\lambda{}_\mu + \partial_\mu \partial_\nu h^\lambda{}_\lambda = -\frac{16\pi G}{c^4}\left(T_{\mu\nu} - \tfrac{1}{2}\eta_{\mu\nu} T^\lambda{}_\lambda\right) \tag{1.10a}$$

$$= -\frac{16\pi G}{c^4}\bar{T}_{\mu\nu}, \tag{1.10b}$$

where we define $\underline{\bar{T}}$ as the traceless part of $\underline{T}$.

The components $g_{\mu\nu}$ of the metric depend on the particular choice of coordinates system. This arbitrary choice does not affect the General Relativity predictions and is only a gauge freedom of the metric description. To simplify the linearized Einstein equation one can choose an appropriate gauge condition which correspond to an infinitesimal change in coordinates $x'^\mu = x^\mu + \epsilon^\mu(x)$. This coordinates change modifies the metric perturbation by

$$h'^{\mu\nu} = h^{\mu\nu} - \eta^{\lambda\nu}\partial_\lambda \epsilon^\mu - \eta^{\rho\mu}\partial_\rho \epsilon^\nu. \tag{1.11}$$

The most convenient choice is the *radiation coordinate system* for which $g^{\mu\nu}\Gamma^\lambda_{\mu\nu} = 0$ and the needed coordinate change can be obtained to first order by solving

$$\partial^\sigma \partial_\sigma \epsilon_\nu = \partial_\mu h^\mu{}_\nu - \tfrac{1}{2}\partial_\nu h^\mu{}_\mu. \tag{1.12}$$

In this coordinate system the linearized Einstein equation has the simple form

$$\partial^\sigma \partial_\sigma h_{\mu\nu} = -\frac{16\pi G}{c^4}\bar{T}_{\mu\nu}, \tag{1.13}$$

for which a particular solution is the usual *retarded potential*.

To this retarded potential solution one can add any solution of the homogeneous radiation and gauge equations

$$\partial^\sigma \partial_\sigma h_{\mu\nu} = 0, \tag{1.14a}$$

$$\partial_\mu h^\mu{}_\nu = \tfrac{1}{2}\partial_\nu h^\mu{}_\mu. \tag{1.14b}$$

The homogeneous solutions are linear combinations of plane wave solutions of the form

$$h_{\mu\nu}(x) = \mathrm{Re}\left[H_{\mu\nu}\exp(ik_\lambda x^\lambda)\right], \tag{1.15}$$

where the amplitude components $H_{\mu\nu}$ and wave 4-vector $\boldsymbol{k}$ satisfy the relations

$$k_\mu k^\mu = 0, \tag{1.16a}$$

$$k_\mu H^\mu{}_\nu = \tfrac{1}{2}k_\nu H^\mu{}_\mu, \tag{1.16b}$$

that results from equations (1.14).

However the radiation coordinates system does not fix completely the choice of coordinates at first order, any further infinitesimal change ϵ_ν that satisfies $\partial^\sigma\partial_\sigma\epsilon_\nu = 0$ is permitted. In particular, one can use the coordinate change

$$\epsilon^\mu(x) = \mathrm{Re}\left[ie^\mu\exp(ik_\lambda x^\lambda)\right], \tag{1.17}$$

which yields the transformation

$$H'_{\mu\nu} = H_{\mu\nu} + k_\mu e_\nu + k_\nu e_\mu, \tag{1.18}$$

on the plane wave amplitude components.

The usual choice of gauge is the so called *transverse-traceless* gauge in which one chooses the transformation to obtain a field which is traceless: $H'^\mu{}_\mu = 0$ and orthogonal to a Galilean observer of velocity $\boldsymbol{u}$: $H'_{\mu\nu}u^\nu = 0$. This choice of gauge fixes all the 4 degrees of freedom of $\boldsymbol{\epsilon}$, and can be set independently for each plane wave by linearity.

To summarize, the wave equations and gauge conditions for a planar perturbation in vacuum (homogeneous equation) in a Galilean observer frame ($u^\mu = \delta^\mu_0$) are

$$k^\mu k_\mu = 0, \tag{1.19a}$$

$$k^\mu H_{\mu\nu} = 0, \tag{1.19b}$$

$$H^\mu{}_\mu = 0, \tag{1.19c}$$

$$H_{0\mu} = 0. \tag{1.19d}$$

Only eight of the nine gauge conditions are independent[1], and $H_{\mu\nu}$ is a symmetric 2-tensor that has *a priori* 10 degrees of freedom. Thus there

[1] $H_{0\mu} = 0$ implies $k^\mu H_{\mu 0} = 0$

are only 2 physical degrees of freedom, the number of degrees of freedom once the gauge conditions are fixed. They represent the two polarization of gravitational waves and are called *plus* and *cross polarizations*.

In particular if one chooses a plane wave along the z-axis, i.e. $k_\mu = (\omega, 0, 0, \omega/c)$, the planar solution has the form

$$h_{\mu\nu}^{TT} = \mathrm{Re}\left\{ \begin{pmatrix} 0 & 0 & 0 & 0 \\ 0 & H_+ & H_\times & 0 \\ 0 & H_\times & -H_+ & 0 \\ 0 & 0 & 0 & 0 \end{pmatrix} \exp[i\omega(z/c - t)] \right\}, \tag{1.20}$$

where "TT" denotes the transverse-traceless gauge.

1.3 Generation of Gravitational Waves

In principle, gravitational waves are produced by any energy or matter form which is described by an energy-momentum tensor that changes with time. Here we will focus on the gravitational field produced by a localized source (confined within a radius R) seen from a large distance, which is the astrophysically relevant scenario. Similarly to electromagnetism, we perform a multipole expansion of the source radiation and keep only the dominant term. We place the spatial origin in the source, and denote $\vec{x}$ the observer spatial position, $\widehat{x} = \vec{x}/r$ the normalized direction to it and $\vec{x}'$ the vector pointing to a particular point in the source. Under the considered scenario, we can use the approximation $|\vec{x} - \vec{x}'| \simeq r - \vec{x}' \cdot \widehat{x}$ and $T_{\mu\nu} = 0$ at infinity, which yield the integral form of the retarded potential solution:

$$h_{\mu\nu}(\vec{x}, t) = \frac{4G}{c^4} \int \frac{\mathrm{d}^3 x'}{|\vec{x} - \vec{x}'|} \bar{T}_{\mu\nu}\left(\vec{x}', t - \frac{|\vec{x} - \vec{x}'|}{c}\right) \tag{1.21a}$$

$$= \frac{4G}{c^4} \int \frac{\mathrm{d}\omega \mathrm{d}^3 x'}{|\vec{x} - \vec{x}'|} \bar{T}_{\mu\nu}(\vec{x}', \omega) \exp\left[-i\omega t + i\omega |\vec{x} - \vec{x}'|/c\right] \tag{1.21b}$$

$$\simeq \frac{4G}{rc^4} \int \mathrm{d}\omega \exp[i\omega(r/c - t)] \int \mathrm{d}^3 x' \bar{T}_{\mu\nu}(\vec{x}', \omega) \exp(-i\omega \widehat{x} \cdot \vec{x}'/c) \tag{1.21c}$$

$$= \frac{4G}{rc^4} \int \mathrm{d}\omega \exp[i\omega(r/c - t)] \bar{T}_{\mu\nu}(\vec{k}, \omega), \tag{1.21d}$$

where $\vec{k} = \frac{\omega}{c}\widehat{x}$. Hence, the metric perturbation (gravitational waves) in the far field regime is a superposition of planar waves.

The Fourier components of energy-momentum tensors are hard to compute in most cases, however at first order one can replace them with quadrupolar moments when the slow-motion approximation applies ($\frac{v}{c} \ll 1$ or $\omega R \ll 1$).

In this quadrupole radiation approximation

$$T_{ij}(\vec{k},\omega) \simeq \int T_{ij}(\vec{x},\omega)\mathrm{d}^3x \tag{1.22a}$$

$$= -\frac{\omega^2}{2c^2}\int x_i x_j T^{00}(\vec{x},\omega)\mathrm{d}^3x \tag{1.22b}$$

$$= -\frac{\omega^2}{2c^2}D_{ij}(\omega), \tag{1.22c}$$

where the last line is just the definition of the energy quadrupolar moment. In the derivation we have used the Gauss theorem and the conservation of the energy-momentum tensor to express the T_{ij} as a function of the time-time component only, and T_{ij} are the only components needed in the transverse-traceless gauge. In the slow-motion approximation the time-time component is dominated by the rest mass density $T_{00} \simeq \rho c^2$, hence we are essentially assuming a rigid body representation of the source, where the second moments of the mass distribution are naturally relevant, and the space and time coordinates are separated. Hence in the quadrupole radiation approximation the source can be described as a non relativistic object, and the mass quadrupole is the analogue of the electric dipole in electromagnetism, both are the lowest order terms in the multipole expansion of wave emission.

Obtaining the metric perturbation in the transverse-traceless gauge from the result above is rather tedious, but it leads to a relatively simple equation

$$h_{jk}^{TT} = \frac{2G}{rc^4}P_{jkmn}\ddot{I}^{mn}(t-\tfrac{r}{c}), \tag{1.23}$$

where the time derivative is defined as $\dot{X} = c\partial_0 X$ and we use the *transverse-traceless projector*

$$P_{jkmn} = \Pi_{jm}\Pi_{kn} - \tfrac{1}{2}\Pi_{jk}\Pi_{mn} \quad \text{with} \quad \Pi_{ij} = \delta_{ij} - \widehat{x}_i\widehat{x}_j; \quad \widehat{x}_i = x^i/r, \tag{1.24}$$

and the *reduced quadrupolar moment*

$$I_{ij} = \int (x_i x_j - \tfrac{1}{3}\delta_{ij}\delta_{km}x^k x^m)\rho(x)\mathrm{d}^3x. \tag{1.25}$$

The transverse-traceless projector is clearly constructed using the projector Π on the plane orthogonal to the propagation direction $\widehat{x}$, as the transverse part of I from which we remove the trace.

Given a metric perturbation, it is interesting to know how much energy it carries, in order to estimate the maximal amplitude that can be created by a source given its energetics constraint. The energy-momentum tensor $\underline{t}$ of a gravitational wave can be derived from the Einstein equation. If one expands the Ricci tensor $\underline{R}$ in terms of $\underline{h}$, the second order term $R^{(2)}_{\mu\nu}$ yields the dominant contribution

$$t_{\mu\nu} \simeq -\frac{c^5}{8\pi G}\left[R^{(2)}_{\mu\nu} - \tfrac{1}{2}\eta_{\mu\nu}\eta^{\lambda\rho}R^{(2)}_{\lambda\rho}\right], \tag{1.26}$$

which, expressed in the transverse-traceless gauge and averaged over several wave cycles, is simply the classical wave energy flux

$$t_{00} = \frac{c^5}{32\pi G}\left\langle \sum_{j,k} \partial_0 h_{jk}^{TT}\, \partial_0 h_{jk}^{TT} \right\rangle = \frac{c^3}{16\pi G}\left\langle \left(\dot{h}_+\right)^2 + \left(\dot{h}_\times\right)^2 \right\rangle. \tag{1.27}$$

Whenever the source can be well described by the quadrupolar radiation approximation discussed above the total emitted power P_{GW} can be obtained using (1.23) and (1.27), which after integrating over the sky yields

$$P_{\mathrm{GW}} = \frac{G}{5c^5}\left\langle \dddot{I}_{mn}\, \dddot{I}^{mn} \right\rangle. \tag{1.28}$$

In order to find which properties of a source are relevant to produce large amounts of gravitational waves we can perform a dimensional analysis. Assuming that our source has typical size R and evolves on time scale T, the quadrupolar momentum is $\dddot{I} = \epsilon \frac{MR^2}{T^3}$ where $\epsilon < 1$ and denotes the typical asphericity of I. Using the speed of the object $v = \frac{R}{T}$ and its Schwartzschild radius $R_S = \frac{2GM}{c^2}$, the emitted power can be expressed as

$$P_{\mathrm{GW}} \propto \frac{c^5}{G}\epsilon^2 \left(\frac{R_S}{R}\right)^2 \left(\frac{v}{c}\right)^6 \simeq 2\times 10^5 \left(\frac{\epsilon}{1}\right)^2 \left(\frac{R_S}{R}\right)^2 \left(\frac{v}{c}\right)^6 \mathrm{M}_\odot \mathrm{c}^2 \mathrm{s}^{-1}. \tag{1.29}$$

Hence a good source of gravitational waves is asymmetric ($\epsilon \sim 1$), compact ($R \sim R_S$) and relativistic ($v \sim c$). We can also obtain an obvious upper limit on the total emitted power of any source by setting all those parameters to 1.

1.4 Gravitational waves properties

After glancing at how gravitational waves are generated the next question to answer is what are their effects on an observer located on Earth.

The simplest physical system we may consider is a set of free-falling test masses which are not subject to any forces (beside gravitation). Then each test mass follows the geodesics equation

$$\frac{\mathrm{d}^2 x^\mu}{\mathrm{d}t^2} + \Gamma^\mu_{\nu\rho}\frac{\mathrm{d}x^\nu}{\mathrm{d}t}\frac{\mathrm{d}x^\rho}{\mathrm{d}t} = 0, \tag{1.30}$$

which in transverse-traceless coordinates yields at first order [2]

$$\frac{\mathrm{d}^2 x^i}{\mathrm{d}t^2} = 0. \tag{1.31}$$

The transverse-traceless coordinates are adapted to gravitational waves and are following the motion of free falling masses. In this coordinate system test masses are fixed and only the distance (light travel time) is changing.

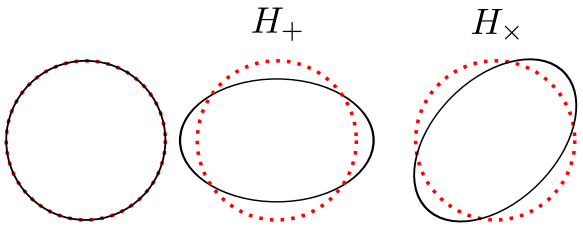

Figure 1.1: Initial configuration and deformation by an h_+ and $h_\times$ perturbation of a ring of free test masses. The red dashed circle is kept as a reference of the initial ring.

This point of view is the most appropriate for interferometric observation of gravitational waves.

Another point of view, which is more Newtonian like and allows to treat similarly gravitation and other forces, is to choose the *Fermi coordinates*. In these coordinates the metric is at first order Minkowski, and the coordinates of test masses follow usual Newton equations with a gravitational wave tidal pseudo-force:

$$\frac{\mathrm{d}^2 X^i}{\mathrm{d}t^2} \simeq \frac{1}{2}\frac{\partial^2 h_{ij}^{TT}}{\partial t^2} X^j, \tag{1.32}$$

which is valid as long as the region considered is small compared to the incoming gravitational wavelength. This approach is the most convenient for comparing gravitational waves and noise sources in a detector, and also for visualizing gravitational wave effects on these test masses.

In the previous section we have shown that gravitational waves are spherical waves in the far field regime, and are well approximated by planar waves if observed in a region of space much smaller than the distance to the source. Hence, in the transverse-traceless gauge for a wave propagating along the z axis we can write the metric as a function of the two polarizations

$$g_{\mu\nu}^{TT} = \begin{pmatrix} -1 & 0 & 0 & 0 \\ 0 & 1+h_+(t) & h_\times(t) & 0 \\ 0 & h_\times(t) & 1-h_+(t) & 0 \\ 0 & 0 & 0 & 1 \end{pmatrix}. \tag{1.33}$$

and the equations of motion (1.32) can be easily integrated and yield

$$X(t) = X(0) + \tfrac{1}{2}h_+(t)X(0) + \tfrac{1}{2}h_\times(t)Y(0), \tag{1.34a}$$
$$Y(t) = Y(0) + \tfrac{1}{2}h_\times(t)X(0) - \tfrac{1}{2}h_+(t)Y(0), \tag{1.34b}$$
$$Z(t) = Z(0). \tag{1.34c}$$

The effects of a positive h_+ or $h_\times$ perturbation on a ring of test masses can be seen on figure 1.1. A plus polarized perturbation stretches the ring along the x axis and squeezes along the y axis, and reversely squeezes along the

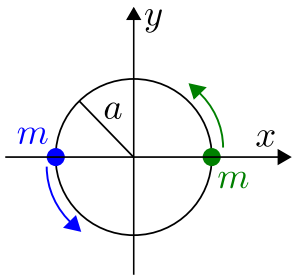

Figure 1.2: Description of the example toy model of two rotating point masses.

x axis and stretches along the y half a period later when the sign of the perturbation flips. The cross polarization has the same effect but rotated by 45°.

1.5 Example of Gravitational Radiation

As an example of the above results, we will study here a simple toy model of gravitational radiation from a pair of rotating point masses shown of figure 1.2. This gives a good illustration of how objects radiate gravitational waves and how to read the gravitational waves polarization by simply looking at the mass quadrupole evolution.

The equations of motion for two point objects of coordinates (x, y, z) and (x', y', z') with same masses m rotating in the Oxy plane at a distance a from O with frequency ω are

$$x(t) = a\cos(\omega t) \qquad x'(t) = -a\cos(\omega t) \tag{1.35a}$$
$$y(t) = a\sin(\omega t) \qquad y'(t) = -a\sin(\omega t) \tag{1.35b}$$
$$z(t) = 0 \qquad z'(t) = 0, \tag{1.35c}$$

which yield a reduced quadrupolar moment (1.25) of the system

$$I = \begin{pmatrix} ma^2\left(\frac{1}{3} + \cos(2\omega t)\right) & ma^2\sin(2\omega t) & 0 \\ ma^2\sin(2\omega t) & ma^2\left(\frac{1}{3} - \cos(2\omega t)\right) & 0 \\ 0 & 0 & 0 \end{pmatrix}. \tag{1.36}$$

One can immediately notice the 2ω dependence which results in gravitational waves being emitted at twice the rotational frequency as we will see below.

In general, the expression of the transverse-traceless projector is not simple and is expressed in matricial form as

$$I^{TT} = \Pi I \Pi - \tfrac{1}{2}\Pi\,\mathrm{Tr}\,(\Pi I)\,. \tag{1.37}$$

However, for some direction of propagation the Π matrix has a very simple form. For instance for propagation along the z and x axis their form is

$$\Pi_z = \begin{pmatrix} 1 & 0 & 0 \\ 0 & 1 & 0 \\ 0 & 0 & 0 \end{pmatrix}, \qquad \Pi_x = \begin{pmatrix} 0 & 0 & 0 \\ 0 & 1 & 0 \\ 0 & 0 & 1 \end{pmatrix}, \tag{1.38}$$

and yield a projection

$$I_z^{TT} = \begin{pmatrix} \frac{1}{2}(I_{xx} - I_{yy}) & I_{xy} & 0 \\ I_{xy} & \frac{1}{2}(I_{yy} - I_{xx}) & 0 \\ 0 & 0 & 0 \end{pmatrix}, \qquad I_x^{TT} = \begin{pmatrix} 0 & 0 & 0 \\ 0 & \frac{1}{2}I_{yy} & 0 \\ 0 & 0 & -\frac{1}{2}I_{yy} \end{pmatrix}. \tag{1.39}$$

Hence using (1.23) and keeping in mind that the polarization is transverse to the direction of propagation, the gravitational waveform from a *face-on* (seen along the z direction) rotating "binary" is

$$h_+ = -\frac{2G}{rc^4} m a^2 \omega_{\mathrm{GW}}^2 \cos(\omega_{\mathrm{GW}} t_{\mathrm{ret}}) \tag{1.40a}$$

$$h_\times = -\frac{2G}{rc^4} m a^2 \omega_{\mathrm{GW}}^2 \sin(\omega_{\mathrm{GW}} t_{\mathrm{ret}}), \tag{1.40b}$$

and from an *edge-on* (seen from the x side) "binary" is

$$h_+ = -\frac{G}{rc^4} m a^2 \omega_{\mathrm{GW}}^2 \cos(\omega_{\mathrm{GW}} t_{\mathrm{ret}}) \tag{1.41a}$$

$$h_\times = 0, \tag{1.41b}$$

where we used the retarded time $t_{\mathrm{ret}} = t - \frac{r}{c}$, and the gravitational wave angular frequency $\omega_{\mathrm{GW}} = 2\omega$.

A good way of interpreting these results is to compare the evolution of the quadrupole moment with the deformation of a ring of test masses orthogonal to the direction of propagation as shown on figure 1.3. Seen from above (along the z axis) the perturbation is rotating with the object, seen from the side (along the x axis) the deformation follows the linear movement of the two point masses. The main conclusion to draw from this toy example which apply for any rigidly rotating body are:

- The gravitational wave frequency is twice the rotation frequency.
- A face-on "binary" produces circularly polarized waves.
- An edge-on "binary" produces linearly polarized waves.

As this example shows only the projection of the source mass evolution on the celestial sphere of the observer is relevant for the observed gravitational wave. This argument explain also why an axi-symmetric source creates only gravitational waves linearly polarized along the symmetry axis, and for an

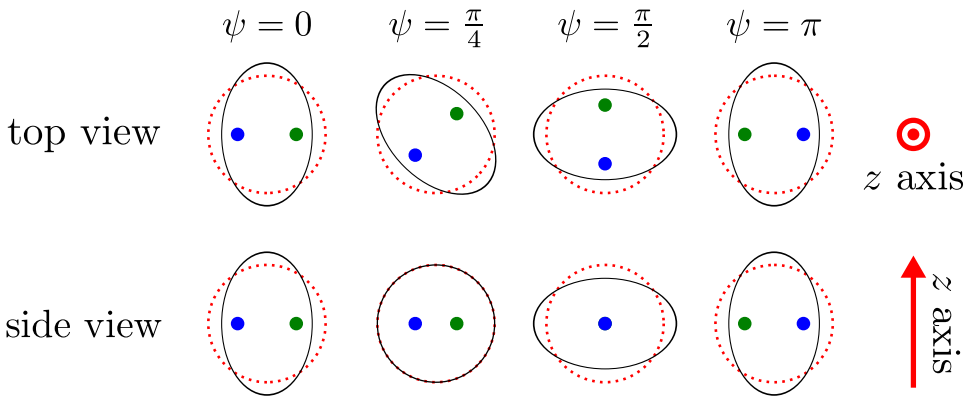

Figure 1.3: Representation of a free mass ring deformed by a rotating "binary" system in the Oxy plane. Both a top view along the z axis and a side view along the x axis are shown. The red dashed line shows the initial ring and the black solid line its deformation at different rotation phases ψ. The blue and green dot represent the retarded position of the two radiating masses. After half a rotation ($\psi = \pi$) the gravitational perturbation is back to its initial state, the wave is clearly evolving at twice the rotation frequency.

observer along the symmetry axis the motion is seen as radially symmetric and thus do not create any gravitational wave.

We can also compare the gravitational wave amplitude between a laboratory generator and a coalescence of neutron stars. A plausible laboratory set up with a pair of 1 ton masses (or a bar) separated by 10 m and rotating at 50 Hz observed from a 100 m distance leads to an amplitude $h \sim 6 \times 10^{-36}$ which is quite a small number. However, a pair of 3×10^{30} kg neutron stars separated by 100 km and seen from a distance of 100 Mpc create an amplitude $h \sim 5 \times 10^{-20}$, which is a more optimistic goal. This explains why all of the gravitational wave sources which are considered are of astrophysical origin.

Simple considerations based on the total available energy are useful in finding likely astrophysical sources. For instance, using the quadrupolar momenta (1.36) in the expression of the radiated power (1.28) we obtain

$$P_{\mathrm{GW}} = \frac{128G}{5c^5} m^2 a^4 \omega^6. \tag{1.42}$$

For an on axis observer the emitted power can be rewritten in terms of gravitational wave amplitudes as

$$h_+^2 + h_\times^2 = \frac{1}{\omega_{\mathrm{GW}}^2} \frac{10G}{r^2 c^3} P_{\mathrm{GW}}. \tag{1.43}$$

We can also relate the total emitted energy E_{GW} to the integrated amplitude

$$h_{\mathrm{rss}}^2 = \int (h_+^2 + h_\times^2)\mathrm{d}t \simeq \frac{1}{\omega_{\mathrm{GW}}^2}\frac{10G}{r^2c^3}E_{\mathrm{GW}}, \tag{1.44}$$

where rss stands for "root-sum-squared". This relation justifies using the h_{rss} quantity as a characterization of the gravitational wave amplitude: it has a direct relationship with the total energy emitted by the source and is an intrinsic property of the wave. As we will see in section 2.3 it can also be easily compared with detector noise. One should note that the frequency dependence is not obvious to interpret: at fixed energy emission lower frequency means higher amplitude, but at fixed quadrupolar deformation the observed amplitude is larger at high frequency.

In the general case where the observed is not optimally positioned or the source is not rotational the h_{rss} - energy relation takes the form

$$h_{\mathrm{rss}}^2 \simeq \frac{\alpha}{\omega_{\mathrm{GW}}^2}\frac{G}{r^2c^3}E_{\mathrm{GW}}, \tag{1.45}$$

where α is a factor of the order of unity which depends on the details of the geometry for the considered problem.

As an numerical example, for a source located at $r = 10\,\mathrm{Mpc}$ emitting $E_{\mathrm{GW}} = 0.01\,\mathrm{M}_\odot\mathrm{c}^2$ at $f_{\mathrm{GW}} = 150\,\mathrm{Hz}$, the observed on-axis-amplitude is $h_{\mathrm{rss}} = 7.5{\times}10^{-22}\,\mathrm{Hz}^{-1/2}$, which is comparable to the sensitivity of currently operating detectors shown on figure 7.1.

For completeness, if the "binary" system is seen from an inclination angle ι the waveform is [6]

$$\begin{pmatrix} h_+(t) \\ h_\times(t) \end{pmatrix} = -\frac{G}{rc^4}ma^2\omega_{\mathrm{GW}}^2 \begin{pmatrix} (1+\cos^2\iota)\cos(\omega_{\mathrm{GW}}t_{\mathrm{ret}}) \\ 2\cos\iota\sin(\omega_{\mathrm{GW}}t_{\mathrm{ret}}) \end{pmatrix}, \tag{1.46}$$

where the plus polarization is defined along the projection of the source x and y axis onto the direction of propagation.

Chapter 2

Gravitational Wave Detectors

In section 1.4 of the previous chapter we have discussed general properties of gravitational waves. Armed with this knowledge we can study instruments which are aiming at detecting gravitational waves. Two main detection schemes have been developed over the years.

The first scheme was initiated and developed in the sixties by Joe Weber [7]. It consists of a solid bar that is stressed by a passing gravitational wave. In its first incarnation the bar stress was read out with a piezo-electric crystal. This type of detector is sensitive in a relatively narrow band (much less than 100 Hz) around the main resonant frequency of the bar, which is usually somewhere in the $700 - 1000$ Hz range. Bar detectors technology have been improved and refined over time and attained at the end of the nineties a sensitivity of $5 - 10 \times 10^{-22}\,\mathrm{Hz}^{-1/2}$ in a ~ 1 Hz band [8].

The second scheme uses an enhanced Michelson interferometer which is directly sensitive to space-time deformation. First efforts in that direction started in the seventies [9] and have continued since then. Among the advantages of an interferometer is its scalability, the effective gravitational pseudo-force (1.32) scales linearly with the size of the instrument, which leads to the kilometer scale instruments currently operated. The latest improvements in design and components of this kind of instruments lead to a sensitivity of $2 - 5 \times 10^{-23}\,\mathrm{Hz}^{-1/2}$ over a few 100 Hz band and a good sensitivity between a few dozen Hz and a few kHz, as can be seen on figure 7.1 which shows the current sensitivity of LIGO and Virgo detectors.

In this chapter we focus on the working principles of interferometric detectors, given that interferometric detectors are currently more sensitive than bar detectors and are expected to detect gravitational waves in the coming years. Unless noted otherwise the presented results are taken from Saulson's book on that subject [10]. As an illustration of these principles we will use the parameters of the Virgo detector during the second Virgo Science Run (VSR2). We defer to section 7.1 for a more detailed description of the performance of the Virgo and LIGO detectors in 2009-2010.

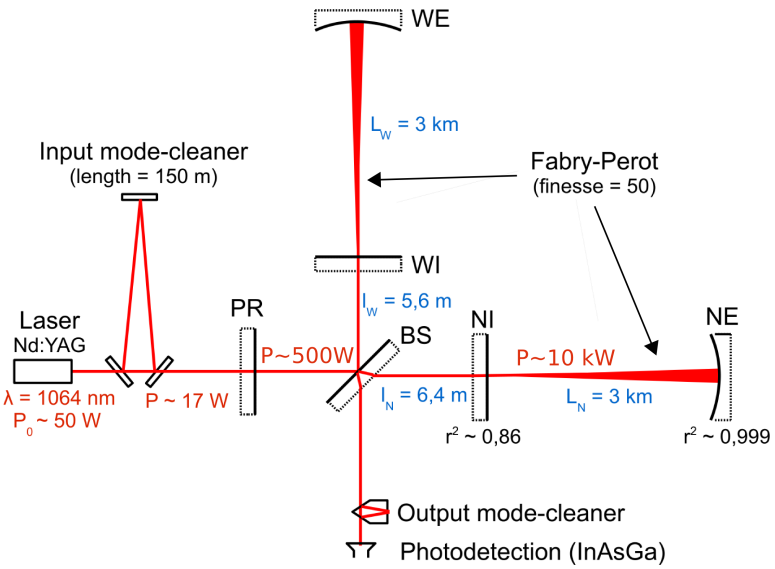

Figure 2.1: Optical scheme of Virgo during VSR2 [11]. Solid lines correspond to sides of mirrors which are reflectively coated. The interferometer is composed of an input laser with wavelength 1.06 μm, which passes through a mode cleaner cavity. The light is split by the beamer-splitter and stored in two 3 kilometer long Fabry-Perot cavities. Each cavity is formed of an input mirror (NI or WI) and an end mirror (NE or WE). Light that is reflected back by the cavities is recombined by the beam-splitter into two beams, one which travels back toward the laser and is reflected by the power recycling mirror (PR), and one which passes through the output mode cleaner and is absorbed by the photo-detector.

2.1 Detection principle

As discussed in section 1.4 the main effect of a passing gravitational wave is a change in "distance" (as measured by light travel time) between free-falling masses, and this change is opposite in two orthogonal directions. The output of a Michelson interferometer is directly related to the differential length between the beam-splitter and the mirror at the end of its orthogonal arms, and is thus perfectly adapted to measure this space-time deformation, as long as the beam-splitter and mirrors can be treated as free-falling masses. In principle, a single arm could be used to measure the deformation, however a differential measurement permits to cancel some of the measurement noise and to achieve a better sensitivity.

A detailed optical scheme of the Virgo detector in 2009 is shown on figure 2.1; we describe the relevance of different parts of this scheme in the following sections. However to understand the detection principle only some of them are needed. The crucial elements are the laser, the photodector and

three optical elements: the beam-splitter (BS) and end of arms mirrors noted WE (west-end) and NE (north-end) on the figure. This constitutes a simple Michelson interferometer. In radiation coordinates the three optical elements are fixed, and we choose the coordinates origin to be on the beam-splitter and the x and y axis along the two arms.

Assuming a plus polarized gravitational wave incoming from the z direction (normal incidence), the metric at a given time t is given by (1.33) which yields the equation for light propagation

$$0 = \mathrm{d}s^2 = g^{TT}_{\mu\nu}\mathrm{d}x^\mu \mathrm{d}x^\nu \tag{2.1a}$$

$$0 = -c^2\mathrm{d}t^2 + (1 + h_+(t))\mathrm{d}x^2 \quad \text{for the arm along } x \tag{2.1b}$$

$$0 = -c^2\mathrm{d}t^2 + (1 - h_+(t))\mathrm{d}y^2 \quad \text{for the arm along } y. \tag{2.1c}$$

That translates for an arm length L_0 into an optical path in the arm along the x direction

$$L_x = \int c\mathrm{d}t = \int_0^{L_0} \sqrt{1 + s\left(t + \frac{x}{c}\right)}\mathrm{d}x \simeq \int_0^{L_0} \left(1 + \tfrac{1}{2}s\left(t + \frac{x}{c}\right)\right)\mathrm{d}x. \tag{2.2}$$

For our particular case $\frac{x}{c} \leq \frac{L_0}{c} = 10\,\mu\mathrm{s}$ which is much shorter than the typical period of our signal in the $10-10^4\,\mathrm{Hz}$ sensitive band. Hence one can perform a long wavelength approximation $h_+(t + \frac{x}{c}) \simeq h_+(t)$, and obtain

$$L_x = L_0 + \tfrac{1}{2}L_0 h_+(t). \tag{2.3}$$

Similarly, for the second arm one obtains

$$L_y = L_0 - \tfrac{1}{2}L_0 h_+(t). \tag{2.4}$$

To study the exact effect of this approximation we look at the particular case of a monochromatic wave $h_+(t) = h_0 \cos\omega t$, for which the rightmost term in equation (2.2) yields

$$L_x \simeq L_0 + \tfrac{1}{2}h_0 L_0 \frac{\sin\left(\omega\left(t + \frac{L_0}{c}\right)\right) - \sin\omega t}{\frac{\omega L_0}{c}} \tag{2.5a}$$

$$= L_0 + \tfrac{1}{2}L_0 h_0 \cos\left(\omega\left(t + \frac{L_0}{2c}\right)\right) + O\left(\left(\frac{\omega L_0}{c}\right)^2\right). \tag{2.5b}$$

Thus the long wavelength approximation induce at first order a frequency dependent phase shift $\delta = \frac{\omega L_0}{2c}$, which can be safely discarded up to a few kHz.

With this approximation the gravitational wave induced phase shift between the two arms can be expressed as

$$\Delta\varphi = \frac{2\pi}{\lambda}\left(2L_x - 2L_y\right) = h_+(t)\frac{4\pi L_0}{\lambda}, \tag{2.6}$$

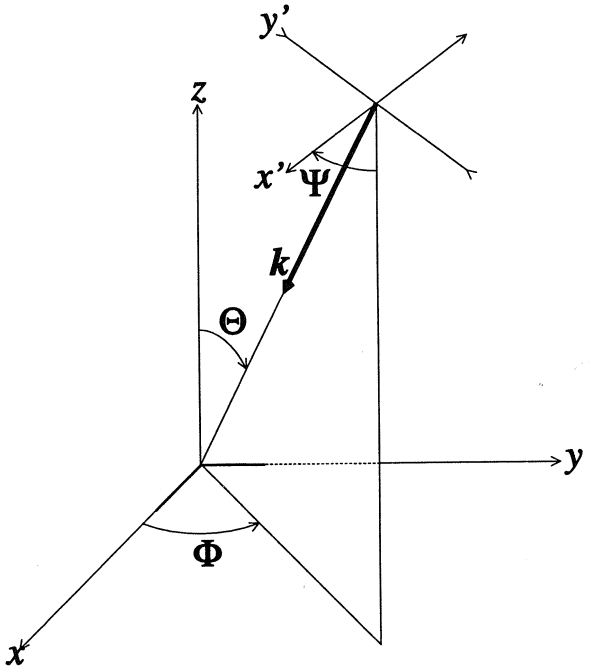

Figure 2.2: Coordinate used to describe antenna pattern functions. The sky location angles (Θ, Φ) and the polarization reference angle Ψ are shown. The (x, y, z) coordinates are fixed to the interferometer, that is the two arms are along the Ox and Oy axes, and the (x', y', z') coordinates are the ones used to define the gravitational wave propagation and polarization. Figure taken from [10].

where λ is the laser wavelength. Reversely this allows us to define a *gravitational wave signal*

$$s(t) = \frac{\lambda}{4\pi L_0}\Delta\varphi = \frac{L_x - L_y}{L_0} = h_+(t). \tag{2.7}$$

In the general case of a gravitational wave with any polarization incoming from a sky location (Θ, Φ), the computation of the signal involves a few projections and yields [12]

$$s(t) = F^+(\Theta, \Phi, \Psi)h_+(t) + F^\times(\Theta, \Phi, \Psi)h_\times(t), \tag{2.8}$$

where the *antenna pattern* functions are

$$F^+(\Theta, \Phi, \Psi) = \tfrac{1}{2}(1 + \cos^2\Theta)\cos 2\Phi \cos 2\Psi - \cos\Theta \sin 2\Phi \sin 2\Psi \tag{2.9a}$$
$$F^\times(\Theta, \Phi, \Psi) = \tfrac{1}{2}(1 + \cos^2\Theta)\cos 2\Phi \sin 2\Psi + \cos\Theta \sin 2\Phi \cos 2\Psi \tag{2.9b}$$

and Ψ is the angle between the projection of the x arm onto the plane orthogonal to the direction of propagation and the x' axis along which the plus polarization is defined as shown on figure 2.2. It should be noted that an interferometer is sensitive only to a single linear combination of the two polarizations, it is completely insensitive to the orthogonal combination which is a solution of

$$F^{+}(\Theta,\Phi,\Psi)h_{+}(t) + F^{\times}(\Theta,\Phi,\Psi)h_{\times}(t) = 0. \tag{2.10}$$

The output light power of a Michelson interferometer is a function of the phase shift between its arms, and is recorded using a set of photo-diodes which, after proper calibration of the instrument, yields the *detector strain* time series

$$d(t) = F^{+}(\Theta,\Phi,\Psi)h_{+}(t) + F^{\times}(\Theta,\Phi,\Psi)h_{\times}(t) + n(t) = s(t) + n(t), \tag{2.11}$$

with $n(t)$ denoting the detector noise. This dimensionless time series is the primary output of a gravitational wave observatory. When working on gravitational wave data three different dimensionless time series can be considered:

- The gravitational wave itself which is described by the two polarizations time series $(h_{+}(t), h_{\times}(t))$.
- The signal $s(t)$ that gravitational waves produce in an interferometric gravitational wave detector that is given in equation (2.8).
- The data $d(t)$ that are measured by a gravitational wave experiment which contain potential signals buried in detector noise.

To avoid confusion between these three quantities we will use the above notations throughout the thesis and avoid using $h(t)$ which could stand for any of these three.

For the simple Michelson configuration considered so far the signal $s(t) \lesssim 10^{-21}$ produced by a reasonable gravitational wave source corresponds to a tiny phase difference $\Delta\varphi \lesssim 10^{-11}$ rad. Hence reducing the noise, that is improving the sensitivity, is the main preoccupation of people involved in a gravitational wave experiment. Sources of noise are numerous and are usually classified into three families: environmental noises due to external perturbation on the detector, technical noises due to the equipments used and fundamental noises due to the physical principles used to perform the measurement. The noise term $n(t)$ considered above is the sum of all these different contributions. The noise reduction work starts with designing more sensitive optical configuration and more effective environmental isolation systems, continues with understanding and removing sources of technical noise once the detectors are constructed, and ends with improving data analysis techniques.

In the next sections we will have a short overview of the most important sources of noise and how they are driving different aspects of current interferometers design, which is a refined enhancement over the original Michelson interferometer.

2.2 Interferometer fundamental noise

In many cases the different contributions to the detector noise $n(t)$ are well described by a colored Gaussian process, that is a Gaussian process that has a non flat spectrum or equivalently that is autocorrelated. The total noise $n(t)$ is just the sum of these different contributions which in most cases can be considered as independent.

With this noise model, the effect of a given noise source $n_i(t)$ on extracting a signal $s(t)$ from the data $d(t)$ is completely characterized by the power spectral density $S_i(f)$. The power spectral density can be obtained simply from the time series $n_i(t)$ by two equivalent methods based on the Fourier transform: the power spectrum is the square of the modulus of Fourier coefficients of the noise time series

$$S_i(f) = |\tilde{n}_i(f)|^2 + |\tilde{n}_i(-f)|^2 = 2|\tilde{n}_i(f)|^2, \tag{2.12}$$

but it is also the Fourier transform of twice the auto-correlation

$$C_i(\tau) = \int_{-\infty}^{\infty} n_i(t) n_i(\tau - t) \mathrm{d}t. \tag{2.13}$$

Throughout this thesis we will use only one-sided spectral densities which are defined only for positive frequencies and necessitate the factor 2 used in equation (2.12). The equivalence of the two definitions comes from the Fourier transform properties: the transform of a convolution of two functions is the point-wise product of the transforms, and the transform of the parity operation is the complex conjugate. A good interpretation of $S_i(f)$ is that it represents the contribution of the different frequencies to the variance of $n_i(t)$ in the time domain.

A quantity closely related to the power spectral density is the amplitude spectral density $A_i(f) = \sqrt{S_i(f)}$ which is usually used to describe detector noise. The reason is that it is linear in the amplitude of the noise and is also a good way of describing the sensitivity of a detector to gravitational waves as discussed in section 2.3.

The principal contributions to the total noise $n(t)$ in a ground interferometer which drive the design of a ground detector are the seismic and thermal vibrations of optical elements, and the quantum noise of photon measurement. As we will see, each of those terms is a dominant one at different frequencies. At low frequency the seismic motion of the ground is the dominant source of noise, at high frequency the shot noise of photon

counting is dominant, and in the mid frequency range the thermal noise is dominant. Of course, once a gravitational wave interferometer is constructed often technical noise sources, and not these fundamental ones are dominant, and a long period of detector commissioning is needed to understand and remove these technical noise sources.

2.2.1 Seismic noise

In order to understand the effect of ground motion, the first question to answer is how optics are fixed to the ground, and, above all, why can they be treated as free falling masses. Let us first consider the principles of a mechanical oscillator.

If we consider a mass m attached with a spring of constant k to the ground, and look at the one dimensional problem with x_g the position of the ground and x the position of the mass, the equation of motion is

$$m\ddot{x} = -k(x - x_g) + F, \tag{2.14}$$

where F is the sum of external forces. We consider here an oscillator in vacuum, where fluid friction is negligible and internal friction in the spring is the dominant damping factor. Internal friction is well modelled [13] by adding a "loss angle" ϕ to the spring constant $k(1+i\phi)$ when writing equations in the frequency domain. For the materials and frequency range we will consider the value of ϕ has been measured to be approximately constant and small.

Writing the equation of motion in the frequency domain in terms of the resonant angular frequency $\omega_0^2 = \frac{k}{m}$ and the quality factor $Q = \frac{1}{\phi} \gg 1$ yields

$$\left(\omega_0^2 - \omega^2 + i\frac{\omega_0^2}{Q}\right) x(\omega) \simeq \frac{1}{m} F(\omega) + \omega_0^2 x_g(\omega). \tag{2.15}$$

If we consider only the external forces term we find at high frequencies ($\omega \gg \omega_0$)

$$\frac{1}{m} F(\omega) = \left(\omega_0^2 - \omega^2 + i\frac{\omega_0^2}{Q}\right) x(\omega) \simeq -\omega^2 x(\omega), \tag{2.16}$$

which is simply the equation of a mass subject only to the external force F, this is the starting point in explaining why our optical elements are free-falling masses.

If we consider only the ground motion term in equation (2.12), the am-

plitude transfer function of a spring is

$$T(\omega) = \left|\frac{x(\omega)}{x_g(\omega)}\right| = \frac{\omega_0^2}{\sqrt{\left(\omega_0^2 - \omega^2\right)^2 + \frac{\omega_0^4}{Q^2}}} \tag{2.17a}$$

$$= 1 \qquad \text{for } \omega \ll \omega_0 \tag{2.17b}$$

$$= Q \qquad \text{for } \omega = \omega_0 \tag{2.17c}$$

$$\simeq \frac{\omega_0^2}{\omega^2} \qquad \text{for } \omega \gg \omega_0. \tag{2.17d}$$

Hence the ground motion is amplified by a factor Q at the resonant frequencies ω_0 with a bandwidth $\frac{\omega_0}{Q}$, and is suppressed at high frequencies. In summary a mechanical oscillator is taking the ground motion at high frequencies and concentrating it around the resonant frequency. For a simple pendulum the equation of motions are the same as long as the oscillation angle is small, hence the same effect is obtained although only in the horizontal directions.

Armed with these results we can explain how mirrors are suspended in Virgo. The mirror suspension chain used in Virgo, is shown on figure 2.3. This so called *Superattenuator* is composed of an inverted pendulum fixed to the ground, and a series of wires and mechanical filters attached to the top of the inverted pendulum. Their purpose is to filter the ground motion by repeatedly applying the $\frac{\omega_0^2}{\omega^2}$ factor to all degrees of freedom, horizontal for the inverted pendulum and wires and vertical for the mechanical filters which are basically vertical springs. The resonant frequencies of these stage are in the 10 mHz – 2 Hz range well below the intended sensitive band 10 Hz – 10 kHz and the quality factors are rather low ($Q < 100$) [15]. A damped oscillator increase the root mean square[1] motion by $\sqrt{Q}$, for this reason low quality factors are chosen in the filtering chain in order to keep the integrated motion (dominated by the low frequency part) small.

Optics are attached to this Superattenuator through a high quality factor fiber or wire ($Q \sim 10^6$). Thus, they cannot be considered as free in the vertical direction, however in the horizontal direction for frequencies well above the pendulum frequency of ~ 0.6 Hz equations of motion are in the free mass regime (2.16). Hence, the test masses are only horizontally free but this is the only direction in which we measure gravitational wave effects.

The net effect of this complicated mechanic is to reduce the ground motion by 14 orders of magnitude in the sensitive band as shown on figure 2.4, this reduces the ground motion from

$$x(f) \sim 10^{-6}\left(\frac{1\,\text{Hz}}{f}\right)^2 \text{m/Hz}^{1/2}, \qquad \text{for } f > 10\,\text{Hz} \tag{2.18}$$

[1] $x_{\text{rms}} = \sqrt{\int x(f)^2 \mathrm{d}f}$ is the integrated motion over all frequency, this also the standard deviation of x in the time domain.

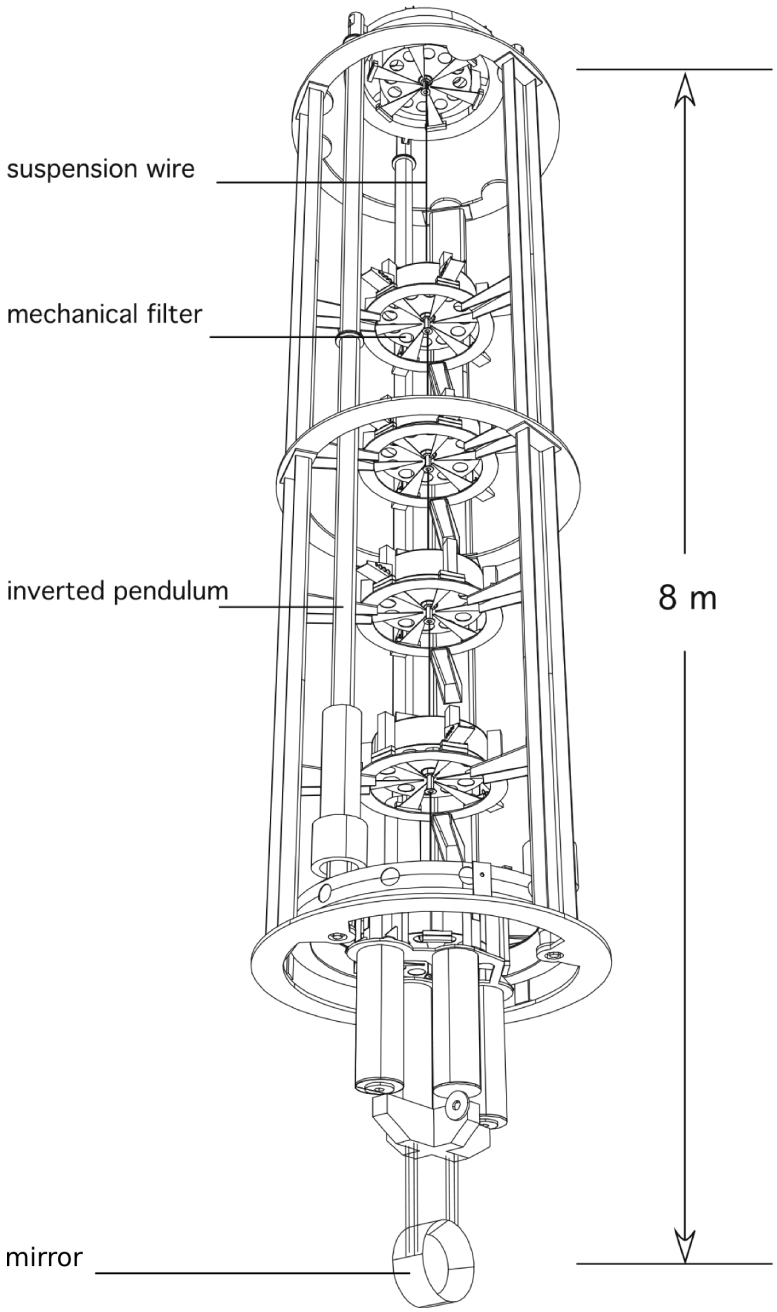

Figure 2.3: Schematics of the Virgo Superattenuator [14]. It is composed of an inverted pendulum fixed to the ground, and a series of wires and mechanical filters attached to the top of the inverted pendulum. The purpose of this chain is to isolate the mirror suspended at the bottom of the apparatus from the ground motion.

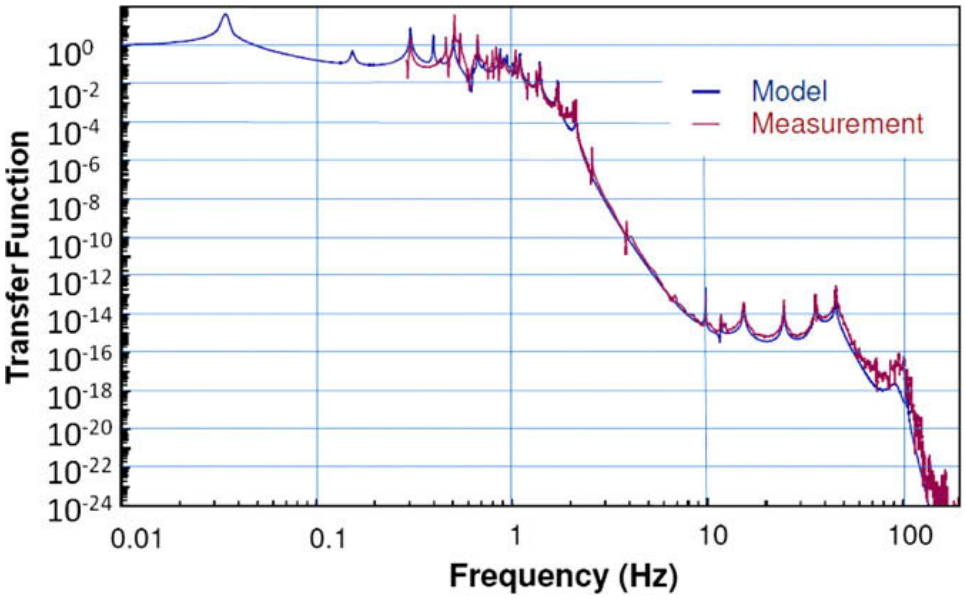

Figure 2.4: Total transfer function of the Virgo Superattenuator between ground motion and motion of the suspended mirrors [14].

to $x(f) \sim 10^{-22}\,\mathrm{m}/\sqrt{\mathrm{Hz}}$ at 10 Hz and even lower at higher frequency, while increasing the root mean square motion by only a few dozens.

The signal that we measure is the fractional difference in lengths $(L_x - L_y)/L_0$ hence the seismic noise at frequencies larger than 10 hertz is

$$A_{\mathrm{seismic}}(f) \sim \frac{x(f)}{L_0} \lesssim 10^{-25}\,\mathrm{Hz}^{-1/2}, \tag{2.19}$$

and can be completely neglected compared to the other noise sources described below. But it remains the dominant source of noise below ~ 1 Hz.

2.2.2 Shot noise

We have seen that gravitational waves induce a phase difference $\Delta\varphi$ between the two interferometer arms. What is measured by the photodector is the output light power. We will assume that the interferometer is tuned to constant phase offset $\pi + \alpha$ between the two arms, as we will see below, $\alpha = 0$ corresponds to an optimal working point. Given this offset, the output power is

$$P_{\mathrm{out}} = P_{in} \sin^2\left(\frac{\alpha + \Delta\varphi}{2}\right) \simeq P_{in}\left[\sin^2\left(\frac{\alpha}{2}\right) + \frac{1}{2}\sin(\alpha)\Delta\varphi\right], \tag{2.20}$$

where we have used $\Delta\varphi \ll 1$. But how small a power fluctuation are we able to measure?

The fundamental limit in measuring a power P_0 is the photon shot noise (also called counting noise), which comes from the discrete nature of light,

each photon carrying a $\frac{h_P c}{\lambda}$ quantum of power, where $h_P = 2\pi\hbar$ is the Planck constant. The mean number of photons arriving during a time τ is Poisson distributed with mean

$$\langle N \rangle = \frac{P_0 \tau \lambda}{h_P c} \tag{2.21}$$

and has fluctuation with standard deviation $\sigma_N = \sqrt{\langle N \rangle}$. Which means that the power measured is a random variable with moments

$$\langle P \rangle = P_0 \qquad \sigma_P = P_0 \frac{\sigma_N}{N} = \sqrt{\frac{P_0 h_P c}{\tau \lambda}}. \tag{2.22a}$$

When no gravitational wave is present, $P_0 = P_{in} \sin^2\left(\frac{\alpha}{2}\right)$ and using equation (2.20) the output power fluctuations σ_P are interpreted as phase fluctuations

$$\sigma_\varphi = \frac{\sigma_P}{P_{in} \frac{1}{2} \sin\alpha} = \frac{1}{\cos\frac{\alpha}{2}} \sqrt{\frac{h_P c}{P_{in} \tau \lambda}}. \tag{2.23}$$

These noise fluctuations are minimized when $\alpha = 0$, i.e. when the output of the interferometer is tuned on a dark fringe.

Using $\Delta\varphi = \frac{4\pi L_0}{\lambda} s(t)$ we can rewrite[2] the phase noise in terms of gravitational wave amplitude spectral density

$$A_{\text{shot}}(f) = \frac{1}{L_0} \sqrt{\frac{c\hbar\lambda}{4\pi P_{in}}}. \tag{2.24}$$

For a 3 kilometer long Michelson interferometer with a 20 Watt laser of wavelength $\lambda = 1.06\,\mu$m we find

$$A_{\text{shot}}(f) \sim 4 \times 10^{-21}\,\text{Hz}^{-1/2}. \tag{2.25}$$

In order to lower this noise floor two sets of optical elements are added to the optical scheme (see figure 2.1). Two input mirrors (WI and NI) which form Fabry-Perot cavities with the end mirrors and effectively lengthen the optical path L_0 as we will see below. For numerical applications we will use the electromagnetic field reflectivity of Virgo input mirrors during VSR2 $r \sim 0.94$. And a power recycling mirror (PR) which increases the input power P_{in} by a factor $g_{rec} \sim 30$ and takes advantage of the dark fringe working point of the interferometer which reflects most of the input power in the laser direction.

Considering an ideal Fabry-Perot cavity with no losses and perfect reflectivity of the end mirror, the cavity reflection of light at angular frequency ω

[2] To convert to the frequency domain we use two results: the arrival time independence of a Poisson process, and that if the fluctuations of a variable x averaged over a time scale τ are $\langle \delta x \rangle = \sqrt{D/\tau}$ then it has an autocorrelation function $A_\tau(t) \sim \frac{D}{\tau} \mathbb{1}(|t| < \tau/2) \sim D\delta(t)$. Taken together this yields a one sided amplitude noise spectral density of $x(f) = \sqrt{2D}$.

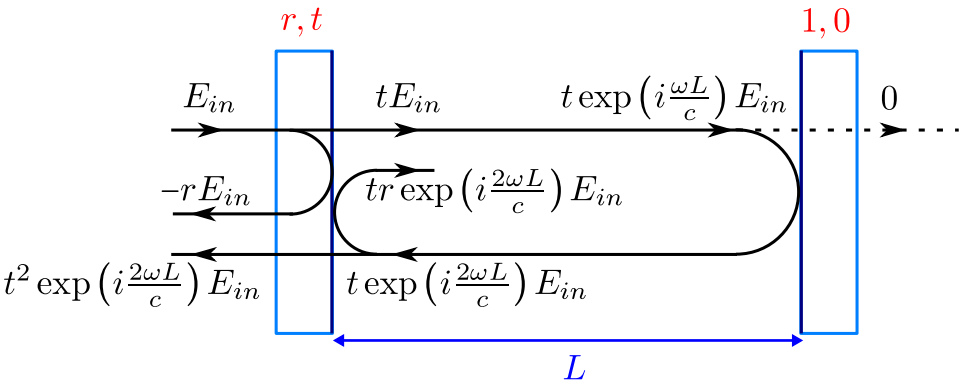

Figure 2.5: Electromagnetic field in a Fabry-Perot cavity with a perfect end mirror and an input mirror of reflectivity r and transmittance t. The input light field E_{in} is shown along with the different fields produce by this input field. The total cavity reflectivity is given in equation (2.26), and only the first two terms are shown on this figure.

is

$$R = -r + t^2 \sum_{n=1}^{\infty} r^{n-1} \left(\exp i \frac{2\omega L}{c} \right)^n = -r + \frac{t^2 \exp i \frac{2\omega L}{c}}{1 - r \exp i \frac{2\omega L}{c}} = \frac{-r + \exp i \frac{2\omega L}{c}}{1 - r \exp i \frac{2\omega L}{c}}, \tag{2.26}$$

where we denote r and t the electromagnetic field reflectivity and transmittance of the input mirror. The reflected light is simply the sum of the directly reflected light, and of the light reflected back into the cavity n times and transmitted through the input mirror in both directions. On figure 2.5 is shown An incoming gravitational wave is included in the length term through

$$\frac{2\omega L}{c} = \frac{2\omega L_0}{c} + \frac{\omega L_0 s(t)}{c} = \frac{2\omega L_0}{c} + \varphi(t). \tag{2.27}$$

Assuming that the cavity length is tuned to be a multiple of the half-wavelength $\lambda/2$, $\exp i \frac{2\omega L_0}{c} = 1$, and using that gravitational wave induced phase shifts are very small we obtain the cavity reflectivity

$$R = \frac{\exp i\varphi(t) - r}{1 - r \exp i\varphi(t)} \simeq \frac{1 - r + i\varphi(t)}{1 - r - ir\varphi(t)}. \tag{2.28}$$

Hence the light field reflected by an arm cavity has a phase change of

$$\arg(R) = \frac{1 + r}{1 - r} \varphi(t) \tag{2.29}$$

and the phase difference $\Delta\varphi$ between the two arms is multiplied by the same factor. In the case of Virgo we obtain $(1 + r)/(1 - r) \sim 30$, the Fabry-Perot cavity stores the light for ~ 30 round trips, which effectively lengthen the optical path by as much.

In the derivation above we have assumed that the arms length is constant between round trips, this is true only when the gravitational wave frequency is much lower that the inverse of the cavity storage time $\tau_s \sim \frac{1+r}{1-r}\frac{2L}{c} \sim 0.6\,\mathrm{ms}$. Hence, for gravitational wave signals with frequencies of a few hundred hertz or more we need to include properly the time evolution of the arm length. For that purpose we use a framework of modulated signals, where the frequency of the light is modulated by the gravitational wave frequency. For a monochromatic gravitational wave the phase modulation $\varphi(t) = \frac{\omega L_0}{c} s(t) = \varphi_0 \cos(\omega_g t)$ is split into a carrier and two sidebands

$$A\cos(\omega t + \varphi_0 \cos(\omega_g t)) \simeq A\cos(\omega t) + \frac{A\varphi_0}{2}\left(\cos(\omega - \omega_g)t + \cos(\omega + \omega_g)t\right). \tag{2.30}$$

In this framework we are no longer interested by the change in phase of the cavity reflectivity but by the amplitude which is transfered from the carrier frequency to the sidebands. The formal computation is quite involved [16] however it can be heuristically retrieved with a simpler picture. We can think of the sideband transfer as light which enters the cavity, bounces back and forth, is converted into a sideband at the end mirror with a probability $\frac{1}{2}\varphi_0$ and then continues its round-trips until it escape the cavity. This picture can be informally written as the cavity transfer function from the carrier to the sideband

$$\begin{aligned} G = {} & (\text{cavity entrance}) \times (n + \tfrac{1}{2} \text{ round trips at frequency } \omega) \\ & \times (\text{conversion to sideband}) \\ & \times (m + \tfrac{1}{2} \text{ round trips at frequency } \omega + \omega_g) \times (\text{cavity exit}). \end{aligned}$$

Which if written formally has the form

$$\begin{aligned} G = {} & t \times \sum_{n=0}^{\infty} r^n \left(\exp i\frac{2\omega L_0}{c}\right)^n \exp i\frac{\omega L_0}{c} \times \tfrac{1}{2}\varphi_0 \times \\ & \exp i\frac{(\omega+\omega_g)L_0}{c} \sum_{m=0}^{\infty} r^m \left(\exp i\frac{2(\omega+\omega_g)L_0}{c}\right)^m \times t \qquad (2.31a) \\ = {} & \frac{\varphi_0}{2} \frac{(1-r^2)\exp i\frac{(2\omega+\omega_g)L_0}{c}}{\left(1 - r\exp i\frac{2\omega L_0}{c}\right)\left(1 - r\exp i\frac{2(\omega+\omega_g)L_0}{c}\right)} \qquad (2.31b) \\ = {} & \frac{\varphi_0}{2} \frac{(1+r)\exp i\frac{\omega_g L_0}{c}}{\left(1 - r\exp i\frac{2\omega_g L_0}{c}\right)}, \qquad (2.31c) \end{aligned}$$

where in the last step we have assumed a perfect tuning of the interferometer. In the long wavelength approximation $\frac{2\omega_g L_0}{c} \ll 1$ that we are already using, the amplitude of the side band transfer is

$$|G| = \frac{\varphi_0}{2}\frac{1+r}{1-r}\frac{1}{\sqrt{1 + \left(\frac{\sqrt{r}}{1-r}\frac{2L_0}{c}\right)^2 \omega_g^2}}, \tag{2.32}$$

which for $\omega_g = 0$ after combining the two sidebands into a phase modulation yields the same phase gain as (2.29), and a has a linear high frequency cut-off with a typical frequency $f_c = \frac{c}{2\pi L}(1-r)/(2\sqrt{r}) \sim 500\,\mathrm{Hz}$.

To conclude, the use of cavities as interferometer arms increase the gravitational wave induced phase shift, and the addition of power recycling lowers the shot noise (2.24). As a result the shot noise amplitude spectral density is

$$A_{\mathrm{shot}}(f) = \frac{1}{L_0}\sqrt{\frac{c\hbar\lambda}{4\pi g_{rec} P_{in}}}\frac{1-r}{1+r}\sqrt{1+\frac{f^2}{f_c^2}}, \tag{2.33}$$

which in the case of Virgo yields

$$A_{\mathrm{shot}}(f) \sim 2\times 10^{-23}\sqrt{1+\frac{f^2}{f_c^2}}\,\mathrm{Hz}^{-1/2}. \tag{2.34}$$

One interesting conclusion we may draw from this result is that at high frequency $f \gg f_c$, the shot noise is independent of the reflectivity r, because for $r \sim 1$ we have $1 + r \sim 2\sqrt{r}$. Hence the increase of stored light power in the arms is compensated by the loss due to the low pass filtering nature of cavities to length modulations.

2.2.3 Thermal noise

We have shown the photon measurement noise allows displacement measurements of the order of $10^{-19}\,\mathrm{m}/\sqrt{\mathrm{Hz}}$, However the position of the mirror surfaces forming the interferometer are not fixed, but are thermally fluctuating. The dominant fluctuations in the $10-1000\,\mathrm{Hz}$ frequency range are coming from the thermal excitation of the pendular motion of the mirrors and of the thermal fluctuation of the mirror surfaces. Both fluctuations are well modelled by an internally damped oscillation excited by a Brownian force.

The fluctuation-dissipation theorem [17] stipulates that for any linear system for which the relationship between the amplitude spectral density of the position and of the external force is

$$\chi(\omega)x(\omega) = F(\omega) \tag{2.35}$$

where the effective thermal force in equilibrium has a one sided power spectral density

$$F^2_{\mathrm{therm}}(\omega) = \frac{4k_B T}{\omega}\mathrm{Im}\left(\chi(\omega)\right). \tag{2.36}$$

This result is a consequence of energy equipartition for Hamiltonian systems in thermal equilibrium, and it clearly relates the force fluctuations to the friction part $\mathrm{Im}\left(\chi(\omega)\right)$ of the equation of motion.

In the case of an internally damped oscillator (2.15) we have

$$\chi(\omega) = m\left(\omega_0^2 - \omega^2 + i\frac{\omega_0^2}{Q}\right) \tag{2.37}$$

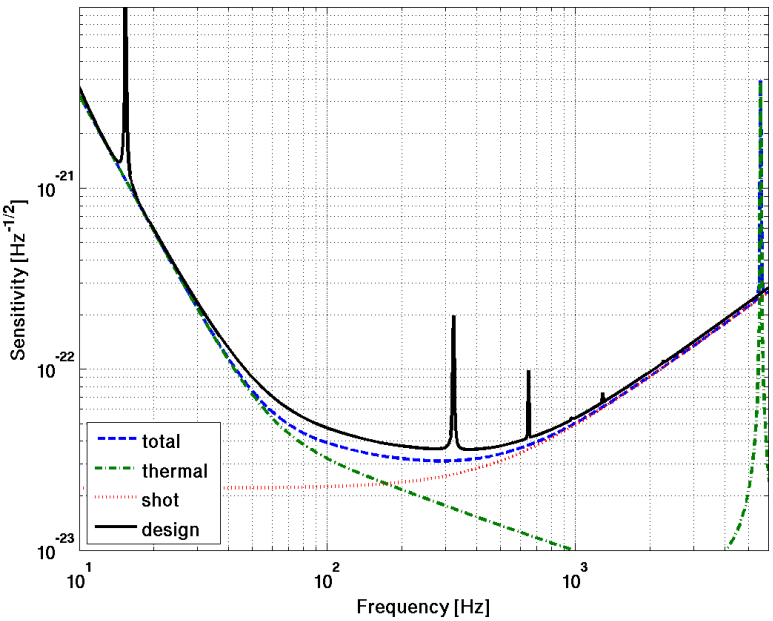

Figure 2.6: Simplified noise budget (blue dashed line) as a quadratic sum of simplified thermal (green dot-dashed line) and shot noise (red dotted line), and actual Virgo design noise budget for VSR2 (black solid line).

and the position fluctuations spectral density is

$$\sqrt{x^2(\omega)} = \frac{\sqrt{F^2_{\text{therm}}(\omega)}}{|\chi(\omega)|} = \frac{\omega_0^2}{\sqrt{\left(\omega_0^2-\omega^2\right)^2+\frac{\omega_0^4}{Q^2}}}\sqrt{\frac{\omega_0}{\omega}}\sqrt{\frac{4k_BT}{mQ\omega_0^3}}, \tag{2.38}$$

where we recognize in the first term the oscillator transfer function (2.17a). This motivates the choice of high quality factor ($Q \sim 10^6$) materials for the mirrors and pendulum, which concentrate the thermal noise in a narrow band around the resonant frequency and lowers considerably $\propto \frac{1}{\sqrt{Q}}$ the broadband noise floor.

In terms of gravitational wave strain for a $m = 20\,\text{kg}$ mirror and $Q = 5{\times}10^5$ the thermal noise is

$$A_{\text{therm}}(f) = \frac{2}{L_0}\sqrt{x^2(f)} \sim T(f)\sqrt{\frac{f_0}{f}}\frac{\text{Hz}}{f_0^{3/2}}1.7\times10^{-18} \tag{2.39a}$$

$$\sim 1.7\times10^{-18}\frac{\text{Hz}^{3/2}}{f_0 f^{1/2}}\,\text{Hz}^{-1/2} \qquad \text{for } f \ll f_0 \tag{2.39b}$$

$$\sim 1.7\times10^{-18}\frac{f_0\,\text{Hz}^{3/2}}{f^{5/2}}\,\text{Hz}^{-1/2} \qquad \text{for } f \gg f_0 \tag{2.39c}$$

where the factor 2 in (2.39a) comes from the quadratic sum of the 4 mirrors forming the two Fabry-Perot cavities. The Virgo mirrors have two main

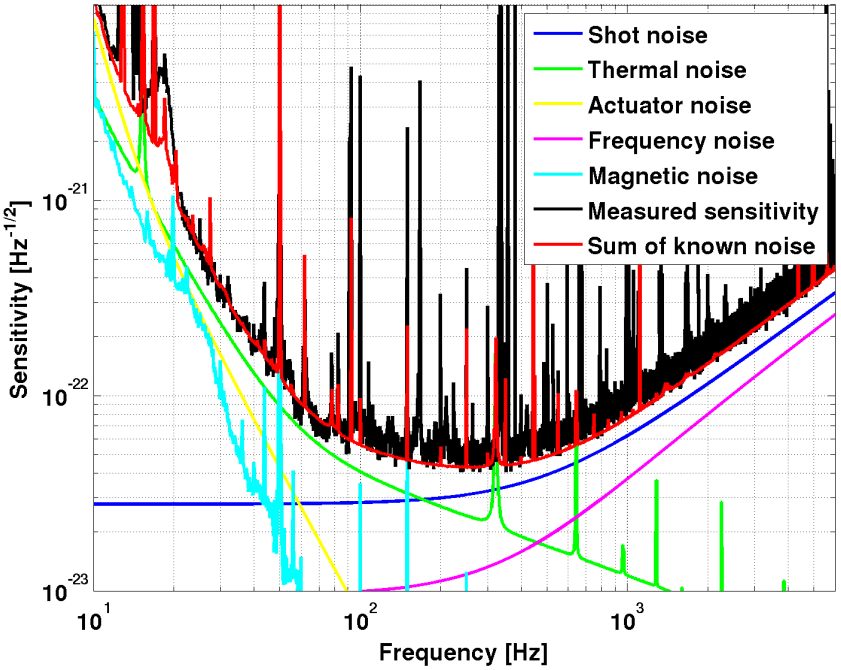

Figure 2.7: Real noise budget for Virgo during VSR2. Only the main contribution to the noise are shown. As shown by the difference between the measured sensitivity and sum of known noises, most of the noise in the interferometer is understood and well modeled.

modes of oscillation: the pendulum mode of the last stage of suspension at $f_0 \simeq 0.6\,\mathrm{Hz}$ and the first internal eigen-mode of the different mirrors $f_0 \sim 5.7\,\mathrm{kHz}$. We are interested by the noise contribution in the sensitive band $10-1000\,\mathrm{Hz}$, which for the pendulum noise corresponds to the high frequency limit (2.39c) and for the main mirror mode corresponds to the low frequency limit (2.39b).

2.2.4 Final sensitivity

We can combine the three noise level estimations obtained above to derive an expected *noise budget* for Virgo [18]. That is the decomposition of the amplitude spectral density of the total detector noise $n(t)$ into different contributions. We simply take the quadratic sum of the thermal and shot noises (the seismic noise is completely negligible at the considered frequencies). This crude estimation is actually quite close to the official design curve of Virgo for VSR2 shown on figure 2.6. However one should remember that this derivation is quite approximate, for instance the effective mass that should be used for internal thermal modes of the mirrors is about a factor 3 smaller

that their total mass [19].

There is also a large number of fundamental noise sources that we have not considered. For instance we have neglected the quantum fluctuations in the radiation pressure applied to the mirrors, or the thermal internal modes of the suspending wire communicated to the mirrors with a $\sqrt{m_{\text{wire}}/m_{\text{mirror}}}$ reduction.

We have also neglected a large number of technical noises that need to be mitigated. For instance we have neglected the fluctuations of the input laser power, e.g. due to laser instability. In Virgo these fluctuations are greatly reduced by modulating the laser power at $\sim 6\,\text{MHz}$, which combined with a homodyne detection replaces the power fluctuations at $10 - 1000\,\text{Hz}$ by the fluctuations at the modulating frequency which are much lower. The input laser has also a fluctuating frequency, these fluctuations are one of the reason for having two arms and a differential measurement. Also the main purpose of the input mode cleaner shown on figure 2.1 is to reduce the noise due to these frequency fluctuations of the laser.

Also some of the technical noise can be dominant, for instance noise coming from imperfect mirrors alignment and control of the cavities which keep them on the dark fringe working point can be comparable or even larger than the thermal noise in the $10 - 100\,\text{Hz}$ band.

As an example, on figure 2.7 is shown a real noise budget for Virgo during VSR2 on a good day of operations. From that figure it is clear that the fundamental noises are not sufficient to explain all the observed noise spectral density, however combined with an estimation of all the technical noise sources the detector spectral density is well understood.

2.3 Comparing gravitational wave sources with detector noise

As we will see in chapter 5, the relevant figure of merit in comparing a signal with noise is the matched filtering signal to noise ratio (SNR)

$$\text{SNR}^2 = 2\int_{-\infty}^{\infty}\frac{|\tilde{s}(f)|^2}{S(|f|)} = 4\int_{0}^{\infty}\frac{|\tilde{s}(f)|^2}{S(|f|)}, \tag{2.40}$$

where $\tilde{s}(f)$ are the Fourier components of the signal and $S(|f|)$ is the one sided power spectral density. In this sense the noise spectral density represents the sensitivity of the detector. For a narrow band signal from an optimally located and polarized source, this equation can be written in terms of h_{rss} as

$$\text{SNR} = \sqrt{2}\frac{h_{\text{rss}}}{\sqrt{S(f)}}. \tag{2.41}$$

And we can directly express the SNR as a function of the gravitational wave energy content using the h_{rss} - energy relation (1.44).

However real detectors have not a purely Gaussian noise as discussed so far, a large number of transient noise excursions are also present in the data and complicate their analysis. As a result the SNR is not a perfect figure of merit for the signal strength, but in practice a good rule of thumb is that an SNR of at least 10 is needed for a gravitational wave detection. The exact value of this threshold depends on other parameters of the search such as the rate of noise transients in the data, the prior knowledge on the sought signal and the details of the analysis used.

Chapter 3

Gravitational Wave sources

In this chapter we give a general overview of interesting gravitational wave sources, and study a few examples in more details. As we have seen in chapter 1 astrophysical objects even at extragalactic distances may yield orders of magnitude larger gravitational wave strains that what could be produced by a laboratory generator. We have derived in equation (1.29) that good sources of gravitational waves are asymmetric, compact and relativistic. Another necessary condition is that the source radiates at frequency where current detectors are sensitive, that is the quadrupolar moments have to evolve in the $10 - 1000\,\mathrm{Hz}$ frequency range in order to be observed by ground based detectors.

The first objects fulfilling these requirements that come to mind are neutron stars and stellar mass black holes, which are compact and their typical evolution frequencies are a few kilohertz, corresponding to the light travel time across their diameter. The term *compact star* or *compact object* is usually used to encompass both neutron stars and black holes when the distinction between the two is not relevant. There are also more exotic gravitational wave sources like cusps or loops in hypothetical cosmic strings.

Usually, sources are observationally classified according to their gravitational wave emission type into three categories: *continuous wave signals* which are quasi-monochromatic and emitted permanently on a human time scale, *transient signals* that have a short duration and correspond to particular cataclysmic events, and *stochastic background* which is an incoherent sum of a large number of such transients or of cosmological events.

3.1 Continuous wave signals

There are two main sources of permanent quasi-monochromatic gravitational waves: rotating neutron stars and compact object binaries that are far from coalescence. In both cases, examples of such systems are known in the Milky Way.

3.1.1 Pulsars

For rotating neutron stars the general picture is that young neutron stars[1] could be not perfectly axisymmetric and have some ellipticity caused for example by stress induced by internal magnetic fields. Assuming an ellipticity $\epsilon = (I_{xx} - I_{yy})/I_{zz}$, where I_{zz} is the moment of inertia along the rotation axis we can reuse our simple binary example of section 1.5 with $2ma^2 = \epsilon I_{zz}$, as the quadrupole radiation depends only on the value of the quadrupolar mass moments and not any other parameter of the mass distribution. Hence for an optimally oriented and positioned observer the signal amplitude is

$$h_0 = \frac{G}{rc^4}\epsilon I_{zz}\omega_{\mathrm{GW}}^2 = 4.3\times10^{-26}\frac{1\,\mathrm{kpc}}{r}\frac{\epsilon}{10^{-6}}\frac{I_{zz}}{10^{38}\,\mathrm{kgm}^2}\left(\frac{f_{\mathrm{GW}}}{200\,\mathrm{Hz}}\right)^2, \tag{3.1}$$

where the gravitational wave frequency f_{GW} is at twice the pulsar rotational frequency observed electromagnetically. The possible values ϵI_{zz} are not well constrained by theory, in the equation above we used optimistic but reasonable values. However in the particular case of pulsars one can give observational upper limits.

Pulsars are neutron stars whose magnetic and rotational axis are not aligned. As a result the electromagnetic radiation (usually in radio wavelengths) is not symmetric around the rotation axis and the observed electromagnetic flux changes periodically as the star rotates. This allows a precise measurement of the rotation frequency, and its time derivative. By assuming that all of the spin-down[2] is due to gravitationally radiated energy

$$I_{zz}\omega\dot{\omega} = -P_{\mathrm{GW}} \propto \epsilon^2 I_{zz}^2 \tag{3.2}$$

we can use the amplitude - power relation (1.43) to derive a spin-down upper limit on the gravitational wave amplitude

$$h_0^{\mathrm{sd}} = \sqrt{\frac{5GI_{zz}}{2r^2c^3}\frac{|\dot{\omega}|}{\omega}}. \tag{3.3}$$

Youngest pulsars, such as the Crab or the Vela pulsars, tend to have the largest values of $|\dot{\omega}/\omega|$ and are therefore the most interesting for gravitational wave observations.

Given that the signal has a narrow frequency band we can use the h_{rss} to compare pulsar signals with noise. Assuming that the gravitational wave amplitude is at the spin-down limit and an observation time τ_{obs}, the relevant quantity is

$$\sqrt{2}h_{\mathrm{rss}}^{\mathrm{sd}} = \sqrt{2\int_0^{\tau_{\mathrm{obs}}} h_0^2\sin^2(\omega_{\mathrm{GW}}t)\mathrm{d}t} \simeq h_0^{\mathrm{sd}}\sqrt{\tau_{\mathrm{obs}}}. \tag{3.4}$$

[1] In general neutron stars are called *young* when their age is $< 10^7$ yr

[2] The spin-down is the decrease in rotational frequency.

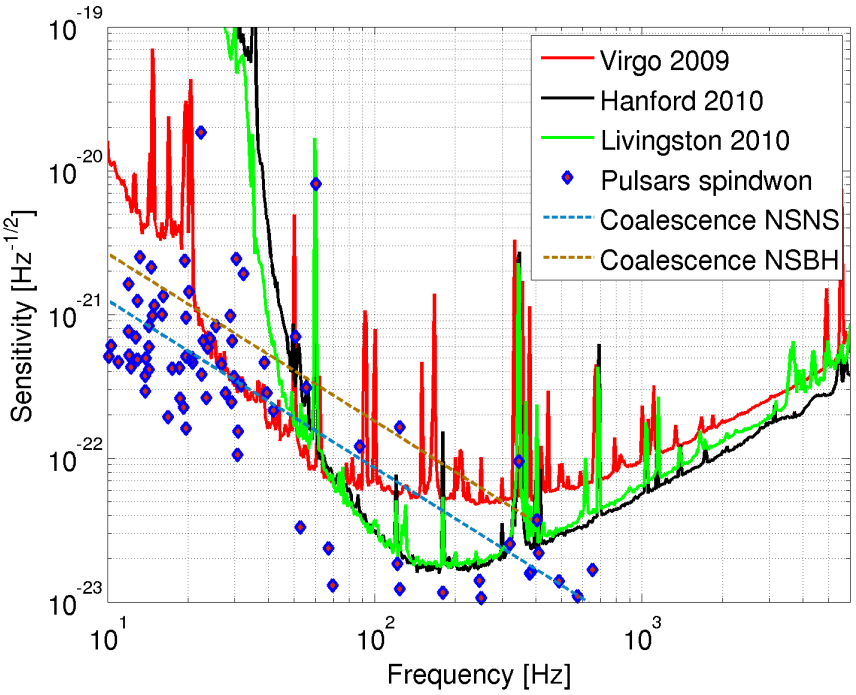

Figure 3.1: Noise amplitude spectral density for LIGO and Virgo detectors in 2009-2010. Overlaid are the spin-down amplitude upper limit (3.4) as a function of emission frequency for a 1 year observation time from a catalog of known pulsars. The dashed lines represent twice the Fourier amplitude of the signal $2|\tilde{s}(f)|$ created by an optimally located ($F_+ = 1$) and optimally oriented ($\iota = 0$) binary coalescence: the blue line is for a binary neutron stars (NSNS) with component masses $1.4M_\odot$ and $1.4M_\odot$ at a distance of 10 Mpc; the brown line is for a neutron star - black hole coalescence (NSBH) with component masses $1.4M_\odot$ and $10M_\odot$ at the same distance. In both cases the amplitude results from the stationary phase approximation of the waveform's zeroth order term (3.12) and is cut at the f_{isco} frequency (3.22). The integral of the squared ratio between the plotted amplitude and detectors noise (2.40) yields the SNR^2 of the corresponding signal.

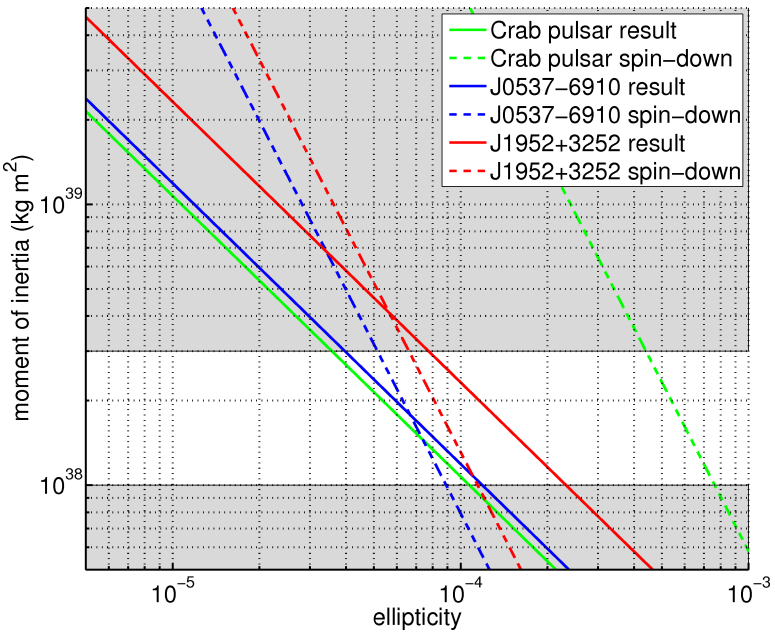

Figure 3.2: Spin-down limits (dashed line) and gravitational wave observation exclusions [20] (solid line) in the moment of inertia versus ellipticity plane, regions above the lines are excluded. Shaded regions are those outside theoretical predictions for neutron star moment of inertia [20].

The reason for using the $\sqrt{2}$ factor is the expression (2.41) of the SNR as a function of $h_{\rm rss}$ and the one sided amplitude spectral density. For the most promising known pulsars this value is shown on figure 3.1 for a 1 year long observation time. By most promising we mean the pulsar with the spin-down amplitude close or above the current detectors noise spectra. We use the parameters of the known pulsars listed in the Australia Telescope National Facility catalog [21, 22]. It should be noted that the actual upper limit on the SNR is a factor of order a few smaller than what one could read from this figure because pulsars are not optimally oriented with regard to each detector and most analyzes are not able to coherently integrate over a year long time.

In the case when no gravitational wave signal is found, one obtains an upper limit on the gravitational wave amplitude h_0, which using (3.1) can be translated into an exclusion region in the I_{zz} versus ϵ plane above a line of fixed $I_{zz}\epsilon$. However an exclusion is already provided by the spin-down limit through (3.2), the electromagnetic measurement of $\omega\dot{\omega}$ forbids the region above a line of fixed $I_{zz}\epsilon^2$. The comparison of these two exclusion regions is shown on figure 3.2 for three pulsars where recent gravitational wave observation was able to beat the spin-down limit.

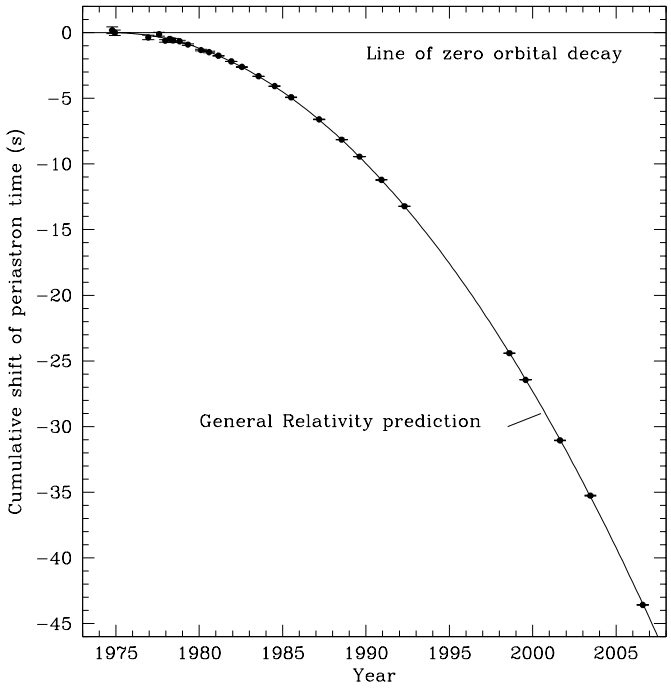

Figure 3.3: Plot of the cumulative shift of the periastron time from 1975-2007 [23]. The points are data with measurement error bars, the curve is the General Relativity prediction.

3.1.2 Binary compact stars

Pairs of gravitationally bound compact stars radiate gravitational waves at twice their rotation frequency as we have seen in the toy example of section 1.5. As we will see in section 3.3.2, the radiation frequency is too low for Earth based interferometers until the last few minutes or seconds before the merger of the two objects. They are usually considered as continuous wave sources only for proposed space borne interferometers which are sensitive at much lower frequencies (of the order of mHz). However such pairs of compact stars far from coalescence are worth mentioning because they provide the only so far observed gravitational wave effect.

The pulsar PSR 1913+16 has been discovered by Hulse and Taylor in 1974 and it forms a close binary system with another compact object [24]. The orbital period measured through precise radio observation of this system is 7.75 hours. Over time a decrease in this period has been observed, and the period derivative is equal to the one predicted from energy loss by gravitational radiation with an accuracy at the few per mil level [23]. A

remarkable way of presenting this result is to compare the shift in periastron time predicted by General Relativity with the observed one. This comparison is shown on figure 3.3, the cumulative shift would be equal to zero if the binary system orbital energy was constant, and the observed shift is in perfect agreement with the General Relativity predictions.

Several others pulsars in close binary systems have been discovered since then, and they all confirm the General Relativity prediction of energy loss [25].

3.2 Stochastic background

Another possibility of observing gravitational waves comes from looking for the incoherent sum of a large number of unresolved sources. As a result of the central limit theorem, gravitational waves at Earth are a random Gaussian process with a spectrum depending on the dominant process forming the incoherent sources. These random waves are called *stochastic gravitational wave background*.

There are many potential sources of this background, such as an incoherent sum of transient or continuous sources in the relatively close-by universe, or a result of density fluctuations in the early Universe just after Big Bang. The latter could provide crucial information on the early Universe physics. For instance, latest results from ground gravitational wave detectors are able to exclude some equations of state for the content of the early Universe or some parameter space of the hypothetical cosmic strings [26].

Observation of a random signal in random detector noise is not obvious, especially if the noise sources are not perfectly understood. However using a network of detectors, one can cross-correlate data from at least two detectors. The signal in the network of instruments will be correlated but noise which is in most cases due to local sources should be uncorrelated. This difference allows one to distinguish signal from noise, but we will not go into the details of how such an analysis is performed.

3.3 Transients

Possible sources of transient gravitational waves are numerous, one of the reason being the imprecise definition of the class of "short signals". In principle "short" means much shorter than the duration of a gravitational wave experiment but in practice it means shorter than a few minutes. We will not present here the full range of proposed sources but we will focus on three particular scenarios: black holes in X-ray binaries, compact binary coalescence, and collapse of massive stars.

When considering how interesting is a particular source of transients gravitational waves, it is important to bear in mind that not only their

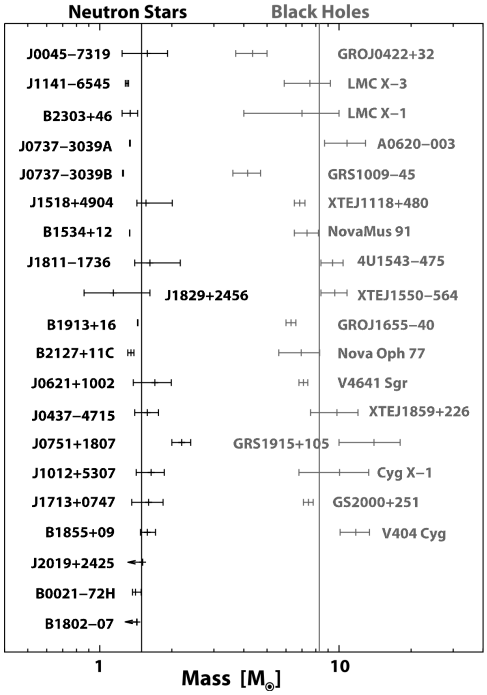

Figure 3.4: Observed masses for neutron stars and black holes. The mass is measured by analyzing Doppler shifts of the non-degenerate companion for black holes. For neutron stars the Doppler shift analysis is performed directly on pulsar radio emission. Figure taken from [27].

amplitude but also the expected rate of such events are crucial. Sources that are expected to be seen once per century or even more rarely are not very appealing.

3.3.1 X-ray binaries

X-ray binaries are binary system composed of a non-degenerate star of the main sequence or the giant branch and a compact object. Matter from the non-degenerate companion is transfered onto the compact object through Roche lobe overflow or stellar winds and forms an accretion disk around it. The accreted matter transforms gravitational potential energy into thermal energy through disk viscosity, and radiates a thermal spectrum peaked around $\sim 10\,\mathrm{keV}$ [28]. These binaries have been observed in X-rays and in most case were found during a bright X-ray outburst. These outbursts are typically several months long and are in general separated by long periods (years or more) of quiescence. These outburst are thought to be due to instabilities in the accretion disk when it reaches a critical surface density and rapidly depletes the disk onto the compact object. The X-ray light curve during the outburst is variable, with, among others, frequent cases of quasi

periodic oscillations at $0.1 - 30\,\mathrm{Hz}$ [29].

Optical observations of these systems were used to measure the mass of the unseen compact object. The measurement is based on analyzing Doppler shift of spectral lines which yields the value of the mass function [29]

$$\frac{(m_1 \sin \iota)^3}{(m_1 + m_2)^2} \leq m_1, \tag{3.5}$$

where m_1 is the mass of the compact object, m_2 the mass of the companion and ι is the angle between the orbital axis and the observer line of sight. The mass function gives an absolute minimum for the mass of the compact object. Additional information on the mass of the compact object can be obtained through the optical spectrum of the companion which yields the star type and constrains m_2. As a result for 20 such systems [28] the mass found for the compact object was greater than $m_1 > 3\,\mathrm{M}_\odot$ and the compact object is thought to be a black hole. These 20 black holes have masses in the $3 - 20\,\mathrm{M}_\odot$ range, this range include the estimation error bars which are between 5% and 50%. A summary of the measured masses for black holes is shown on the right side of figure 3.4. In addition there are also currently of the order of 20 black hole candidates for which X-ray spectra properties suggest the presence of a black hole but the Doppler shift of the companion spectrum have not been sufficiently measured to constrain the candidate black hole mass [28].

These unique known cases of stellar mass black holes, which allows many interesting observations across the electromagnetic spectrum[3] that allow to measure black holes properties like the spin or to derive indirect limits on their radius and event horizon. These objects could also be a source of gravitational waves which are a direct probe of black hole properties.

Black holes are macroscopic objects whose stable state is fully described by three parameters: mass, spin and charge. For astrophysical black holes the charge is assumed to be zero as the forming matter is globally neutral. For a black hole of mass M the spin $\boldsymbol{S}$ is usually parameterized using the *dimensionless spin* $\chi = \frac{|\boldsymbol{S}|c}{GM^2}$, which is always smaller than 1 [30] in order to respect the cosmic censorship principle[4]. For an astrophysically reasonable scenario of a black hole spun up through matter accretion the maximal spin is slightly lower $\chi < 0.998$. The limit is imposed by angular momentum extraction through photons [31] and gravitational waves [32] emitted during the matter infall.

When the black hole horizon is deformed just after its creation or by infalling matter, it radiates gravitational waves in order to reach a stable

[3] One should note that the following interpretations of the measurements are not very reliable for the moment.

[4] Which states that all astrophysical singularities are hidden behind an event horizon. In Kerr black hole geometry an event horizon forms only for $\chi \leq 1$.

state. After an initial transient period the emission is dominated by a superposition of discrete quasi-normal modes, and the most slowly damped mode is the spheroidal $l = m = 2$ mode which radiates a ringdown waveform

$$\begin{pmatrix} h_+(t) \\ h_\times(t) \end{pmatrix} = A \exp\left[-\frac{\pi f_0}{Q}(t-t_0)\right] \theta(t-t_0) \begin{pmatrix} (1+\cos^2\iota)\cos\left[2\pi f_0(t-t_0)+\phi_0\right] \\ 2\cos\iota\sin\left[2\pi f_0(t-t_0)+\phi_0\right] \end{pmatrix}, \tag{3.6}$$

where ι is the angle between the black hole spin and the line of sight, and the frequency f_0 and quality factor Q can be analytically approximated (within 5%) by [33]

$$Q \simeq 2(1-\chi)^{-0.45}, \tag{3.7a}$$

$$f_0 \simeq 32\,\mathrm{kHz} \times \left[1 - 0.63(1-\chi)^{0.3}\right] \frac{M_\odot}{M}. \tag{3.7b}$$

Assuming the accretion spin-up limit on black hole spin $\chi < 0.998$ for known black holes the expected gravitational wave frequency is in the 600 Hz–10 kHz range, and the expected quality factor is in the $2 - 33$ range.

The fundamental question is what are the plausible amplitudes for gravitational wave signals emitted by known black holes in X-ray binaries, and how do they compare with detector noise. We will choose as an example Cyg X-1 which is a near-by binary at a distance of 2 kpc with a black hole mass in the $6.8 - 13.3\,\mathrm{M}_\odot$ range [28]. The large black hole mass means a lower frequency range where current detectors are more sensitive. For instance at 2 kHz the sensitivity is at $\sim 2 \times 10^{-22}\,\mathrm{Hz}^{-1/2}$ (see figure 3.1) which for a typical detection threshold of SNR ~ 10 correspond to a sensitivity of $h_{\mathrm{rss}} \sim 10^{-21}\,\mathrm{Hz}^{-1/2}$. Using (1.44) this sensitivity corresponds to a gravitationally radiated energy $E_{\mathrm{GW}} \sim 10^{-7}\,\mathrm{M}_\odot\mathrm{c}^2$, during a time of the order of $\frac{Q}{f_0} \sim 10\,\mathrm{ms}$.

This radiated energy should be compared with the available matter around the black hole. For a simple order of magnitude argument, the difference of potential energy for a mass m between a point at infinity and on the black hole horizon is of the order of $\frac{GM}{R_S}m = \frac{1}{2}mc^2$. Thus the accretion rate give us an upper limit on the radiated power.

As extreme examples, the SS 433 X-ray binary has a very large persistent accretion rate $\sim 10^{-11}\,\mathrm{M}_\odot\mathrm{s}^{-1}$ [34], which is orders of magnitude smaller than $\frac{E_{\mathrm{GW}}}{c^2}\frac{f_0}{Q} \sim 10^{-5}\,\mathrm{M}_\odot\mathrm{s}^{-1}$, the lower limit for gravitationally visible signals. However higher accretion on short time scales could happen during an outburst, for instance for GRS 1915+105 the total mass of the disk is $\sim 4 \times 10^{-4}\,\mathrm{M}_\odot$ [35] for a 4×10^7 km radius, but only the inner $c\frac{Q}{f_0} \sim 3 \times 10^3$ km could fall into the black hole and excite the longest lived quasi-normal mode. As an example, the observed variation in the emission spectrum on seconds time scale have been interpreted [36] as step changes in the inner radius of the disk between 20 and 100 km. Assuming a uniform density, the emitted gravitational energy could be as high as $2 \times 10^{-12}\,\mathrm{M}_\odot\mathrm{c}^2$. But it is improbable as

the inner parts of the disk are expected to have smaller surface density than the outer parts [37].

Furthermore, the expected gravitationally radiated energy is much smaller than the total available potential energy. For instance for a radially falling point test particle of mass m onto a Schwarzschild black hole only

$$\sim 0.01mc^2(m/M) \tag{3.8}$$

is radiated. Hence the estimate in the preceding paragraph should be reduced by several orders of magnitude.

In conclusion, even though X-ray binaries are highly variable objects with infrequent bright outburst and sub second evolution time scales, they do not involve enough mass transfers to be interesting gravitational wave sources. Even an improvement by a factor 100 in sensitivity expected for distant future third generation detectors [38], which corresponds to a factor 10^4 in gravitational wave energy sensitivity, are not sufficient to make black holes in X-ray binary a relevant source. The study of black holes in these systems will still need to rely solely on electromagnetic observations.

3.3.2 Compact binary coalescence

We have already seen a very crude model of how a compact binary radiates gravitational waves in our toy example of section 1.5. In the case where neither of the compact objects has a significant spin, that picture is actually quite close to the real model. The only missing component is the energy loss of the system through gravitational radiation, which slowly shrinks the orbit and the orbital period.

In the general case of two point like objects of mass m_1 and m_2, bound on a circular orbit and separated by a distance d, a simple Newtonian calculation yields the mechanical energy

$$E = -\frac{G\mu M}{2d}, \tag{3.9}$$

in terms of the total mass $M = m_1+m_2$ and the reduced mass $\mu = m_1m_2/(m_1+m_2)$. By equating the time derivative of E to the power emitted through gravitational quadrupolar radiation (1.28) one obtains a differential equation on d, which assumes a quasi-static evolution. The solution of this equation can be recast in terms of orbital angular frequency ω using Kepler's third law

$$d = \left(\frac{GM}{\omega^2}\right)^{\frac{1}{3}}. \tag{3.10}$$

We will not go here into the details, but with a relatively simple calculation one obtains the time evolution of the gravitational wave angular

frequency $\omega_{\mathrm{GW}} = 2\omega$ [39]

$$\omega_{\mathrm{GW}}(t) = \frac{1}{4}\left[\frac{G^{5/3}}{5c^5}\mathcal{M}_c^{5/3}(t_c - t)\right]^{-3/8}, \tag{3.11}$$

where $\mathcal{M}_c = \mu^{3/5}M^{2/5}$ is the *chirp mass* which parameterizes at first order the inspiral evolution and t_c is the *coalescence time* at which the two point object merge. The resulting gravitational wave for an observer with inclination ι is

$$\begin{pmatrix} h_+(t) \\ h_\times(t) \end{pmatrix} = -\frac{G}{rc^4}2\mathcal{M}_c^{5/3}(G\omega_{\mathrm{GW}}(t)/2)^{\frac{2}{3}}\begin{pmatrix} (1+\cos^2\iota)\cos\left(\int^t \omega_{\mathrm{GW}}(t')\mathrm{d}t'\right) \\ 2\cos\iota\sin\left(\int^t \omega_{\mathrm{GW}}(t')\mathrm{d}t'\right) \end{pmatrix}. \tag{3.12}$$

The result (1.46) we obtained for the toy model discussed in section 1.5 can also be obtained from the above formula by noticing that in that case the reduced mass is $\mu = m/2$ and the distance between the objects is

$$d = 2a = \left(\frac{GM}{2\omega_{\mathrm{GW}}^2}\right)^{\frac{1}{3}}. \tag{3.13}$$

Hence as the orbit shrinks the frequency and the amplitude of the emitted signal increases. In order to compare this waveform with detector noise its Fourier transform is needed to compute the SNR as explained in section 2.3. However a good approximation of this Fourier transform can be obtained by using the stationary phase approximation, and it also yields some insight on the inspiral signal. We will not go into the details of the stationary phase calculation, but the result up to a constant factor can be obtained with a simple argument. The amplitude of the signal in (3.12) grows as $f^{2/3}$ and the length of time Δt during which the signal can be considered monochromatic is the solution of

$$1 \sim (f(t+\Delta t) - f(t))\Delta t \simeq \frac{\mathrm{d}f}{\mathrm{d}t}\Delta t^2. \tag{3.14}$$

If ones neglects the amplitude evolution of the signal during that time[5] the Fourier amplitude reads

$$|\tilde{h}_+(f)| \propto f^{2/3}\Delta t \simeq \frac{f^{2/3}}{\sqrt{\frac{\mathrm{d}f}{\mathrm{d}t}}} \propto f^{-7/6}, \tag{3.15}$$

where we used equation (3.11) to obtain the frequency derivative. This result shows that even though the instantaneous amplitude at low frequency is smaller, the longer integration time yields a higher contribution to the SNR at low frequency than at high frequency. The comparison between this

[5]The stationary phase approximation consists in assuming that the first two relative time derivatives of the amplitude can be neglected with regard to the phase derivative.

Fourier amplitude with appropriate normalization for an optimally located and oriented source [40]

$$|\tilde{s}(f)| = \frac{G^{5/6}}{2rc^{3/2}} \frac{\sqrt{5/6}}{\pi^{2/3}} \mathcal{M}_c^{5/6} f^{-7/6} \tag{3.16}$$

and detectors noise is shown on figure 3.1. Note that $2|\tilde{s}(f)|$ is shown on the figure as the SNR^2 computation (2.40) has a factor 4 in its expression. Typically binary systems can be seen out to several dozen Mpc with current detectors, within this range a merger rate of $\sim 10^{-2}\,\mathrm{yr}^{-1}$ is expected [40].

The assumption of circular orbits is well justified by gravitational waves circularizing the orbit in the course of the inspiral. By comparing the energy and angular momentum lost through gravitational radiation one obtains [41] a relationship

$$d(e) \propto \frac{e^{12/19}}{1-e^2} \simeq e^{12/19}, \quad \text{when } e \ll 1 \tag{3.17}$$

between orbital separation and eccentricity. For small eccentricities can be rewritten using (3.10) as a relation between eccentricity and orbital frequency

$$e \propto \omega^{-19/18}. \tag{3.18}$$

Thus the initial eccentricity becomes insignificant after the binary inspiral which covers several decades in frequency between formation of the binary and $\sim 10\,\mathrm{Hz}$ at which current gravitational waves detectors start to be sensitive. This orbital circularization has been studied in more details in population synthesis models [42] with the conclusion that the eccentricity can be neglected ($e \lesssim 10^{-5}$) for binary systems emitting in the sensitive band of ground detectors.

Of course the waveform described by equations (3.11) and (3.12) is only a zeroth order approximation, more precise waveforms are obtained through a *post-Newtonian* expansion of the above formalism, that is an expansion in different orders of v^2/c^2 corrections. For instance the angular frequency evolution of a waveform that includes corrections inclusively up to v^4/c^4 (called 2PN order) is expressed in function of dimensionless time

$$\Theta = \frac{c\mu}{5GM^2}(t_c - t), \tag{3.19}$$

and has the form [43]

$$\omega_{\mathrm{GW}}(\Theta) = \frac{c^3\Theta^{-3/8}}{4GM}\left[1 + \left(\frac{743}{2688} + \frac{11}{32}\frac{\mu}{M}\right)\Theta^{-2/8} - \frac{3\pi}{10}\Theta^{-3/8} + \left(\frac{1855099}{14450688} + \frac{56975}{258048}\frac{\mu}{M} + \frac{371}{2048}\frac{\mu^2}{M^2}\right)\Theta^{-4/8}\right], \tag{3.20}$$

with the corresponding integral

$$\int \omega_{\mathrm{GW}}(t)\mathrm{d}t = \phi_0 - \frac{2M\Theta^{5/8}}{\mu}\left[1 + \left(\frac{3715}{8064} + \frac{55}{96}\frac{\mu}{M}\right)\Theta^{-2/8} - \frac{3\pi}{4}\Theta^{-3/8} + \left(\frac{9275495}{14450688} + \frac{284875}{258048}\frac{\mu}{M} + \frac{1855}{2048}\frac{\mu^2}{M^2}\right)\Theta^{-4/8}\right]. \quad (3.21)$$

The full 2PN expansion also includes higher order terms than just the quadrupolar radiation, however this *restricted post-Newtonian waveform* captures most of the phase and amplitude evolution, and will be a sufficient approximation for the purpose of characterizing a search for unmodeled sources.

One should note that these post-Newtonian expansions are only valid as long as $|\Theta| \gtrsim 1$ and the size of the considered objects is smaller than the distance between them. In the final part of the coalescence many non-perturbative effects appear, neutron stars can be tidally disrupted, the evolution changes from an adiabatic inspiral to a rapid plunge and eventually the two compact objects collide and merge. For the case of two black holes full general relativity numerical calculations are able to consistently calculate merger waveforms using different approaches [44], but for cases involving neutron stars the merger behavior is not well understood. The lack of precise knowledge on the nuclear matter equation of state is one of the reasons beside the computer simulations complexity.

However for the problem of first gravitational wave detection this effects will be largely unseen because they happen at high frequency where detectors are less sensitive. The typical frequency at which the post-Newtonian description fails is the frequency of the innermost stable circular orbit of a test mass [4], which corresponds to a gravitational wave frequency

$$f_{\mathrm{isco}} = \frac{c^3}{6\sqrt{6}\pi GM} \simeq 4.4\frac{M_\odot}{M}\,\mathrm{kHz}, \quad (3.22)$$

and $\Theta \sim 1$. For instance for two $1.4\,\mathrm{M}_\odot$ neutron star the ISCO frequency is 1.6 kHz. For a search which is limited to below 500 Hz the merger evolution is out of band for binary systems with total mass $M < 10M_\odot$, and is negligible for binary systems with total mass of order a few dozen solar masses, especially given the few kilohertz frequency of the quasi normal modes (3.7) from the resulting black hole.

Spinning compact objects

For the moment we have only considered non-spinning compact objects, however these objects may acquire significant spins either during their formation or by different types of mass transfers[6] from a companion in its giant branch

[6]For instance Roche lobe overflow accretion or common envelope phase.

phase. Usually the spin is described by the dimensionless spin $\chi = \frac{|\boldsymbol{S}|c}{GM^2}$, where $\boldsymbol{S}$ is the total angular momentum of the object. For neutron stars the maximal spins in observed pulsars are $\chi \simeq 0.04$, but for black holes they can be much more significant with observed spins $\chi \sim 0.1 - 0.99$, though these measurements come with many caveats [45, 46]. Also, some upper limits on the spin can be theoretically derived, for neutron star with realistic equation of state the break-up limit is $\chi \lesssim 0.7$ [47] and for black holes the maximal spin that can be obtained through accretion is $\chi \sim 0.998$ [31].

During the time that the inspiral sweeps through detectors sensitive band one can neglect the gravitational radiation of each of the individual objects and consider the spins $\boldsymbol{S}_1$ and $\boldsymbol{S}_2$ of both objects as constant in magnitude. Detailed calculation of the binary evolution equation of motion have been performed at 2.5 PN [48] and higher orders. There are two major effects on the gravitational waveform: the orbital frequency time evolution (3.20) is modified at 1PN and higher orders, and the orbital plane is precessing, which translates into a time dependent ι in (3.12). Only the second effect is important from the point of view of a search that does not rely on template waveforms.

In the simplified case of one spinning body ($\boldsymbol{S}_1 = 0$) the leading order evolution is an orbital angular momentum $\boldsymbol{L}$ and spin $\boldsymbol{S}_2$ that are precessing around the total angular momentum $\boldsymbol{J} = \boldsymbol{L} + \boldsymbol{S}_2$, with $\boldsymbol{L}$ that is decreasing in magnitude due to gravitational radiation emission [48]. The equations of motion are then:

$$\dot{\boldsymbol{S}}_2 = \boldsymbol{\omega}_p \wedge \boldsymbol{S}_2, \tag{3.23a}$$

$$\dot{\boldsymbol{L}} = \boldsymbol{\omega}_p \wedge \boldsymbol{L} - \epsilon_{RR}\boldsymbol{L}, \tag{3.23b}$$

$$\dot{\boldsymbol{J}} = -\epsilon_{RR}\boldsymbol{L}, \tag{3.23c}$$

where the precession frequency $\boldsymbol{\omega}_p$ and the angular momentum radiation rate ϵ_{RR} are

$$\boldsymbol{\omega}_p = \frac{G\boldsymbol{J}}{2d^3c^2}\left(1 + 3\frac{M}{m_2}\right), \tag{3.24a}$$

$$\epsilon_{RR} = \frac{32G^3}{5c^5}\frac{\mu M^2}{d^4}. \tag{3.24b}$$

The solution is that the *tilt angle* $\kappa = \arccos(\hat{\boldsymbol{L}} \cdot \hat{\boldsymbol{S}}_2)$, where $\hat{\boldsymbol{L}} = \boldsymbol{L}/L$ and analogously for $\hat{\boldsymbol{S}}_2$, between the orbital momentum and spin is a constant of motion, and that as long as the total angular momentum changes slowly during one precession period, i.e. $\frac{\dot{J}}{\omega_p J} = \frac{\epsilon_{RR} L}{\omega_p J} \ll 1$, the precession direction $\propto \boldsymbol{J}$ stays fixed. The latter holds true whenever the post-Newtonian development is valid unless the spin $\boldsymbol{S}_2$ is significant and anti-aligned with $\boldsymbol{L}$, in that case a situation where $J \sim 0$ may happen and lead to the so called transitional precession or tumbling.

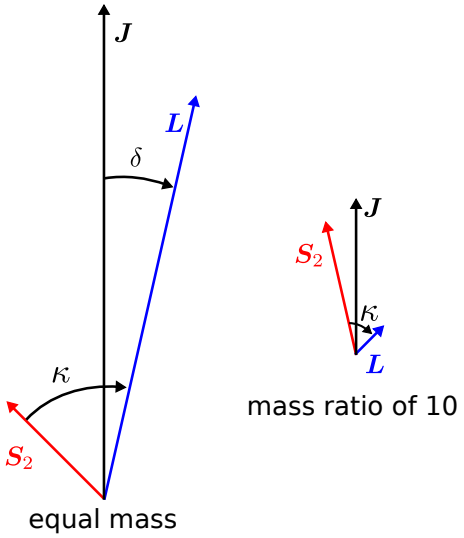

Figure 3.5: Sketch of the total angular momentum $\boldsymbol{J}$, orbital momentum $\boldsymbol{L}$ and a compact object spin $\boldsymbol{S}_2$ for a binary system containing one spinning body. Shown are also the tilt angle κ between the spin and the orbital angular momentum, and the angle δ between the total and the orbital angular momentum. The left sketch corresponds to an equal mass system at ISCO frequency and the right sketch correspond to a mass ratio of $m_2/m_1 = 10$ at ISCO frequency. In both cases $\chi_1 = 0$, $\chi_2 \sim 1$ and the tilt angle $\kappa = 45°$. In any case as the binary inspirals the alignment of vectors will qualitatively evolve from the left to the right configuration.

Hence the general picture shown on figure 3.5 is that the orbital plane precesses around the fixed axis $\hat{\boldsymbol{J}}$, the orbital angular momentum slowly decreases in magnitude and the orbital inclination angle δ between the two increases.

For circular orbits the orbital momentum magnitude is

$$L = \mu d^2 \omega = \mu (GM)^{2/3} \omega^{-1/3}, \tag{3.25}$$

and decreases with frequency. At the high frequency limit where L is minimal, that is at the ISCO frequency $L_{\rm isco} = \sqrt{6}\frac{G\mu M}{c}$ and should be compared to the individual objects spins

$$\frac{S_i}{L_{\rm isco}} = \frac{\chi_i m_i^2}{\sqrt{6} m_1 m_2}. \tag{3.26}$$

Hence for a near equal mass binary the spin contribution can be comparable to the orbital momentum only at plunge time and the precession will not significantly affect the orbital plane as $\boldsymbol{J}$ and $\boldsymbol{L}$ will be nearly parallel during the inspiral. On the contrary, for large mass ratios the spin of the

more massive object can dominate the total angular momentum and lead to significant precession. For instance this is the case for a neutron star - black hole binary where $m_2/m_1 \sim 10$ and $\chi_2 \sim 0.7$ are reasonable values. In both cases the approximation of a single spinning body captures the important features of the binary system precession.

3.3.3 Massive star collapse

Stars with large masses (above $10\,M_\odot$ at star birth) are believed to produce an iron core during their evolution [49]. This core collapses once it exceeds the Chandrasekhar mass limit of electron degenerate pressure support. The collapse stops when the center of the core exceeds nuclear density by about a factor two, which generates a rebound of the core and launches a shock wave that propagates through the infalling core. In about 0.1 s a hot proto-neutron star with a radius[7] of ~ 30 km and an standing accretion shock at ~ 150 km are created. Afterwards two scenarios are possible: either the proto-neutron star cools and forms a neutron star or it accretes to much matter and collapses into a black hole. The final state depends among others on the mass and rotation of the initial star.

In the standard core-collapse model the cooling proto-neutron star radiates copious amounts of neutrinos which are able to revive the shock, push off the accreting mater and explode the star. In numerical simulations of core-collapse successful explosions are difficult to obtain, as they require complex instabilities such as the standing accretion shock instability and multi dimensional modelling [50]. The ejected matter radioactively decays on a time scale of weeks and produces an optical brightening on the same time scale, this brightening is called a supernova.

Supernovae are observationally classified according to their optical spectra into two main types: in type I supernovae no hydrogen line is present and in type II supernovae a hydrogen spectra line is visible. This two main classes are subdivided into subclasses according to the presence or absence of other spectral features. An important subclass are type Ia which are produced by the run-away combustion of a white dwarf. These supernovae are important tracers in the field of cosmology but are not relevant as a gravitational wave source. The other subclasses of type I supernovae and all type II supernovae are thought to be produced by a massive star collapse.

In this thesis we are mostly interested by astrophysical events that could produce a gamma ray burst. One of the main models of production for these bursts is the collapse of rapidly rotating massive stars. We will discuss in detail the gamma ray production from these systems in section 4.1, the important point here is that in the current models either a black hole with a nuclear density torus or a highly magnetized neutron star is needed to

[7] For a settled cold neutron star the radius is at about half this value.

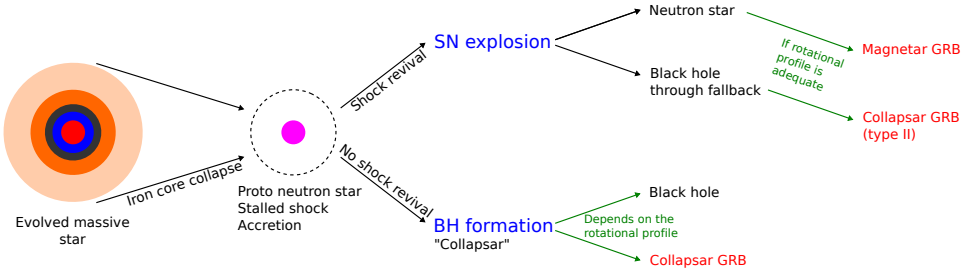

Figure 3.6: Graphical summary of different jet producing models described in the text. The result depends strongly on the initial rotational profile of the evolved star and the evolution of this profile. Figure idea courtesy of Christian Ott.

produce such a burst. Several extreme extensions of the standard core-collapse scenario have been proposed to produce these central engines, and are thought to concern only a small fraction ($\sim 1\%$) of core collapses. In all cases the starting point is a core bounce, followed by the formation of a proto-neutron star and a standing accretion shock. However the later stages are largely unknown and several models have been proposed [51]:

Magnetar This model is the closest one to the standard core-collapse picture. The main difference is that the produced neutron star is rapidly spinning with a period of the order of 1 ms that is near breakup, and with a very large magnetic field ($\sim 10^{15}$ G) which is produced through a dynamo effect [52]. A successful supernova explosion is needed in this model in order to prevent the collapse of the neutron star to a black hole as described in the collapsar model.

Collapsar This is the most popular model to explain gamma ray bursts in stellar collapse [53]. It involves the collapse of the proto-neutron star into a black hole as it exceeds the mass that can be supported by neutron degenerated pressure and rotation, and the creation of a dense accretion disk around the hole which requires a large angular momentum in the initial core. This model is divided into two types[8] depending on how the black hole is created.

Type I In this scenario the shock revival is not successful, no supernova is produced and the proto-neutron star promptly (in less than a few seconds) collapses to a black hole as the outer core continues to accrete. Polar accretion is more rapid than equatorial, as the rotating matter needs to shed angular momentum in order to fall onto the central object. As a result an equatorial

[8] Note that two types of the collapsar model do not have any relationship with the two types of observed supernovae.

disk is formed around the black hole and is accreted on a time scale of $10 - 100\,\mathrm{s}$.

Type II In this scenario the shock revival is successful, but a significant fraction of the infalling core (0.1 to several $M_\odot$) stays gravitationally bound throughout the explosion and accrete onto the proto-neutron star which forms a black hole - disk system as in the case of type I collapsar. The typical time for this fall back is $\sim 100\,\mathrm{s}$.

Supranova In this last model the supernova explosion is fully successful, however the proto-neutron star is "hypermassive", it exceeds the maximal mass of a non-rotating neutron star and its larger mass is supported by centrifugal force. The maximal supported mass is increased by $\sim 20\%$ in case of rigid rotation and $\sim 50\%$ for differential rotation. As the neutron-star slows down due to dipole radiation it eventually collapses to a black hole and disk systems on a month time scale. This model seems to be excluded by the observed association between supernova and gamma ray burst [49] with delays of $\sim 1\,\mathrm{day}$. However, for differential rotation support the collapse time could be as short as $\sim 1\,\mathrm{s}$, given that magnetic braking will lead to a uniformly rotating star.

A graphical summary of these models is shown on figure 3.6, they all involve relativistic motion of matter at nuclear densities. If this motion is not spherically symmetric it can generate large amounts of gravitational radiation. Given that gamma ray bursts are extra-galactic (and in most cases cosmological) events, only process that could produce gravitational waves detectable at more than 1 Mpc are of interest to us.

In currently operating gravitational wave detectors the best sensitivity is $\sim 2 \times 10^{-23}\,\mathrm{Hz}^{-1/2}$ at 150 Hz frequency (see figure 7.1). For a gravitational wave detection an event with let say $\mathrm{SNR} \gtrsim 10$ is required, hence only gravitational waves with $h_{\mathrm{rss}} \gtrsim 2 \times 10^{-22}\,\mathrm{Hz}^{-1/2}$ can be observed. Which using equation (1.44) at a distance of 1 Mpc corresponds to a gravitationally radiated energy $E_{\mathrm{GW}} \sim 10^{-5}\,\mathrm{M}_\odot\mathrm{c}^2$. One should note that the sensitivity to gravitationally radiated energy is strongly dependent on frequency. In the shot noise dominated regions the detectors sensitivity is linearly growing with frequency (2.33) and the energy is quadratic in both frequency and h_{rss}. So above a few hundred hertz the sensitivity is $E_{\mathrm{GW}} \propto f^4$ and at 1 kHz only sources radiating more than $E_{\mathrm{GW}} \sim 10^{-2}\,\mathrm{M}_\odot\mathrm{c}^2$ are of interest.

We will start our survey of possible gravitational wave emission mechanisms with the common standard core-collapse part. It has been studied in details in the context of garden variety core-collapse supernovae [54], however these results do not include extreme rotation nor high magnetic fields that are present in the context of gamma-ray bursts.

Core bounce During the initial core infall and bounce a quadrupolar deformation may arise, especially at high rotation. Numerical studies [55] show that the emitted gravitational waves have the shape of a sharp spike followed by a ringdown. For their most rapidly rotating models, typically an energy $E_{\mathrm{GW}} \sim 10^{-9}\,\mathrm{M}_\odot\mathrm{c}^2$ is emitted with a peak frequency in the 100 – 200 Hz range. Thus the core bounce is not an interesting extragalactic source.

Rotational instability Rapidly rotating star could develop bar mode[9] type instabilities. Dynamically formed instability seem to be excluded by modern core-collapse simulations due to insufficient rotational kinetic energy. However other type of instabilities have been seen to develop in numerical simulations at lower rotational energy. The typical observed [56] growth time and duration of these instability is on the order of a few 100 ms and the emitted energies are $E_{\mathrm{GW}} \sim 10^{-7}\,\mathrm{M}_\odot\mathrm{c}^2$ at twice the rotational frequency (that is at ~ 1 kHz in their simulation). However analytical arguments [57] suggest that in extreme cases the emitted energy could be as high as $10^{-2}\,\mathrm{M}_\odot\mathrm{c}^2$, which would be sufficient for a gravitational wave observation at extragalactic distances.

g-Modes During the accretion of matter onto the proto-neutron star various mode of the compact object can be excited, especially given that the accretion is expected to be turbulent and modulated by the standing accretion shock instability of the stalled shock. This could lead to the excitation of neutron star core g-modes for which buoyancy is the main restoring force [58] through a controversial acoustic mechanism [59]. In the most extreme case, as much as $10^{-4}\,\mathrm{M}_\odot\mathrm{c}^2$ could be gravitationally radiated at about 800 Hz. One should note that these simulations have been performed assuming axis symmetry, hence the gravitational polarization is constrained to be linear.

There are several other emission mechanisms that are either out of the sensitive frequency band or too low in amplitude to be included in the discussion above: other types of proto-neutron star accretion induced excitations radiate energies which are several order of magnitude smaller than g-modes; neutrino and asymmetric outflow emission are too low in frequency $\lesssim 1$ Hz; black hole quasi-normal modes discussed in section 3.3.1 are too high frequency at several kilohertz; neutron star r-modes are also promising sources of gravitational waves but they long duration $\gtrsim 100$ s require new analysis methods that are currently under development and beyond the scope of this thesis.

The rapid rotation present in the context of gamma ray bursts could lead to more extreme emission mechanisms on top of the ones described

[9] That is a bar shaped mass excess.

above. These mechanisms are the most promising for detection of extra-galactic sources, the first one could be associated with any of the extreme collapse models, but the two latter can only be involved in the collapsar or supranova model as they require an accretion disk around a black hole.

Core fragmentation Neutron star modes instability if not saturated could lead to the fragmentation of the proto-neutron star into several blobs of nuclear matter containing a fraction of the neutron star mass [60]. These blobs would inspiral on a time scale of minutes and generate gravitational waves similarly to a standard binary described in section 3.3.2. Analogously to neutron star binaries, core fragmentation could be seen up to several megaparsec away with current detectors.

Disk fragmentation In scenarios that contain a black hole surrounded by an accretion disk, gravitational instability may arise in the disk and produce blobs of mass $\sim 0.1 - 1\,\mathrm{M}_\odot$ [61]. As in the core fragmentation mechanism these fragments inspiral around the central black hole, at first more rapidly than in the binary scenario due to viscous torque which is dwarfed by the gravitational torque once the inspiraling fragment is close enough. In cases where the gravitational torque dominates the viscous one for orbital frequencies $\lesssim 100\,\mathrm{Hz}$ these inspirals could be seen at $\sim 10\,\mathrm{Mpc}$.

Disk precession If the accretion disk is tilted with regard to the black hole spin axis, the accretion disk will precess around the spin axis [62]. In most optimistic evaluations the disk could radiate up to $10^{-4}\,\mathrm{M}_\odot\mathrm{c}^2$ at 150 Hz over several seconds. However fits to gamma ray curves in which the disk precession explains the temporal variability in the light curve show precession at much lower typical frequency (several Hz).

All of the above optimistic models and the extreme cases of rotational instability and g-Modes discussed before predict a gravitational radiation around 100 Hz with a mass quadrupole evolution well approximated by a rotating bar. Hence the inclination dependence of the + and × polarization is expected to be the same as for a binary (3.12). The rate of such events within a given radius is of the same order of magnitude as for the CBC case, that is one per century within a dozen Mpc distance.

In conclusion gravitational radiation in stellar collapse is much more uncertain than in compact binary coalescence. Typical signal to noise ratio for these events could vary from the same one as for an inspiral at the same distance down to 5 orders of magnitude lower, as the core bounce is the only reliable and well modeled emission process. However massive star collapse producing gamma ray bursts are thought to be extreme cases of stellar collapse, which motivates an opportunistic search for gravitational waves in association with them as they could also be in the upper range of predicted gravitational radiation.

Chapter 4

Gamma-ray bursts

Gamma-ray bursts (GRB) as their name implies are short bright bursts of gamma-rays observed on the sky. They were first discovered in the early 70's by the Vela spacecrafts launched by the US government in order to monitor the application of the Partial Test Ban Treaty on nuclear weapon tests in air, in outer space and under water.

After this initial discovery a large number of dedicated spacecrafts have been designed and operated in order to understand the nature of these transient events. These spacecrafts have enabled a more detailed study of the γ-ray light curve and spectroscopy but also in most recent missions rapid followups (down to minutes after the event) of the GRB afterglows in X-ray, optical and radio band. Several thousands GRBs have been observed to date, with current new detection rate of approximately 1 per day.

The observed distribution of GRBs is isotropic and for the fraction with measured redshifts (median redshift ~ 2) the typical distance is of the order of 10 Gpc. Assuming an isotropic γ-ray emission the typical energies emitted by each burst are $10^{-3} - 1\,M_\odot c^2$. Based on the distribution of durations shown on figure 4.1 GRBs have been observationally classified into two groups: short GRBs with a duration of less than 2 seconds and long GRBs which are longer than 2 seconds. The duration is characterized by the length T_{90} of the time interval containing the 5 to 95% of above background photon counts in the $15 - 350$ keV energy range. The exact range used depends slightly on the γ-ray detector. This classification is also supported by γ-ray spectra, as short bursts tend to have a harder spectrum than long bursts.

Long bursts are thought to be generated by stellar collapse in massive stars. The two main results supporting this model are: associations with a supernova emission for several long bursts[1], and a predominant localization in galaxies with active star formation regions[2].

[1] However for at least two long bursts no supernova optical bump has been observed with upper limits a factor ~ 100 lower than typical supernova light curves.

[2] Massive stars are very short lived, there is only a few million years between formation

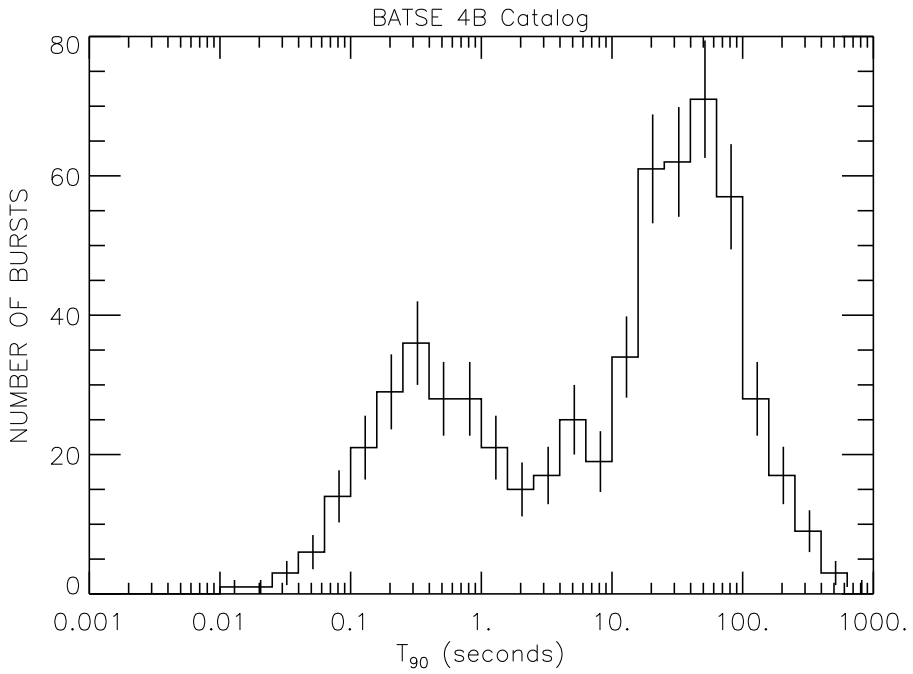

Figure 4.1: Distribution of durations of GRB in the 4B catalog of the BATSE detector [63]. The T_{90} is the duration of the time span that contains the 5 to 95% interval of total observed background subtracted γ-ray count in the 15 – 350 keV energy range.

The progenitors of short GRBs are less observationally constrained, among others due to a much smaller sample of afterglow observations, but they are thought to be generated by compact binary coalescence involving a neutron star and another compact object. The hypothesis is motivated by their predominant localization in galaxies with an old stellar population and large distances from the galaxy center explained by supernova kicks during the neutron star formation.

For a historical discussion of the GRB field and the current results and prospectives see for instance the recently published book by Vedrenne and Atteia [51].

4.1 Relativistic jets

The large energy emission under the assumption of an isotropic γ-ray emissions is difficult to explain with any of the above progenitors. Hence the emission is believed to be beamed along narrow cones and produced by col-

and core collapse.

limated jets. This model is also supported by the observation of achromatic breaks in the afterglow light curves, which are explained by the observer seeing the edge of the relativistic jet as it slows down. It is also supported by much smaller energies observed once the jet slows down in the radio band where the emission is close to being isotropic. The typical inferred angles are $5 - 20°$, and the corresponding beaming corrected energies are $\sim 10^{-3}\,\mathrm{M}_\odot\mathrm{c}^2$, similar to the energy emitted by a typical, $\sim$ week long, supernova optical bump.

The observed light curves are highly variable with variation time scale t_{var} as short as milliseconds. In order to allow such rapid evolution the emitting region has to be smaller than $ct_{\mathrm{var}} \sim 300\,\mathrm{km}$, otherwise the time structure would be washed out by propagation delays. Given the large radiated energy coming from such a small source the γ-ray spectrum should be sharply cut-off at $\sim 1\,\mathrm{MeV}$ due to pair production $\gamma\gamma \to e^+e^-$ opacity. Such cut-offs are not seen in GRB spectra, which is well explained by bulk relativistic motion of the emitting region.

In the standard model of GRB emission [51] the relativistic motion of the emitting region (with $\Gamma = 1/\sqrt{1-(v/c)^2} \sim 10 - 1000$) shortens the apparent size of the emission region and blue shifts the emitted photons. But before looking at relativistic jet properties let us review the different proposed mechanisms for creating such jets.

4.1.1 Jet progenitors

There are thus two main astrophysical events expected to create GRBs: a compact binary coalescence involving at least one neutron star, or the collapse of a massive star. As discussed in section 3.3.3, the latter scenario could create a central engine composed of a black hole and a dense accretion disk or a rapidly spinning magnetar. For binary coalescence the formation of a black hole and a dense accretion disk is also likely.

Several mechanisms have been proposed for extracting energy from the central engine into an electromagnetic fireball [51].

Neutrino annihilation The newly formed accretion disk dissipates energy through neutrino radiation. The $\nu\bar{\nu}$ annihilation cross-section is largest along the rotation axis where the interactions are the least tangential.

Magnetic fields Large magnetic fields are expected in both the magnetar and the black hole with accretion disk scenarios. For the latter the initial magnetic field in the disk can be enhanced by dynamo processes or by extracting rotational energy of the black hole through the Blandford-Znajek mechanism [64]. This large $\sim 10^{15}\,\mathrm{G}$ rotating magnetic fields creates a strong electric field under which vacuum is unstable to electron-positron pair production. In this scenario the jet

can also be Poynting flux dominated, with most of the energy carried by bulk magnetic lines carried with the relativistic outflow.

The expansion of the fireball generated by either of the two mechanism is collimated by the geometry of the systems, as the mass density is much larger in the equatorial plane than in the polar region. The reason being that baryon loading efficiently slows down the expansion. This collimation can be further enhanced at larger distances from the central engine by the outflow punching through the stellar envelope of the massive star or through a baryonic wind driven of the accretion disk by the neutrino flux. In the case of Poynting flux dominated jets the collimation can also be due to magnetic fields.

4.1.2 Jet properties

Observer time scales

Let us consider a surface moving at relativistic speed with a Lorentz factor $\Gamma = 1/\sqrt{1-(v/c)^2}$. The time evolution of the surface for an observer at rest is $x(t) = vt$. For photons emitted at positions x_1 and x_2 the time difference between their arrivals for an observer along the direction of propagation is

$$\Delta T_{\text{prop}} = \frac{x_2 - x_1}{v} - \frac{x_2 - x_1}{c} \underset{\Gamma \gg 1}{\simeq} \frac{x_2 - x_1}{2c\Gamma^2}. \tag{4.1}$$

This result relaxes the condition on the size of the emitting region from $ct_{\text{var}} \sim 3 \times 10^5\,\text{m}$ to for instance $c\Gamma^2 t_{\text{var}} \sim 3 \times 10^9\,\text{m}$ if $\Gamma \simeq 100$.

In practice the geometry of the jet is not planar but conic as shown on figure 4.2. The surface to consider is a spherical shell with a Lorentz factor Γ limited to a cone of opening angle θ . For an observer at infinity only the interior of a conic cut with an opening angle Γ^{-1} is visible due to relativistic beaming. Moreover, for an observer whose line of sight forms an angle ζ with regard to the jet axis greater than $\sim \theta + \Gamma^{-1}$ the jet is completely invisible.

Due to this geometry, for an observer at infinity, photons emitted by different visible parts of a shell at radius R will arrive spread out in time by

$$\Delta T_{\text{ang}} = \frac{\Delta R}{c} = \frac{R}{c}\left(1 - \cos\Gamma^{-1}\right) \underset{\Gamma \gg 1}{\simeq} \frac{R}{2c\Gamma^2}, \tag{4.2}$$

the same time as the propagation delay ΔT_{prop} (4.1) between the source of the jet and the radius R.

Fireball model

Let us take a step back and study more carefully the expansion of a relativistic fireball in spherical symmetry. As an initial condition one of the processes described above deposits an energy E_0 into a region of size $R_{\text{in}} \simeq 10^5\,\text{m}$ containing a mass M_0. This mass M_0 is dominated by the amount of baryons

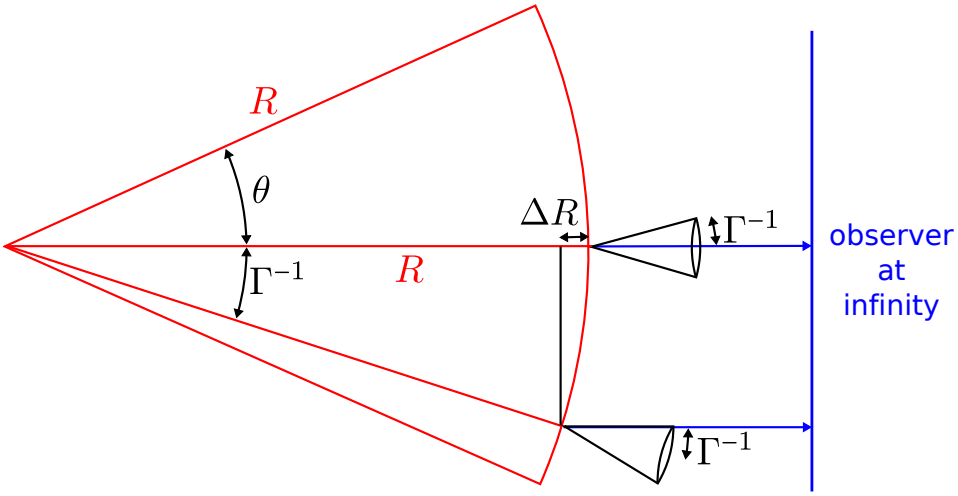

Figure 4.2: Geometry of the outflow of a single shell in a jet. The shell is limited in a jet opening angle θ. For a shell with Lorentz Γ only a conic cut with angle Γ^{-1} is visible to an observer at infinity due to relativistic beaming. The width of the shell due to the spherical curvature as seen by an observer at infinity is $\Delta R = R\left(1 - \cos\Gamma^{-1}\right)$.

present in the deposition region, and we will assume it is small, $M_0c^2 \ll E_0$. The very large optical depth prevents any efficient radiative energy transport and the relativistic fireball expands adiabatically[3] with $TV^{1/3} = TR = const.$ The total energy $E = \Gamma M_0(c^2 + kT/m_p)$ is conserved and the initial thermal energy ($\Gamma \sim 1$ and $kT/m_p \gg c^2$) is converted into bulk kinetic energy ($E \sim \Gamma M_0c^2$). In the regime where the thermal energy dominates over the bulk kinetic energy the total energy is proportional to the temperature $E \propto \Gamma T \propto \Gamma R^{-1}$. Using the conservation of the total energy, we obtain that the Lorentz factor Γ grows linearly with the expansion radius up to a maximal value $\Gamma_{\rm sat} \sim E_0/M_0c^2$ at a typical radius $R_{\rm sat} = \Gamma_{\rm sat}R_{\rm in} \simeq 10^7 - 10^8\,{\rm m}$ where the bulk kinetic energy becomes dominant.

After the saturation of the initial accelerating expansion the fireball grows linearly with a constant bulk Lorentz factor $\Gamma \sim \Gamma_{\rm sat}$. At a typical radius $R_{\rm ph} \sim 10^9 - 10^{11}\,{\rm m}$ the fireball becomes optically thin but most of the initial energy has already been transfered to the bulk motion of baryons, hence the radiated thermal spectrum is weak.

As a consequence electrons need to be reaccelerated in order to produce γ-rays. In the standard fireball scenario this is done through internal shocks in the outflow. The basic picture is that the central engine energy deposition

[3]For ideal gases the adiabatic expansion law is $PV^{\gamma-1} = const$ and $\gamma = 4/3$ for relativistic gases.

is fluctuating, if an initial expanding shell with Lorentz factor Γ_1 is followed by a faster shell $\Gamma_2 > \Gamma_1$ the two shells will eventually collide and produce a shock. For a central engine with a variability time scale $t_{\rm var}$, the two shells meet at a radius $R_{\rm IS} = v_1 t = v_2(t - t_{\rm var})$. Assuming that Γ_1 and Γ_2 are of the same order of magnitude and using $v = c\sqrt{1 - 1/\Gamma^2}$ one obtains

$$\frac{t_{\rm var}}{t} = \frac{\Gamma_2^2 - \Gamma_1^2}{2\Gamma_1^2\Gamma_2^2} \sim \frac{1}{\Gamma^2}. \tag{4.3}$$

Thus the typical radius at which the internal shocks occur is

$$R_{\rm IS} \sim c\Gamma^2 t_{\rm var} \sim 10^{12} - 10^{13}\,{\rm m} \tag{4.4}$$

for $\Gamma \sim 100$ and $t_{\rm var} \sim 1\,{\rm s}$. The shock accelerates a small part of the present electrons which are expected to radiate the observed γ-ray spectrum through synchrotron radiation and inverse Compton scattering.

Electromagnetic model

An alternative to the fireball model is the electromagnetic model [65] in which the jet is dominated by the Poynting flux. We will not go here into the details of this less popular model, but the main features are that the energy injection causes the expansion of a magnetized elongated bubble. The front of this bubble (or jet) becomes unstable and produces γ-rays at a typical distance

$$R_{\rm dec} \sim 10^{13} - 10^{15}\,{\rm m} \tag{4.5}$$

from the central engine.

4.2 Gamma-ray burst spacecrafts

In 2009-2010 most of GRBs have been detected by the Gamma-Ray Burst Monitor on the Fermi spacecraft [66], the Burst Alert Telescope on the Swift spacecraft [67], and the third Interplanetary Network of spacecrafts [68]. There are several other missions which have detected only a few GRBs during that time due to a much smaller field of view. We will discuss below only these three major sources of GRB triggers.

The detection time and sky locations of GRBs are distributed through the Gamma-ray bursts Coordinates Network (GCN), a public alert system intended to trigger low latency followups [69]. The reported time corresponds to the crossing of an internal threshold in the spacecraft that depends among others on the γ-ray flux and local background. Thus the reported time $T_{\rm GRB}$ corresponds to the start of the γ-ray light curve.

4.2.1 Third Interplanetary Network

The third Interplanetary Network (IPN) started its operations in 1990 and has been operating since then. It consists of γ-ray detectors fixed on various spacecrafts in low Earth orbit, eccentric Earth orbit, on their way or in orbit around other planets. These detector are roughly isotropic and the network as a whole operates as a full-time all-sky monitor with a 50% detection threshold at a $6 \times 10^{-7}\,\mathrm{erg\,cm^{-2}s^{-1}}$ flux (~ 1 photon $\mathrm{cm^{-2}s^{-1}}$) in the $25 - 150\,\mathrm{keV}$ energy range. The localization is performed through triangulation of the times of arrivals of γ-rays between different spacecrafts in the network.

However in most cases the data are retrieved with $\sim 1\,\mathrm{day}$ latency and the sky position is computed with a much larger delay, thus the detection and sky location information are not reported through GCN in most cases. For cases where the detection is reported the sky location errors are of the order of a few arcminute.

4.2.2 Swift

The Burst Alert Telescope (BAT) on the Swift spacecraft is a coded aperture telescope with a field of view of 1.4 steradian. It is sensitive for fluxes $\sim 10^{-8}\,\mathrm{erg\,cm^{-2}s^{-1}}$ in the $15 - 150\,\mathrm{keV}$ energy range, with a sky location accuracy of several arcminutes. The sky location is performed by analyzing the shadow pattern of a coded mask onto an array of CdZnTe detector elements, and can be further refined if an X-ray or optical afterglow is detected by the other instruments present on the Swift spacecraft.

4.2.3 Fermi

The Gamma-Ray Burst Monitor (GBM) on the Fermi spacecraft is composed of NaI and BGO scintillation detectors which cover a field of view of 9 steradians. The NaI detectors are used for sky localization, and are sensitive to fluxes ~ 0.4 photons $\mathrm{cm^{-2}s^{-1}}$ in the $8\,\mathrm{keV} - 30\,\mathrm{MeV}$ energy range. These detectors are essentially thin disk and the observed flux is proportional to the cosine of the angle between the γ-ray source and the disk axis. The sky location reconstruction is based on comparing the fluxes between disks with different orientations located on the spacecraft. The typical statistical error of this sky location method is ~ 1 degree or more.

4.2.4 Sky localization model

For the GBM the sky location errors are large enough that they need to be included in a gravitational wave analysis triggered by these GRBs. The sky location probability distribution is well modeled by a Gaussian distribution on the sphere also called *Fisher distribution* [70]. The probability distribution for the angle θ between the reported sky location and the true sky

location is

$$P_{\mathrm{F}}(\theta;\kappa) = \frac{\kappa \sin\theta}{\mathrm{e}^{\kappa} - \mathrm{e}^{-\kappa}} \mathrm{e}^{\kappa\cos\theta}, \tag{4.6}$$

where κ parameterizes the width of the distribution. This probability distribution is smoothly going from a Dirac distribution for $\kappa = \infty$, a good approximation of a planar 2D Gaussian distribution for $\kappa \gg 1$, and of a uniform distribution on the sphere for $\kappa = 0$.

Sky location errors are usually specified in terms of the angular radius σ containing 68% of the probability distribution. For small errors ($\sigma < 30°$) κ can be expressed as a function of σ

$$\kappa(\sigma) \simeq \frac{1}{(0.66\,\sigma)^2}, \tag{4.7}$$

with a 1% accuracy. Also the 95% containment radius for small angles is $\sigma_{95\%} \simeq 1.65\sigma$, note that this is different from the usual one dimensional Gaussian coverage where $\sigma_{95\%} \simeq 2\sigma$.

In addition to a statistical error σ_{stat} that depends on the GRB flux, sky locations by the GBM also have a systematic error, due to the imperfect modeling of the detector response and scattering of γ-rays on the spacecraft and Earth's atmosphere. This systematic error is estimated by comparing the sky localizations between the GBM and other detectors [71]. Currently this systematic error is modeled using two Fisher distributions [72]. A "core" distribution which has a width $\sigma_{\mathrm{core}} = 3.2°$ and contains a fraction $f_{\mathrm{core}} = 0.7$ of the distribution, and a "tail" distribution which has a width $\sigma_{\mathrm{tail}} = 9.5°$. For these parameters a 95% coverage is obtained for an angular radius of 7.5°.

In total, the sky location probability distribution of GBM is well modeled by

$$P_{\mathrm{GBM}}(\theta) = f_{\mathrm{core}} P_{\mathrm{F}}\left[\theta;\kappa\left(\sqrt{\sigma_{\mathrm{stat}}^2 + \sigma_{\mathrm{core}}^2}\right)\right] + (1-f_{\mathrm{core}}) P_{\mathrm{F}}\left[\theta;\kappa\left(\sqrt{\sigma_{\mathrm{stat}}^2 + \sigma_{\mathrm{tail}}^2}\right)\right], \tag{4.8}$$

which is shown on figure 4.3.

4.3 Gamma-ray burst and gravitational wave coincidence

As we have seen in section 3.3.2 and 3.3.3 central engines which produce γ-ray bursts are also good sources of gravitational waves. A crucial question is the expected time delay between the arrival of γ-rays T_γ and gravitational waves T_{GW} to an observer located on Earth. In the discussion below we will use different time delays values as discussed in different models and add an error safety margin only at the end in the final estimate.

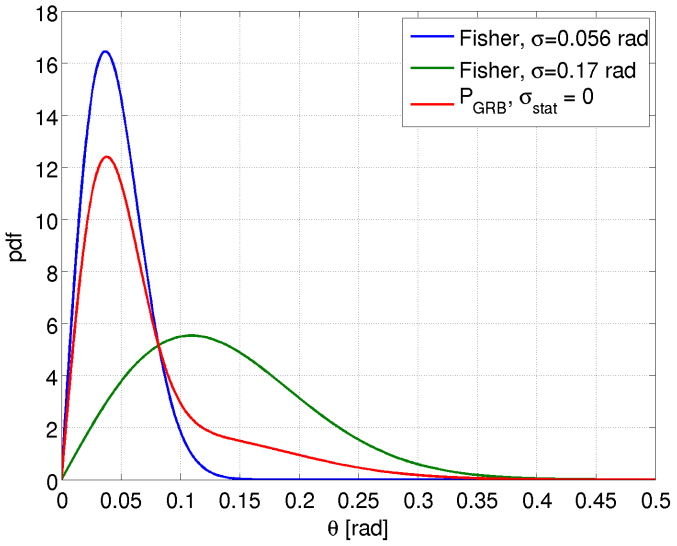

Figure 4.3: Fisher probability distribution function for 1 sigma coverage at angular radius 0.056 rad = 3.2° (blue line) and 0.17 rad = 9.5° (green line). The systematic sky localization error probability distribution function for the GBM (4.8) is shown in red. It is the sum of the two shown Fisher distributions with appropriate weighting factors.

For this timing discussion we will place ourselves from the point of view of an observer located in the Solar system. We delay by light time propagation all the times of events happening in the GRB progenitor or jet, i.e. the time of a particular event is the time at which a message emitted by this event and propagating with speed of light would arrive to the observer.

4.3.1 Coalescence model

For the compact binary coalescence model of short GRBs the timing question is relatively simple. We will use the time of the merger of the two compact objects delayed by light propagation to the observer as a zero time reference for the discussion. That is the zero time is the coalescence time as would be measured by a gravitational wave detection.

As shown in section 3.3.2 gravitational wave are predominantly emitted during the inspiral phase which enters gravitational wave detector sensitive band at most 50 s before the merger (see equation (3.11)), hence the gravitational wave emission time $T_{\rm GW}$ is contained in $[-50, 0]$ s.

After the merger an accretion disk is produced on a viscous time scale < 1 s and launches the relativistic jet. The time delay between the start of the jet and the arrival of γ-rays to the observer is $R_{\rm IS}/2\Gamma^2 c \simeq t_{\rm var} \leq T_{90} \lesssim 2$ s in the fireball model. The sum of these two delays means that the γ-ray emission

arrival time T_γ is contained in $[0, 3]$ s. For the alternative electromagnetic model the emission radius for short GRBs is $R_{\rm dec} \sim 10^{13}$ m and the typical Lorentz factors are $\Gamma \geq 10 - 50$ [73], hence the delay is $R_{\rm dec}/2\Gamma^2 c \lesssim 200$ s.

Including both jet models the relative time of arrival between gravitational waves and γ-rays is estimated to lie in the range

$$T_{\rm GW} - T_\gamma \in [-250, 0]\,\text{s}. \tag{4.9}$$

4.3.2 Stellar collapse model

For the stellar collapse model of long GRBs we will use as a zero time reference the formation of the proto-neutron star time delayed by the light propagation to the observer. This reference does not necessarily correspond to any observable around Earth but it is a well defined point of all long GRB central engine models.

First, the relativistic jet is created at most several seconds after the proto-neutron star in the type I collapsar and supranova model, in the magnetar model the jet is created after ~ 10 s [52], and in the type II collapsar the jet is launched only after ~ 100 s when the black hole forms through fall back. Hence $T_{\rm jet} \in [0, 100]$ s.

Second, the jet plows through the stellar envelope at a fraction of the speed of light, the time for this propagation between jet creation and break out is $T_{\text{break out}} - T_{\rm jet} \lesssim 100$ s.

Third, the jet accelerates to relativistic speeds after the break out and produce γ-rays in the fireball model after an apparent time $T_\gamma - T_{\text{break out}} \simeq t_{\rm var} \leq T_{90} \sim 100$ s, and in the electromagnetic model with typically $R_{\rm dec} = 10^{15}$ m and $\Gamma \geq 100$ the apparent delay is $T_\gamma - T_{\text{break out}} \lesssim 200$ s. Taking these three effects into account the observed time is $T_\gamma \in [0, 400]$ s.

For gravitational waves all the mechanisms discussed in section 3.3.3 predict an emission within seconds of the creation of the proto-neutron star or the black hole and accretion disk system. The latter being contemporaneous with the creation of the jet, the gravitational wave arrival time $T_{\rm GW}$ is contained in $[-5, T_{\rm jet} + 5]$ s.

4.3.3 Coincidence with GRB trigger

In total when taking both the coalescence and the stellar collapse model into account the relative time of arrival between gravitational wave and γ-rays is

$$T_{\rm GW} - T_\gamma \in [-400, 5]\,\text{s}. \tag{4.10}$$

Note that cases where $T_{\rm GW} \sim 100$ s happens correspond to cases where $T_{\rm GW} \simeq T_{\rm jet}$, and we still obtain $T_{\rm GW} \lesssim T_\gamma$.

In the discussion above T_γ is the time of arrival of the "main" γ-ray emission produced by the relativistic jet. For the case of short GRBs this

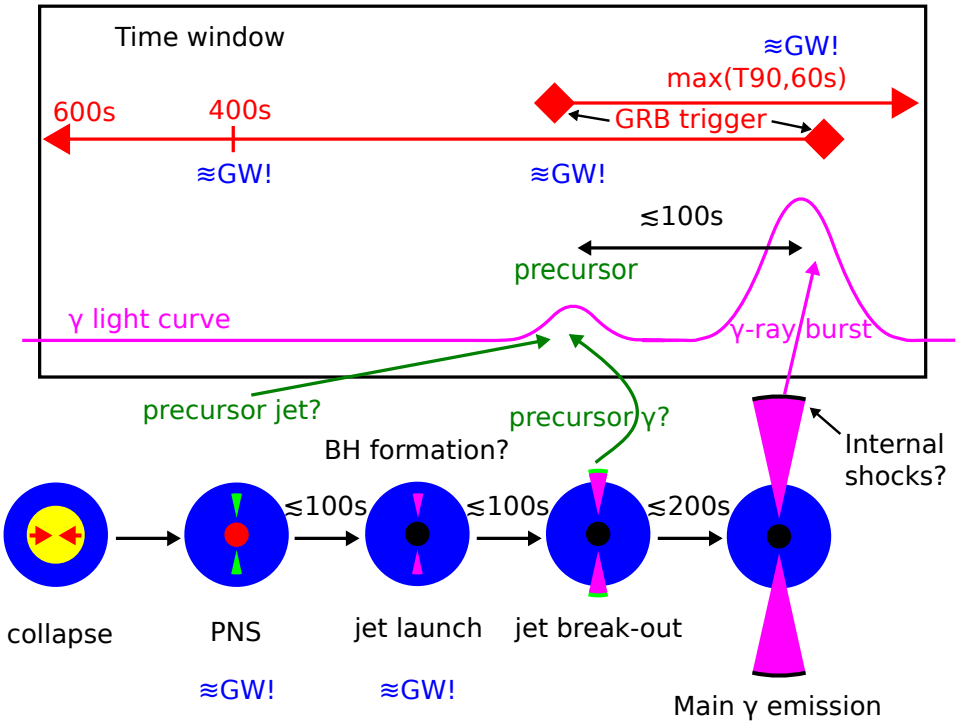

Figure 4.4: A graphical summary of the discussion in sections 4.3.2 and 4.3.3 of the gravitational wave coincidence window around the GRB trigger time for the stellar collapse model of long GRBs. The bottom part shows the stellar evolution with the formation of a relativistic jet and the possible emission times of γ-rays and gravitational waves. The middle part shows a fiducial γ-ray light curve where the γ-ray detector may trigger either on a precursor or on the main emission peak. The top part shows the discussed time window choice and the gravitational wave emission times compared to the γ-ray light curve.

time is approximately equal to the spacecraft trigger time T_{GRB}, and the difference between the two is at most a few seconds and is not relevant.

However for long GRBs the light curve can be composed of multiple peaks and the spacecraft may trigger on a small burst preceding the main emission peak. This difference can be conservatively taken into account by assuming that the main emission peak is anywhere in the observed light curve, that is $T_\gamma - T_{\mathrm{GRB}} \in [0, T_{90}]$. Hence gravitational waves should arrive in a time window around the GRB trigger time

$$T_{\mathrm{GW}} - T_{\mathrm{GRB}} = [-400, T_{90} + 5]\,\mathrm{s}. \tag{4.11}$$

A particular example of significant γ-ray emission arriving before the main emission are so called *precursors*. For instance in the catalog of GRBs

detected by BATSE a precursor has been observed in approximately 10% of cases [74], and 20% of these precursors are separated by more than 100 s from the following emission. The three main explanations for these precursors are:

fireball precursor: the jet becomes optically thin before all the thermal energy is transformed into bulk jet motion, hence the jet emit a thermal radiation before the main internal shock induced emission [75], as a consequence $T_{\mathrm{GRB}} \simeq T_{\mathrm{break\ out}}$.

progenitor precursor: the observer is slightly outside the jet cone and the precursor is produced at break out by a mildly relativistic cocoon around the jet [76], again as consequence $T_{\mathrm{GRB}} \simeq T_{\mathrm{break\ out}}$.

two step engine: in the type II collapsar model a weak jet may be created during the formation of the proto-neutron star, and precede the main jet created by the torus around the final black hole [77], as a consequence $T_{\mathrm{GRB}} \simeq T_{\gamma} - T_{\mathrm{jet}}$.

These precursors confirm that searching in the few hundred seconds before the GRB trigger time is necessary to include the main gravitational wave emission measurements. As a conclusion, the standard coincidence time window used in the analysis described in chapter 7 is

$$T_{\mathrm{GW}} - T_{\mathrm{GRB}} = [-600, \max(T_{90}, 60)]\ \mathrm{s}, \tag{4.12}$$

which includes an additional 50% in the lower bound to account for estimation errors. Roughly 20% of GRBs have durations above the 60 s limit, but the duration is not reported for all GRBs which justify imposing a sizeable minimal upper bound. We neglect the additional 5 seconds to the T_{90} value, as $< 10\%$ errors on the T_{90} are not relevant. A summary of the long GRB progenitor evolution and associated gravitational wave and γ-ray emission that justify this coincidence window choice is shown on figure 4.4.

4.4 Polarization of gravitational waves associated with GRBs

The observation of a GRB provides a time and a sky location at which to search for associated gravitational waves. Given that the relativistic jet producing the γ-rays is launched along the rotation axis of the central engine, the rotation axis is approximately pointing at the observer and we will show in this section that the emitted gravitational waves are predominantly circularly polarized.

4.4.1 Jet opening angles

As mentioned before, jets which are emitting GRBs are thought be collimated. A study of 230 GRB afterglows seen by Swift shows that the median opening angle of the jet is $\theta \sim 5°$ with the largest inferred angles $\theta \leq 25°$ [78]. However short GRBs form only 5% of that sample as afterglows are rarely observed for short GRBs, and for these the inferred angles are $10 - 20°$.

There are also attempts at deriving the jet opening angle based on observed correlations between different properties of the prompt gamma emission. These methods are not well explained astrophysically and are thus less reliable than observation of jet breaks in afterglows. A recent study of 382 GRBs detected by the GBM on Fermi shows that the distribution of inferred opening angles for long and short GRBs is well fitted by a lognormal distribution, with respectively a mean value of 8° and 50° [79].

Given the relativistic beaming of the γ-ray emission, the line of the observer needs to form an angle $\zeta \leq \theta + \Gamma^{-1}$ with the jet axis. For long GRBs typically $\Gamma^{-1} \lesssim 10^{-2} \sim 0.5°$ and for short GRBs $\Gamma^{-1} \lesssim 10^{-1} \sim 5°$, hence to simplify the discussion we can assume that the observer is within the jet cone ($\zeta \leq \theta$) in both case scenarios.

4.4.2 Gravitational wave circular polarization

We have shown in section 4.1.1 that the relativistic jet is launched along the rotational axis $\boldsymbol{J}$ of the central engine. In sections 3.3.2 and 3.3.3 we have discussed the main models of gravitational wave emission that could be associated with GRBs: either the coalescence of two compact objects or extremely rotating cases of stellar collapses that involve bar like deformations (rotational instability, core and disk fragmentation, disk precession). In both cases the gravitational wave emitting body is well approximated by a rigidly rotating quadrupolar mass distribution, and the magnitude of this quadrupolar moment of mass is evolving slowly compared to the rotation. Thus the gravitational wave emission has a polarization which depends on the axis inclination angle ι as

$$\begin{pmatrix} h_+(t) \\ h_\times(t) \end{pmatrix} = A(t) \begin{pmatrix} (1+\cos^2\iota)\cos\left[2\pi\phi(t)\right] \\ 2\cos\iota\sin\left[2\pi\phi(t)\right] \end{pmatrix}. \tag{4.13}$$

The inclination angle being equal to the angle ζ between the line of sight and the jet axis. For $\iota = 0$, both polarization are equal in amplitude and are phase shifted by $\pi/2$, the gravitational wave is circularly polarized. But this property stays approximately true even for large inclination angles, for instance for $\iota = 60°$ the ratio of amplitude is 0.8, which is compatible with circular polarization given the $\sim 20\%$ amplitude calibration errors in current gravitational wave detectors. Only for ι close to 90° the observed signal

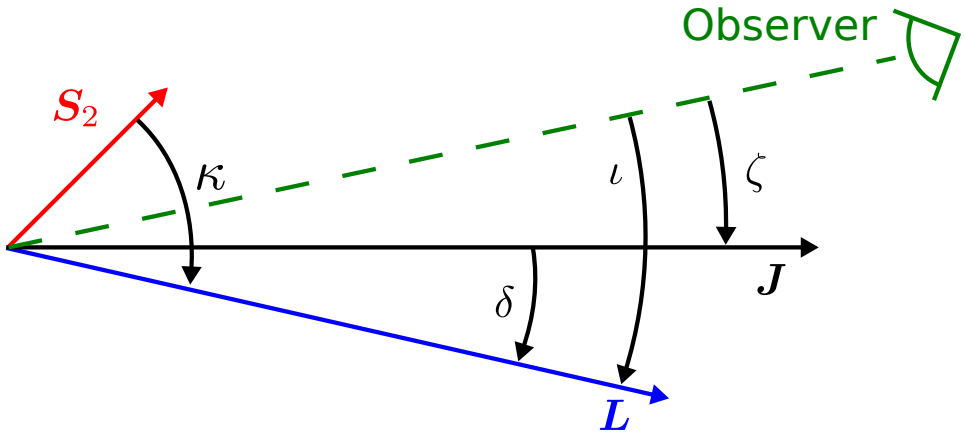

Figure 4.5: Sketch of the total angular momentum $\boldsymbol{J}$, orbital momentum $\boldsymbol{L}$, black hole spin $\boldsymbol{S}_2$ and direction to observer for a binary system with one spinning body. The angles used in the text are shown: κ – the tilt angle between black hole spin and orbital momentum, δ – the angle between orbital and total angular momentum, ι the orbital inclination angle seen by the observer and ζ the jet inclination angle.

becomes strongly elliptically polarized[4]. Hence for both short and long GRBs the incoming gravitational wave signal can be considered circularly polarized.

One exception to the above discussion is the case of neutron star - black hole binary coalescence with a rapidly spinning black hole. As discussed in section 3.3.2 in this case the black hole spin is much larger than the orbital angular momentum, and the spin of the central engine is aligned with the former whereas the gravitational wave emitting quadrupole rotates around the latter. Which means that $\zeta \neq \iota$ and *a priori* ι is not constrained by the GRB observation. Four different relevant angles can be defined for such a system and are shown on figure 4.5.

However a closer inspection shows that the black hole spin and orbital orientations are correlated, that is the cosine of the black hole tilt angle κ is not uniformly distributed. During the formation of the binary the black hole is expected to form first, it tidally interacts and accretes matter from its non-degenerate companion which aligns the black hole spin with the orbital angular momentum. The alignment is degraded by the supernova kick at the neutron star birth. Large kicks would cause a large misalignment but would also disrupt the binary. A detailed population synthesis analysis of this process shows that 50% of compact object binaries are formed with $\kappa < 45°$ [80]. Moreover, for $\kappa \gtrsim 60°$ relativistic hydrodynamics simulations show that the neutron star is promptly accreted onto the black hole, and no accretion disk is formed to power the GRB [81]. Thus it is reasonable

[4]Which would account for half the cases if ι was uniformly distributed on a sphere.

to assume that the difference between the jet inclination and the emitting quadrupole axis inclination is $|\iota - \zeta| \leq \delta \leq \kappa \leq 45°$. Unless both ζ and δ are in their upper range and in the same direction, this means that $\iota < 60°$ and the observed gravitational wave signal is circularly polarized. This affirmation is quantitatively estimated in section 7.3.

4.5 GRB event rate

As mentioned in section 3.3, when searching for transient signals not only the amplitude of potential signals but also their rate is important. The rate density of GRBs depends on the distance considered, and in many cases a uniform rate density over the universe cannot be used. On one hand the properties such as metallicity of typical galaxies and their density changes at cosmological times, and on the other hand the galaxy density is not uniform at small distances. However here we are only interested in typical distances of dozens to hundreds of Mpc where the galaxy distribution is roughly uniform but cosmological effects are not yet relevant. Also the GRB observational selection effects are less of an issue at these smaller distances. Hence we can assume a local constant rate density which can be inferred from the γ-ray spacecrafts observations [82].

In practice three types of GRB rate densities can be defined:

Observed rate which corresponds to the rate as seen by actual spacecrafts.

Observable rate which takes into account the limited field of view of some detectors. This is the rate as if all γ-ray detectors had a uniform all-sky sensitivity.

True rate which takes into account the beaming factor. It counts all GRB progenitors regardless of whether the jet cone includes Earth or not.

Usually the observable rate is estimated, as the observed rate is depending on the current observational capability which are evolving with time and the true rate is strongly dependent on the typical jet opening angle which is not well constrained by observations[5].

For long GRBs the inferred local density rate of observable GRBs is $\rho_{\text{long}} \sim 0.5\,\text{Gpc}^{-1}\text{yr}^{-1}$ with a precision of a factor a few, whereas for short GRBs the inferred density rate is $\rho_{\text{short}} \sim 10\,\text{Gpc}^{-1}\text{yr}^{-1}$ with similar errors. In addition, several very close-by and low-luminosity long GRBs have been observed, and these cases are considered as outliers compared to the general long GRB distribution. Based on this limited number of events a rate density of under luminous GRBs $\rho_{\text{faint}} \sim 500\,\text{Gpc}^{-1}\text{yr}^{-1}$ has been inferred [83, 84]. This rate is a factor ~ 1000 larger than the rate of usual long GRBs.

[5]The true rate can vary by three orders of magnitude depending on whether a very small $\sim 1°$ or very large $\sim 30°$ typical opening angle is assumed.

These rates can be used to estimate the expected number of GRBs within a given distance, which can be used as a rough estimation of the expected number of gravitational wave detections associated with GRBs [85]. For a given gravitational wave observation time T with two or more detectors, an effective field of view Ω for the satellites providing GRB triggers and a gravitational wave detection horizon distance R the expected number of coincident detections is

$$\langle N \rangle = \rho \frac{4\pi}{3} R^3 T \frac{\Omega}{4\pi}. \tag{4.14}$$

If we use the field of view of the GBM on Fermi of 9 sr, and rough numbers of one year of data with a horizon distance of ~ 25 Mpc the expected detection numbers are: for long GRBs $N_{\text{long}} \sim 2\times10^{-5}$, for short GRBs $N_{\text{short}} \sim 5\times10^{-4}$ and for under luminous GRBs $N_{\text{faint}} \sim 2 \times 10^{-2}$. These numbers are low, but are expected to be multiplied by ~ 1000 when advanced detectors are constructed and operated at their design sensitivity.

4.6 Relevance of triggered searches

An important question to answer before embarking on searching for gravitational waves associated with GRBs is whether such a search is relevant compared to a blind all-sky all-time search. The main issue is that if the γ-ray beaming is important, a search trigger by GRB observations will miss many potential gravitational wave events as gravitational wave emission is roughly isotropic. In order to assess the relative detection rate we will use a simple toy model for the gravitational wave source population and analyzes.

For sources we assume a standard siren toy model, with a uniform distribution in space and orientation, and all progenitors having the same gravitational wave emission with a rotator emission pattern (1.46). That is with a gravitational wave power flux angular dependence

$$F(\iota) = \frac{(2\cos\iota)^2 + (1+\cos^2\iota)^2}{8}, \tag{4.15}$$

where ι is the inclination angle of both the rotation axis and the jet cone.

For the γ-ray emission we assume a fixed jet opening angle θ_c and a top-hat emission, that is a uniform γ flux inside the jet cone and no emission outside the jet cone. For the γ-ray observation part we assume that γ-ray detectors will successfully observe all progenitors that include Earth in their jet opening cone up to distances much larger than the horizon distance for gravitational wave observation. For the gravitational wave observation we will neglect the effects of detectors antenna patterns and assume that a signal will be detected at a given confidence level if the h_{rss} at Earth is larger than some threshold depending on the analysis: $A_{\text{all-sky}}$ for the all-sky search and A_{trig} for the GRB triggered search. This latter assumption means that the efficiency curve is approximated by a heavy side function.

For a given progenitor at distance r and with inclination ι the amplitude at Earth is

$$h^2_{\rm rss}(\iota) = \frac{K^2}{r^2} F(\iota), \tag{4.16}$$

where K is a constant characterizing the gravitational wave energy emission of the standard siren. Hence at a given inclination angle the standard sirens are detected up to a distance

$$r_{\rm horizon}(\iota) = \frac{K}{A_{\rm search}} F(\iota)^{1/2}, \tag{4.17}$$

that depends on the amplitude detection threshold $A_{\rm search}$ of the considered search. The detection volume as a function of inclination is thus

$$V(\iota) = \frac{4\pi}{3} r^3_{\rm horizon}(\iota), \tag{4.18}$$

and needs to be marginalized over inclination to obtain an effective detection volume. Given that we assume an isotropic symmetry axis distribution for the progenitors and bipolar jets the inclination distribution is $p(\iota) = \sin\iota$ with $\iota \in [0, \pi/2]$.

Let us define the dimensionless integral

$$I(\theta_c) = \int_0^{\theta_c} F(\iota)^{3/2} \sin\iota {\rm d}\iota, \tag{4.19}$$

that is needed for inclination angle marginalization. The marginalization over ι yields the effective volume for an all-sky search

$$V^{\rm all\text{-}sky}_{\rm eff} = \frac{4\pi}{3} \frac{K^3}{A^3_{\rm all\text{-}sky}} I\left(\tfrac{\pi}{2}\right). \tag{4.20}$$

For the triggered search the marginalization on ι is limited to $\iota < \theta_c$ as progenitors with higher inclinations are not detected by γ-ray detectors, hence the effective volume for a triggered search is

$$V^{\rm trig}_{\rm eff}(\theta_c) = \frac{4\pi}{3} \frac{K^3}{A^3_{\rm trig}} I\left(\theta_c\right). \tag{4.21}$$

Given that the detection rate for both searches is just the same progenitor rate density times different effective volumes, the expected ratio of the number of detections is

$$R(\theta_c) = \frac{N_{\rm trig}}{N_{\rm all\text{-}sky}} = \frac{I(\theta_c)}{I(\pi/2)} \frac{A^3_{\rm all\text{-}sky}}{A^3_{\rm trig}}. \tag{4.22}$$

And a GRB triggered search is relevant compared to an all-sky search for finding gravitational waves coming from GRB progenitors as long as this

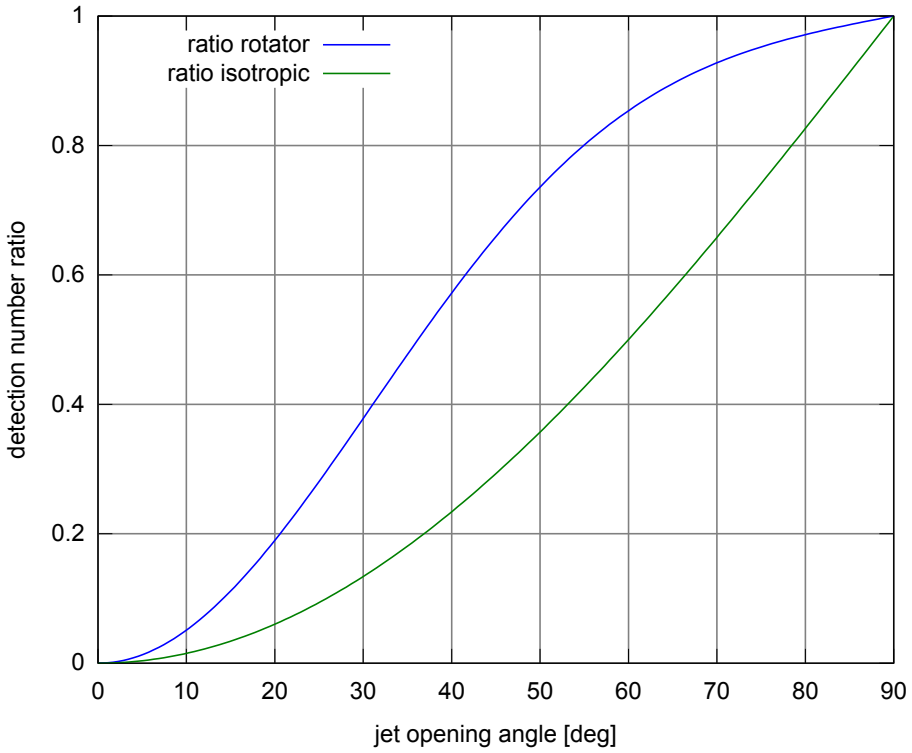

Figure 4.6: The expected ratio of detection numbers between equally sensitive triggered and all-sky searches is shown as a function of the jet opening angle θ_c. The blue line is for a rotator emission (4.15) as used to compute the ratio in equation (4.22). The green is for an isotropic gravitational wave emission hypothesis, that is $R(\theta_c) = 1 - \cos(\theta_c)$.

fraction is not much smaller than 1. An example of $R(\theta_c)$ for an equal sensitivity $A_{\text{all-sky}} = A_{\text{trig}}$ is shown on figure 4.6, this is a pessimistic limit as the purpose of an externally triggered search is to obtain $A_{\text{trig}} < A_{\text{all-sky}}$, but this example choice simplifies the rescaling for other sensitivity ratios. The comparison with an isotropic emission ($F(\iota) = 1$) assumption shows that the beaming of the gravitational wave emission improves the expectation for a triggered search by a factor about 3 for small jet opening angles.

An alternate way of looking at the event number ratio (4.22) is to derive the sensitivity gain $G = A_{\text{all-sky}}/A_{\text{trig}}$ required for the triggered search to obtain a ratio of 1

$$G(\theta_c) = \left[\frac{I(\pi/2)}{I(\theta_c)}\right]^{1/3}, \tag{4.23}$$

which is shown on figure 4.7. Unsurprisingly, for low jet opening angles a tremendous gain in sensitivity is required to compensate the large loss in event rates due to γ-ray beaming. As discussed in section 4.4.1 current

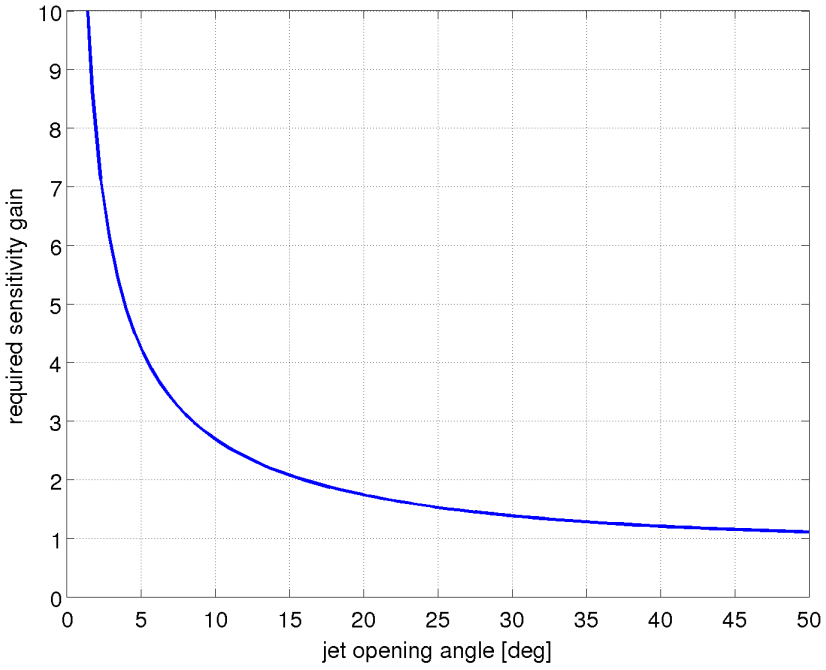

Figure 4.7: Sensitivity gain $G(\theta_c)$ required to obtain the same detection number for both the all-sky and triggered search in the considered toy model as a function of the jet opening angle θ_c.

observations place the typical jet opening angle in the $5 - 30°$ range, hence a sensitivity improvement between a factor 1.25 and 4 is required for the GRB triggered search to obtain the same number of detections as an all-sky search.

However, even at the same respective statistical significance level, a gravitational wave detection in association with a GRB is subjectively more convincing than a gravitational wave detection without any counterpart, and a multi-messenger observation should provide much richer astrophysical consequences. Hence even for a small ratio such as $R \sim 0.1$ a GRB triggered search is relevant.

Chapter 5

Gravitational wave data analysis tools

As we have seen in chapter 2 the primary output of a gravitational wave observatory is the detector strain

$$d(t) = F^{+}(\Theta, \Phi, \Psi)h_{+}(t) + F^{\times}(\Theta, \Phi, \Psi)h_{\times}(t) + n(t) = s(t) + n(t). \quad (5.1)$$

Depending on the signal type various data analysis technique are used to detect the signal $s(t)$ in data $d(t)$. We will focus here on techniques useful for detection of short (less than a few seconds) signals, especially the case when the exact waveform (shape of the signal) is not known.

A fundamental difficulty of a search for short gravitational waves is the behavior of the noise term in the data. The noise is not only composed of a stationary colored Gaussian noise as one could assume based on chapter 2. Not only the spectral density of the noise is evolving with time, but also a large number of transient noise excursions are present in the data. These transients, commonly called *glitches*, are poorly understood and render gravitational wave data analysis challenging but also interesting.

In the first two section we discuss very generic concepts in statistical signal analysis. In section 5.3 we introduce the Bayesian statistics framework in the context of gravitational wave data analysis. In that framework we discuss questions pertaining to signal shape in sections 5.4 and 5.5, and to the response of a network of gravitational wave detectors in sections 5.6 through 5.9. The two aspects are combined in section 5.10 to define a full gravitational wave trigger generation procedure.

These data analysis statistical tools described in this chapter are used in the search for gravitational wave bursts associated with gamma-ray bursts described in chapter 7. An applied discussion of how these tools enter the analysis pipeline and with which parameters is given in section 7.2 of that chapter.

5.1 Optimal matched filtering

Let us start with the simple case of a perfectly known signal $s(t)$ in a stationary colored Gaussian noise. Given a data time series $d(t)$, the purpose of data analysis is to choose between two hypothesis:

- H_0 – data contain only detector noise,
- H_1 – data contain detector noise and the signal $s(t)$.

In this simple case there is an optimal way of distinguishing between the two hypothesis, i.e. there is an optimal mapping from $d(t)$ to $\{0, 1\}$. In frequentist statistics the commonly used definition of optimality is to choose a mapping which yields the lowest false dismissal probability for a given *false alarm probability* (FAP). According the the Neyman-Pearson lemma [86], this optimal mapping is obtained by comparing the likelihood ratio

$$\Lambda(d(t)) = \frac{P(d(t)|H_1)}{P(d(t)|H_0)}, \tag{5.2}$$

with a threshold that is fixed by the desired FAP. Of course this formalism assumes that $P(d(t)|H_1)$ and $P(d(t)|H_0)$ are known, i.e. that the noise is well understood. It should be noted that any monotonic function of Λ can be used as well.

In general in frequentist statistics, a function of data that increases when data are better explained by the signal hypothesis H_1 than by the noise hypothesis H_0 is called a *detection statistic*. For a given detection statistic one chooses a threshold, data with detection statistic above that threshold are called "signal detection" and below are "noise". The particular choice depends on the desired trade-off between low false alarm and low false dismissal probability. The likelihood ratio is an example of a detection statistic, and the Neyman-Pearson lemma shows that it is an optimal choice for separating two simple hypothesis.

For the case of a colored Gaussian noise with one-sided power spectral density $S(f)$ the probability of obtaining a time series $d(t)$ is

$$P(d(t)|H_0) \propto \exp\left(-\tfrac{1}{2}\int_{-\infty}^{\infty} \frac{2|\tilde{d}(f)|^2}{S(|f|)}\mathrm{d}f\right), \tag{5.3}$$

where we use the following definition of the Fourier transform

$$\tilde{d}(f) = \int_{-\infty}^{\infty} d(t)\exp(-2\pi f t)\mathrm{d}t. \tag{5.4}$$

The factor 2 in (5.3) comes from using the one-sided power spectral density which is twice the two sided power spectral density

In this framework of multivariate Gaussian probabilities one naturally introduces a scalar product

$$(a,b) = \int_{-\infty}^{\infty} \frac{2\tilde{a}(f)^* \tilde{b}(f)}{S(|f|)} \mathrm{d}f, \tag{5.5}$$

that is based on the noise covariance matrix. This allows to write the likelihood ratio as

$$\Lambda(d|s) = \exp\left[-\tfrac{1}{2}\left[(d-s,d-s)-(d,d)\right]\right]. \tag{5.6}$$

In order to simplify the expression, one usually uses the log-likelihood

$$L = 2\log\Lambda = (d,d) - (d-s,d-s) = 2\,(d,s) - (s,s)\,, \tag{5.7}$$

note the factor 2 which is not a standard choice. The expectation value of the log-likelihood when a signal s is present is

$$\langle L\rangle = (s,s) = \mathrm{SNR}^2, \tag{5.8}$$

where the last equation defines the *signal to noise ratio* (SNR). The SNR is thus a good figure of merit when comparing a given signal s to detector noise, as it is directly related to the expected value of the detection statistic.

In practice the sought waveform is never perfectly known. At least its overall amplitude A and the time of arrival t_0 are not known, and in most cases there are several other parameters describing the possible waveforms. Hence the two hypothesis which we need to distinguish are

- H_0 – data contain only detector noise,
- H_1 – data contain detector noise and the signal $s(A,t_0,p) \in \mathcal{M}$, where $\mathcal{M}$ is the manifold of possible signals spanned by A, t_0 and other parameters p. We denote by $\mathcal{P}$ the space covered by these other parameters p.

For this scenario the Neyman-Pearson lemma does not apply, the second hypothesis is not simple. There is not any known optimal test for this kind of scenario in the framework of frequentist statistics. However the generalized log-likelihood ratio detection statistic [87], which uses the maximum statistic of the known signal case over the signal manifold $\mathcal{M}$,

$$S = \max_{A,t_0,p} 2\log\Lambda(d|s(A,t_0,p)), \tag{5.9}$$

is efficient in many cases. For stationary colored Gaussian noise, the maximization over A can be performed analytically and yields

$$S = \max_{t_0,p} \frac{(d,s(t_0,p))^2}{|s(t_0,p)|^2}, \tag{5.10}$$

that is the maximum of the projection of data d onto any unit vector in the signal manifold $\mathcal{M}$. This statistic is the basis of *matched filtering* [88], that is a search for a given family of gravitational wave signals.

In practice, maximization over t_0 can be performed relatively quickly using the properties of the Fourier transform, but the maximization over p is much more tedious and uses a discrete grid of points[1] in the parameter space $\mathcal{P}$.

5.2 Discrete sampling and multivariate Gaussian distributions

In the previous section we have used a continuous representation of data and signal either in the time or frequency domain. Actual data are sampled or resampled at some sampling frequency f_s. Usually f_s is somewhere in the $1-20\,\mathrm{kHz}$ range, for instance the sampling frequency for LIGO is $16384\,\mathrm{Hz}$ and for Virgo it is $20\,\mathrm{kHz}$. Hence what is actually measured during a time T is not $d(t)$ but a data vector $\boldsymbol{d}$ with components

$$d_l = d(l/f_s) \qquad l \in [\![1, M]\!], \quad M = Tf_s, \tag{5.11}$$

This discrete measurement adds a host of issues related to edge effect, aliasing and round-offs, but it has the advantage of simplifying the mathematical concept needed. Working in finite dimension space we can write the scalar product (5.5) as a simple sum

$$(\boldsymbol{a}, \boldsymbol{b}) = \sum_{k=0}^{M-1} \frac{2\tilde{a}_k^* \tilde{b}_k}{|S_k|} = \boldsymbol{a}^\dagger \boldsymbol{R} \boldsymbol{b}, \quad k \in [\![0, M-1]\!] \tag{5.12}$$

where

$$\tilde{a}_k = \frac{1}{M} \sum_{l=1}^{M} a_l \exp\left(-i2\pi \frac{kl}{M}\right), \tag{5.13}$$

are the coefficients of $\boldsymbol{a}$ in the Fourier basis (and analogously for $\boldsymbol{b}$), and $\boldsymbol{R}$ is the scalar product matrix which is diagonal in the Fourier basis with $\frac{2}{|S_k|}$ coefficients on the diagonal. This simple form of the scalar product is the reason for using the frequency representation.

In finite dimension multivariate Gaussian distribution are easier to define. For a positive self-adjoint[2] matrix $\boldsymbol{R}$, a vector $\boldsymbol{b}$ and a scalar c, the Gauss

[1] An exception to this rule are dimensions in the signal manifold which are vector spaces, in that case an analytical maximization analogous to the one on A can be performed. We will see an example in section 5.5

[2] which means $\boldsymbol{R}^\dagger = \boldsymbol{R}$ and eigen values of $\boldsymbol{R}$ are positive, i.e. all matrices that represent a scalar product

integral is

$$\begin{aligned}\int_{\mathbb{R}^M} \exp\left(-\tfrac{1}{2}\boldsymbol{x}^\dagger \boldsymbol{R}\boldsymbol{x} + \boldsymbol{b}^\dagger \boldsymbol{x} + c\right) \mathrm{d}\boldsymbol{x} \\ = \int_{\mathbb{R}^M} \exp\left[-\tfrac{1}{2}(\boldsymbol{x} - \boldsymbol{R}^{-1}\boldsymbol{b})^\dagger \boldsymbol{R}(\boldsymbol{x} - \boldsymbol{R}^{-1}\boldsymbol{b}) + \boldsymbol{b}^\dagger \boldsymbol{R}^{-1}\boldsymbol{b} + c\right] \mathrm{d}\boldsymbol{x} \\ = \sqrt{\det 2\pi \boldsymbol{R}^{-1}} \exp\left(\tfrac{1}{2}\boldsymbol{b}^\dagger \boldsymbol{R}^{-1}\boldsymbol{b} + c\right). \quad (5.14)\end{aligned}$$

This permits the computation of the normalization constant for Gaussian probabilities, for instance for equation (5.3) where we have omitted it so far. Of course the normalization of the distribution can also be defined for infinite dimension spaces, but the definition of a determinant is much more complex in that case.

5.3 Bayesian statistics

For the case of composite hypothesis[3] we have stated that in general, there is no optimal detection statistic. However this problem can be solved in the framework of Bayesian statistic by introducing prior probabilities on the parameters of the composite hypothesis and using conditional probabilities. Priors reflect on the observer *a priori* opinion on the value of parameters in the composite hypothesis coming from other observations or can reflect on the observer ignorance of these parameters. This additional information permits to combine the composite hypothesis into a simple one by marginalizing over the hypothesis parameters. The price to pay is that the prior needs to be defined which is far from obvious, and that the designed test will be optimal only for those priors. It should be noted that ad-hoc tests like the generalized log-likelihood ratio test can often be retrieved in the Bayesian framework for a particular choice of priors, hence another advantage of Bayesian test construction is that the priors are explicit and not hidden.

In a Bayesian framework the likelihood ratio for our composite hypothesis is

$$\Lambda(d) = \int \Lambda(d|As(t_0, p))p(A, t_0, p)\mathrm{d}A\mathrm{d}t_0\mathrm{d}p, \quad (5.15)$$

where $p(A, t_0, p)$ is the prior on the signal parameters. A flat prior on t_0 is the least questionable of choices, in most cases the time of arrival of gravitational wave is not known, and in the cases where there is some information on time (e.g. coming from an electromagnetic observation) the search is restricted to a limited time window in which the prior is also flat. The choice of priors for the waveform shape parameter space $\mathcal{P}$ is less obvious, but is also assumed flat in most cases or with variation small enough that they can be neglected compared with the dependence of $\Lambda(d|As(t_0, p))$ on p. The prior on A is the

[3] hypothesis with unknown parameters

hardest to choose because we actually have some prior expectation on it. For instance for an astrophysically sound scenario of standard siren distributed uniformly in space one expect a distribution of amplitude

$$p(A) \propto \frac{1}{A^4} \qquad \text{for } A \gg A_c, \tag{5.16a}$$

$$p(A) \simeq 0 \qquad \text{for } A \ll A_c, \tag{5.16b}$$

where A_c is a characteristic amplitude of the standard siren signal at Earth. The behavior at large A is just the effect of a uniform distribution in space ($p(r) \propto r^2$) and signal amplitude inversely proportional to the distance as shown in (1.44). The low amplitude cut-off is actually a redefinition of the signal hypothesis H_1. Only signals that are comparable or stronger than the sensitivity of detectors are of interests, any signal that has an amplitude orders of magnitude below the noise spectral density is in fact included in the null hypothesis H_0. This low amplitude cut-off is of no importance and is included here only to obtain a well normalized prior distribution.

In practice $\Lambda(d|As(t_0,p))$ has the form of a Gaussian quadratic exponent (see equation (5.6)), so one chooses a Gaussian amplitude prior

$$p(A) = \frac{1}{\sqrt{2\pi A_c^2}} \exp(-\tfrac{1}{2}A^2/A_c^2), \tag{5.17}$$

in order to obtain an integral that can be computed analytically. The marginalization over amplitude yields

$$\Lambda(d|s(t_0,p)) = \int \frac{\mathrm{d}A}{\sqrt{2\pi A_c^2}} \exp\left[A\,(d,s) - \tfrac{1}{2}A^2\,(s,s) - \tfrac{1}{2}\frac{A^2}{A_c^2}\right] \tag{5.18a}$$

$$= \frac{1}{\sqrt{A_c^2\,(s,s)+1}} \exp\left[\frac{1}{2}\frac{(d,s)^2}{(s,s)+1/A_c^2}\right], \tag{5.18b}$$

where we used the Gauss integral (5.14) with $\boldsymbol{R} = (s,s) + 1/A_c^2$, $\boldsymbol{b} = (d,s)$ and $c = 0$ to perform the integral. In terms of log-likelihood one obtains

$$L(d|s(t_0,p)) = \frac{(d,s)^2}{(s,s)+1/A_c^2} - \log\left(A_c^2\,(s,s)+1\right). \tag{5.19}$$

The likelihood ratio should be compared to the generalized likelihood ratio test of section 5.1

$$S(d|s(t_0,p)) = \max_A \Lambda(d|As(t_0,p)) = \exp\left[\frac{1}{2}\frac{(d,s)^2}{(s,s)}\right]. \tag{5.20}$$

By considering only the parts of both detection statistics that depend on the data the two tests are exactly the same. In both cases one compares $(d,s)^2$ with a threshold. Hence the usual matched filtering for a single template

at a known time is optimal if one assumes a Gaussian prior on the signal amplitude distribution.

Let us expand the above argument to the parameter space spanned by the time t_0 and shape p of the waveform, we will denote points in that space by $\boldsymbol{x} = (t_0, p)$. As explained above we will assume a flat prior on this parameter space. In order to simplify the computation we will choose the templates to be noise normalized: $(s(\boldsymbol{x}), s(\boldsymbol{x})) = 1$, and as a consequence the characteristic amplitude A_c is in principle a function of $\boldsymbol{x}$. We will replace $s(\boldsymbol{x})$ by $u(\boldsymbol{x})$ in the equations below to emphasize that the waveforms are noise normalized. Using the result of equation (5.18b) the likelihood ratio marginalized over $\boldsymbol{x}$ is

$$\Lambda(d) = \int \frac{\mathrm{d}\boldsymbol{x}}{\sqrt{1 + A_c(\boldsymbol{x})^2}} \exp\left[\frac{1}{2}\frac{(d, u(\boldsymbol{x}))^2}{1 + 1/A_c(\boldsymbol{x})^2}\right], \tag{5.21}$$

where we omitted a constant probability factor coming from the flat prior on $\boldsymbol{x}$.

In order to compute this integral we need to choose a dependence of A_c on $\boldsymbol{x}$. Choosing A_c constant over the waveform parameters greatly simplifies the integral, but it is not well justified as we do not expect the astrophysical waveform parameters to exactly fit detectors noise spectra. However under that assumption the integration can be performed approximately.

If we consider the factor in the exponent

$$E(d|\boldsymbol{x}) = \frac{(d, u(\boldsymbol{x}))^2}{1 + 1/A_c^2}, \tag{5.22}$$

and expand it around its maximum value $\boldsymbol{x}_0(d)$

$$E(d|\boldsymbol{x}_0) = \max_{\boldsymbol{x}} E(d|\boldsymbol{x}) = \frac{(d, u(\boldsymbol{x}_0))^2}{1 + 1/A_c^2}, \tag{5.23}$$

which means writing

$$E(d|\boldsymbol{x}) \simeq \frac{(d, u(\boldsymbol{x}_0))^2}{1 + 1/A_c^2} - (\boldsymbol{x} - \boldsymbol{x}_0)^\dagger \boldsymbol{H}(\boldsymbol{x_0})(\boldsymbol{x} - \boldsymbol{x}_0), \tag{5.24}$$

where $\boldsymbol{H}(\boldsymbol{x_0})$ is the Hessian matrix of $E(d|\boldsymbol{x})$ evaluated at the maximum, and yields the quadratic fit to $E(d|\boldsymbol{x})$ at $\boldsymbol{x} = \boldsymbol{x}_0$. If the maximum is sufficiently large ($E(d|\boldsymbol{x}_0) \gg 1$), is far from any edge of the parameter space and there is no secondary maximum of comparable height, then the integral is

$$\Lambda(d) \simeq \sqrt{\frac{2\pi \det \boldsymbol{H}(\boldsymbol{x}_0)}{1 + A_c^2}} \exp\left[\frac{1}{2}\frac{(d, u(\boldsymbol{x}_0))^2}{1 + 1/A_c^2}\right], \tag{5.25}$$

where we used the Gauss integral (5.14) with $\boldsymbol{R} = \boldsymbol{H}(\boldsymbol{x}_0)$ and $\boldsymbol{x} - \boldsymbol{x}_0$ as the integration variable. The log-likelihood is thus

$$L(d) = 2\log\Lambda(d) \simeq \frac{(d, u(\boldsymbol{x}_0))^2}{1 + 1/A_c^2} + \log\left[2\pi \det \boldsymbol{H}(\boldsymbol{x}_0)\right] - \log\left[1 + A_c^2\right], \quad (5.26)$$

where one should remember that $\boldsymbol{x}_0$ is a function of the data d.

This should be compared to the usual matched filtering statistic (5.10) which we can write with the above notations as

$$S(d) = \max_{\boldsymbol{x}} (d, u(\boldsymbol{x}))^2 = (d, u(\boldsymbol{x}_0))^2 . \quad (5.27)$$

Hence this statistic is equal to the optimal Bayesian likelihood ratio test under the assumption that the dependence of A_c and of the Hessian determinant $\det \boldsymbol{H}$ on the parameters $\boldsymbol{x}$ can be neglected. This approximation on the Hessian is easily justified whenever $L(d|\boldsymbol{x}_0) \gg 1$, in that case the statistic is weakly depending on the Hessian through the logarithm of the determinant term only. However the dependence on A_c is directly in the exponential factor and should have a greater influence over the statistic, unless a regime of loud signals can be assumed. Given that in the case where $A_c(\boldsymbol{x}) \gg 1$ over the parameter space, the amplitude factor in the exponent can be safely neglected as it affects the statistic only through the logarithmic factor.

5.4 Time-frequency representation

In section 5.2 we have introduced the discrete time (5.11) and frequency (5.13) representations of a data vector. These two representations form two extreme choices between good frequency resolution (frequency representation) and good time resolution (time representation), but there are many possible intermediary trade-offs between the two.

Before exploring other time-frequency representations, it is convenient to move to a basis that is adapted to the noise scalar product. We have written data vectors as

$$\boldsymbol{a} = \sum a_k \boldsymbol{t}_k = \sum \tilde{a}_k \boldsymbol{f}_k, \quad (5.28)$$

where the vectors $\boldsymbol{t}_k$ (respectively $\boldsymbol{f}_k$) correspond to a single time bin (respectively frequency bin). By rescaling the basis frequency vector $\boldsymbol{f}_k \to \boldsymbol{f}_k^w = \boldsymbol{f}_k\sqrt{|S_k|/2}$ the new frequency coefficients are noise normalized ($a_k \to a_k^w = a_k/\sqrt{|S_k|/2}$) and the scalar product (5.5) is represented by the identity matrix

$$(\boldsymbol{a}, \boldsymbol{b}) = \left(\sum \tilde{a}_k^w \boldsymbol{f}_k^w, \sum \tilde{b}_l^w \boldsymbol{f}_l^w\right) = \sum \tilde{a}_k^w \tilde{b}_k^w . \quad (5.29)$$

The resulting coefficients are called *whitened* in reference to white noise, and any unitary change of basis will conserve the simple form of the scalar

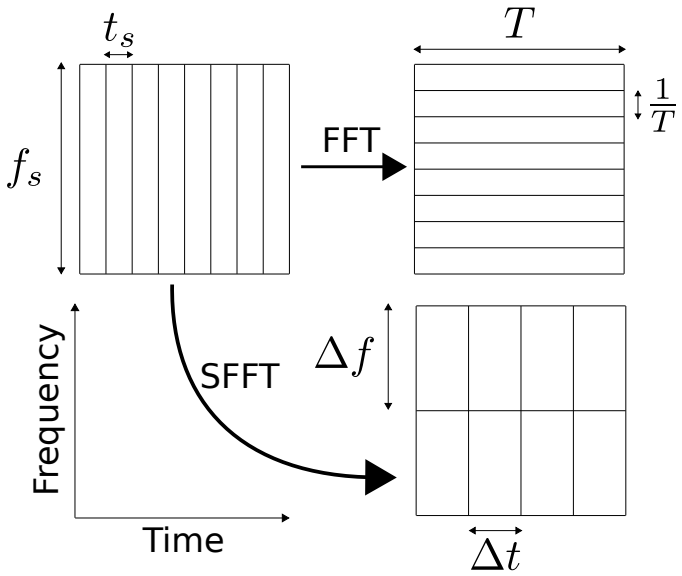

Figure 5.1: Sketch of time, frequency and time-frequency representations. The upper left diagram shows the time representation: the time resolution is very fine, but each bin contains all the frequency content. The upper right diagram shows the frequency representation: the frequency resolution is very fine, but each bin contains data from all the considered time. In the lower right part is a time frequency representation, each bin contains information about data in a Δt time and over a frequency band which is Δf wide. The frequency coefficient can be obtained from the time frequency using the fast Fourier transform (FFT) and the reverse can be done by using the inverse fast Fourier transform (IFFT). The time-frequency coefficients can be obtained from the time coefficient using a short fast Fourier transform (SFFT) of duration Δt.

product. For instance for the inverse discrete Fourier transform coefficients we obtain

$$(\boldsymbol{a}, \boldsymbol{b}) = \sum_k a_k^w b_k^w. \tag{5.30}$$

The basic principle of a time-frequency representation, is to choose a set of basis function which is limited in time and frequency, unlike the time $\boldsymbol{t}_k^w$ or frequency $\boldsymbol{f}_k^w$ basis vectors. This basic principle is graphically represented on figure 5.1, the basis functions of a time-frequency representation are also called *pixels* in reference to the rectangular grid they form in the plane.

The simplest form of a time-frequency basis, is obtained using the short fast Fourier transform (SFFT), that is a Fourier transform on a short stretch of data. Instead of using all the time samples in the time T, we cut the data into blocks of m samples and perform the short Fourier transform on each of them independently. This is equivalent to projecting the data onto a time

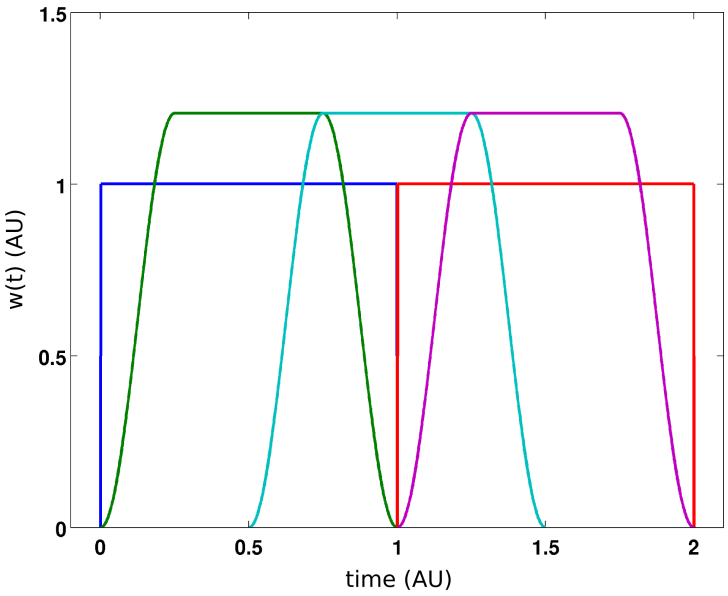

Figure 5.2: Two example windows for time-frequency representations. Two rectangular windows as in (5.32) with no overlap, and three modified hann windows overlapped by 50%. The modified hann window is composed of a hann window $w(t) = \sin^2(\pi x)$ with a flat section inserted in the middle. Windows as shown have equal normalization.

limited sine-wave (limited within a window $\Delta t = mt_s$) instead of projecting onto a sine-wave that stretches along the whole data duration T. Thus a time-frequency coefficient is

$$\tilde{a}^w_{j,k} = \frac{1}{m}\sum_{l=1}^{m} a^w_{l+(j-1)m} \exp\left(-i2\pi\frac{kl}{m}\right), \quad k \in [\![0, m-1]\!], \quad j \in [\![1, M/m]\!], \tag{5.31}$$

and corresponds to the projection on a basis function

$$\boldsymbol{u}_{j,k} = t \longmapsto \exp\left[i2\pi f_k(t-t_j)\right] \mathbb{1}(t-t_j > 0)\mathbb{1}(t-t_j < \Delta t), \tag{5.32}$$

where $f_k = k\frac{f_s}{m} = k\Delta f$ and $t_j = jmt_s = j\Delta t$. We have assumed that M/m is an integer and for all practical applications this will be true.

An important property is that the time-frequency volume for each basis function is the same, that is $\Delta t\Delta f = 1$ for any choice of Δt, in particular for the time and for the frequency representation, which correspond to respectively the $m = 1$ and $m = M$ case. This is a particular case of the Heisenberg-Gabor inequality [89] which states that the time width σ_t and frequency width σ_f as measured by the second moments in the time and frequency domain are bound from below by $\sigma_t\sigma_f \geq \frac{1}{4\pi}$. A related property is that the time-frequency transformation is orthonormal, and hence the variance of all coefficients is equal for a white noise or for whitened coefficients, regardless of the representation choice.

We have presented here the simplest form of time-frequency representation which has the advantage of being straightforward and orthonormal. There are some relatively simple generalizations. By changing the shape of the amplitude window applied to the sine-wave to form a basis function from a rectangle to some smoothly evolving function one obtains new time-frequency representations. The main advantage of the smooth amplitude evolution is that the functions are better localized in frequency, an example is shown on figure 5.2. Usually these functions are used to form an over-complete frame by overlapping the smooth windows in the time domain. Another more complex choice is to use a wavelet basis or frame.

5.5 From matched filtering to clustering

In the previous section we have considered the case where the waveform parameter space is well known and we have derived that the maximum of a matched filtering with template signals is a reasonable detection statistic choice. However this choice is in practice realizable only if the parameter space $\mathcal{P}$ has a small dimension, otherwise covering the parameter space with a grid of templates is computationally prohibitive.

As noted before, there are some cases where the maximization over some dimensions of the parameter space can be done analytically. The main example is when the signal manifold $\mathcal{M}$ can be expressed as a Cartesian product of a linear space E and some manifold $\mathcal{P}$, i.e. for all parameters in $\mathcal{P}$ there are $\dim E$ independent signal templates and all their linear combinations are in the signal manifold. We have actually already looked at the case of $\dim E = 1$ when marginalizing over the gravitational waveform amplitude.

Let us focus on the case of $\dim E = 2$, the result will be easily generalizable to higher dimensions. That is for all parameters $p \in \mathcal{P}$ we have two orthogonal noise normalized templates $u_1(p)$ and $u_2(p)$. If we assume a Gaussian prior on the amplitude of each template with characteristic amplitude A_{1c} and A_{2c}, the marginalized likelihood ratio is simply[4] an extension of (5.18)

$$\begin{aligned}\Lambda(d|p) = \int & \frac{\mathrm{d}A_1}{\sqrt{2\pi A_{1c}^2}} \frac{\mathrm{d}A_2}{\sqrt{2\pi A_{2c}^2}} \\ & \exp\left[(d, A_1 u_1) + (d, A_2 u_2) - \tfrac{1}{2}\left(A_1^2 + A_2^2\right) - \tfrac{1}{2}\left(\frac{A_1^2}{A_{1c}^2} + \frac{A_2^2}{A_{2c}^2}\right)\right] \quad (5.33a) \\ = & \frac{1}{\sqrt{A_{1c}^2 + 1}} \frac{1}{\sqrt{A_{2c}^2 + 1}} \exp\left[\frac{1}{2}\frac{(d, u_1)^2}{1 + 1/A_{1c}^2} + \frac{1}{2}\frac{(d, u_2)^2}{1 + 1/A_{2c}^2}\right], \quad (5.33b)\end{aligned}$$

[4] Among the pairs of orthonormal templates we choose the one that has an uncorrelated prior.

where we used the Gauss integral (5.14) with

$$\boldsymbol{R} = \begin{pmatrix} 1 + 1/A_{1c}^2 & 0 \\ 0 & 1 + 1/A_{2c}^2 \end{pmatrix}, \qquad \boldsymbol{b} = \begin{pmatrix} (d, u_1) \\ (d, u_2) \end{pmatrix}, \qquad c = 0. \tag{5.34}$$

This can be rewritten in terms of log-likelihoods (5.19) as

$$L(d|p) = L(d|u_1(p)) + L(d|u_2(p)). \tag{5.35}$$

One important thing to note is that for data which is consistent with Gaussian noise the value of $\Lambda(d|p)$ can be smaller than 1, or equivalently $L(d|p)$ can be negative.

This approach is pushed further when the parameter search has a very high dimension, like for the case of gravitational wave bursts searches where the signal shape is not well constrained. In most cases the only considered signal constraints is that the signal is short ($\lesssim 1\,\mathrm{sec}$) and in the detectors sensitive frequency band. The usual approach is then:

1. Use a basis $\mathcal{U}$ of orthonormal[5] time-frequency functions, like wavelets or plain time-windowed short Fourier transforms, that covers the desired time-frequency span.

2. Compute a detection statistic, e.g. (5.19), for each basis function.

3. Find clusters of basis functions that have a large value of the detection statistic. In general the clustering considers basis functions to be nearby if they are close in time and frequency.

4. For each cluster compute the sum of the statistic over basis functions, this yields the detection statistic for that cluster.

5. The maximum of the detection statistic over clusters yields the detection statistic for the chosen time-frequency span.

Let us interpret this procedure in the light of the Bayesian framework described above. We will start by considering two extreme cases of clustering (step 3): "no clustering", that is each cluster contains only one basis function; "full clustering", that is all basis functions are always in one giant cluster that covers the complete time-frequency span.

In the first case of "no clustering" the above procedure results in a detection statistic which is the maximum over basis functions

$$L(d) = \max_{u \in \mathcal{U}} L(d|u), \tag{5.36}$$

and is very similar to the usual matched filtering test (5.10), although the time grid is very coarse and is comparable to the duration of the basis functions. Hence in that case the underlying prior on the signal shape is that the signal will have a good match to one of the basis functions.

[5] In the noise scalar product (5.5) sense.

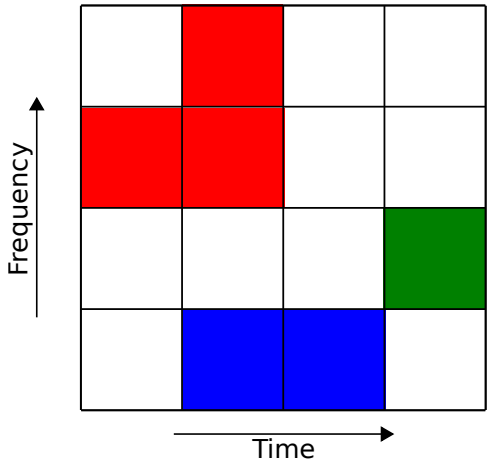

Figure 5.3: Shown is an illustration of a small time-frequency map. White pixels are below threshold and the three colors show three 4-connected clusters. In case of 8-connected clustering the three pixels in the lower right part of the figure form a single cluster.

In the second case of "full clustering", the detection statistic is the sum over basis functions

$$L(d) = \sum_{u \in \mathcal{U}} L(d|u), \tag{5.37}$$

which is just the case of two templates (5.35) expanded to the full basis $\mathcal{U}$ of time-frequency functions. Hence the underlying signal hypothesis is that of a colored Gaussian noise burst, where the spectral shape of the burst are controlled by the choice of characteristic amplitude A_{uc} that define the individual likelihoods $L(d|u)$.

An intermediate choice is to set a threshold on the per pixel (basis function) likelihood $L(d|u)$, and consider as a cluster all groups of 4-connected (or 8-connected)[6] pixels that are above threshold. Illustrative examples of clusters are on figure 5.3. The likelihood ratio for a cluster $\mathcal{C}$ is then

$$L(d|\mathcal{C}) = \sum_{u \in \mathcal{C}} L(d|u), \tag{5.38}$$

and the detection statistic for the given span of data is the maximum of $L(d|\mathcal{C})$ over all defined clusters.

This a priori ad-hoc method can be justified in the Bayesian framework for one particular threshold choice when the signal prior is a colored Gaussian noise in any possible connected shape[7] in the time-frequency domain. For any given time-frequency signal shape we approximate it by a cluster $\mathcal{C}$ of

[6] 4-connected clusters have each pixel touching a neighbor with an edge. In 8-connected clusters pixels touch their neighbors either with an edge or a vertex.

[7] Actually, there are some potential signals that are unconnected in the time-frequency

basis functions, and the associated likelihood ratio is given by (5.38). This justifies the use of over-complete frames for time-frequency representation, as they can provide a better fit to the shape of the signal in the time-frequency domain.

As we do not know a priori which cluster $\mathcal{C}$ to use, we need to marginalize over the set $\mathfrak{C}$ of possible clusters. Following the same argument as for matched filtering we will maximize the likelihood ratio instead of marginalizing, which yields a detection statistic of the form

$$L(d) = \max_{\mathcal{C}\in\mathfrak{C}} L(d|\mathcal{C}) + 2\log(p(\mathcal{C})), \tag{5.39}$$

where $p(\mathcal{C})$ is the prior for the given cluster. We have no good prior information on the signal shape, hence a flat prior is a reasonable choice. Defining what a "flat" prior is for the space of possible clusters is not obvious, one possibility is to define the prior as:

- Uniform in the pixel number $k = |\mathcal{C}|$ with k between 1 and the total pixel number $M = |\mathcal{U}|$, which yields a $\frac{1}{M}$ factor to the prior.
- Uniform in the location on the time-frequency plane, which yields also a factor $\frac{1}{M}$ to the prior, as long as the cluster is small compared to the time-frequency plane.
- Uniform in the cluster shape, this contribution is not simple to compute, the number of cluster shapes $c(k)$ is known to grow exponentially [90] with the number of pixels in the cluster, for instance for 4-connected cluster the growth has been estimated numerically [91] to be $\log c(k) \sim k \log 4$, and for 8-connected clusters [92] to be $\log c(k) \sim k \log 6.5$. Hence there is a factor $\frac{1}{c(k)}$ contributing to the prior.

With this definition the 4-connected cluster prior is $p(\mathcal{C}) \simeq \frac{1}{4^k M^2}$ and the detection statistic is

$$L(d) = \max_{\mathcal{C}\in\mathfrak{C}} \left[\sum_{u\in\mathcal{C}} \left(L(d|u) - 2\log 4 \right) \right] - 4\log M. \tag{5.40}$$

In order to perform the above maximization trying all possible clusters is not actually needed. Selecting the clusters of connected pixels with $L(d|u) > 2\log 4$ and taking the maximum over this subset should yield a comparable result. The reason is that for a cluster of this subset removing one pixel will diminish the total statistic for that cluster, and adding a pixel will also diminish the total statistic as it will add a negative contribution, unless the additional pixel allows to connect two clusters from the subset and yield a

domain, e.g. eccentric binary mergers are expected to emit a burst of gravitational waves at each periapsis which results into a series of disconnected bursts. However for most other sources the connected assumption is valid.

larger total statistic. Hence this approximation add to our prior that the signal amplitude is unimodal[8] in the time-frequency domain.

In conclusion, the procedure of selecting clusters of pixels above some likelihood ratio threshold is a reasonable approximation for the optimal Bayesian test, which uses a colored Gaussian random process with a unimodal time-frequency shape as a signal prior. One crucial argument against the derivation above is that in real data analysis the noise is known to be non-Gaussian, hence any desire of optimality obtained from the Gaussian assumption is in principle futile. An optimal test for one signal and noise assumption has no reasons to be a good test for any other assumptions. Even worse, an optimal test makes full usage of the given assumption, and, at least in principle, will be less robust to deviations from this assumption than a near optimal test. In section 5.7 we will explore some additional tests which adds robustness to tests that use the Gaussian noise assumption.

5.6 Coherent analysis

So far, we have only considered searching for a signal in a single data stream. In practice a network of gravitational wave detectors is operated and combining data from across a network of detectors allows good rejection of noise glitches. For a network of D detectors the vector of data streams can be written as

$$\begin{pmatrix} d_1(t) \\ \vdots \\ d_D(t) \end{pmatrix} = \begin{pmatrix} F_1^+(\theta,\phi,\psi)h_+(t-t_1) + F_1^\times(\theta,\phi,\psi)h_\times(t-t_1) + n_1(t) \\ \vdots \\ F_D^+(\theta,\phi,\psi)h_+(t-t_D) + F_D^\times(\theta,\phi,\psi)h_\times(t-t_D) + n_D(t) \end{pmatrix}, \tag{5.41}$$

where $d_i(t)$ and $n_i(t)$ are respectively the data and the noise from detector i, $(F_i^+, F_i^\times)$ are its antenna patterns, and t_i is the light travel time between Earth's center and detector i for a planar gravitational wave propagating along the (θ,ϕ) direction. Here we use the (θ,ϕ,ψ) Euler angles defined in a detector independent frame, a standard choice is to set the frame at the Earth center with the z-axis in the north pole direction, and the x-axis pointing at the Greenwich meridian. We will call this coordinates system *Earth fixed*. The Earth fixed angles can be related to the detector specific angles $(\Theta_i, \Phi_i, \Psi_i)$ used for instance in equation (2.9) through a rotation operations that we will not discuss here.

In this thesis we focus on sources with known sky locations, hence we can easily time shift the data so that the gravitational waves contribution is synchronized. Furthermore, if we use a time-frequency representation of

[8] i.e. the signal has a shape with a single peak in the time-frequency domain.

whitened data, the amplitudes for a given time-frequency pixel[9] are

$$\begin{pmatrix} d_1^w(j,k) \\ \vdots \\ d_D^w(j,k) \end{pmatrix} = \begin{pmatrix} F_1^{+w}(k) \\ \vdots \\ F_D^{+w}(k) \end{pmatrix} h_+(j,k) + \begin{pmatrix} F_1^{\times w}(k) \\ \vdots \\ F_D^{\times w}(k) \end{pmatrix} h_\times(j,k) + \begin{pmatrix} n_1^w(j,k) \\ \vdots \\ n_D^w(j,k) \end{pmatrix}, \quad (5.42)$$

where the antenna patterns coefficients are whitened analogously to the other coefficients. Note that the astrophysical signal is not whitened because the division by the amplitude spectrum is detector dependent, which explains why it is included in the antenna patterns. We will write this equation more compactly for a single time-frequency pixel as

$$\boldsymbol{d} = \boldsymbol{F}^+ h_+ + \boldsymbol{F}^\times h_\times + \boldsymbol{n}, \quad (5.43)$$

where we drop the explicit reference to the given pixel and whitening. One should note that under the Gaussian noise assumption the noise vector $\boldsymbol{n}$ is multivariate Gaussian distributed with identity variance because noise is assumed to be uncorrelated between detectors. Hence we are exactly in the case of matched filtering with two templates $\boldsymbol{F}^+$ and $\boldsymbol{F}^\times$, that is summarized in (5.33). The only difference is that vectors are here in the detector space instead of being in the waveform space.

In order to apply results from section 5.5 we first need to orthonormalize the two template vectors $\boldsymbol{F}^+$ and $\boldsymbol{F}^\times$. The first step is to orthogonalize the basis, there is no unique possibility, however a common choice is to use the so called *dominant polarization frame*. It can be shown that it corresponds to a particular choice of the polarization reference $\psi = \psi_{\mathrm{DP}}$, hence the name.

The construction of the dominant polarization frame consists in looking at the network response

$$\boldsymbol{f}(\psi) = \boldsymbol{F}^+ h_+ + \boldsymbol{F}^\times h_\times \quad (5.44)$$

of the network to all linearly polarized signals $(h_+, h_\times) \propto (\cos 2\psi, \sin 2\psi)$ and choose one vector $\boldsymbol{f}^+$ along the highest network response. The second orthogonal vector $\boldsymbol{f}^\times$ will happen to correspond to the lowest network response and the orthogonal (i.e. rotated by $\pi/4$) polarization. This justify the choice of the dominant polarization frame, as this frame is adapted to the sensitivity of the network.

The magnitude of the network response

$$M = |\boldsymbol{f}(\psi)|^2 = |\boldsymbol{F}^+ \cos 2\psi + \boldsymbol{F}^\times \sin 2\psi|^2 \quad (5.45a)$$

$$= |\boldsymbol{F}^+|^2 \cos^2 2\psi + |\boldsymbol{F}^\times|^2 \sin^2 2\psi + 2\boldsymbol{F}^\times \cdot \boldsymbol{F}^+ \sin 2\psi \cos 2\psi \quad (5.45b)$$

$$= |\boldsymbol{F}^+|^2 \frac{1+\cos 4\psi}{2} + |\boldsymbol{F}^\times|^2 \frac{1-\cos 4\psi}{2} + \boldsymbol{F}^\times \cdot \boldsymbol{F}^+ \sin 4\psi, \quad (5.45c)$$

[9] A more general derivation that works through the calculations for a given finite number of pixels is described in [93].

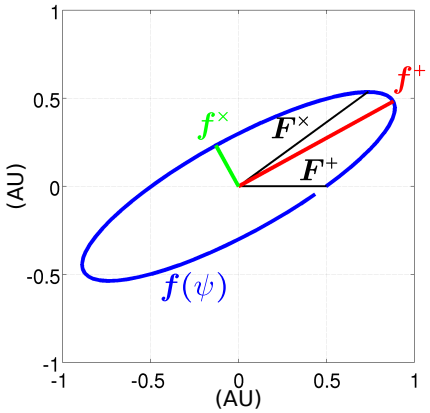

Figure 5.4: Sketch of the network response (5.44) as a function of signal polarization, the response in the dominant polarization frame to plus (resp. cross) polarized signal is given in red (resp. green). Shown is the signal plane spanned by $\boldsymbol{F}^+$ and $\boldsymbol{F}^\times$. The horizontal axis is the projection on the unit vector parallel to $\boldsymbol{F}^+$ and the vertical axis is the projection on the vector orthogonal to it.

is maximal when

$$0 = \frac{\partial M}{\partial \psi} = -2\left(|\boldsymbol{F}^+|^2 - |\boldsymbol{F}^\times|^2\right)\sin 4\psi_{\mathrm{DP}} + 4\boldsymbol{F}^\times \cdot \boldsymbol{F}^+ \cos 4\psi_{\mathrm{DP}}, \tag{5.46a}$$

that is for a polarization

$$\psi_{\mathrm{DP}} = \frac{1}{4}\arctan\left(\frac{2\boldsymbol{F}^\times \cdot \boldsymbol{F}^+}{|\boldsymbol{F}^+|^2 - |\boldsymbol{F}^\times|^2}\right), \tag{5.47}$$

and the two orthogonal vectors are then

$$\boldsymbol{f}^+ = \boldsymbol{F}^+ \cos 2\psi_{\mathrm{DP}} + \boldsymbol{F}^\times \sin 2\psi_{\mathrm{DP}}, \tag{5.48a}$$
$$\boldsymbol{f}^\times = -\boldsymbol{F}^+ \sin 2\psi_{\mathrm{DP}} + \boldsymbol{F}^\times \cos 2\psi_{\mathrm{DP}}. \tag{5.48b}$$

These two vectors correspond to respectively the semi-major and semi-minor axis of the ellipse sketched on figure 5.4, this ellipse is drawn by the network response vector (5.44) when varying $\psi \in [0, \pi]$. To obtain the normalized template vectors we just need to divide by the norm which yields

$$\boldsymbol{e}^+ = \boldsymbol{f}^+/|\boldsymbol{f}^+|, \tag{5.49a}$$
$$\boldsymbol{e}^\times = \boldsymbol{f}^\times/|\boldsymbol{f}^\times|. \tag{5.49b}$$

The last step before using equation (5.33) is to choose a prior on the gravitational wave signal. A relatively uninformed and simple to use choice is a Gaussian prior on h_+ and $h_\times$ with standard deviation σ_h. In that case the

priors on the amplitude for the two templates $\boldsymbol{e}^+$ and $\boldsymbol{e}^\times$ are Gaussian with characteristic amplitudes $A_{1c} = \sigma_h|\boldsymbol{f}^+|$ and $A_{2c} = \sigma_h|\boldsymbol{f}^\times|$, which following the results of equation (5.33b) yields a log-likelihood

$$L(\boldsymbol{d}|\sigma_h) = \frac{|\boldsymbol{e}^+ \cdot \boldsymbol{d}|^2}{1 + 1/(\sigma_h|\boldsymbol{f}^+|)^2} + \frac{|\boldsymbol{e}^\times \cdot \boldsymbol{d}|^2}{1 + 1/(\sigma_h|\boldsymbol{f}^\times|)^2} - \log(1+\sigma_h^2|\boldsymbol{f}^+|^2) - \log(1+\sigma_h^2|\boldsymbol{f}^\times|^2). \tag{5.50}$$

Choosing a particular σ_h is not obvious, it should correspond to a value that is expected from astrophysical models but also should not be too far from the detectors sensitivity. A way of using a less informed prior is to marginalize over σ_h, for instance uniformly over a discrete set of amplitudes $\mathcal{A}$. This yields a marginalized log-likelihood

$$L(\boldsymbol{d}|\mathcal{A}) = 2\log\left\{\sum_{\sigma_h\in\mathcal{A}} \frac{\exp\left[\frac{1}{2}L(\boldsymbol{d}|\sigma_h)\right]}{|\mathcal{A}|}\right\}, \tag{5.51}$$

which is a reasonable detection statistic for a single time-frequency pixel when no good prior on the gravitational wave is available. To obtain a full detection statistic for gravitational wave bursts we just need to follow the cluster construction of section 5.5 and sum the per pixel log-likelihood over pixels in clusters.

However, for some sources a good prior on the polarization is available. As explained in section 4.4 for gravitational waves associated with gamma ray bursts we can reasonably assume a circular polarization, that is[10] $h_\times = \pm i h_+$. In that case we have a right polarized template $\boldsymbol{f}^{\circlearrowright} = \boldsymbol{f}^+ + i\boldsymbol{f}^\times$ and a left polarized template $\boldsymbol{f}^{\circlearrowleft} = \boldsymbol{f}^+ - i\boldsymbol{f}^\times$, but we are not interested in linear combinations between the two. Hence a reasonable detection statistic is to use the normalized template[11] $\boldsymbol{e}^{\circlearrowright} = \boldsymbol{f}^{\circlearrowright}/|\boldsymbol{f}^{\circlearrowright}|$ to define a right log-likelihood

$$L(\boldsymbol{d}|\ \circlearrowright, \sigma_h) = \frac{|\boldsymbol{e}^{\circlearrowright} \cdot \boldsymbol{d}|^2}{1 + 1/(\sigma_h|\boldsymbol{f}^{\circlearrowright}|)^2} - \log(1 + \sigma_h^2|\boldsymbol{f}^{\circlearrowright}|^2), \tag{5.52}$$

and analogously a left log-likelihood. We then take the maximum[12] over left or right circular polarization hypothesis, and marginalize over the amplitude priors as it is done in equation (5.51). The resulting detection statistic is

$$L(\boldsymbol{d}|\text{circular}) = 2\log \sum_{\sigma_h\in\mathcal{A}} \frac{\max\left\{\exp\left[\frac{1}{2}L(\boldsymbol{d}|\ \circlearrowright, \sigma_h)\right], \exp\left[\frac{1}{2}L(\boldsymbol{d}|\ \circlearrowleft, \sigma_h)\right]\right\}}{|\mathcal{A}|}. \tag{5.53}$$

[10] We consider here only time-frequency coefficients with positive frequencies, that is $k < m/2$. Coefficients with negative frequencies are complex conjugates of the positive one, the sign of the i factor is reversed for them, but they are redundant with the positive frequencies and are not considered in the analysis.

[11] Note that defining the dominant polarization is not needed for constructing the left and right circularly polarized unit vectors. Any other polarization reference is equally good and would yield the same unit vector multiplied by a complex unit.

[12] In principle, we should perform a proper marginalization as in equation (5.51), but it is much more computationally intensive and does not change significantly the result.

For instance for the analysis described in chapter 7 the amplitude set used is $\mathcal{A} = 10^{-\{23, 22.5, 22, 21.5, 21\}}\,\mathrm{Hz}^{-1/2}$, this choice corresponds well to the sensitivity of current detectors and plausible astrophysical scenarios.

5.7 Consistency tests

For the moment we have only considered the case of Gaussian noise. However, in actual gravitational wave data a large number of spurious glitches are present. The detection statistics we have derived so far depend on the data through the squared projection of data on some template vector. When a glitch is present, the data vector will not be aligned with the projection vector in most cases, however it can still have a significant scalar product and hence yields a large value of the detection statistic. This shows that these detection statistics are not robust to detector glitches, as expected given the input noise priors. In this section we will present some tests which are able to reject these glitches and increase the robustness of the detection procedure.

5.7.1 Projection statistics

In order to reject such spurious events a number of consistency tests has been developed [94], here we will focus on tests that do not assume any waveform shape [95]. Their basic principle is to compare data from a network of detectors and see if they fit expectations for gravitational wave signals. The basic principle is that the gravitational wave signal is correlated across a network in a particular way dictated by the $\boldsymbol{f}^+$ and $\boldsymbol{f}^\times$ vectors, and noise is uncorrelated between detectors.

As noted before, any gravitational wave signal generates a network response in signal plane spanned by $\boldsymbol{f}^+$ and $\boldsymbol{f}^\times$, or along the two axis generated by $\boldsymbol{f}^{\circlearrowleft}$ and $\boldsymbol{f}^{\circlearrowright}$ if the signal can be assumed circularly polarized. Whenever the number of detectors is greater than the dimension of that signal space one can use it to separate gravitational wave signal from spurious glitches. Data vectors which contain signal should be only slightly deviated from that space by detector noise. Thus events that are far away from that plane, i.e. data for which the projection on the orthogonal space, called the *null space*, is large can be classified as glitches and rejected. A sketch of the configuration for 3 detectors and the network response plane is shown on figure 5.5.

In practice for a network of 3 non-aligned detectors the null space is spanned by the null vector

$$\boldsymbol{e}^n = \boldsymbol{e}^+ \wedge \boldsymbol{e}^\times, \tag{5.54}$$

and in principle for Gaussian noise with or without signal the squared mag-

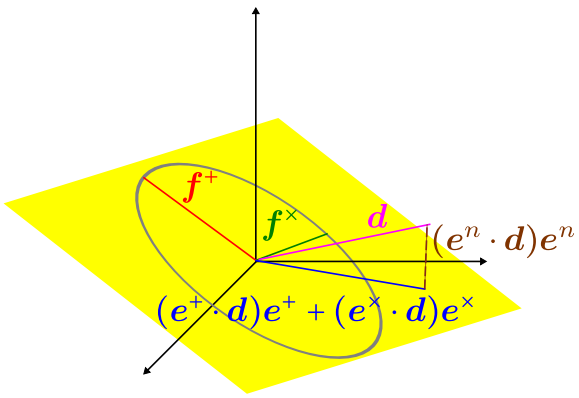

Figure 5.5: Shown is the three dimensional space of detector strains (3 detector case). The yellow plane is the plane spanned by the detector response vectors. The grey ellipse is the sensitivity to linearly polarized waves with different polarizations (see figure 5.4). The red and green lines are the sensitivities to the plus and cross polarization in the dominant polarization frame. The magenta line is the vector of detector strains for one noise realization. The blue line is its projection on the detector response plane, and the burgundy dashed line is its projection on the null space.

nitude of the projection

$$E_n = |\boldsymbol{e}^n \cdot \boldsymbol{d}|^2, \tag{5.55}$$

called *null energy*, should be χ^2 distributed and any event that has a sufficiently large null energy can be rejected.

In the case where we can assume circularly polarized signals, which is relevant for the analysis presented in this thesis, we have developed additional projection tests. A null projection can be performed on the null vectors orthogonal to right or left polarized signals

$$\boldsymbol{f}^{n\circlearrowright} = \frac{\boldsymbol{f}^+}{|\boldsymbol{f}^+|^2} - i\frac{\boldsymbol{f}^\times}{|\boldsymbol{f}^\times|^2}, \tag{5.56a}$$

$$\boldsymbol{f}^{n\circlearrowleft} = \frac{\boldsymbol{f}^+}{|\boldsymbol{f}^+|^2} + i\frac{\boldsymbol{f}^\times}{|\boldsymbol{f}^\times|^2}. \tag{5.56b}$$

Note that the null right vector is not parallel to the left vector unless the two modules $|\boldsymbol{f}^+|$ and $|\boldsymbol{f}^\times|$ are equal. Given that the exact polarization[13] is not known, the relevant quantity is the minimum of the two projections which we call *circular null energy*

$$E_{n\bigcirc} = \min\left(E_{n\circlearrowright}, E_{n\circlearrowleft}\right) = \min\left(|\boldsymbol{e}^{n\circlearrowright} \cdot \boldsymbol{d}|^2, |\boldsymbol{e}^{n\circlearrowleft} \cdot \boldsymbol{d}|^2\right), \tag{5.57}$$

[13] between left and right circular

where we have used the normalized null circular vector $\boldsymbol{e}^{n\circlearrowright}$ and $\boldsymbol{e}^{n\circlearrowleft}$. This energy also has a distribution centered around 1, but it is not simply related to a χ^2 distribution.

In practice, the distribution of the null energies defined above will not be distributed around 1 for a Gaussian noise with a gravitational wave signal. Significant deviation can be present due for instance to calibration errors or inaccurate assumption on the polarization. A method that has proven to be robust and effective [95], is to compare the above energies with their so called *incoherent* parts, that is the part which involves only squares of data from each detector. More explicitly, for a projection vector $\boldsymbol{e}$ the energy is of the form

$$E = |\boldsymbol{e} \cdot \boldsymbol{d}|^2 = \sum_{1 \leq i,j \leq D} e_i^* e_j d_i d_j^* \tag{5.58}$$

and its incoherent part is the sum of the diagonal terms

$$I = \sum_{i=1}^{D} |e_i|^2 |d_i|^2. \tag{5.59}$$

For the case of circular null energy the incoherent parts of left and right energies are equal, so there is no ambiguity in defining the incoherent circular null energy.

Noise glitches are uncorrelated between detectors hence the expectation value of the energy is its incoherent part: $\langle E \rangle = I$. On the contrary, for a gravitational wave signal, the amplitudes in different detectors will cancel out (at least approximately) when projected onto a null vector and one expects

$$1 \gg \frac{E}{I} \sim \frac{1}{I} + \text{calibration and polarization relative errors} \gtrsim 0.1, \tag{5.60}$$

where we assumed 10% calibration/polarization errors in the last inequality. Hence requiring E/I small will prove as being a good discriminant between signal and glitches.

When comparing an energy to its incoherent part, the projections onto vectors in the signal plane become interesting. Indeed, for a glitch the two are still expected to be equal, but for signals one expect a coherent buildup in the energy. The general picture is that for two aligned detectors and a noiseless signal one obtains $E = |a+a| = 4|a|^2$ and $I = |a|^2 + |a|^2 = 2|a|^2$, where a is the amplitude of the signal projected onto the relevant vector. This kind of test is weaker than a null test, because it mostly relies on phase consistency between detectors, however it can usefully complement null tests which rely on phase and amplitude consistency, especially when amplitude calibration errors are large.

There are several choices of energies that give a coherent buildup [96], we have developed another one tailored to the circular polarization assumption,

that we call *circular energy*,

$$E_{\bigcirc} = \max\left(|\boldsymbol{e}^{\circlearrowleft} \cdot \boldsymbol{d}|, |\boldsymbol{e}^{\circlearrowright} \cdot \boldsymbol{d}|\right), \tag{5.61}$$

which is the maximum of the projection onto the left and right circular vectors, and as for the circular null energy the incoherent parts of the two terms in the maximum are equal.

5.7.2 Coherent cuts

In the previous section we have introduced several energies and their incoherent parts: the null, circular null and circular energies. In each case the energy involves either a coherent cancellation or a coherent build-up of gravitational wave amplitudes compared to the incoherent part. The goal is to use these pairs of variables to separate gravitational wave signals from glitches, and especially to remove all glitches of high amplitude while keeping most signals with sufficiently high amplitude.

For a sufficiently loud[14] signal of amplitude A all energy related quantities have an A^2 dependence

$$E \propto A^2, \tag{5.62a}$$
$$I \propto A^2, \tag{5.62b}$$
$$E - I \propto A^2. \tag{5.62c}$$

However for the case of a glitch of amplitude A in a single detector the difference $E-I$ involves only cross-terms between the glitch and some Gaussian noise in another detector. Hence the leading terms for high amplitudes are

$$E \propto A^2, \tag{5.63a}$$
$$I \propto A^2, \tag{5.63b}$$
$$E - I \propto A. \tag{5.63c}$$

For signal and glitches the cross-correlation term $E - I$ has a different behavior, we use this property to construct a family of functions

$$f(I, E|\alpha) = \frac{|E - I|}{(E + I)^{\alpha}}, \tag{5.64}$$

which compared to a threshold r are able to reject glitches while keeping the signal. Depending on whether coherent build-up or cancellation of gravitational wave signal is expected for the particular energy considered, one should keep either cases where $E - I$ is positive or negative. Each choice of (r, α) corresponds to a different line in the I versus E plane which tries

[14] for which the Gaussian noise contribution can be neglected

to separate gravitational wave signal from glitches, and at given value of α the amount of rejected triggers increases with r regardless of their type. An example of such a separation line is shown on figure 7.11.

Two particular values of α motivate this functional form. Using the amplitude dependencies for signal (5.62) and glitches (5.63) we find that for $\alpha = 1$

$$p\left[r < f(I, E|1)\right] \propto \text{const} \qquad \text{for signal,} \tag{5.65a}$$

$$p\left[r < f(I, E|1)\right] \propto \frac{1}{A} \qquad \text{for glitches,} \tag{5.65b}$$

hence a given choice of r rejects a fixed fraction of all possible signals forms independently of their amplitude, and keeps a fraction of possible glitches forms which is decreasing with amplitude. The reverse happens for $\alpha = 0.5$, where

$$p\left[r < f(I, E|0.5)\right] \propto A \qquad \text{for signal,} \tag{5.66a}$$

$$p\left[r < f(I, E|0.5)\right] \propto \text{const} \qquad \text{for glitches,} \tag{5.66b}$$

and for a given choice of r a constant fraction of glitches is kept, while the fraction of rejected signals is decreasing with amplitude. Between these two extreme choices of amplitude dependence there is a continuum of possible separation tests with different trade-offs between keeping all loud signals and rejecting all loud glitches.

In principle the choice of r could be determined analytically by selecting a desired false alarm or false dismissal probability. However, in practice this threshold depends on the ratio of magnitude between the cross-correlation and auto-correlation terms in the projector operator[15], on the calibration errors (and model errors for circular energies) and above all on the particular distribution of glitches in each detector. Hence, in practice, the values of r for each coherent cut is selected by a numerical tuning procedure that will be detailed in section 7.2.3.

5.8 Robust statistics

In section 5.6 we have always assumed that interferometer noise is Gaussian which led to statistics that are very sensitive to non-Gaussian glitches. Coherent consistency tests developed in section 5.7 allows to reject some of these glitches. A complementary approach is to include a non-Gaussian noise distribution in the Bayesian statistic derivation. Here we model the noise distribution with a power-law distribution, this is motivated by a relatively good fit of the power-law distribution with the tail of the distribution in real data. We are designing a robust detection statistic for events with large

[15] i.e. on the diagonal and off-diagonal terms of the $e_i^* e_j$ operator in equation (5.58).

amplitude, hence the exact shape of the distribution at low amplitudes is not important. In the derivation below we will assume for each detector a noise probability distribution of the form

$$p(x) = \frac{B}{A + |x|^{\alpha}}, \tag{5.67}$$

the exact values of A and B will not be relevant, only the exponent α is important. For real data this exponent is typically in the $1 - 7$ range.

5.8.1 Two non aligned detectors statistic

For the case of two detectors as usual we assume the noise to be independent between detectors and the power-law noise distribution hypothesis has the form

$$P(\boldsymbol{d}|H_0) = \frac{b_{\alpha_1}}{a_{\alpha_1}^{\alpha_1} + |d_1|^{\alpha_1}} \frac{b_{\alpha_2}}{a_{\alpha_2}^{\alpha_2} + |d_2|^{\alpha_2}}, \tag{5.68}$$

where d_1 and d_2 are respectively the whitened strains in the first and the second detector, α_1 and α_2 are the power law slopes for each detector, and the constant a_α, b_α are chosen so that the single detector noise distribution is normalized and has a standard deviation equal to 1.

For a given known signal the probability of the signal with noise hypothesis H_1 is

$$P(\boldsymbol{d}|H_1, h_+, h_\times) = \frac{b_{\alpha_1}}{a_{\alpha_1}^{\alpha_1} + |d_1 - F_1^+ h_+ - F_1^\times h_\times|^{\alpha_1}} \frac{b_{\alpha_2}}{a_{\alpha_2}^{\alpha_2} + |d_2 - F_2^+ h_+ - F_2^\times h_\times|^{\alpha_2}}, \tag{5.69}$$

where F_i^+ and $F_i^\times$ are the whitened antenna pattern coefficients defined in equation (5.42). In this case of non-Gaussian noise distribution, the only signal prior which can be analytically marginalized on is the flat prior, that is the Gaussian prior in the limit of infinite characteristic amplitude. Without any polarization assumptions we obtain

$$P(\boldsymbol{d}|H_1) = \int P(\boldsymbol{d}|h_+, h_\times + \text{noise}) \mathrm{d}h_+ \mathrm{d}h_\times \tag{5.70a}$$

$$= \frac{1}{\det \boldsymbol{F}} \int \frac{b_{\alpha_1} \mathrm{d}n_1}{a_{\alpha_1}^{\alpha_1} + |n_1|^{\alpha_1}} \int \frac{b_{\alpha_2} \mathrm{d}n_2}{a_{\alpha_2}^{\alpha_2} + |n_2|^{\alpha_2}} \tag{5.70b}$$

$$= \frac{1}{\det \boldsymbol{F}}, \tag{5.70c}$$

where

$$\boldsymbol{F} = (\boldsymbol{F}^+ \boldsymbol{F}^\times) = \begin{pmatrix} F_1^+ & F_1^\times \\ F_2^+ & F_2^\times \end{pmatrix} \tag{5.71}$$

is the two by two Jacobian matrix that comes from the change of variables

$$n_1 = d_1 - F_1^+ h_+ - F_1^\times h_\times, \tag{5.72a}$$

$$n_2 = d_2 - F_2^+ h_+ - F_2^\times h_\times. \tag{5.72b}$$

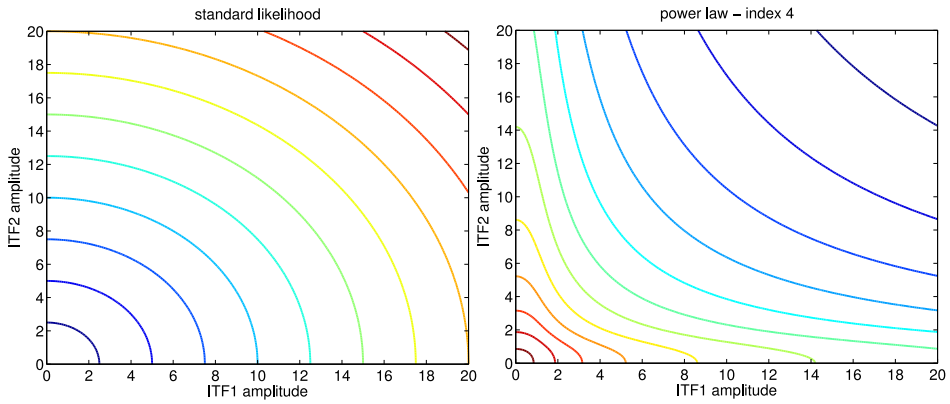

Figure 5.6: Contour lines for Gaussian type and powerlaw type detection statistic. The left panel show isolines for (5.76) and the right panel for $S(\boldsymbol{d}) = (1+|d_1|^4)(1+|d_2|^4)$. In both case the x and y axes are the magnitudes of d_1 and d_2, respectively.

Thus the likelihood ratio is

$$\Lambda(\boldsymbol{d}) = \frac{P(\boldsymbol{d}|H_1)}{P(\boldsymbol{d}|H_0)} = \frac{(a_{\alpha_1}^{\alpha_1} + |d_1|^{\alpha_1})(a_{\alpha_2}^{\alpha_2} + |d_2|^{\alpha_2})}{b_{\alpha_1} b_{\alpha_2} \det(F)} \tag{5.73a}$$

$$\simeq \frac{|d_1|^{\alpha_1}|d_2|^{\alpha_2}}{b_{\alpha_1} b_{\alpha_2} \det(F)} \qquad \text{for large } |\boldsymbol{d}|. \tag{5.73b}$$

If we discard terms that do not depend on detectors data the obtained detection statistic is

$$S(\boldsymbol{d}) = |d_1|^{\alpha_1}|d_2|^{\alpha_2}. \tag{5.74}$$

The fundamental difference compared to the log-likelihood statistic derived before is that a significant amplitude in both detectors is required in order to yield a large detection statistic as can be seen on the contour lines on figure 5.6. This means that the statistic is much more robust to single detector glitches.

This behavior is more clear if one compares this statistic with $\alpha_1 = \alpha_2 = 1$

$$S_1(\boldsymbol{d}) = |d_1||d_2|, \tag{5.75}$$

and the Gaussian statistic (5.50) in the loud signal limit with terms which are not depending on the data dropped

$$S_2(\boldsymbol{d}) = |d_1|^2 + |d_2|^2. \tag{5.76}$$

In both cases the statistic grows quadratically with the amplitude of the signal, whereas for a glitch the Gaussian statistic still grows quadratically with the amplitude, while the robust statistic grows only linearly.

5.8.2 Three non aligned detectors statistic

For the case of three detectors the statistic computation is more cumbersome. The noise probability distribution is still the product of the individual detectors distributions p_1, p_2 and p_3

$$P(\boldsymbol{d}|H_0) = \frac{b_{\alpha_1}}{a_{\alpha_1}^{\alpha_1} + |d_1|^{\alpha_1}} \frac{b_{\alpha_2}}{a_{\alpha_2}^{\alpha_2} + |d_2|^{\alpha_2}} \frac{b_{\alpha_3}}{a_{\alpha_3}^{\alpha_3} + |d_3|^{\alpha_3}} = p_1(d_1)p_2(d_2)p_3(d_3). \quad (5.77)$$

But the marginalization on the flat prior of signal amplitude is more complex

$$P(\boldsymbol{d}|H_1) = \int p_1(|d_1 - F_1^+ h_+ - F_1^\times h_\times|)p_2(|d_2 - F_2^+ h_+ - F_2^\times h_\times|)p_3(|d_3 - F_3^+ h_+ - F_3^\times h_\times|)\mathrm{d}h_+\mathrm{d}h_\times. \quad (5.78)$$

This is an integral of a three dimensional probability distribution over a two dimensional plane, whose offset is given by the observed data $\boldsymbol{d}$ and orientation by the antenna pattern vectors $\boldsymbol{F}^+$ and $\boldsymbol{F}^\times$. Similarly to the two-detector case shown on the right panel of figure 5.6, the probability distribution is concentrated around the three Cartesian axes that correspond to each detector, and the vector which is normal to this plane is the null vector $\boldsymbol{e}^n$ defined in equation (5.54). If we assume that this normal is not nearly parallel[16] to any of the three Cartesian axis, we can approximate the integral by three integrals each around the intersection of the plane with one of the axis. The coordinate of the intersection between the signal plane and the x axis is $X_0 = \frac{\boldsymbol{e}^n \cdot \boldsymbol{d}}{\boldsymbol{e}^n \cdot \boldsymbol{e}_1}$, the coordinates of the intersection points with the y and z have an analogous form.

At each intersection point we approximate the integral with an integral along the plan orthogonal to the given axis and divide the result by a slope factor $|\boldsymbol{e}^n \cdot \boldsymbol{e}_i|$ in order to correct at first order the orthogonal plane simplification. These integrals along the orthogonal planes are respectively equal to $p_1(X_0)$, $p_2(Y_0)$, $p_3(Z_0)$. The final result is

$$P(\boldsymbol{d}|H_1) \simeq \frac{1}{\sqrt{\det \boldsymbol{F}^\dagger \boldsymbol{F}}} \left(\frac{p_1(X_0)}{\boldsymbol{e}^n \cdot \boldsymbol{e}_1} + \frac{p_2(Y_0)}{\boldsymbol{e}^n \cdot \boldsymbol{e}_2} + \frac{p_3(Z_0)}{\boldsymbol{e}^n \cdot \boldsymbol{e}_3} \right), \quad (5.79)$$

where the $\sqrt{\det \boldsymbol{F}^\dagger \boldsymbol{F}}$ factor corresponds to a change of variables analogous to (5.72), the peculiar form comes from the non-square nature of $\boldsymbol{F}$.

The full expression of the likelihood ratio is quite complex, but in the large amplitude limit it can be usefully approximated if one sets all constant factors to 1 with the exclusion of exponents. This simplified likelihood ratio

[16] Which will be true as long as the second and third least sensitive detector have comparable sensitivities.

is

$$\Lambda(\boldsymbol{d}) = \frac{|d_1|^{\alpha_1}|d_2|^{\alpha_2}|d_3|^{\alpha_3}}{\sqrt{\det \boldsymbol{F}^\dagger \boldsymbol{F}}} \left(\frac{1}{1+|X_0(\boldsymbol{d})|^{\alpha_1}} + \frac{1}{1+|Y_0(\boldsymbol{d})|^{\alpha_2}} + \frac{1}{1+|Z_0(\boldsymbol{d})|^{\alpha_3}} \right), \tag{5.80}$$

and if we discard terms that do not depend on data the obtained detection statistic is

$$S(\boldsymbol{d}) = |d_1|^{\alpha_1}|d_2|^{\alpha_2}|d_3|^{\alpha_3} \left(\frac{1}{1+|X_0(\boldsymbol{d})|^{\alpha_1}} + \frac{1}{1+|Y_0(\boldsymbol{d})|^{\alpha_2}} + \frac{1}{1+|Z_0(\boldsymbol{d})|^{\alpha_3}} \right). \tag{5.81}$$

As in the two-detector case, the detection statistic has a large value if the event is seen in all detectors. Moreover, the value of the detection statistic is decreased if the event deviates from the signal plane, i.e. when the data projection on the null vector is large.

5.8.3 Power law slope estimation

The remaining question in the above derivation is which power-law slope α_i should be used for each detector. Given that the noise behavior of each detector is time and frequency dependent, the best approach is to determine these coefficients based on the data, similarly to what it is done in order to estimate the noise power spectrum for data whitening. Among others, such a procedure needs to be robust to the presence of desirable signal in the data. The ad hoc method that we use for a detector i is the following one

- Use the whitened coefficients at a given frequency from the same stretch of data as the one used for power spectrum estimation. That is, based on equation (5.31), the $d_i^w(j,k)$ amplitudes for $j \in [\![1, M/m]\!]$.
- Compute the median $E_{50\%} = \text{prctile}_{50\%}(|d_i^w(j,k)|^2)$ and the 99 percentile $E_{99\%} = \text{prctile}_{99\%}(|d_i^w(j,k)|^2)$ energy in these coefficients.
- Choose $\alpha_i(k) = \sqrt{44}\dfrac{E_{50\%}}{E_{99\%}}$.

This method has no simple justification but has proven effective in real data analysis. It has as well some valuable properties. The method is robust to real signals, the expected signal duration is less than 1% of the used data stretch duration, hence the 50 and 99 percentiles are not affected by the presence of a signal. Moreover, if the noise has a long tail, the chosen α_i coefficient will be small and the robust statistic will grow slowly with the noise amplitude for that detector. This reflects on our limited trust in large amplitude deviation from a detector and frequency which is known to contain a large noise tail.

The overall normalization of the exponent α_i is not really important, especially in the two-detector case. The $\sqrt{44}$ prefactor is chosen in order

to obtain $\alpha_i = 1$ for pure Gaussian noise[17], which yields a statistic that is growing with the square of the signal amplitude as it is the case for the Bayesian statistics.

5.9 Sky location statistic

In the sections above we have assumed that the source sky location is known with sufficient precision compared to the resolution of the interferometer networks that the sky location errors can be safely neglected. However, as shown in section 4.2, for some satellites the sky localization is rather poor. The resulting difference in time delays between pairs of detectors for different sky positions in the reconstructed sky location error box can be large. That is, sufficiently large that signal between detectors can coherently build up instead of canceling for null energies (and vice-versa for circular energy).

The sky location error can be taken into account with the Bayesian formalism developed above. Electromagnetic observation by satellites give a sky location prior (4.6) or (4.8) of the source, and given that the null hypothesis H_0 is independent of the sky location, the Bayesian marginalization over the sky position Ω yields the likelihood ratio

$$\Lambda(\boldsymbol{d}) = \frac{\int P(\boldsymbol{d}|\Omega, H_1) P_{\rm EM}(\Omega) \mathrm{d}\Omega}{P(\boldsymbol{d}|H_0)} = \int \Lambda(\boldsymbol{d}|\Omega) P_{\rm EM}(\Omega) \mathrm{d}\Omega, \tag{5.82}$$

where $\Lambda(\boldsymbol{d}|\Omega)$ is one of the likelihoods derived previously, for instance the exponential of half the log-likelihood (5.51) or its equivalent (5.53) with the circular polarization assumption.

In practice, such a marginalization is computationally very expensive, and for the consistency tests and the robust statistic computation we need a single sky location. Therefore we use the usual workaround of maximizing instead of marginalizing the likelihood ratio. This will also provide a maximum likelihood estimator of the source sky location, which can be used to compute auxiliary statistics. Indeed, the posterior probability distribution of the sky locations is

$$P(\Omega|\boldsymbol{d}) = \frac{P(\boldsymbol{d}|\Omega, H_1) P_{\rm EM}(\Omega)}{\int P(\boldsymbol{d}|\Omega, H_1) P_{\rm EM}(\Omega) \mathrm{d}\Omega} \propto \Lambda(\boldsymbol{d}|\Omega) P_{\rm EM}(\Omega), \tag{5.83}$$

where the proportionality constant do not depend on Ω. Hence Ω_0 which maximizes the likelihood ratio is also the most likely posterior sky position based on the electromagnetic and gravitational wave observations.

To perform this maximization a simple choice is to scan a discrete grid of sky positions covering most of the probability distribution. For a disk shaped

[17] The $d_i^w(j,k)$ are complex Gaussian distributed (i.e. Gaussian with 2 degrees of freedom), the resulting ratio is $\frac{E_{99\%}}{E_{50\%}} \simeq \sqrt{44}$.

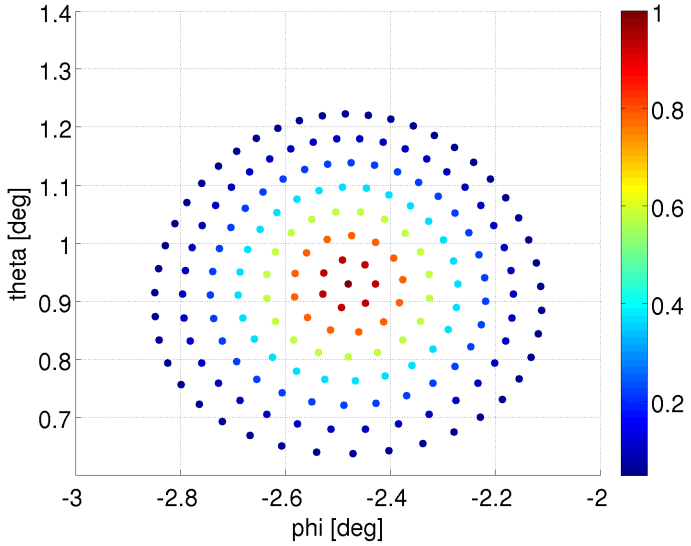

Figure 5.7: Example grid of sky position for a GBM sky location error box. The x and y axis are the standard Earth fixed spherical coordinates (θ, ϕ) in radians, color coded is the sky location prior $P_{\mathrm{EM}}(\Omega) = P_{\mathrm{F}}(\alpha; \kappa)/2\pi \sin(\alpha)$ where α is the angular distance from the center of the grid. Here $\sigma \simeq 0.175 \simeq 10°$, $\theta_{\mathrm{step}} = 4.2 \times 10^{-2}$ rad and the grid cover at least a disk of angular radius $\sigma_{95\%} = 1.65\,\sigma$.

error box region $\mathcal{O}$, an example of a grid on the sphere is to consider a single central point and concentric circles of points around it each spaced by at most θ_{step}, each circle being separated from the next one by an angular radius θ_{step}. An example of such a grid is shown on figure 5.7. This angular step θ_{step} depends on the maximal time tolerance t_{tol} between pairs of detectors which does not significantly affect the coherent consistency tests. For a pair of detectors (i, j) separated by a light travel time vector $\vec{t}_{ij}$ the time difference of gravitational wave arrival for a sky position $\hat{\Omega}$ is

$$t_{ij}(\Omega) = \vec{t}_{ij} \cdot \hat{\Omega}, \tag{5.84}$$

and a sky location error $\mathrm{d}\theta$ leads to a timing error

$$|\mathrm{d}t_{ij}(\Omega)| \leq |\vec{t}_{ij}| |\sin\left(\cos^{-1} \hat{t}_{ij} \cdot \hat{\Omega}\right) \mathrm{d}\theta|, \tag{5.85}$$

where the equality is obtained if the error is in the same direction as $\vec{t}_{ij}$. This means that given a time tolerance t_{tol}, a single grid point Ω covers at least all the sky position within an angular radius

$$\theta_r = \frac{t_{\mathrm{tol}}}{|\vec{t}_{ij}| \sin\left(\cos^{-1} \hat{t}_{ij} \cdot \hat{\Omega}\right)}. \tag{5.86}$$

As a conservative choice of the angular step θ_{step} we minimize the angular radius coverage θ_r over the sky location error box and the available detectors pairs, and use twice the obtained value which is

$$\theta_{\text{step}} = 2 \min_{\Omega \epsilon \mathcal{O}} \min_{(i,j)} \frac{t_{\text{tol}}}{|\vec{t}_{ij}| \sin\left(\cos^{-1} \hat{t}_{ij} \cdot \hat{\Omega}\right)}. \tag{5.87}$$

The reason for using twice the minimized θ_r is that any point in the error box is within half a step[18] of a grid point.

5.10 Combining clustering and coherent analysis

For the moment we have considered separately the question of clustering (signal shape) and of coherent analysis of a network of gravitational wave detectors. Let us combine the two and obtain the detection statistic used to rank gravitational wave triggers. The operation consists simply in replacing the single stream log-likelihood ratio $L(d|u)$ in equation (5.40) with the coherent log-likelihood ratio for a single time frequency pixel such as (5.53). The rest of the clustering procedure is kept the same, the log-likelihood ratio passing over some threshold forms clusters, and the detection statistic for the cluster $\mathcal{C}$ is the sum of the log-likelihood over the cluster

$$L(d|\mathcal{C}) = \sum_{u \epsilon \mathcal{C}} L(d|u, \text{circular}) + 2 \log P_{\text{EM}}(\Omega), \tag{5.88}$$

where $P_{\text{EM}}(\Omega)$ is the prior probability of the analyzed sky position Ω.

This procedure yields for an excess energy present in the data one cluster for each sky positions in the analyzed grid of sky positions. In principle one should marginalize over the possible sky positions, but as mentioned before, we replace the marginalization with maximization for simplicity. Given that any trigger found can be rejected by one of the coherent cuts or a data quality check, this maximization needs to be done on a per event basis. A reasonable choice is to consider clusters "overlapping" in time and frequency as coming from the same physical event, and keep only the cluster with the highest value of the detection statistic (5.88). To obtain a simple implementation, we assume that two clusters are "overlapping" if the two bounding rectangles around each cluster have a non empty intersection.

In addition clustering, to refine the signal shape marginalization the trigger production is performed for different aspect ratios of the time-frequency basis, that is for different choice of the short FFT time length Δt. This allows to construct clusters which are a better fit to the time-frequency shape

[18] A point in the middle of a square of grid points separated by θ_{step} is not distant by $\theta_{\text{step}}/\sqrt{2}$ but by at most $\theta_{\text{step}}/2$ because the metric is not Euclidean. Only the distance in the direction parallel to $\vec{t}_{ij}$ is relevant.

of possible signals. The maximization over this aspect ratio is performed in exactly the same way as for the maximization over the sky positions.

As a result, for each physical event one obtains a single cluster which maximizes the detection statistic (5.88). The time-frequency basis, sky location and pixels defining this cluster are used to compute other auxiliary statistics, mainly the robust statistic of section 5.8 and the projections energies used in coherent cuts. These auxiliary statistics are summed over pixels in the cluster in the same way as the log-likelihood in equation (5.88). These properties together with all the statistic fully define a gravitational wave trigger.

5.11 Conclusion

In this section we have described the basics analysis tools which we will use in searching for gravitational wave bursts associated with GRBs, however these tools are quite generic and in principle can be applied to any search for gravitational wave bursts. In section 7.2 we will give a detailed description of how these tools are used and the parameters which tailor the analysis to the specific needs of searching in association with GRBs.

Chapter 6

Background estimation

In addition to the colored Gaussian noise discussed in chapter 2 a large number of instrumental and environmental glitches are present in the data collected by gravitational wave interferometers. The sources of these glitches are understood for some mechanisms, but there are many sources that are not understood and in all cases the exact non-linear couplings between noise sources and the measured dark fringe signal are not known. As a result, the background distribution of any of the statistics discussed in chapter 5 is *a priori* not known.

However, for statistics that use information from a network of at least two detectors, a powerful method of measuring this background distribution is available. The method consists in time shifting the data from the different detectors in the network by times that are much larger than the gravitational wave travel time between the detectors and the typical autocorrelation time of the data analysis method used. For this reason this method is usually called the *time slide* background estimation, and has already been used by Weber in the 70' [97]. The underlying assumption is that the noise in different detectors is uncorrelated, this is true for most sources of glitches with several exceptions like glitches in timing clocks synchronization and extraordinary large scale electromagnetic transients, these need to be discarded by environmental and instrumental probes. The only remaining source of correlated "glitches" are gravitational waves and we use time slides in the background estimation method to remove this correlation. Hence, the analysis of time shifted data yields a realization of coincident or coherent events due to noise only, and multiple realizations can be obtained by changing the time slide step. This standard method is used in most current searches for gravitational wave transients [98, 99, 100, 101, 102].

But the method has some limitations which we will discuss in this chapter. The most obvious limitation is that the number of possible time shifts is not infinite but limited to the duration of the data run divided by the minimal length of a time slide step which constrains the statistics of the

background estimation. A more subtle limitation is that the different realizations are not completely independent but reuse the same data over and over. This is reasonable as long as the most significant events are due to a random coincidence of relatively quiet events in each detector and not to an uncommon event in one detector coincident with very common events in the others. Another potential limitation comes from the background non-stationarity. For instance detector noise tends to be higher during day time or bad weather than during night time or calm weather, and too large time slides may wash out these correlated effects.

In the section below we discuss both these limitations in the context of a simplified coincident analysis, that is an analysis that creates triggers for each detector independently and then searches for coincidences between trigger lists. This is a good representation of some analysis, and is simple enough to be tractable analytically. We test these analytically results for the toy analysis with Monte Carlo simulations. Most of the results presented here have been published previously in an article [103] and a conference proceeding [104].

6.1 Poisson statistics limitation

We start by looking into the first limitation coming from reusing the same data. For the moment we assume that detectors trigger rates are stationary.

6.1.1 Definitions

Poisson approximation for trigger generation

Background triggers in each detector are due to rare glitches. Often these glitches come in groups, but most analysis pipelines cluster their triggers, so each glitch group results in only one final trigger. This clustering procedure is reasonable as long as the resulting trigger rate is much lower than the inverse of the typical clustering time length. In this limit the clustered triggers can be considered as independent events. Thus we will assume that each detector produces random background triggers, which are Poisson distributed in time.

Problem description

We then look at the coincidence between two Poisson processes. In this chapter we will use the following notations for describing Poisson processes:

$\boldsymbol{\alpha_i}$ – the Poisson rate parameter of the trigger distribution in detector i, which means that the probability of obtaining n triggers during a time t is $(\alpha_i t)^n \exp(-\alpha_i t)/n!$.

$\mathbf{FA_i}$ – the measured rate of triggers in detector i, i.e. the observed number of triggers divided by the total time T.

FA($\mathcal{T}$) – the measured coincidence rate for a given time slide $\mathcal{T}$.

In particular for zero lag ($\mathcal{T} = 0$) the measured rate is FA(0). In these terms the time slide method uses

$$\widehat{\mathrm{FA}} = \frac{1}{R}\sum_{k=1}^{R} \mathrm{FA}(\mathcal{T}_k), \tag{6.1}$$

as an estimator of FA(0), where R is the number of time slides and $\mathcal{T}_k$ is the k^{th} time slide step.

Poisson process model

To model a Poisson process with event rate α_1 we discretize the data stream duration T with bins of length Δt, the discretization time scale, e.g. either the detector sampling rate or the clustering time scale. Thus, for each bin an event is present with a probability[1] $p = \alpha_1 \Delta t$.

To ease the calculation we describe the Poisson process realizations with a continuous random variable. We take $\boldsymbol{x}$ uniformly distributed in the volume $[0,1]^N$ where $N = \frac{T}{\Delta t}$ is the number of samples, then compare x_k (the k^{th} coordinate of $\boldsymbol{x}$) with p. When $x_k < p$ there is an event in time bin k, otherwise there is none. Thus $\boldsymbol{x}$ characterizes one realization of a Poisson process, and it can be easily seen that the uniform distribution of $\boldsymbol{x}$ leads to a Poisson distribution of events.

Coincidences

In order to simplify the modeling of the coincidence between two processes we use a binned coincidence definition. More precisely, for two Poisson processes with event rates respectively α_1 and α_2, we define a coincidence when there is an event in the same time bin k of duration Δt for both processes. This is different from the usual definition, where events are considered in coincidence when they are less than a given time window apart. This binning time coincidence has on average the same effect as defining as coincident events those that are less than $\pm\frac{1}{2}\Delta t = \pm\tau_c$ apart. Note that the bin duration Δt is equal to twice the usual coincidence tolerance duration τ_c. The analytical results are derived using this non standard definition, but they are in an excellent agreement with Monte Carlo simulations that are performed using the usual definition of time coincidence.

[1] Here we model the Poisson process by a binomial distribution, recalling that when $p \ll 1$ the binomial distribution tends toward a Poisson distribution

6.1.2 The case of two detectors

Time slides between two detectors

Let $\boldsymbol{x}, \boldsymbol{y} \in [0,1]^N$ be two realizations of Poisson processes with respectively $p = \alpha_1 \Delta t$ and $q = \alpha_2 \Delta t$. There is a coincident event in time bin k when $x_k < p$ and $y_k < q$. So the total number of coincidences for this realization is

$$\sum_{k=1}^{N} \mathbb{1}(x_k < p)\mathbb{1}(y_k < q) \tag{6.2}$$

where

$$\begin{cases} \mathbb{1}(a) = 1 & \text{if } a \text{ is true} \\ \mathbb{1}(a) = 0 & \text{if } a \text{ is false} \end{cases} \tag{6.3}$$

Thus the mean number of coincidences in the zero lag is as expected

$$\text{Mean} = \int_{x_1} \cdots \int_{x_N} \int_{y_1} \cdots \int_{y_N} \sum_{k=1}^{N} \mathbb{1}(x_k < p)\mathbb{1}(y_k < q) \underbrace{\mathrm{d}x_1 \cdots \mathrm{d}x_N \mathrm{d}y_1 \cdots \mathrm{d}y_N}_{\mathrm{d}V} = Npq. \tag{6.4}$$

To consider a number R of time slides we take a set of R circular permutations of $[\![1, N]\!]$. Time-sliding a vector $\boldsymbol{x}$ by the circular permutation π transforms the vector $\boldsymbol{x}$ into the vector of coordinates $x_{\pi(k)}$. Then the mean number of coincidences coming from the time slide estimator is simply

$$\text{Mean} = \int_{x_1} \cdots \int_{x_N} \int_{y_1} \cdots \int_{y_N} \frac{1}{R} \sum_{\pi} \sum_{k} \mathbb{1}(x_k < p)\mathbb{1}(y_{\pi(k)} < q)\mathrm{d}V = Npq, \tag{6.5}$$

thus there is no bias resulting from the use of time slides.

Computation of the variance

In order to have an estimate of the statistical error, we compute the variance with R time slides. The second moment of the time slide estimator is

$$\begin{aligned} \mathrm{M}_2 &= \int_{x_1} \cdots \int_{x_N} \int_{y_1} \cdots \int_{y_N} \left[\frac{1}{R} \sum_{\pi} \sum_{k} \mathbb{1}(x_k < p)\mathbb{1}(y_{\pi(k)} < q) \right]^2 \mathrm{d}V \\ &= \int \cdots \int \frac{1}{R^2} \sum_{\pi_1} \sum_{\pi_2} \sum_{k} \sum_{l} \mathbb{1}(x_k < p)\mathbb{1}(x_l < p)\mathbb{1}(y_{\pi_1(k)} < q)\mathbb{1}(y_{\pi_2(l)} < q)\mathrm{d}V. \end{aligned} \tag{6.6}$$

We can then move the sums in front of the integrals. To compute the integrals we distinguish two cases: when $k \neq l$ the integrals on x_k and x_l are independent, and the integration over $x_1, \ldots, x_N$ gives a p^2 contribution; otherwise the integration gives a p contribution. Analogously for the y variables we obtain q or q^2 depending on whether $\pi_1(k) = \pi_2(l)$ or not.

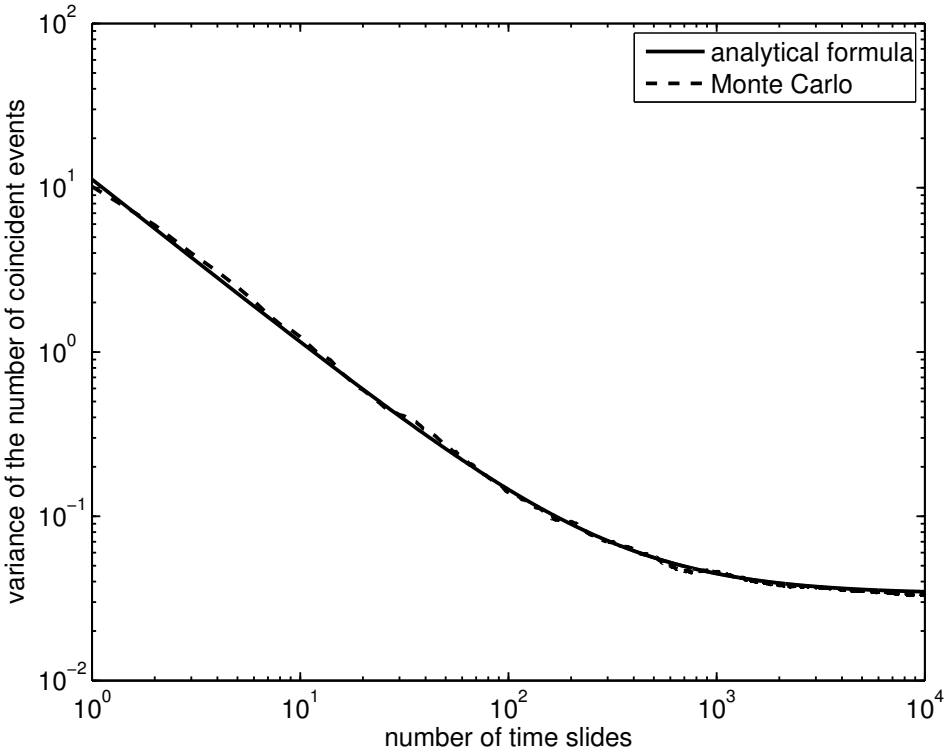

Figure 6.1: The solid line is the analytical formula (6.8) of the variance and the dashed line is the Monte Carlo variance as a function of the number of time slides. The Monte Carlo has been performed with $\alpha_1 = 0.7\,\mathrm{Hz}$, $\alpha_2 = 0.8\,\mathrm{Hz}$, $\tau_c = 1\,\mathrm{ms}$, 500 trials and a $T = 10^4\,\mathrm{s}$ data stream length.

The computation of this integral, detailed in appendix A.1, yields

$$\mathrm{Var} = Npq\left[\frac{1}{R} + p + q + \frac{pq - (p+q)}{R} - 2pq\right] \tag{6.7}$$

$$\simeq Npq\left[\frac{1}{R} + p + q\right], \tag{6.8}$$

where the last line is an approximation in the limit p, q, $\frac{1}{R} \ll 1$, which is reasonable as far as gravitational wave analysis is concerned.

Interpretation

Each term in equation (6.8) can be interpreted. The $\frac{1}{R}$ is what we would expect if we considered R independent Poisson process realizations instead of R time slides. The $p+q$ comes from the estimation of the Poisson process event rate. Indeed, the estimation of the event probability p from a single

realization of a Poisson process with a mean number of events Np is $\hat{p} = p+\delta p$, where δp is the random statistical error with variance $\langle \delta p^2 \rangle = \frac{p}{N}$. This yields the mean rate of coincidences

$$\text{Mean} = N\hat{p}\hat{q} = N\,(p+\delta p)\,(q+\delta q) \simeq Npq + Np\delta q + Nq\delta p \tag{6.9}$$

which corresponds to a variance of $\left\langle N^2p^2\delta q^2 + Nq^2\delta p^2 \right\rangle = Npq(p+q)$, because δp and δq are independent errors. Thus, when using only one realization for the single detector triggers, we have a statistical error on the single detector process rate. This statistical error is systematically propagated to the coincidence rate of each time slide, which yields the extra terms in the variance as compared to independent process realizations. One can see that this extra term is important when $\frac{1}{R} < \max(p,q)$; for cases where the coincident false alarm rate is maintained fixed (pq constant), the effect is most noticeable when p and q are very different.

This gives an estimate of the variance of the number of coincident events in a data stream of length T. After converting to the estimation of the coincidence false alarm rate we obtain

$$\text{Mean}\,\widehat{\text{FA}} = \frac{\text{Mean}}{T} = \alpha_1\alpha_2\Delta t, \tag{6.10}$$

$$\text{Var}\,\widehat{\text{FA}} = \frac{\text{Var}}{T^2} \simeq \alpha_1\alpha_2\frac{\Delta t}{T}\left[\frac{1}{R} + \alpha_1\Delta t + \alpha_2\Delta t\right]. \tag{6.11}$$

One should note that the variance is different from what one would naively expect if each background time shift trial was independent, i.e.

$$\text{Var}_{\text{naive}}\widehat{\text{FA}} = \alpha_1\alpha_2\frac{\Delta t}{T}\frac{1}{R}. \tag{6.12}$$

To verify these results, a Monte Carlo simulation has been performed. The Poisson processes are created as described in section 6.1.1, using a sampling rate of 16384 Hz, then a simple coincidence test with a window of $\tau_c = 1$ ms is applied. The time shifts are done by adding an integer number of seconds to all events and applying a modulo T operation. The formula has been tested using 500 realizations of $T = 10^4$ s long Poisson processes, and using between 1 and 10^4 time slides for each realization. Figure 6.1 shows that the analytical formula (6.8) and the Monte Carlo agree well for any number of time slides, and that the variance starts saturating when a few hundreds time slides are used. We can see that the identification of the sampling time and the coincidence time window has no consequences on the result, the effect between the choice of binning and windowing coincidences represents a higher order correction.

Straightforward extensions of the model

In real data analysis, there are times when one of the detectors does not take science quality data for some reason. Thus, the data set is divided into

disjoint segments, and the background estimation is often done by circular time slides on each segment separately. Afterwards the results from all the segments are combined to get the background false alarm estimation. The computation discussed above extends to this case with minimal changes. The circular permutations have to be changed to circular by block permutations, everything else can be kept identical.

Another caveat is that for real data analysis the coincidence procedure is often more complicated. Some of those complications are at the level of event consistency tests, e.g. do the two coincident events have a similar frequency? We can model this by adding some parameter f distributed uniformly in $[0,1]$ attached to each event, and then requesting a coincidence in the parameter f.

For this model the results will be the same as those above, up to a factor of order 1. Indeed, instead of applying a window of size Δt to our events, we are now working in a 2 dimensional (for instance time-frequency) space and using a rectangular window in this 2 dimensional parameter space. The procedure in both cases is the same — applying an M dimensional rectangular windows to events distributed uniformly in an M dimensional space — up to the dimension of the space.

6.1.3 The case of three detectors

Time slides between three detectors

In the case of three detectors one natural extension is to ask for events that are seen by at least two detectors, which means look for coincidence between two detectors for each detector pair, but counting the coincidences between three detectors only once. This "OR" strategy in a interferometer network has been shown to be more efficient than a direct three fold coincidence strategy ("AND" strategy) [105]. For time slides, when shifting the events of the second detector with some permutation π, we choose to shift the events of the third detector by the same amount but in the opposite direction with π^{-1}, so that the time delay for any of the detector pairs is different for each time shift. To write compact equations we abbreviate $X = \mathbb{1}(x_k < p)$, $Y = \mathbb{1}(y_{\pi(k)} < q)$, $Z = \mathbb{1}(z_{\pi^{-1}(k)} < r)$, $\mathrm{d}V = \mathrm{d}x_1 \cdots \mathrm{d}x_N \mathrm{d}y_1 \cdots \mathrm{d}y_N \mathrm{d}z_1 \cdots \mathrm{d}z_N$, where $r = \alpha_3 \Delta t$ is the event probability per bin of the third detector and the vector $\boldsymbol{z}$ describes its realizations. Thus, the mean number of coincidences in the framework described in section 6.1.2 becomes

$$\text{Mean} = \int \cdots \int \frac{1}{R} \sum_{\pi} \sum_{k} [XY + YZ + XZ - 2XYZ] \, \mathrm{d}V \tag{6.13a}$$

$$= N \left[pq + pr + qr - 2pqr \right]. \tag{6.13b}$$

Computation of the variance

The second moment can be written compactly as

$$\begin{aligned}\mathrm{M}_2 = &\int\cdots\int \frac{1}{R^2}\sum_{\pi_1}\sum_{\pi_2}\sum_{k}\sum_{l}\\ &\big[XYX'Y' + XZX'Z' + YZY'Z' + 4XYZX'Y'Z' + 2XYX'Z' + 2XYY'Z'\\ &\quad +2XZY'Z' - 4XYX'Y'Z' - 4XZX'Y'Z' - 4YZX'Y'Z'\big]\,\mathrm{d}V, \quad (6.14)\end{aligned}$$

where the $'$ denotes whether the hidden variables are π_1, k or π_2, l.

The computation of this integral, detailed in appendix A.2, yields

$$\begin{aligned}\mathrm{M}_2 = \frac{N}{R}\Big\{&(pq+pr+qr-2pqr)\\ &+(R-1)\left[pq(p+q+pq)+pr(p+r+pr)+qr(q+r+qr)+6pqr\right.\\ &\left.-4pqr(p+q+r)\right]+\left[(R-1)(N-3)+(N-1)\right](pq+pr+qr-2pqr)^2\Big\},\end{aligned} \quad (6.15)$$

and can be approximated in the limit $p, q, r, \frac{1}{R} \ll 1$ by

$$\mathrm{Var} \simeq N(pq+pr+qr)\left(\frac{1}{R}+p+q+r+\frac{3pqr}{pq+pr+qr}\right). \quad (6.16)$$

Interpretation

Similarly to section 6.1.2 the extra terms in equation (6.16) can be explained through the error in the estimation of the single detector event rate. Using the same notations as in section 6.1.2 the mean coincidence number is

$$\begin{aligned}\mathrm{Mean} &= N\left(\hat{p}\hat{q}+\hat{p}\hat{r}+\hat{q}\hat{r}\right) &(6.17a)\\ &\simeq N\left[pq+pr+qr+(q+r)\delta p+(p+r)\delta q+(p+q)\delta r\right]. &(6.17b)\end{aligned}$$

Using the independence of single detector estimation errors and recalling that $\langle\delta p^2\rangle = \frac{p}{N}$ we obtain the variance of this mean value

$$\begin{aligned}\mathrm{Var} &= N^2\left[\langle\delta p^2\rangle(q+r)^2+\langle\delta q^2\rangle(p+r)^2+\langle\delta r^2\rangle(p+q)^2\right]\\ &= N\left[(pq+pr+qr)(p+q+r)+3pqr\right], \quad (6.18)\end{aligned}$$

that corresponds to the extra terms in equation (6.16).

After converting to the estimation of the false alarm rate we obtain

$$\mathrm{Mean}\,\widehat{\mathrm{FA}} \simeq (\alpha_1\alpha_2+\alpha_1\alpha_3+\alpha_2\alpha_3)\Delta t, \quad (6.19)$$

$$\begin{aligned}\mathrm{Var}\,\widehat{\mathrm{FA}} \simeq &(\alpha_1\alpha_2+\alpha_1\alpha_3+\alpha_2\alpha_3)\frac{\Delta t}{T}\\ &\left(\frac{1}{R}+\alpha_1\Delta t+\alpha_2\Delta t+\alpha_3\Delta t+\frac{3\alpha_1\alpha_2\alpha_3}{\alpha_1\alpha_2+\alpha_1\alpha_3+\alpha_2\alpha_3}\Delta t\right). \quad (6.20)\end{aligned}$$

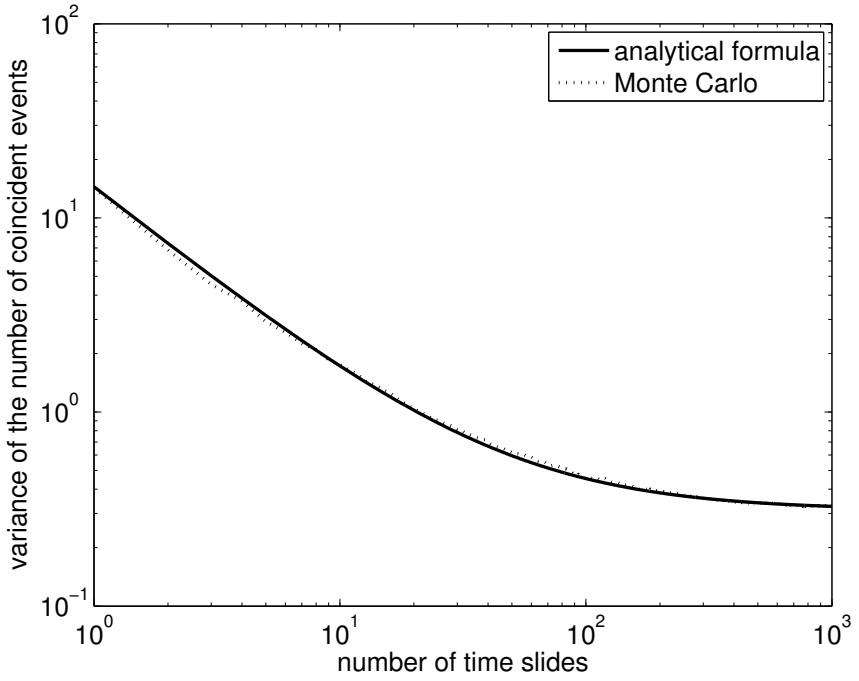

Figure 6.2: The solid line is the analytical formula (6.16) of the coincident event number variance and the dotted line is the Monte Carlo variance as a function of the number of time slides. The Monte Carlo has been performed with $\alpha_1 = 0.04\,\mathrm{Hz}$, $\alpha_2 = 0.08\,\mathrm{Hz}$, $\alpha_3 = 0.16\,\mathrm{Hz}$, $\tau_c = 31\,\mathrm{ms}$, 500 trials and a $T = 10^4\,\mathrm{s}$ data stream length.

To check the 3 detector results we performed a Monte Carlo similar to the one for the 2 detector case (see section 6.1.2). The only difference is the number of detectors, and we have chosen a different coincidence window[2] $\tau_c = 31\,\mathrm{ms}$. To check that the assumption of equal and opposite time slides has no impact on the result, the data in the second detector are shifted by $\mathcal{T}_k$ and in the third detector by $3\mathcal{T}_k$ in the Monte Carlo simulation. Figure 6.2 shows that the Monte Carlo and the 3 detector "OR" formula (6.16) agree really well.

The case of D detectors

For the sake of completeness, we generalize the interpretation done in section 6.1.2 to the case of D detectors in the "AND" configuration. This generalization of equation (6.9) to D detectors yields a variance on the number of

[2]This accounts for the largest light travel time in the LIGO-Virgo network (27 ms) and some timing error in each detector.

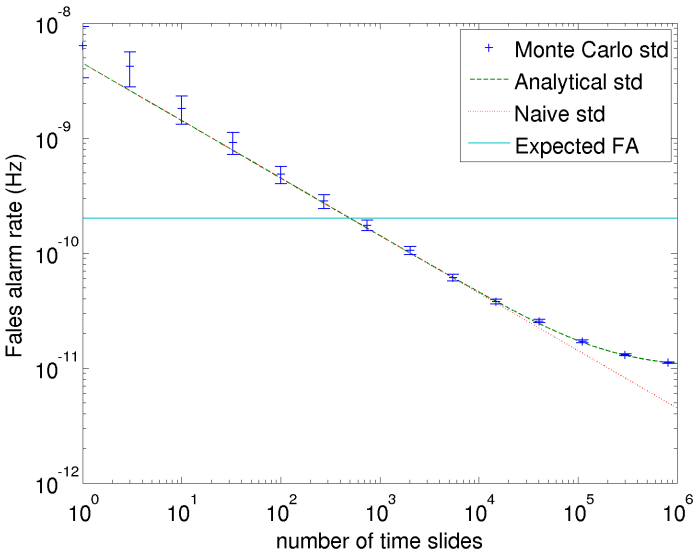

Figure 6.3: The plus markers are the standard deviations of the time slide estimator $\widehat{\mathrm{FA}}$ taken from a Monte Carlo simulation, the dashed green line is the standard deviation coming from the exact theoretical formula (6.11), the dotted red line is coming from the naive formula (6.12), and the solid cyan line is the expected false alarm rate. The parameters used are: $\alpha_1 = 2 \times 10^{-4}\,\mathrm{Hz}$, $\alpha_2 = 5 \times 10^{-5}\,\mathrm{Hz}$, $\Delta t = 20\,\mathrm{ms}$, and a $T = 10^7\,\mathrm{s}$. 500 trials are used for the Monte Carlo simulations, and the corresponding Poisson counting error bars on the standard deviation are shown. The large deviation of the Monte Carlo simulations at low R is due to the limited number of trials, as the number of events seen in 500 trials for ~ 10 time slides is close to 1.

coincidences

$$\mathrm{Var} \simeq N \prod_{i=1}^{D} p_i \left(\frac{1}{R} + \sum_{i=1}^{D} \prod_{j \neq i} p_j \right), \tag{6.21}$$

where p_i is the probability for detector i to have an event in a given time bin.

The interpretation can also be generalized in the "OR" case, that is requiring coincidence between any pair of detectors, although the computation is more cumbersome as detailed in appendix A.3 and yields

$$\mathrm{Var} \simeq N \left[\left(\sum_{i<j} p_i p_j \right) \left(\frac{1}{R} + \sum_{i=1}^{D} p_i \right) + \frac{1}{2} \sum_{i \neq j,\, j \neq k,\, k \neq i} p_i p_j p_k \right]. \tag{6.22}$$

6.1.4 Discussion

We finally discuss the consequences of the above results on gravitational wave data analysis. As an example, we choose a fiducial data run with the

following properties:

- a duration of $T = 10^7$ s, that is roughly 4 months
- two detectors with a light travel time separation of 10 ms, and we use the same time as the coincidence window[3], so that $\Delta t = 20$ ms, assuming perfect timing accuracy of trigger generators.
- a desired coincidence false alarm rate of 2×10^{-10} Hz, i.e. a 2×10^{-3} background probability which corresponds to a "3-sigma" detection threshold.

Note that the desired coincidence false alarm rate is several orders of magnitude smaller that the one is the tests shown on figures 6.1 and 6.2. The parameters for these previous tests were chosen to show the saturation effect with a small number of time slide and not as representative of a realistic scenario.

For illustration we consider two special cases of single detector thresholds choices. One realistic case, where thresholds are set so that the single detector trigger rate in each detector is roughly the same. One extremely asymmetric case, where in one of the detectors there is only one trigger. This extreme case is instructive as it shows clearly the limits of the time slide background estimation method.

Realistic case In this case we assume comparable but different trigger rates in each detector with $\alpha_1 = 2\times10^{-4}$ Hz and $\alpha_2 = 5\times10^{-5}$ Hz, which yields correctly the desired coincidence rate $\alpha = \alpha_1\alpha_2\Delta t = 2\times10^{-10}$ Hz. Using equation (6.11) the fractional error of the false alarm estimation is

$$\begin{aligned} \frac{\sigma_\alpha}{\alpha} &\simeq 22.4\left(\frac{1}{R} + 5\times10^{-6}\right)^{\frac{1}{2}} && p = 4\times10^{-6},\ q = 10^{-6} \\ &\simeq 0.71 && \text{for } R = 1000 \\ &\simeq 0.05 && \text{for } R \to \infty. \end{aligned}$$

The 22.4 factor comes from the desired detection confidence threshold as $22.4 \simeq 1/\sqrt{2\times10^{-3}}$. For 1000 time slides we get a typical error of 70% in the false alarm estimation, and the error saturates at 5% for $R \gtrsim 2\times10^5$. For illustration, the dependence of σ_α on R is shown on figure 6.3. In this particular fiducial case, the Poisson fluctuations do not impede the background estimation, as with $\sim 10^4$ time slides a reliable estimate of the expected false alarm can be obtained.

Extreme case In this extreme case the single detector trigger rates are $\alpha_1 = \frac{1}{T} = 10^{-7}$ Hz and $\alpha_2 = \frac{\alpha}{\alpha_1\Delta t} = 0.1$ Hz, which gives using equation

[3] As noted in section 6.1.1, coincident triggers are defined as less that $\pm\frac{1}{2}\Delta t$ apart.

(6.11) the fractional error of the false alarm estimation

$$\begin{aligned} \frac{\sigma_\alpha}{\alpha} &\simeq 22.4\left(\frac{1}{R} + 2\times 10^{-3}\right)^{\frac{1}{2}} && p = 2\times 10^{-9},\ q = 2\times 10^{-3} \\ &\simeq 1.2 && \text{for } R = 1000 \\ &\simeq 1 && \text{for } R \to \infty. \end{aligned}$$

So the error saturates at 100%, and this saturation is achieved for $R \gtrsim 500$.

Those two examples show that the maximal number of useful time slides and the false alarm estimation precision strongly depends on the relative properties of the two detectors. In particular when there is much more triggers in one detector than in the other, the background can be badly estimated and increasing the number of time slides will not help.

One subtlety to consider is that background estimation can actually correspond to two slightly different questions. The first question is how many background coincidences will be recorded if the instrument continued to collect for a very long time. That is what is the coincidence rate we obtain in the limit of infinite number of independent realizations of detectors data containing only noise and no signal. The results obtained in this section pertain to this question.

The other question is how the observed coincidences in the zero lag are consistent with the data in each detector assuming that there is only noise in the detectors. That is how exceptional are the zero lag coincidences compared to time shifted (or random) coincidences of the same data. The main difference compared to the previous question is that the data are not independent between the measured background estimate and the statistical significance of the zero lag.

All-sky searches [99, 100, 101, 98, 102] analyze all the available data without distinction, and use the same data to perform the background estimation. The time slide method of background estimation is answering the second question. In that case the saturation discussed above is not relevant, because the errors on the estimate of the single detector event rate discussed in section 6.1.2 are biasing in the same way the event number of the time shifted and of the zero lag coincidence, and the final background estimation is not affected. A Monte Carlo confirmation of this is shown in appendix A.4. The price to pay is that if the presence of gravitational waves is significantly affecting the single detectors trigger rate (above some threshold) the estimated background coincidence rate is elevated, as the single detector triggers composing the gravitational wave events cannot be *a priori* labeled as a gravitational waves.

However, for the case of gravitational wave searches triggered by external observations, such as gamma-ray bursts, only a small amount of data around

the external trigger time (called the *on-source* region) is used for the purpose of finding gravitational waves. The data further away from the external trigger time (called the *off-source* region) can be use for background estimation and are statistically independent. The drawback is that the saturation term discussed above are affecting the background estimation, but the gain is that the presence of gravitational waves is much less likely in the off-source than in the on-source region, and the estimated background is not elevated by the presence of a gravitational wave in the on-source region. In this on-source/off-source scheme the time slide method of background estimation is answering the first question.

6.2 Rate fluctuations limitation

In the previous section we have modeled the trigger time distribution for each gravitational wave detector as a stationary Poisson process. However, the trigger rate produced by each detector is usually not constant in time, for instance it depends on weather conditions [106]. In this section we will study how this non stationary rate of triggers affects the background estimation errors.

Intuitively, non stationary data can become problematic for the time slide method whenever the time step of the slide is equal or larger than the rate fluctuation time scale T_{F}.

For example, if there are two storms that happen at two separate detector sites at the same time, they will produce an elevated rate of triggers at both detectors that will increase the coincidence rate. This increased coincidence rate scales as the product of the trigger rate increase factors at each detector. However, if we use a time slide with a step longer than the storms duration, the increased coincidence rate will only scale as the sum of the trigger rate increase factors at each detector. This case would yield an underestimation of the background coincidence rate. Obviously the opposite scenario is possible, where two storms that do not happen at the same time are brought together by the time slides, which results in an overestimation of the background coincidence rate.

This kind of effect is in practice alleviated by using time slides that are limited in time, usually shorter than 1 hour. However, each time slide step has to be different from the others by the filters (trigger generator) auto-correlation lengths which is usually of the order of 1 second. Thus for two detectors the maximal number of time slides shorter than 1 hour is limited to a few thousands. This is the main motivation for breaking the non stationarity barrier and using longer time steps.

In the following sections we will present a systematic method of quantifying the background estimation error introduced by this kind of phenomena when random time slides are used. That is time slides that are on a circu-

lar ring and have time steps distributed uniformly in the $[0, T]$ range. For simplicity, we will discuss this issue in the 2 detector case only.

6.2.1 Measure of rate fluctuations

As a measure of a detector trigger rate fluctuation we look at the variance of the binned trigger rate. We divide the data into P bins of length $\Delta T = T/P$, where T is the duration of the run. By computing the standard deviation of the measured trigger rate in each time bin, we obtain a parameter $a_1(P)$ characterizing the amplitude of the rate fluctuations with time scale ΔT

$$\mathrm{FA}_1 = \mathrm{Mean}_{i\in[\![1,\,P]\!]}\mathrm{FA}_1^i, \tag{6.23}$$

$$a_1(P) = \mathrm{Std}_{i\in[\![1,\,P]\!]}\mathrm{FA}_1^i/\mathrm{FA}_1. \tag{6.24}$$

Where FA_1^i is the rate measured[4] in time bin i.

The effects of the Poisson distribution of triggers on the background estimation error have already been discussed in section 6.1. We will study here only the additional errors due to non stationary data, therefore we will use the mean coincidence rate equation $\alpha = \alpha_1\alpha_2\Delta t$.

For a given set of R time slides $\{\mathcal{T}_k\}$ the background estimation error is

$$\alpha_{\mathrm{Err}} = \alpha(0) - \frac{1}{R}\sum_k \alpha(\mathcal{T}_k) \tag{6.25}$$

$$\simeq \frac{1}{P}\sum_{i=1}^{P}\alpha_1^i\alpha_2^i\Delta t - \frac{1}{RP}\sum_{i=1}^{P}\sum_k \alpha_1^i\alpha_2^{\pi_k(i)}\Delta t, \tag{6.26}$$

where we have approximated each time slide T_k with the nearest circular permutation of time bins π_k. In this equation the α_1^i are local trigger rates, and we treat them as equally distributed random variables with the first two moments measured from real data using (6.23) and (6.24) (we treat α_2^i analogously).

Under those assumptions the mean of α_{Err} is null and a detailed computation described in appendix A.5 yields the standard deviation

$$\frac{\mathrm{Std}(\alpha_{\mathrm{Err}})}{\alpha_1\alpha_2\Delta t} = \left[\frac{1}{P}\left(1+\frac{1}{R}\right)a_1^2(P)a_2^2(P)\right]^{\frac{1}{2}}. \tag{6.27}$$

To obtain an estimator of the background estimation error, we maximize (6.27) over all time scales ΔT, which is equivalent to maximizing over P and yields

$$\frac{\mathrm{Std}(\alpha_{\mathrm{Err}})}{\alpha_1\alpha_2\Delta t} = \max_P\left[\frac{1}{P}\left(1+\frac{1}{R}\right)a_1^2(P)a_2^2(P)\right]^{\frac{1}{2}}. \tag{6.28}$$

[4] number of triggers in time bin i divided by ΔT

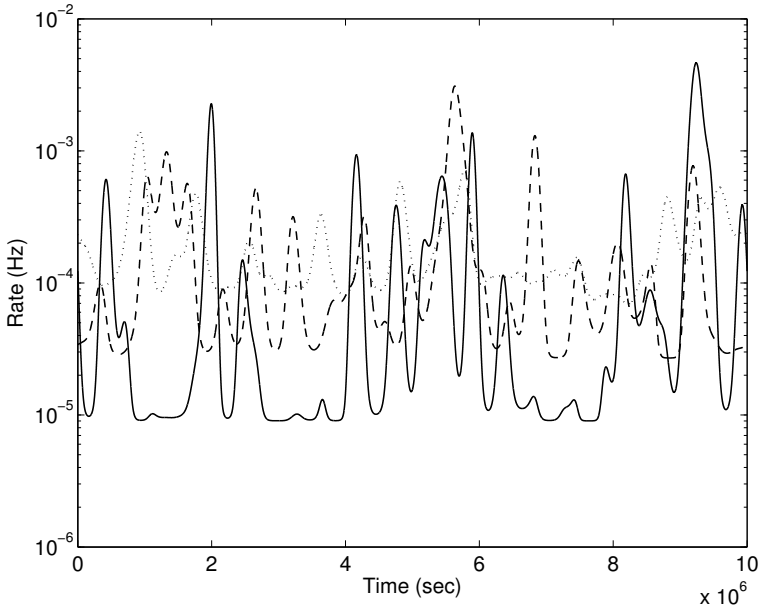

Figure 6.4: Shown are the generated rate fluctuations with time scale $T_{\mathrm{F}} = 10^5$ sec and three amplitude factors: $A = 1$ for the dotted line, $A = 2$ for the dashed line, and $A = 3$ for the solid line. In all three cases the mean rate is 2×10^{-4} Hz.

6.2.2 Rate fluctuations model

In order to compare the analytical results of section 6.2.1 with simulations, one needs to generate a non-homogeneous Poisson process. It does not need to be an accurate model of real detectors, but only to have some cursory resemblance.

In order to generate rate fluctuations with time scales larger than some given T_{F} we proceed as follows

- Generate a white Gaussian noise
- Low pass filter the Gaussian noise with a frequency cut at $1/T_{\mathrm{F}}$
- Normalize the resulting process to unit variance
- Pass it through a non linear memory-less filter $x \to 1 + \exp(Ax)$, where A is a parameter that characterizes the amplitude of the fluctuations
- Normalize the resulting process to the desired mean rate

Examples of the resulting rate fluctuations for several amplitude factors are shown on figure 6.4.

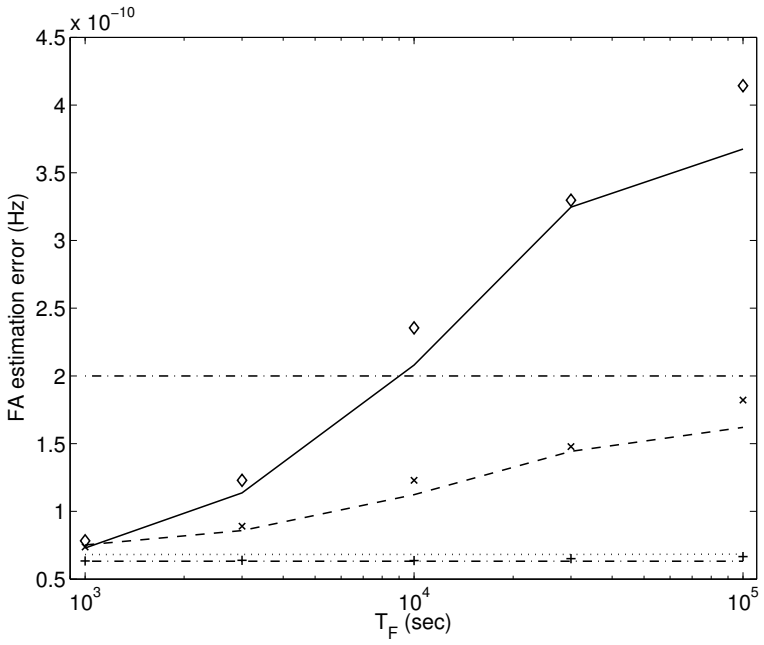

Figure 6.5: The dotted, dashed and solid lines are the theoretical predictions of the standard deviation (6.30) for respectively $A = 1$, $A = 2$, and $A = 3$ as a function of the rate fluctuation time scale T_{F}. The plus, cross and diamond markers denote the Monte Carlo standard deviation (6.29) for respectively $A = 1$, $A = 2$, and $A = 3$. The upper dot-dashed line is the desired false alarm rate $\alpha = 2 \times 10^{-10}\,\mathrm{Hz}$, and the lower dot-dashed line is the contribution of Poisson error (6.11) only for $R = 10^4$ time slides. The parameters used are: $\alpha_1 = 2 \times 10^{-4}\,\mathrm{Hz}$, $\alpha_2 = 5 \times 10^{-5}\,\mathrm{Hz}$, $\Delta t = 20\,\mathrm{ms}$, and a $T = 10^7\,\mathrm{s}$. The maximization over P is done on a discrete grid from 20 to 10000 with logarithmic steps. 1000 trials are used for the Monte Carlo simulations.

6.2.3 Monte Carlo verification

In order to verify how accurate are the predictions of (6.28), we perform a Monte Carlo simulation and compare predicted and measured standard deviation. For the comparison to be as close as possible to the real case scenario, we generate rate fluctuations as described in section 6.2.2, and then use this local rate to generate triggers.

We look at two sets of time slides: time slides with random time steps $\{\mathcal{T}_k\}$, and a set of closely spaced linear steps $\{\mathcal{S}_k\}$. The second set is used as a reference background estimation which is not affected by trigger rate fluctuations, given that its longest time step is smaller than the time scale of trigger rate fluctuations. Finally, the standard deviation of the difference

between the two rate measures

$$\mathrm{FA}_{\mathrm{Err}} = \frac{1}{R}\sum_k \mathrm{FA}(\mathcal{S}_k) - \frac{1}{R}\sum_k \mathrm{FA}(\mathcal{T}_k), \tag{6.29}$$

is compared to the predicted standard deviation, which is the quadratic sum of the Poisson (6.11) and non stationary rate (6.28) errors

$$\mathrm{Std}_{\mathrm{Th}}(\mathrm{FA}_{\mathrm{Err}}) = \left[\mathrm{Std}(\alpha_{\mathrm{Err}})^2 + 2\,\mathrm{Std}(\widehat{\mathrm{FA}})^2\right]^{\frac{1}{2}}, \tag{6.30}$$

as the Poisson error plays a role both for the $\{\mathcal{S}_k\}$ and $\{\mathcal{T}_k\}$ time slides.

On figure 6.5 are shown the results of the comparison of the theoretical and Monte Carlo standard deviations. The theoretical prediction explains well the error observed in the simulation. However, one can notice that the Monte Carlo error is slightly above the theoretical prediction. This shows that the presented method is not able to measure it fully, and is rather a good rule of thumb than a precise prediction. For instance the predicted error decreases with the coarseness of the maximization over P, and the time binning is losing some of the structure of the trigger rate fluctuations.

The parameters used correspond to a realistic scenario and are the same as on figure 6.3. The set of linear time slides $\{\mathcal{S}_k\} = \{k \times 0.1\,\mathrm{sec}\}_{k\in[\![1,10^4]\!]}$ has a time step of only 100 ms which would not be used in a real analysis, but is allowed here because the simulated triggers have a delta auto-correlation and time steps are limited only by the $\Delta t = 20$ ms time coincidence window.

One can see that for moderately non stationary data ($A = 1$), the associated error is buried in the Poisson error. However, for larger amplitude factors the associated error becomes greater than the measured rate, which renders the background estimation useless. When $T_{\mathrm{F}}\alpha_i \ll 1$, the trigger rate fluctuations are averaged out by Poisson counting, this explains why the estimation error is increasing with T_{F}.

6.3 Case of triggered gravitational wave search

The toy analysis used to derive the results above is not an accurate description of a real gravitational wave data analysis, but it is still able to yield some order of magnitude conclusion, for instance for the search in association with gamma-ray bursts described in chapter 7.

In that case a period of $T_{\mathrm{on}} \sim 600\,\mathrm{s}$ is analyzed and $T_{\mathrm{off}} \sim 10^4\,\mathrm{sec}$ of data around that period is used for background estimation. We will assume that the 3 hours are short enough that rate fluctuations do not play an important role. Hence only the Poisson limitation is relevant in that case, and the saturation terms play a role as different data are used for background estimation and for gravitational wave detection.

The analysis used is coherent and not coincident, hence the results derived here cannot be applied directly, however as a worst case scenario we

can verify the effects for the extremely asymmetric case of the discussed toy analysis. Given that the sky position is known for this analysis the effective time coincidence window in the coherent analysis is rather tight[5] and we will assume $\Delta t = 10^{-3}$ s here. As a reference we use the false alarm threshold for a "3-sigma" detection that is $\alpha \simeq 2\times10^{-3}/T_{\rm on} \simeq 3\times10^{-6}$ Hz, and in the extreme case the single detector rates are $\alpha_1 = 1/T_{\rm on}$ and $\alpha_2 = \alpha/(\alpha_1\Delta t) \simeq 2$ Hz. Using equation (6.11) we obtain[6] the fractional error on the false alarm estimation

$$\begin{aligned}
\frac{\sigma_\alpha}{\alpha} &\simeq 5.5\left(\frac{1}{R} + 2\times10^{-3}\right)^{\frac{1}{2}} && p \simeq 1.7\times10^{-5},\ q = 2\times10^{-3}\\
&\simeq 0.3 && \text{for } R = 1000\\
&\simeq 0.25 && \text{for } R \to \infty.
\end{aligned}$$

Hence 1000 time slides of the background estimation region of duration $T_{\rm off}$ are sufficient to obtain a reasonable estimate of the background in the on-source region even in the extremely asymmetric scenario. One should remember that this case is not representative of actual coherent searches as loud single detector events are well removed by coherent consistency tests. Compared to the previous discussions of the extremely asymmetric case in section 6.1.4 the Poisson limitation is not as important, the reason is that here the time length $T_{\rm off}$ of data used in the background estimation is much larger than the detection period $T_{\rm on}$ and not equal as it was the case previously.

[5] see the time tolerance discussed in section 7.2.2

[6] Note that here $T = T_{\rm off}$.

Chapter 7

GRB analysis for S6/VSR2-3

In this chapter we present the methods and main results of the search for gravitational waves in LIGO and Virgo data in association with GRBs reported by the Gamma-ray bursts Coordinates Network [69] in 2009-2010. This analysis follows the scheme established with earlier data from LIGO and Virgo. The first searches considered single GRBs [107, 108], then gravitational wave detectors engaged in long science runs and the searches considered large samples of GRBs [109, 85, 110]. In particular the analysis described here represents an incremental improvement of the search for gravitational wave bursts in the 2005-2007 LIGO and Virgo data [85].

Beside the availability of new data (which also inevitably leads to new problems related to them) the main challenges of this analysis compared to the previous one are:

- Large sky location errors of GRBs detected by the GBM detector on the Fermi spacecraft which was launched in 2008. This was not an issue in the 2005-2007 analysis where most GRBs were well localized by Swift. In 2009-2010 roughly half of the GRB sky locations were provided by each spacecraft.
- A more predominant role of Virgo in the gravitational wave detector network. The LIGO detectors are roughly aligned but Virgo has completely different antenna patterns functions. This required designing new coherent glitch rejection tests.
- More informed GRB astrophysics inputs resulted in a change in the analyzed parameter space (time window, frequency range, gravitational wave polarization assumption).

7.1 Data set

In the years 2009-2010, data were taken for the sixth LIGO science run (S6) and for the second and third Virgo science runs (VSR2 and VSR3). During

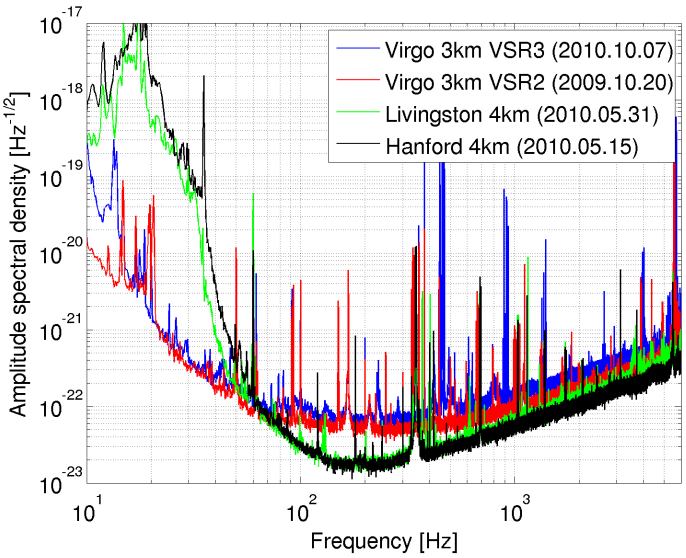

Figure 7.1: Noise amplitude spectral density for "good days" in LIGO and Virgo detectors in 2009-2010. For Virgo both a good spectrum during VSR2 and during VSR3 are shown.

that period the LIGO laboratory operated two 4 km detectors: H1 at the Hanford observatory in the state of Washington, USA and L1 at the Livingston observatory in the state of Louisiana, USA; the Virgo collaboration operated the Virgo detector (V1) in Cascina, Italy. The light time of flight between the H1-L1, H1-V1 and L1-V1 pairs are respectively 10 ms, 27 ms and 26 ms.

The joint LIGO-Virgo run was held from 2009 July 7 to 2010 October 20. For Virgo VSR2 started on 2009 July 7 and ended on 2010 January 8 to allow an upgrade. The Fabry-Perot cavity mirrors suspension was changed from steel wires to fused silica fibers. In the process a lower reflectivity for the cavity input mirror was chosen, which modified the shape of the noise spectrum in the shot noise dominated region at high frequency as can be seen on figure 7.1. Virgo data taking resumed with VSR3 on 2010 August 11 and ended on 2010 October 20. For LIGO the S6 run was split into four periods: S6A from 2009 July 7 to 2009 September 1, S6B from 2009 September 26 to 2010 January 12, S6C from 2010 January 16 to 2010 June 26 and finally S6D from 2010 June 26 to 2010 October 20. During the break between S6A and S6B some seismic isolation of auxiliary mirrors was added and read-out photo-diodes were changed, the break between S6B and S6C was dedicated to glitch hunting, and finally the boundary between S6C and S6D was purely administrative.

The sensitivity of the different detectors evolved during the different pe-

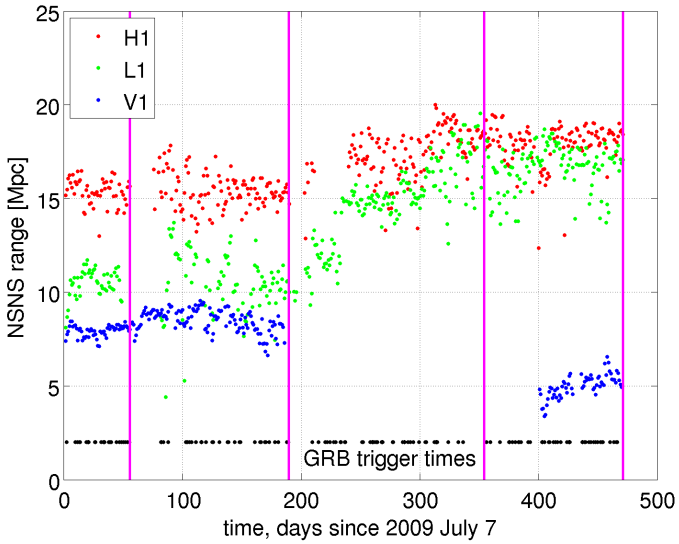

Figure 7.2: Time evolution of the inspiral range for H1, L1 and V1 during the joint 2009-2010 run. Each dot represents the average inspiral range in a given day, considering only science data after CAT1 flagged times are removed (see end of this section for definitions of data quality flags). The red, green and blue dots are respectively the inspiral ranges for H1, L1 and V1. The black dots mark the time of the analyzed GRBs listed in table B.1, and the magenta vertical lines mark the end of the four LIGO science run periods: S6A, S6B, S6C and S6D.

riods of the run. A standard figure of merit of the sensitivity is the *inspiral range* which is the distance at which a $1.4\,M_\odot$ neutron stars binary inspiral yields an SNR = 8, where the SNR is marginalized uniformly over sky position and inclination of the binary. Given that the magnitude of the spectrum of an inspiral signal is decreasing with frequency as shown on figure 3.1, this figure of merit is a good integrated measure of the sensitivity of a detector in the few dozens to few hundred hertz frequency range. The time evolution of the inspiral range in 2009-2010 for the three detectors is shown on figure 7.2.

The inspiral range is an integrated measure of noise amplitude spectral density. Hence this figure of merit includes mostly the Gaussian part of the noise and depends weakly on the amount of glitches present in the data. As a figure of merit of the glitches present in the data we use the threshold in reconstructed SNR at which the trigger rate above this threshold is kept constant and equal to 1 per minute. The triggers were produced by the same trigger generation procedure as the GRB search presented here, and is a good representation of the glitches as seen by that analysis. This figure of merit is shown on figure 7.3 for the three detectors along with the value

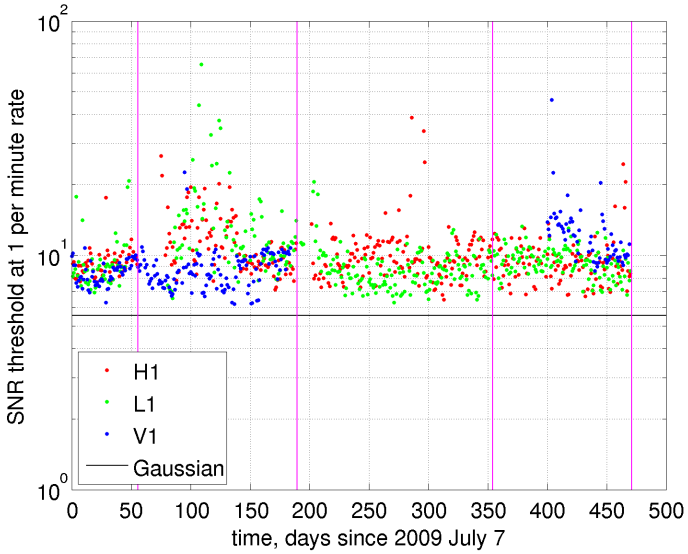

Figure 7.3: Time evolution of the reconstructed SNR threshold for glitches with a false alarm rate of 1 per minute during the joint 2009-2010 run. Each dot represents the SNR at which a gravitational wave signal would have a false alarm rate of 1 per minute in a given detector on a given day. The single detectors triggers are produced using the analysis described in section 7.2 on single detector streams. This analysis is limited to the 64 – 500 Hz frequency band. The times that are marked by either category 1 or 2 data quality flags or during hardware injections are not used in this analysis (see end of this section for definitions of data quality flags). The black solid line shows the corresponding threshold for Gaussian noise. The magenta vertical lines mark the end of the four LIGO science run periods: S6A, S6B, S6C and S6D.

expected for Gaussian noise. The ratio between the measured SNR threshold and the Gaussian expectation shows how much sensitivity at the given false alarm rate is lost due to the presence of glitches. For instance, for the simple toy coincident GRB analysis of data from two interferometers discussed in section 6.3, if we choose SNR thresholds which correspond to a 1 per minute false alarm rate, and use an effective coincidence time window of 1 ms, the coincidence rate is $\simeq 3 \times 10^{-7}$ Hz. This corresponds to a false alarm probability of 2×10^{-4} for the standard GRB analysis time window (4.12), and is sufficiently low to be a reasonable gravitational wave candidate threshold. For such an analysis the SNR thresholds shown on figure 7.3 mean that a little less than a factor 2 in sensitivity is lost due to the presence of glitches in the data for most parts of the run.

For H1 the run started with a typical range of ~ 16 Mpc and increased to ~ 19 Mpc during the transition from S6B to S6C. L1 started with a lower

Interferometer	Amplitude	Phase	Time
H1 S6	20%	10°	20 μs
L1 S6	20%	10°	20 μs
V1 VSR2	5.5%	3°	8 μs
V1 VSR3	7%	3°	8 μs

Table 7.1: Calibration error budget for the LIGO and Virgo detectors in 2009-2010 [11, 111, 112, 113]. Values represent the estimated 1 sigma deviations in the calibration for the amplitude and phase response and also the timing errors. This budget is valid at least in the 40 – 500 Hz frequency range.

range of ~ 12 Mpc, which increased to ~ 15 Mpc at the transition between S6B and S6C, and continued to improve during S6C up to ~ 18 Mpc. From the point of view of glitches, both for the Hanford and Livingston detectors, the S6B period has been plagued with a large amount of glitches compared to the rest of the run.

For Virgo the range during VSR2 improved from ~ 7 Mpc to ~ 9 Mpc with a low rate of glitches during the summer 2009 which then increased as bad weather in the end of Autumn caused lots of micro seismic up-conversion through scattered light [106]. This increased amount of glitches is not visible on figure 7.3 as the seismic up-conversion in Virgo is well vetoed by data quality flags. For VSR3 the range was low at ~ 5 Mpc throughout the run due to bad radius of curvature matching and astigmatism in the newly installed mirrors. The run started with a very large glitch rate, but the situation improved during the first month as different problems with this new configuration were fixed.

The raw photo-diode data are digitized at a sampling rate of 20000 Hz for Virgo and 16384 Hz for LIGO. Science data are collected when an interferometer reaches stable operation condition, which is decided by the operator(s) and scientist(s) present on site. The raw data are calibrated based on the response to continuous injection of sinusoidal lines into coils controlling the test masses and regular periods of dedicated calibration studies [11]. The budget of calibration errors is summarized in table 7.1. Sample strain noise curves are shown on figure 7.1 for periods were each of the interferometer had a good sensitivity.

The science run is broken into shorter time spans by periods of interferometer down time caused for instance by large environmental disturbances, malfunctions or maintenance operations. Moreover, during the periods where an interferometer is in a properly working condition, short periods of bad behavior are marked by data quality flags which are among others based on auxiliary instrumental and environmental channels [114]. These flags are gathered in different categories depending on how serious and well under-

stood the problem is:

Category 1 flags (CAT1) mark periods of obvious problems (data missing, calibration failure, interferometer loosing control, ...) that would severely affect power spectrum estimation, these data should not be used.

Category 2 flags (CAT2) mark periods where large glitches of understood origin are present (overflows, magnetic and laser glitches, strongly coupled scattered light due to large seismic motion, ...), these data are analyzed but triggers from these times should not be considered. Typically these flags remove $\leq 5-10\%$ of the remaining science time.

Category 3 flags (CAT3) mark periods with glitches whose origin and/or coupling is only partially understood or whose effect is limited (nearby trains, signal processing overloads, moderate seismic motion). Triggers from these times should be considered with caution. Typically these flags remove an additional $\leq 10-15\%$ of the remaining science time.

Hardware injections (CAT4) mark periods of gravitational wave signal injections into the interferometers through coils that are controlling the mirrors position. These injections are used among others to test the safety of the different data quality flags, i.e. that the apparent motion of mirrors which would be due to a real gravitational wavedoes not trigger any flag.

7.2 Analysis pipeline description

In this section we will describe in detail the pipeline used to analyze S6 and VSR2-3 data in association with GRBs circulated through GCN. A previous version of this pipeline, called X-Pipeline [96], has been used for the analysis of data in the previous LIGO and Virgo data run [85].

7.2.1 Network selection

The input to the analysis are gravitational wave data and information about the GRB triggers. The calibrated gravitational wave data are read with a sampling frequency of 16384 Hz for LIGO and 4096 Hz for Virgo[1] in blocks of 256 s. These data are low pass filtered with a cut-off at 506 Hz to prevent anti-aliasing and down-sampled to 1024 Hz. Afterwards data are high-passed

[1] In Virgo photo-diode data are digitized at a sampling frequency of 20000 Hz, and calibrated data are produced at the same sampling frequency. However, the calibrated data are also produced at lower sampling frequencies of 16384 Hz and 4096 Hz. We use the lowest sampling frequency available as only the frequency content below 500 Hz is of interest to us.

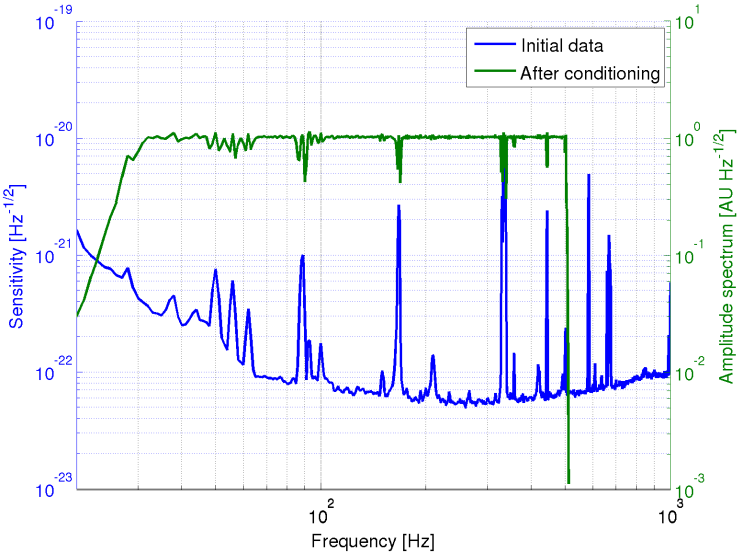

Figure 7.4: Shown is the amplitude spectral density of real Virgo data with a 1 Hz resolution before and after the data conditioning procedure described in the text. The blue line shows the amplitude spectral density of the data collected by the detector. The green line shows the conditioned data with an arbitrary overall rescaling. The high pass filter clearly removes the data fluctuation below 30 Hz and the anti-aliasing filter above 500 Hz. The lack of frequency content above 512 Hz is due to the data down-sampling. The amplitude spectral density in between is flat with the exception of frequency ranges that contained lines, these frequency ranges see their contribution downgraded which is not detrimental to the analysis as the detector does not have a good sensitivity at these frequencies.

filtered above 32 Hz to limit whitening filters transients, frequencies below 32 Hz are anyway not of interest as the sensitivity at low frequencies is very poor. The power spectrum of the filtered data is estimated using the median-mean average of the power in 1 second long FFTs from the whole block of data. The block of data is whitened using this estimate saturated below the high-pass filter cut-off and above the low-pass filter cut-off, and linearly interpolated to obtain the needed 1/256 Hz frequency resolution. The goal of the saturation is to prevent the whitening to remove the effect of the low and high-pass filters. The effect of this whole data conditioning procedure on the data amplitude spectral density is shown on figure 7.4. In order to prevent the filter transients to corrupt gravitational wave event candidates, the first and last 4 seconds of data are discarded from event production. As a result a 256 s block of data covers only its inner 248 s.

In order to analyze a given search time window, called *on-source* window,

the desired time stretch is covered with 256 s blocks, starting 4 s before the start of the time window, overlapped by 8 seconds and ending at least 4 s after the end of the time window. As a result the whole on-source window is covered with contiguous inner parts of blocks.

For each GRB trigger the γ-ray - gravitational wave coincidence window (4.12) discussed in section 4.3.3 is considered. To analyze this time window all detectors which have good quality data available at that time are used to form a gravitational wave detector network. The good quality criteria are:

- Science data present and no CAT1 flags overlapping with the blocks forming the on-source window. Otherwise the whitening procedure for one block will be corrupted, e.g. by the presence of a very loud glitch.
- No CAT2 flags or hardware injections in a tight $[-5, 1]$ s window around the GRB trigger time, where the arrival of gravitational waves is most likely.
- Less than 5% of time removed by CAT2 flags and hardware injections in the on-source window, so that a 95% detection efficiency point is not ruled out by the data quality vetoes. That efficiency point is needed for some parts of the automatic pipeline tuning described in section 7.2.3, and for reasonable 90% confidence level exclusions.

All detectors with good quality data form the network of detectors available for a given GRB, and only GRBs whose network contains at least two detectors are analyzed. There is also an additional requirement which treats the network as a whole:

- If the union of CAT2 flags and hardware injection times from all the detectors in the network exceeds 5%, one detector from the network has to be removed by hand to lower the total flagged time to be less than 5%.

This has happened for only one case in the analyzed GRBs sample, for that case only 2 detectors were forming the network, and that GRB has thus not been analyzed.

Exceptionally, when gravitational wave data are not available in the 10 minutes before the GRB trigger time a reduced time window is used

$$T_{\mathrm{GW}} - T_{\mathrm{GRB}} = [-120, \max(T_{90}, 60)] \text{ s}. \tag{7.1}$$

This window still covers most of the possible gravitational wave and γ-ray emission scenarios. This reduced window is used only if it allows to include an additional detector into the network and this addition improves significantly the sensitivity of the pipeline. This trade-off removes the most extreme time delay scenarios for the important gain in sensitivity, and was used in the analysis of the previous LIGO-Virgo science run [85].

7.2.2 Trigger generation

Following the discussion in chapter 5, we generate time-frequency maps using FFT integration length for all powers of two between 1/128 Hz and 1/4 Hz. This covers the parameter space of signals shorter than a few seconds and with frequencies below 500 Hz, which is the relevant parameter space for GRBs as discussed in section 3.3. Only time-frequency pixels with central frequency above 64 Hz are considered, given the rapidly decreasing sensitivity of LIGO detectors at low frequency (see figure 7.1).

For these time-frequency maps the circular detection statistic equal up to a constant offset to half the statistic (5.53) is computed, a threshold at the 99 percentile value over the map is used to define 8-connected clusters[2], and the circular detection statistic is summed over each cluster. Time-frequency maps of auxiliary statistics are also computed and summed over pixels in each cluster. The auxiliary statistics used are:

- The robust detection statistic described in section 5.8, which includes a non-Gaussian hypothesis in its construction and is robust against loud glitches in a single detector.

- Whenever 3 detectors are available, the coherent and incoherent part of the null energy (5.55). These are used to check that the three data streams are coherently cancelling out following the constraints given by the two independent polarizations of gravitational waves.

- The coherent and incoherent circular null energy (5.57), which are used to check that the data streams are coherently cancelling out following the assumption of circular polarization of gravitational waves.

- The coherent and incoherent parts of the circular energy (5.61), which are used to check that the data streams are coherently adding up if one assumes a circular polarization. Note that this test requires only phase consistency between detectors, and not phase and amplitude consistency as the null energy tests do.

Beside the GRB trigger time and duration used for constructing the on-source window, a GRB observation by a satellite provides sky location information. For detectors with poor spatial resolution, such as the GBM on Fermi, a maximization over the sky location error box $\mathcal{O}$ needs to be performed as discussed in section 5.9. The maximization is performed using a discrete grid, which is designed to cover 95% of the sky location probability

[2] In practice this is quite close to the Bayesian derived optimal threshold for 4-connected clusters of $\sim 2\log 4 \simeq 2.8$ shown in equation (5.40). In both Gaussian noise and typical interferometer data the 99 percentile value of (5.53) is $\simeq 3.2$ and the 98 percentile one is $\simeq 2.8$. More relevantly, for 8-connected clusters and real data the value of $2\log 6.5 \simeq 3.8$ is attained for approximately the 99.5 percentile.

distribution given by the γ-ray detector (see for instance equation (4.8) for the GBM).

As shown by equation (5.88) clusters that are reconstructed in improbable parts of the sky location error box are downgraded by the sky location probability. For simplicity we use a Fisher sky location probability distribution (4.6) with $\sigma = (\sigma_{\rm stat}^2 + \sigma_{\rm sys}^2)^{1/2}$ to compute this penalty factor. The values of σ used for each GRB are given in table B.2 of appendix B. For the GBM $\sigma_{\rm sys} = 7.5^\circ$ is used as it provides a 95% coverage equal to the actual core plus tail systematic error distribution shown on figure 4.3.

If the auxiliary statistic used for coherent consistency tests are computed for a wrong sky location, the inappropriate time delays between detectors will cause real signals to fail the tests. To determine the grid angular spacing needed to avoid this issue a time tolerance of $t_{\rm tol} = 0.5\,$ms is used, in practice the obtained coverage has a lower timing error $\lesssim 0.2\,$ms in most cases, and the timing error is below 0.4 ms over 90% of the error box in the worst case scenario. This is a sufficiently low timing error for signals with frequency below 500 Hz.

As described in section 5.10, among triggers coming from analyzing different sky positions in the grid and different FFT resolutions only the loudest triggers are selected. Moreover for each 256 s block only the loudest 62 triggers[3] are kept to reduce the computing load of managing a large number of uninteresting triggers. This is a zero level threshold on the trigger false alarm rate for further processing.

Once produced, triggers are collected for each block forming the on-source window, and then triggers marked by CAT2 flags or falling outside the on-source window are discarded. Furthermore triggers which fail coherent consistency tests that are based on the auxiliary statistic and described in section 5.7 are also removed, and the remaining triggers are ranked according to the detection statistic. The highest ranked trigger with detection statistic $S_{\rm max}$ is a gravitational wave event candidate for that particular on-source window.

7.2.3 Analysis Tuning

The goal of an analysis pipeline is to separate gravitational wave signals from noise. To optimize a pipeline and estimate its efficiency both samples of data containing only noise (background set) and samples containing signal embedded in noise (injections set) need to be analyzed.

We have discussed in details how to produce samples of detector noise in chapter 6. In particular for this GRB search data from the $\pm 1.5\,$h around the GRB trigger with the exclusion of the on-source time window are used to construct background samples. 824 time slides with steps of 6 s are used

[3] Which correspond to a fixed rate of 0.25 Hz over the inner part of the block.

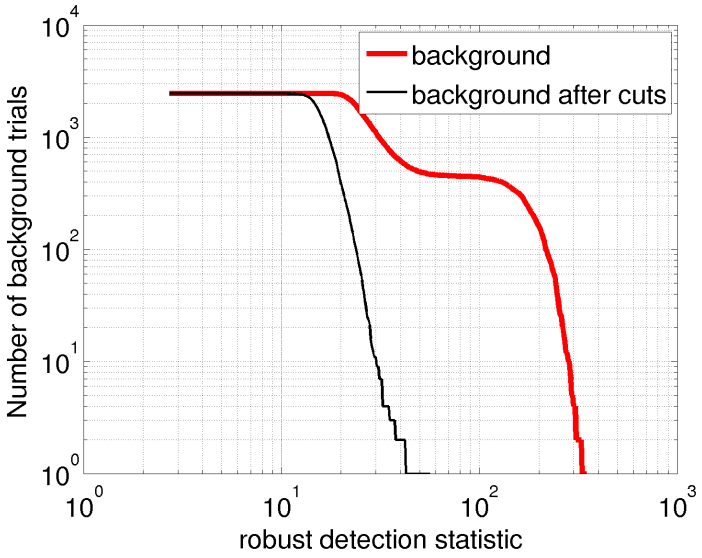

Figure 7.5: Cumulative histogram of the loudest event in terms of the robust detection statistic for a sample of ~ 2500 background trials for the first GRB listed in table B.1 of appendix B. The red line shows the distribution before the coherent consistency cuts are applied and the black line after their application. The cumulative distribution $\mathcal{C}(S_{\max})$ corresponds to the latter but normalized to start at 1 instead of the number of trials.

and the same data quality criteria as for the on-source window are applied to discard bad quality background samples. These background data samples are processed in exactly the same way as the on-source data, which yields a cumulative distribution $\mathcal{C}(S_{\max})$ of the loudest event detection statistic. An example is shown on figure 7.5.

Gravitational wave injections

In order to produce samples of data with gravitational wave signal, waveforms with different parameters are added in software to the on-source data and the same trigger production and processing is applied to these samples[4]. The waveforms used are chosen to cover the analyzed waveform parameter space and to be representative of our expectations for compact binary coalescence and stellar collapse models. One should note that performing the injections into the on-source data has the drawback of being biased by the

[4]One caveat is that for data with injections time-frequency maps and clusters are produced only for the 16 s around the injection time in order to reduce the computational load. However the data conditioning and whitening is still performed on the whole 256 s block of data, and this optimization does not yield any significant changes in the recovered triggers.

possible presence of a gravitational wave candidate in the data. However this affects the efficiency at a given injection amplitude by at most a few percents.

For the stellar collapse model of long GRBs we have seen in section 3.3.3 that no precise waveform is known. However the most likely scenario of extra-galactically visible signal is produced by a slowly evolving rotating quadrupolar mass distribution, which given the GRB observation has a rotation axis inclination $\lesssim 5^\circ$ with respect to the observer (see section 4.4). Hence as a crude but simple waveform model we use elliptical sine-Gaussian waveforms

$$\begin{pmatrix} h_+(t+t_0) \\ h_\times(t+t_0) \end{pmatrix} = A_0 \begin{pmatrix} \cos(2\pi f_0 t)(1+\cos^2\iota) \\ \sin(2\pi f_0 t) 2\cos\iota \end{pmatrix} \exp\left(-\frac{(2\pi f_0 t)^2}{2Q^2}\right), \tag{7.2}$$

with $Q = 9$ and construct three sets of waveforms with central frequencies f_0: 100, 150 and 300 Hz. For each set the peak time t_0 is distributed uniformly inside the on-source window, the inclination angle ι is distributed uniformly in $\cos(\iota)$ between 0° and 5°, and the amplitude factor A_0 is chosen such that $h_{\mathrm{rss}} = 2.5 \times 10^{-21}\,\mathrm{Hz}^{-1/2}$ for $\iota = 0$. We will refer to these three families by CSG100, CSG150 and CSG300, where "CSG" stands for circular sine-Gaussian as the limitation on ι makes the waveform polarization nearly circular. An example of the gravitational wave time series for a CSG100 waveform is shown on figure 7.6.

For the compact binary coalescence model of short GRBs good waveform models are available as discussed in section 3.3.2. We use non-spinning second order restricted post-Newtonian inspiral waveforms (3.12) with frequency evolution (3.20). Two waveform sets are constructed to represent the double neutron star (NSNS) coalescence and the neutron star - black hole (NSBH) coalescence scenarios.

NSNS For this set a nominal distance r of 10 Mpc is used. For both neutron stars the mass follows a Gaussian distribution with a $1.4\,\mathrm{M}_\odot$ mean and $0.2\,\mathrm{M}_\odot$ standard deviation, also a lower bound of $0.9\,\mathrm{M}_\odot$ and an upper bound of $3\,\mathrm{M}_\odot$ is applied to this distribution [115].

NSBH For this set a nominal distance r of 20 Mpc is used. Both the black hole and neutron star mass follow Gaussian distributions with respectively $10 \pm 6\,\mathrm{M}_\odot$ and $1.4 \pm 0.4\,\mathrm{M}_\odot$, and respectively limited to a mass range $[2, 25]\,\mathrm{M}_\odot$ and $[0.9, 3]\,\mathrm{M}_\odot$. The wider distribution of the neutron star mass is motivated by the lack of observation of NSBH binaries and the wider mass distribution found in binary population synthesis simulations [116].

For both sets the inclination angle is uniformly distributed in $\cos(\iota)$ between 0° and 30°, which is representative of the measured jet opening angles for short GRBs. The binary coalescence time t_0 is distributed uniformly in the

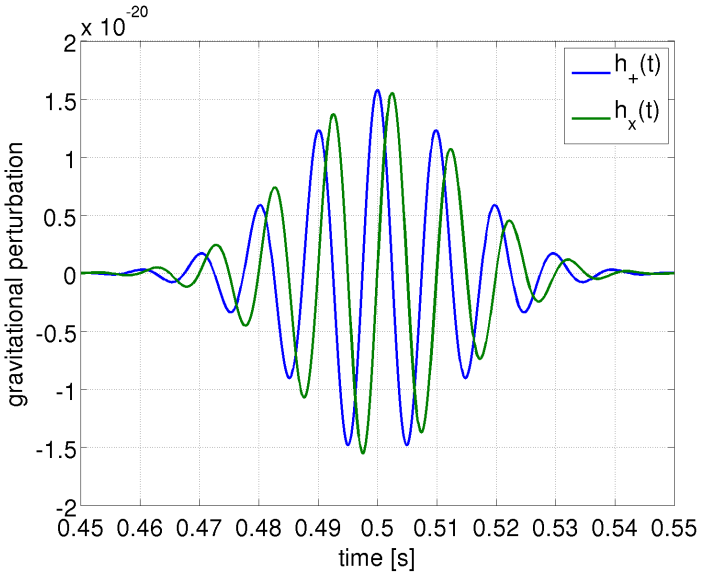

Figure 7.6: Example of circular sine-Gaussian gravitational waveform. The $h_+(t)$ and $h_\times(t)$ time series are shown for a central frequency $f_0 = 100\,\mathrm{Hz}$, a peak time $t_0 = 0.5\,\mathrm{s}$, a quality factor $Q = 9$, an inclination angle $\iota = 0$, and the amplitude A_0 chosen to yield $h_{\mathrm{rss}} = 2.5 \times 10^{-21}\,\mathrm{Hz}^{-1/2}$.

on-source window. An example of the gravitational wave time series for a NSBH waveform is shown on figure 7.7.

For both the inspiral and elliptical sine-Gaussian rotator model the h_{rss} (amplitude) at the observer location is dependent on the inclination of the system with respect to the observer. The gravitational wave emission energy flux dependence for a rotator emission pattern is

$$F(\iota) = \frac{h_{\mathrm{rss}}(\iota)^2}{h_{\mathrm{rss}}(0)^2} = \frac{(2\cos\iota)^2 + (1+\cos^2\iota)^2}{8}, \tag{7.3}$$

which we normalized to the optimal face-on orientation. Hence relative to the optimal orientation the h_{rss} available to the observer for an inclined system is rescaled by the $F^{1/2}(\iota)$ factor which is shown on figure 7.8. If one compares a face-on and an edge-on system the received gravitational wave amplitude is a factor ~ 3 larger for the face-on system if all other aspects of the systems are the same.

For the 5 sets of waveforms described above the sky position of the source is distributed according to the given γ-ray detector sky localization distribution. In addition, the interferometers calibration errors reported in table 7.1 are taken into account by jittering the amplitude and time of the injected waveform independently in each detector. The phase error is converted into a timing error using the central frequency for sine-Gaussian waveforms, and

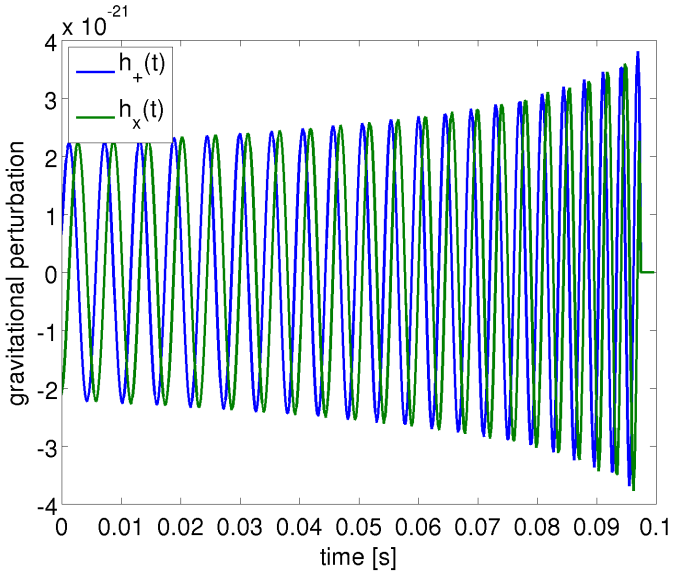

Figure 7.7: Example of the last 100 ms of an inspiral waveform. The $h_+(t)$ and $h_\times(t)$ time series are shown for a binary of masses $m_1 = 1.4\,\mathrm{M}_\odot$ and $m_2 = 10\,\mathrm{M}_\odot$, an inclination angle $\iota = 0$ and a distance of 10 Mpc.

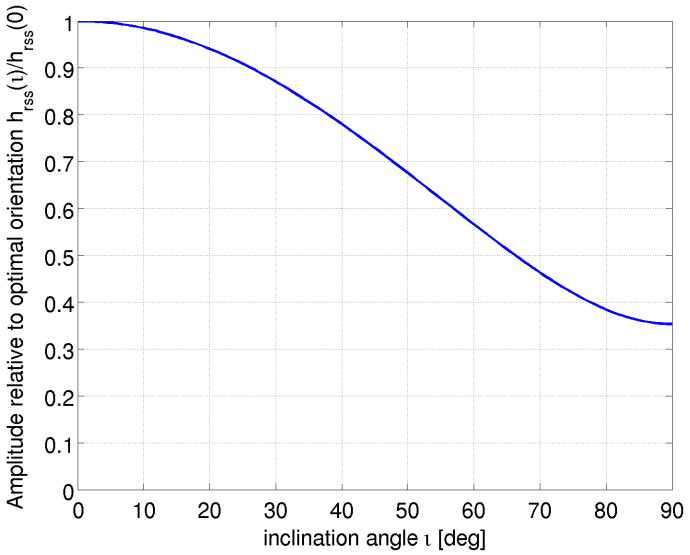

Figure 7.8: Dependence of the observed gravitational wave amplitude in terms of h_{rss} as a function of the rotator or inspiral inclination angle with respect to the observer. The relative amplitude factor $F^{1/2}(\iota)$ is given by equation (7.3).

using a 150 Hz frequency at which detectors are most sensitive for the broadband inspiral injections.

These injections are considered to be detected (or found) if within a small time window[5] around the injection time t_0 a trigger is present with a detection statistic above some threshold $S_{\text{threshold}}$ and passing all consistency and data quality cuts.

In order to measure the detection efficiency as a function of amplitude A (or equivalently distance) for each of the waveform sets, 600 injection parameters are drawn from the distributions described above and for each parameter set the injection is repeated with a range of scaling factors. We construct the range of scaling factors using one very small scale which is used for sanity checks of injection recovery and a set of 24 logarithmically separated scales between ~ 0.03 and 100:

$$A/A_0 \in \{0.001\} \cup \{100/1.4^k\}_{k \in [\![0,24]\!]} = \{0.001, 0.0316, 0.0442, \ldots, 71.477, 100\}, \tag{7.4}$$

where A_0 is the nominal amplitude. This ensures that detection efficiency curves go from 0 to 100% efficiency.

Automatic tuning

The generic principle of automatic tuning is to select from a pool of possible analysis parameters $\mathcal{R}$ a set R which optimizes the analysis sensitivity, according to some figure of merit.

The figure of merit which we use is the ϵ-efficiency injection amplitude A^{ϵ}_{CL}, that is the amplitude at which the detection efficiency at a confidence level CL is equal to ϵ for a given waveform family. For instance, for $\epsilon = 50\%$ and CL = 99.7% this amplitude can be easily converted into the typical distance at which a given source family can be detected at a 3-sigma level.

In order to construct this amplitude both background and injections sample sets are needed. Given the cumulative distribution of loudest event detection statistic $\mathcal{C}(S_{\text{max}})$ constructed from the background set, for a given detection confidence level CL, the detection statistic threshold S_{CL} is the solution of $1-\text{CL} = \mathcal{C}(S_{\text{CL}})$. This solution can be easily obtained by computing the CL percentile of the S_{max} samples. This defines the injection detection threshold $S_{\text{threshold}} = S_{\text{CL}}$ and the corresponding detection efficiency curves $e_{\text{CL}}(A)$. The amplitude A^{ϵ}_{CL} is then the solution of $e_{\text{CL}}(A^{\epsilon}_{\text{CL}}) = \epsilon$ and is obtained by interpolating points in $e_{\text{CL}}(A)$. An example of an efficiency curve for circular sine-Gaussian signals is shown on figure 7.9. Such efficiency curves can also be drawn in terms of distance instead of amplitude as shown on figure 7.10.

[5] In our analysis equal to ±100 ms for sine-Gaussian waveforms and $[-5, 0.1]$ s for inspiral waveforms. The larger window for inspiral waveforms takes into account their long duration and extended emission before the coalescence time.

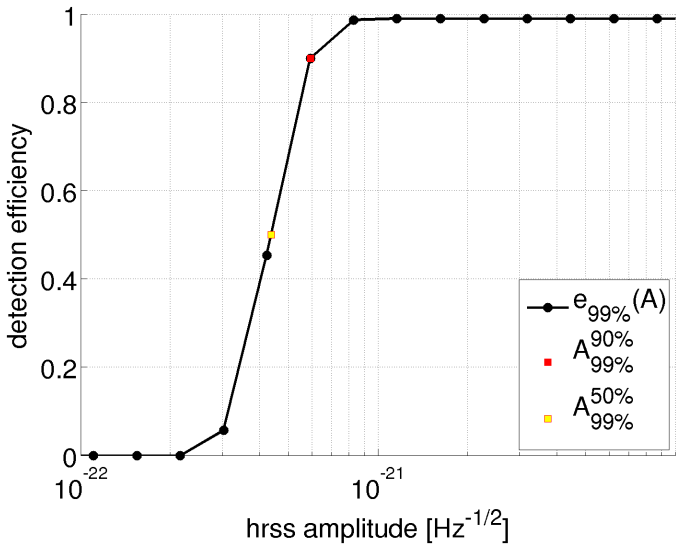

Figure 7.9: Example of a detection efficiency curve for circular sine-Gaussian at 150 Hz. This example is the detection efficiency for the first GRB listed in table B.1 of appendix B, and 300 injections are performed to estimate the injection at each amplitude. In this example $e_{99\%}(A)$ is shown as black dots and the amplitude A is scaled in terms of $h_{\rm rss}$. The black line shows the linear interpolation in log scale of the efficiency curve, and two amplitude examples: 90% efficiency amplitude $A^{90\%}_{99\%}$ (red square) and 50% efficiency amplitude $A^{50\%}_{99\%}$ (yellow square) are shown. The reason why the efficiency curve saturates slightly below 100% is that for this particular example 1.5% of the on-source time is vetoed by data quality flags.

If more than one family of waveforms is used, as is the case for this search, a compound figure of merit which takes into account all the possible signals needs to be formed. Given that *a priori* the injection amplitudes cannot be meaningfully compared between different families[6] we use a relative compound figure of merit.

For each parameters set R and waveform family i we have described how to construct the figure of merit $A^{\epsilon}_{\rm CL}(R,i)$. For each waveform set there is an optimal parameters choice which yield a minimal detection amplitude

$$A^{\epsilon}_{\rm CL}({\rm optimal},i) = \min_{R\epsilon\mathcal{R}} A^{\epsilon}_{\rm CL}(R,i). \tag{7.5}$$

As the compound figure of merit we use the average relative distance from

[6] For instance the choice of 10 Mpc and 20 Mpc nominal distance for respectively NS-NS and NS-BH do not correspond to the astrophysical distance expectations for each event family, and these expectations are not determined well enough to be used.

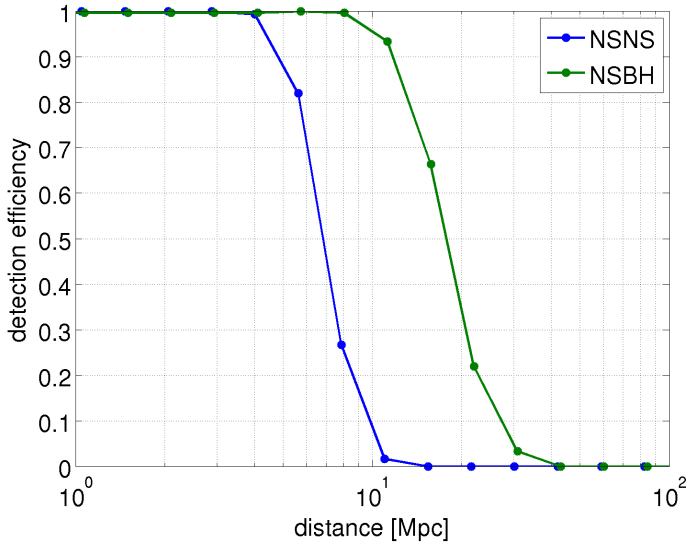

Figure 7.10: Detection efficiency curve for neutron star - neutron star (NSNS) and neutron star - black hole (NSBH) inspiral waveform families. For both families $e_{99\%}(r)$ is shown in terms of distance and 300 injections with parameters distributed as described in the text are performed to estimate the efficiency at each distance. In this example the results for the first GRB listed in table B.1 of appendix B are used, but the reduction of detection efficiency due to data quality flags is not shown for the sake of clarity.

this optimal value in the mean square sense

$$\mathrm{FOM}^{\epsilon}_{\mathrm{CL}}(R) = \sum_i \left(\frac{A^{\epsilon}_{\mathrm{CL}}(R,i) - A^{\epsilon}_{\mathrm{CL}}(\mathrm{optimal},i)}{A^{\epsilon}_{\mathrm{CL}}(\mathrm{optimal},i)} \right)^2, \tag{7.6}$$

and the parameter set R_{tuned} for which the minimum is attained

$$\mathrm{FOM}^{\epsilon}_{\mathrm{CL}}(R_{\mathrm{tuned}}) = \min_{R \epsilon \mathcal{R}} \mathrm{FOM}^{\epsilon}_{\mathrm{CL}}(R), \tag{7.7}$$

is our parameter tuning choice.

The amplitude used to compute $\mathrm{FOM}^{\epsilon}_{\mathrm{CL}}(R)$ are also used to quote the final sensitivity of the analysis pipeline. In order to avoid biasing these quoted sensitivities, a statistically independent set of injection and background samples is used to tune the parameters choice R_{tuned} and to quote the sensitivity.

Tunable parameters

For the automatic tuning we use the space of parameters $\mathcal{R}$ formed by:

- the choice between the circular detection statistic and the robust detection statistic as the final ranking of events,
- the shape of the coherent consistency cut on the following energies:
  - the circular energy,
  - the circular null energy,
  - the null energy if present.

The tuning is done in two steps according to two figures of merit: first with $\mathrm{FOM}^{95\%}_{99\%}(R)$ and then with $\mathrm{FOM}^{50\%}_{99\%}(R)$. The main reason for using the relatively low detection confidence level of 99% is computational. A systematic extensive background estimation through the time slide method is computationally expensive and that confidence level was determined to be a good trade-off between reasonable tuning and limited computational resources.

To draw a line separating signal from glitches in the incoherent versus coherent energy plane the two parameter (r, α) family of functions

$$\frac{|E - I|}{(E + I)^{\alpha}} > r, \tag{7.8}$$

discussed in section 5.7.2 is used. The parameter α characterizes the shape of the line, and r the "strength" of the cut of that shape. The tuning of the separation line is performed in two steps:

- In the first step the family of separation function is used with $\alpha = 1$, which for growing amplitudes rejects a fixed fraction of signals and an increasing fraction of glitches. The purpose of this tuning is to robustly reject all loud glitches. This fixed fraction of loud signal rejection is the reason for tuning at the $\epsilon = 95\%$ efficiency, otherwise the detection efficiency curves could saturate far from the 100% efficiency point.
- In the second step of tuning the family of separation functions is used with $\alpha = 0.8$, while the separation function chosen in the first step is applied. The choice of detection statistic in the first part of the tuning is not taken into account. The purpose of this step is to reject the remaining glitches while keeping the best detection sensitivity, here characterized by the 50% detection efficiency point.

In both cases the threshold r to which the separation function is compared to is optimized over a discrete grid of values

$$\begin{aligned}\pi_{\mathrm{grid}} = \{&0, 1, 1.01, 1.03, 1.06, 1.1, 1.15, 1.2, 1.27, 1.35,\\ &1.45, 1.57, 1.71, 1.9, 2.1, 2.4, 2.7, 3, 3.3, 3.6, 4\}.\end{aligned} \tag{7.9}$$

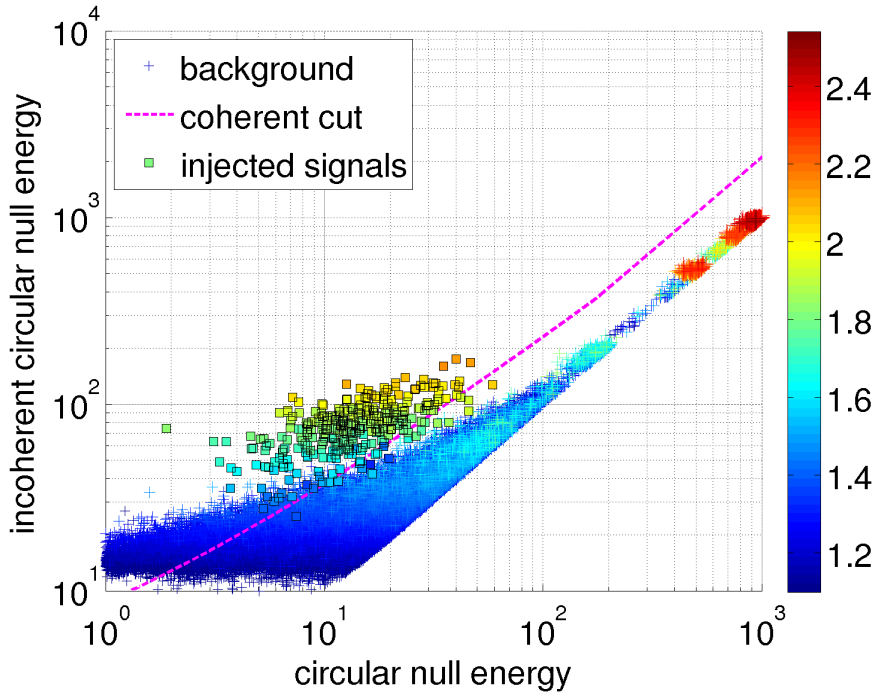

Figure 7.11: Scatter plot of the incoherent circular null energy versus the circular null energy, the decimal logarithm of the detection statistic (here the robust one) is color coded. The data from the first GRB listed in table B.1 of appendix B are used as an example. The background triggers are marked by pluses and injected signals at the amplitude corresponding to a 90% efficiency are shown as squares. The dashed magenta line show the tuned separation line, with triggers below this line being rejected as glitches. This line is formed by the common effect of two rejection lines (7.8) with $(\alpha, r) = (1, 2.1)$ selected by the first part of the tuning and $(\alpha, r) = (0.8, 3.5)$ for the second part of the tuning. The first part is dominating at high energies and is parallel to the diagonal, the second part dominates at low energies and slowly approaches the diagonal as the energies increase. The transition between the two can be seen as a small kink at circular energy ~ 200. Note that the background triggers that are passing the coherent cuts in the lower left corner of the plot are of no importance, as their detection statistic value is very small.

Hence in total the tuning parameter space in each step is

$$\mathcal{R} = \{\text{circular}, \text{robust}\}^{\text{det stat}} \times \pi_{\text{grid}}^{\text{circular}} \times \pi_{\text{grid}}^{\text{circular null}} \times \pi_{\text{grid}}^{\text{null}}, \tag{7.10}$$

and an optimal point in that grid is chosen for each step. An example of the separation in the incoherent versus coherent energy plane is shown on figure 7.11.

This automatic tuning procedure defines the shape of cuts on each coherent/incoherent energy couple and chooses one of the two detection statistic. This tuning is done independently for each GRB trigger, as the result strongly depends on the interferometers present in the network, the antenna patterns for the particular sky location of the GRB and the rate of glitches in each detector at that time. Note that this tuning procedure is safe, in the sense that it does not look at triggers in the GRB on-source window, only at background and signal samples. For this reason it is called *closed-box* tuning in contrast with the final *open-box* results which look at the loudest event in the on-source window.

7.2.4 Analysis optimization procedure

In the previous section we have discussed the details of the analysis used for the GRB search in S6/VSR2-3 data and the automatic tuning procedure used. There was actually a long development process that eventually lead to these particular choices of detection statistics and coherent cuts shapes, which we have considerably improved compared to the ones used for the analysis of the previous data run [85].

The main goal of these changes was to improve the detection sensitivity of the search, and we choose each incremental improvement by manually repeating the automatic tuning idea on a larger scale. That is, by performing the automatic tuning analysis on a dozen of GRBs with two different choices of non-automatic analysis changes, and including an improvement whenever it had a significant[7] improvement in detection sensitivity for some GRBs in the sample and no decrease in the sensitivity for any GRB in the sample. We will not give the detailed results of all this development tests, which would easily double the length of this thesis, but describe several features among the most important.

The starting point for the construction of the robust detection statistic was to realize that coherent consistency tests are needed because glitches are not considered when constructing usual detection statistics. In its initial version the noise was modeled by a Gaussian core with a Gaussian tail, the resulting statistic was improving cases where detectors are very glitchy but it also decreased the sensitivity for cases where data quality is good. Actually

[7] The typical threshold for "significant" improvement is > 10% change in the 50% efficiency amplitude.

the resulting statistic for the 2-detector case was quite close to taking the minimum of the SNR in each detector, compared to the typical quadratic sum of SNRs used in detection statistics based on the Gaussian noise hypothesis.

This motivated us to explore other kinds of SNR averages, like arithmetic, geometric and harmonic mean, as an ad-hoc detection statistic. The geometric mean $\sqrt{\mathrm{SNR}_1\mathrm{SNR}_2}$ (see equation (5.75)) proved to be quite effective, and the idea of changing the exponents from fixed $1/2$ to adaptive α_i which depends on the detector glitchiness (see equation (5.74)) followed naturally from the definition of the geometric mean. In practice it is just a weighted geometric average, and the particular weight choice procedure described in section 5.8.3 was selected from several other procedures which proved to be less effective. The interpretation of the robust static as a likelihood ratio was done *a posteriori* once it has proved to be an effective statistic.

As another example, we introduced the two coherent tests which include the circular polarization because frequently the two LIGO detectors and Virgo are sensitive to independent polarizations for a given sky position. That is the scalar product $(F^{+}_{\mathrm{LIGO}}F^{\times}_{\mathrm{LIGO}}) \cdot (F^{+}_{\mathrm{Virgo}}F^{\times}_{\mathrm{Virgo}})$ is close to zero. In that case gravitational wave strains as seen by the LIGO and the Virgo detectors have *a priori* no reason to be coherent. This issue has affected only a few GRBs in the 2005-2007 data run as in most cases at least two LIGO detectors were present and the antenna patterns scalar product was far from zero. However, for the 2009-2010 data set, frequently the gravitational wave network is formed of one of the LIGO detectors from one side and the Virgo detector from the other side, due to the good duty cycle of Virgo.

The coherent tests developed for the 2005-2007 run are completely inefficient in that case. On the contrary for this analysis the circular polarization assumption introduces expected correlations between the different linear projection seen by the detectors. This assumption allowed us to construct the circular energy and null circular energy coherent tests based on the same method as the previously used coherent tests. We remind the reader that this assumption is astrophysically reasonable as shown by the thorough study of the γ-ray and gravitational wave emission models as discussed in chapters 3 and 4.

As a final example, the two step procedure for tuning the shape of the separation line in the incoherent versus coherent energy plane started from the choice made in the previous data run to use a single step using a shape very close to the family of function (7.8) with $\alpha = 0.5$. This choice was very effective for obtaining low gravitational wave amplitude upper limits from non detection results. However, as it effectively fits the glitch distribution uniformly over the detection statistic, very loud glitches are having the same chances at passing the coherent consistency cut as quiet ones, which is disastrous for any potential detection claims. In order to prevent any loud glitch from passing coherent consistency we tried first the simple case of using a single step with $\alpha = 1$ with the 50% efficiency amplitude as a figure of merit,

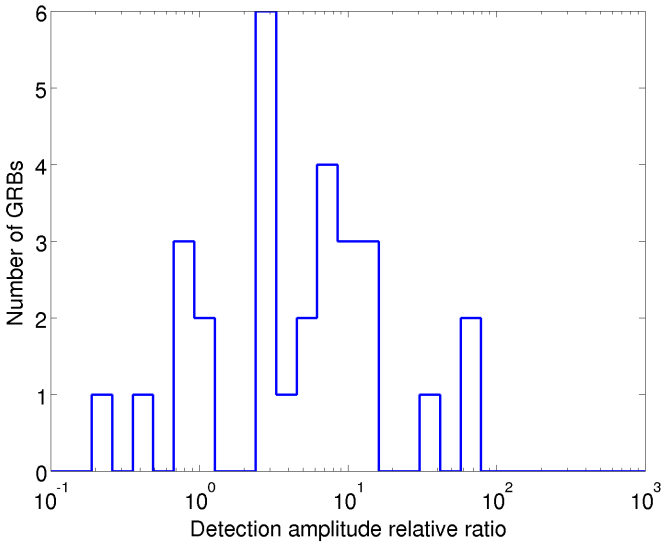

Figure 7.12: Comparison between the sensitivity of the analysis as used during the 2005-2007 run and of the analysis described on the subset of analyzed GRBs that happened during S6A. As a figure of merit of the detection sensitivity we use the 50% efficiency amplitude $A^{50\%}_{99\%}$(old) at 99% detection confidence for the 2005-2007 analysis and $A^{50\%}_{99\%}$(new) for the current analysis. The histogram shows $[A^{50\%}_{99\%}(\text{old}) - A^{50\%}_{99\%}(\text{new})]/A^{50\%}_{99\%}(\text{new})$ for the circular sine-Gaussian waveforms at 150 Hz.

which came with the unsightly drawback of some efficiency curves saturating at $\sim 70\%$. Then we determined that $\alpha \simeq 0.8$ is a good middle ground between the two solutions above, by testing a set of different values in $[0.5, 1]$. Finally we included the additional first step with $\alpha = 1$ to provide additional robustness against loud glitches.

In all those developments the driving goal was to obtain an analysis which systematically rejects all loud glitches, which means that any potential detection candidate will not be masked by a long low probability background tail. As a summary of the obtained gain in detection sensitivity the histogram on figure 7.12 shows how much sensitivity would have been lost if the analysis from 2005-2007 was used on the current data. This comparison does not show that the 2005-2007 analysis was poorly performed, but that it is inadequate for the current data set. That is poorly sky localized GRB triggers, gravitational wave networks with only non-aligned detectors and a focus on gravitational wave detection.

Another part of the optimization concerns minimizing the computational load of performing the analysis. The main challenge here was coming from the large sky location error boxes provided by the GBM on Fermi. The

analysis of such an error box is in principle a factor ~ 100 slower than for a well localized GRB, as the sky location error box to scan occupies a few hundreds square degree on the sky and roughly one point per square degree is needed to cover an error box. However we implemented several computational optimizations to reduce this factor to only ~ 10.

Not only the computation time is limited but also the random access memory available on a typical computing node is not sufficient to hold time-frequency maps for the whole coincidence window (4.12), which is much longer than the one used previously. We needed develop some book-keeping to split the window into manageable blocks that are 256 s long, and concatenate the results from them. The implementation is flexible enough that the analysis pipeline we describe here, is currently being adapted to perform gravitational wave searches in association with nearby supernovae which require days long coincidence windows.

In this whole development process also many small technical issues were found and fixed, such as improving the data whitening robustness when large fluctuations at low frequency (~ 10 Hz) are present or correcting the way data quality flags are used.

7.3 Circular polarization assumption validation

In the analysis we just described, we use the assumption of circular polarization of the incomming gravitational waves to separate the signal from noise. In section 4.4 we have shown by theoretical arguments that gravitational waves coming from GRBs should be approximately circularly polarized, and the effect of deviation from circularity is smaller or equal to the effects of calibration errors. In this section we validate these theoretical arguments by actually testing the sensitivity of the analysis. We focus here on the model for which the theoretical argument is the most tenuous, the coalescence model of spinning compact objects, where for large jet opening angles and black hole tilt angles the precession of the orbital plane can lead to oscillation between linearly and circularly polarized gravitational wave emission. To confirm that this borderline case is not an issue, we analyze a sample of spinning inspiral signals.

For spinning inspiral injections we use the same mass distribution as for the neutron star – black hole injections described in section 7.2.3. We consider dimensionless spin magnitude to be uniformly distributed in the $[0, 0.98]$ range for black hole and in the $[0, 0.4]$ range for neutron stars, these values cover the astrophysically reasonable range as described in section 3.3.2. We assume the neutron star spin direction to be uniformly distributed, but for black holes we consider two cases: a uniform distribution of spin direction[8], and a top-hat distribution with the black hole tilt angle

[8]That is a uniform distribution in $\cos(\kappa)$.

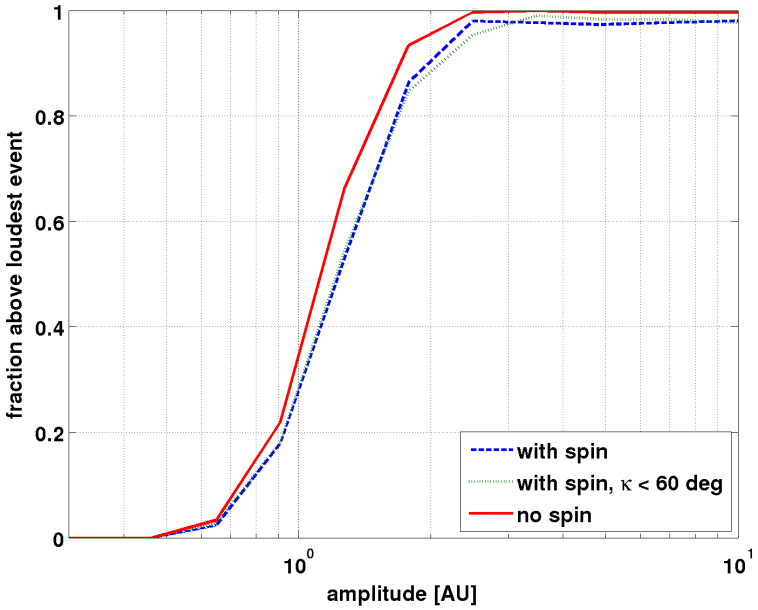

Figure 7.13: Detection efficiency curve $e_{99\%}(A)$ for three distribution of neutron star - black hole coalescence: uniform spin distribution (blue dashed line), black hole tilt angle limited to below 60° (green dotted line) and non-spinning objects (red solid line). See text for details on the distribution parameters, these curves show the detection efficiency for the first GRB listed in table B.1 of appendix B. For the three curves, $A = 1$ correspond to a reference distance of 20 Mpc.

$\kappa < 60°$ which we derived as being astrophysically reasonable and relatively safe from the point of view of circular polarization. In both cases we assume the initial total angular momentum inclination ζ to be uniformly distributed within the typical jet opening angle of 30°. For a reminder on the different angle definition see figure 4.5. The inspiral waveforms were generated using the `SpinTaylor` generator from the `LAL` package [117] which implements the waveform generation procedure described in [118] and has a 3.5PN order in phase evolution.

The efficiency curve for both sets of waveforms are shown on figure 7.13. The test case was chosen to represent an *a priori* bad scenario in which a stringent test on circularity has been chosen by the automatic tuning. The separation line used is shown on figure 7.11, and the two detectors in the network for that case see independent linear polarizations. Compared to a non-spinning inspiral signals the decrease in sensitivity is modest: the 50% efficiency amplitude is higher by only 10%, the 90% efficiency amplitude is higher by 20% and a few percent of spinning injections are always rejected by

coherent cuts regardless of the amplitude. This is an acceptable loss considered the tremendous glitch rejection gain coming from coherent consistency cuts. Moreover these efficiency curves convolute two effects: the rejection by the circular polarization test and the modification of amplitude/frequency evolution by the spin. For instance the SNR of the spinning injections is lower by 2% in the median case and by 10% in the lower quartile, when compared to non-spinning injections with the same parameters. Hence the actual effect of the coherent test is even smaller than what is suggested by the figure. More surprisingly, the limitation of the κ distribution does not have any visible effect, which means that the astrophysical assumption on the tilt angle κ given in section 4.4 are not actually necessary.

A similar study was performed for typical double neutron star coalescence parameters, and as expected a completely negligible effect was observed.

7.4 Results

When LIGO and Virgo were taking data in 2009-2010 various γ-ray satellites have reported on the detection of 407 GRBs, these include GRBs reported through the GCN but also taken from GRB catalogs of the Fermi and Swift spacecrafts. Out of these, 164 GRBs had sufficient good quality data available from at least two gravitational wave detectors, but we report results for only 153 of them. The discarded GRBs come from cases of 2-detector networks where the GRB sky location is near the blind spot of one of the detectors, which means that the network is essentially containing only one detector, and data cannot be cleaned by coherent consistency tests. The rejection criterion is based on the behavior of the background distribution after all quality and coherent consistency tests are applied. The time and coordinates of the 153 GRBs along with the analysis results are given in table B.1 of appendix B.

For a gravitational wave analysis in association with external triggers 4 main results can be derived. Two detection statements: either on a GRB per GRB basis, or by taking all GRBs as a population. When the recovered candidate events are not significant for both detection statements, exclusion limits on GRB parameters or on the GRB population parameters can be set. We discuss these 4 statements in the sections below.

7.4.1 Per GRB detection

The per GRB results are relatively simple to derive. The gravitational wave candidate event is defined as the loudest trigger found in the on-source window which passes all quality and coherent consistency tests. The p-value, that is the probability of the loudest event to be due to background fluctuations only, can be easily computed from the cumulative background loudest event statistic distribution $\mathcal{C}(S_{\max})$. If we note $S_{\max}^{\text{on-source}}$ the statistic of the

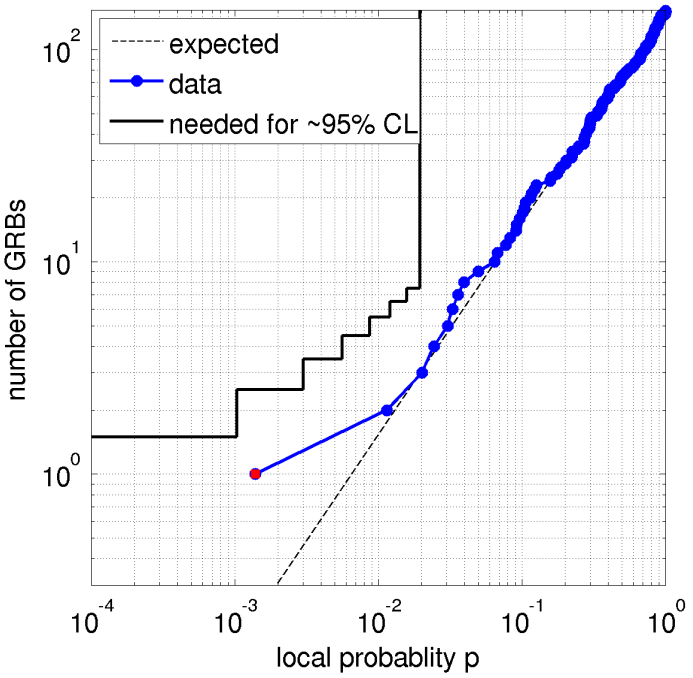

Figure 7.14: Distribution of observed p-values for the analyzed GRBs listed in table B.1 of appendix B. The red dot marks the largest deviation of the low p-value tail from the uniform distribution null hypothesis. As a visual guideline of the consistency with the null hypothesis the black line shows the threshold for a 2-sigma detection with the binomial test (7.13) described in section 7.4.3. Any point of the p-value distribution above and to the left of this curve would be unusual.

loudest on-source event, its p-value is $p = \mathcal{C}(S_{\max}^{\text{on-source}})$. The p-value can be reinterpreted in terms of Gaussian standard deviations: for p-values below the 3-sigma level ($p \leq 2.7 \times 10^{-3}$) the candidate event can be considered as gravitational wave "evidence" and for p-values below the 5-sigma level ($p \leq 5.7 \times 10^{-7}$) as gravitational wave "detection". One should note that these per GRB p-values do not take into account the *trial factor* of analyzing multiple GRBs. As an example of trial factors if we set a 10^{-5} p-value threshold on an experiment and repeat the experiment 100 times the probability of obtaining an event below this p-value threshold is 10^{-3} and the trial factor is 100. We properly take this into account in the population detection statement described in section 7.4.3.

To select significant events that deserve a more detailed followup we set *a priori* a threshold of p-value at 1%. In only one case, GRB100917 which happened on September 17 2010, this threshold was crossed as can be seen

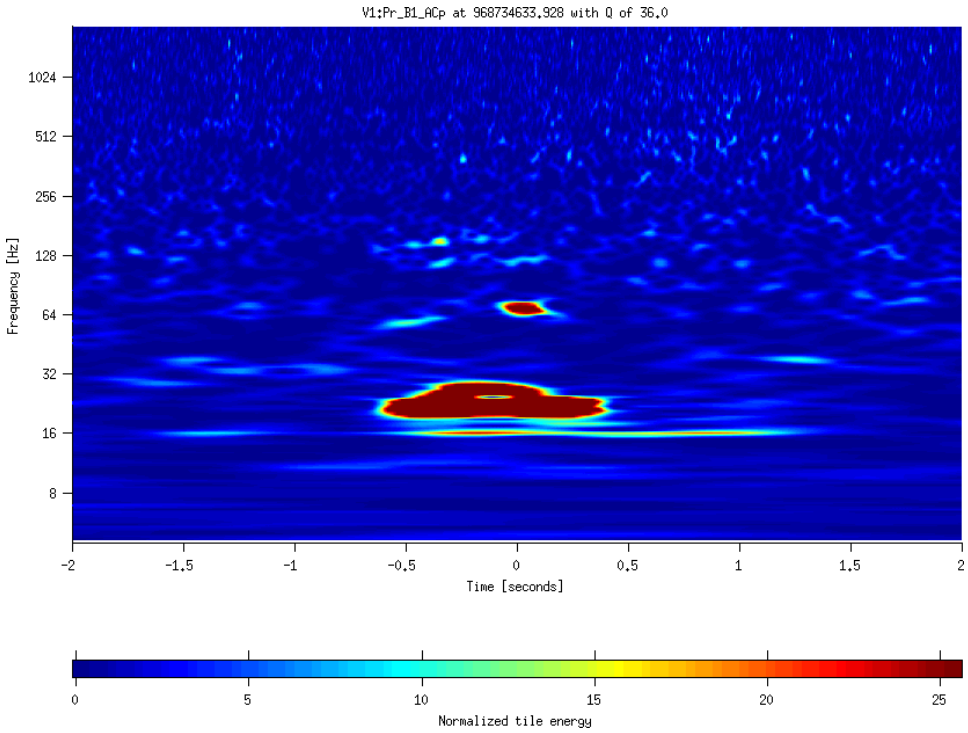

Figure 7.15: Time frequency representation of the signal energy deviation from the Gaussian hypothesis in the photo-diode read out of the output port of the Virgo interferometer at the time of the event candidate of GRB100917. The upper red blob of energy corresponds to the Virgo contribution to the triple detector candidate event.

on figure 7.14 and found in table B.1 of appendix B. The event was found in a network of three detectors H1, L1 and V1, and is formed by a trigger of SNR ~ 11 in V1 that spans the 60 – 80 Hz frequency range and is ~ 200 ms long. The data in H1 is slightly deviating from the Gaussian hypothesis with SNR ~ 4 and data in L1 are completely consistent with Gaussian noise. At this time and for that particular sky location[9] the L1 sensitivity is about a factor 2 poorer than in H1 and V1 at the frequency band of the trigger, the latter two being roughly equal. Hence the lack of signal in L1 is consistent with the SNR found in H1, however the large discrepancy in SNR between H1 and V1 is not consistent with a gravitational wave signal, unless the calibration is erroneous by 2-sigma in H1 and V1 and in opposite directions (see table 7.1). The trigger in V1 could be due to micro-seismic up-conversion through scattered light which form a characteristic arch shape [106], with a single bounce fringe at 30 Hz and a double bounce fringe 60 Hz visible in the interferometer output photo-diodes at the time of the candidate shown on

[9]This GRB was well localized in the sky by Swift.

figure 7.15. However the two triggers corresponding to the arches are not well aligned in time and it remains unclear whether the higher frequency trigger in V1 forming the gravitational wave candidate is due to the up-conversion. In conclusion, this event cannot be ruled out as being due to a gravitational wave signal. However this is event is suspicious given that it is possibly explained by seismic up-conversion in V1 and not well consistent between H1 and V1. In any case this event is not statistically significant given the number of analyzed GRBs as shown in section 7.4.3.

7.4.2 Per GRB exclusion

Whenever the loudest event found in the on-source window is not a detection candidate a loudest event exclusion on some model can be drawn. As a source model we assume each of the 5 waveform families described in section 7.2.3. For the compact binary coalescence model the only free parameter left is the distance, hence naturally the exclusion sets a lower limit on the distance. For the sine-Gaussian model the only free parameter is the amplitude, however it can be cast in terms of the easier to interpret distance using the $h_{\rm rss}$ - gravitational wave energy relation (1.44), which we recall here

$$h_{\rm rss}^2 = \int (h_+^2 + h_\times^2) {\rm d}t \simeq \frac{1}{\omega_{\rm GW}^2} \frac{10G}{r^2 c^3} E_{\rm GW}. \tag{7.11}$$

For the distance exclusions considered here we use $E_{\rm GW} = 10^{-2}\,{\rm M}_\odot {\rm c}^2$ as an energy reference, but the distance exclusion for other energies can be easily obtained, given that changing the energy by a factor x will change the distance exclusion by a factor $\sqrt{x}$.

For a given waveform model the loudest event statistic is used as the detection threshold $S_{\rm threshold} = S_{\rm max}^{\rm on\text{-}source}$ defining the loudest event efficiency curve $e_{\rm loudest}$ which directly yields the exclusion limit. If the efficiency curve $e_{\rm loudest}(r)$ is drawn in terms of distance instead of amplitude, the distance $r_{90\%}$ at which the curve passes through the 90% efficiency point gives the exclusion distance at 90% confidence level. This is the distance at which in 90% of cases the event corresponding to the signal would be louder that the loudest event found in the data, and this exclusion is performed according to frequentist statistics.

The detailed 90% exclusion distances on a per GRB basis are given in table B.1 of appendix B. Summary histograms of the exclusion distance for each waveform are given on figure 7.16 for circular sine-Gaussian waveforms and on figure 7.17 for binary inspiral waveforms. The median and quartiles of these distributions are given in table 7.2.

7.4.3 Population detection

The goal of the population detection is to combine the loudest event p-values from the sample of analyzed GRBs to determine whether their distribution

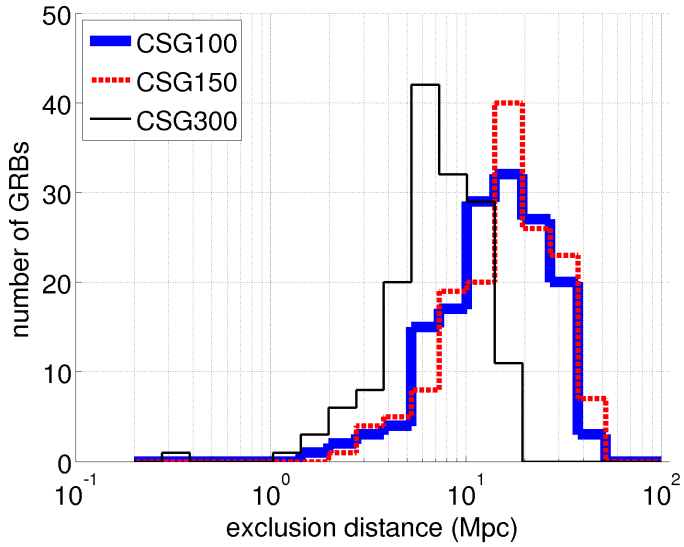

Figure 7.16: Histograms across the sample of analyzed GRBs of the distance exclusions at the 90% confidence level for the 3 families of circular sine-Gaussian models considered. A standard siren gravitational wave emission of $E_{\rm GW} = 10^{-2}\,{\rm M}_{\odot}{\rm c}^2$ is assumed. The lower exclusion distances for the highest frequency family is well explained by the $h_{\rm rss}$ - $E_{\rm GW}$ relation (7.11) and the sensitivity dependence as a function of frequency.

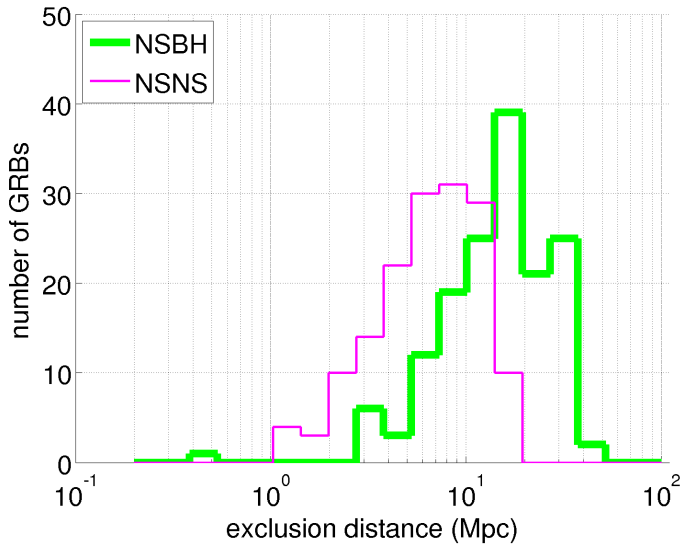

Figure 7.17: Histograms across the sample of analyzed GRBs of the distance exclusions at the 90% confidence level for the 2 families of binary inspiral models considered.

Quartile	CSG100	CSG150	NSBH	CSG300	NSNS
	Exclusion distance (Mpc)				
25%	9.8	10.5	9.6	5.3	4.3
50% (median)	15.5	17.3	15.7	7.1	6.9
75%	22.8	25.0	23.0	10.3	10.1

Table 7.2: Shown are the three quartiles of the 90% confidence distance exclusions for the 5 considered signal models. The three quartiles are the points where the cumulative distribution crosses respectively the 25%, 50% and 75% point, in particular the second quartile is the median.

significantly deviates from the null hypothesis, which is p-values uniformly distributed in $[0, 1]$. This deviation might be either due to a single very loud event (with a very small p-value) or to a population of several moderately loud events.

For detecting this deviation from the null hypothesis a binomial distribution based test was used in recent searches for gravitational waves in association with GRBs [109, 85]. The binomial test looks at the tail of low p-values from the sample of N analyzed GRBs, that is the left most part of the p-value distribution shown on figure 7.14. The length $N_{\text{tail}} \simeq fN$ of the tail is chosen as a fraction f of the total sample. A larger fraction allows to look for a tail of more numerous weaker events at the price of loosing sensitivity to the single loud event case. For the analysis presented here we choose $f = 5\%$.

The binomial test considers the N_{tail} lowest p-values sorted in increasing order: $p_1, ..., p_{N_{\text{tail}}}$. For each $k \leq N_{\text{tail}}$ the binomial probability of obtaining k or more p-values below p_k is

$$P_{\geq k}(p_k) = \sum_{l \geq k} \binom{N}{l} p_k^l (1 - p_k)^{N-l}. \tag{7.12}$$

These probabilities are combined by just taking their minimum, that is the largest deviation from the null hypothesis for each of the N_{tail} different tails considered. In order to obtain a population detection statistic that grows with the signal we use

$$S_{\text{binomial}} = -\log \min_{1 \leq k \leq N_{\text{tail}}} P_{\geq k}(p_k). \tag{7.13}$$

The main drawback of the binomial test is that it does not include in any way the difference in sensitivity for different GRBs in the sample. These variations in sensitivity come from differences in antenna pattern factors and noise levels. For a given GRB k the *a priori* probability for the presence of a detectable signal from a family i is proportional to the volume to which the search is sensitive $V_k(i) \propto (1/A_{99\%}^{50\%}(i))^3$. For this reason we have developed an enhancement of the binomial test to include this sensitivity information

and reduce the trial factor by effectively removing the GRBs for which the available network of detectors is not sensitive at all. Given the absolute detection prior is hard to quantify, we use the relative probability

$$R_k(i) = \frac{V_k(i)}{\max_k V_k(i)}, \tag{7.14}$$

and average it over the 5 waveform families considered

$$R_k = \frac{1}{5}\sum_{i=1}^{5} R_k(i), \tag{7.15}$$

to account for our ignorance on the exact progenitor model. In total, a more refined population detection statistic is

$$S_{\text{pop det}} = -\log \min_{1\leq k\leq N_{\text{tail}}} \binom{N}{k} \prod_{l\leq k} \frac{p_l}{R_l}, \tag{7.16}$$

where the fractions p_l/R_l are arranged in increasing order, and the inclusion of a low sensitivity GRB is penalized by an $1/R_l$ factor. As the fractions p_l/R_l can be greater than 1 we replaced the binomial probability by a binomial trial factor times the product of the fractions, the motivation being that the p-values in the tail are small, hence the approximation

$$P_{\geq k}(p) \simeq \binom{N}{k} p^k \tag{7.17}$$

is valid. Moreover this detection statistic includes not only the information on the number of p-values in the tail but also some information about their distribution.

In order to assess the difference in sensitivity between $S_{\text{pop det}}$ (7.16) and S_{binomial} (7.13), we performed a usual signal versus background sensitivity estimation. The background samples for N GRBs are simply generated from a uniform distribution on $[0, 1]$, and the population detection threshold is chosen at the 99.7 percentile (3-sigma level) of the obtained population detection statistic background distribution. Whereas signal samples for N GRBs are generated using the injections already used for the per GRB efficiency curve estimation. These injections are performed on a discrete grid of distances corresponding to the grid of amplitudes (7.4). To translate the detection statistic of these injections into p-values we use a power-law fit to the background distribution $\mathcal{C}(S_{\max})$ of each GRB and retrieve the p-value corresponding to the detection statistic. To create one sample of p-values for N GRBs with signal at fixed distance, we pick randomly for each GRB one injection at that distance, and take the minimum of the retrieved p-value and a random number drawn from a uniform distribution on $[0, 1]$. This last step corresponds to our choice of considering only the loudest event coming from the analysis of a GRB time window, which might be a noise event.

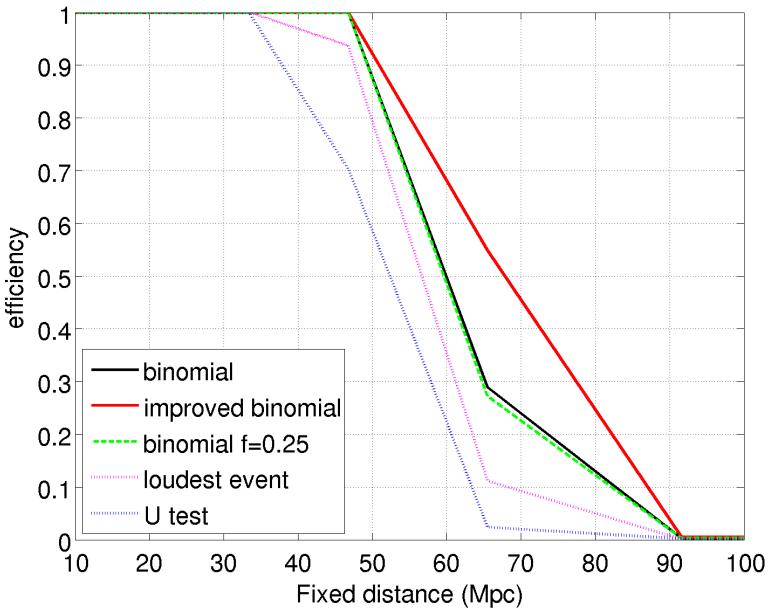

Figure 7.18: Efficiency of detecting a population of CSG150 signals as a function of distance for various population detection tests. Black curve – the standard binomial test (7.13), red curve – the weighted binomial test (7.16), green dashed curve – the standard binomial test but with $f = 0.25$, magenta dotted curve – p-value of most significant event and blue dotted curve – the Mann–Whitney U test. Note that the two binomial test curves are almost exactly the same.

In principle this signal generation is not representative of a reasonable signal population model as the signal for each GRB is at the same distance and not uniformly distributed in a volume. However we verified that this effect is not important by generating uniformly distributed in volume distances, and interpolating the detection statistic from the adjacent points in the distance grid to obtain the detection statistic of an injection at that random distance. With this cross-check study we obtained the same conclusions as the ones presented below for the simpler signal population model.

The obtained efficiency curve for the sample of GRBs analyzed in S6 is shown on figure 7.18. Along with the standard binomial test (7.13) and the weighted binomial test (7.16) three other tests are shown: the standard binomial test with $f = 0.25$ which shows that the test sensitivity is not strongly dependent on the choice of the fraction f, the loudest event p-value and the more general purpose Mann-Whitney U test [119]. Three of these tests have been used in previous searches for gravitational waves associated with GRBs: the standard binomial test in the 2005-2007 search

for gravitational wave bursts [85], the binomial test with $f = 0.25$ in the 2003-2005 search for gravitational wave bursts [109] and the Mann-Whitney U test in the 2005-2007 search for binary inspirals [110]. The loudest event p-value, that is the smallest single GRB background probability, corresponds to the binomial test with a $N_{\text{tail}} = 1$. The comparison shows that most population detection tests are more sensitive than just looking at the most significant GRB. The U test is a non-parametric test for deciding whether two samples are drawn from two different distributions, one being uniformly larger than the other. Here we compared the tested sample to a background sample drawn from a uniform distribution. The poor sensitivity of the U test is not very surprising given that this test is not specifically constructed for the uniform distribution null hypothesis.

In principle the population detection statistic (7.16) could be further improved by using absolute detection priors instead of relative ones, or as a further step by deriving a likelihood ratio detection statistic. We have derived such a likelihood ratio detection statistic but no significant gain in sensitivity was obtained and the detection statistic became more model depended. Given how uncertain the models are, we will use the weighted binomial test (7.16) as a good trade-off between sensitivity and simplicity.

The p-value distribution from table B.1 of appendix B is shown on figure 7.14, and the 2-sigma threshold of the standard binomial test is shown as a visual guideline of the consistency of the distribution with the uniform null hypothesis. However for population detection the weighted binomial test (7.16) is actually used, and the value of the detection statistic along with the background distribution is shown on figure 7.19. The observed population of p-value is consistent with the background distribution, and the probability of being due to background is $\simeq 25\%$. Hence no evidence for gravitational waves is found in the analyzed sample of GRBs.

7.4.4 Population exclusion

Analogously to the per GRB case, the lack of significant signal motivates an exclusion statement. As a population model we will assume that all GRBs are standard sirens as discussed in section 7.4.2 and that the distance distribution has two components: a fraction F of GRBs are uniformly distributed within a volume of radius R, the rest being effectively located at infinity.

This population may seem very *ad-hoc* at first glance, but it can be interpreted in several astrophysically relevant ways.

- There are indications of a local population of under-luminous long GRBs whose rate density would be ~ 1000 higher than the more commonly observed cosmological GRBs [83, 84]. The fraction F can be interpreted as the fraction of analyzed GRBs being in that local population. Note however that the existence of this population is based on only a few outlying GRBs.

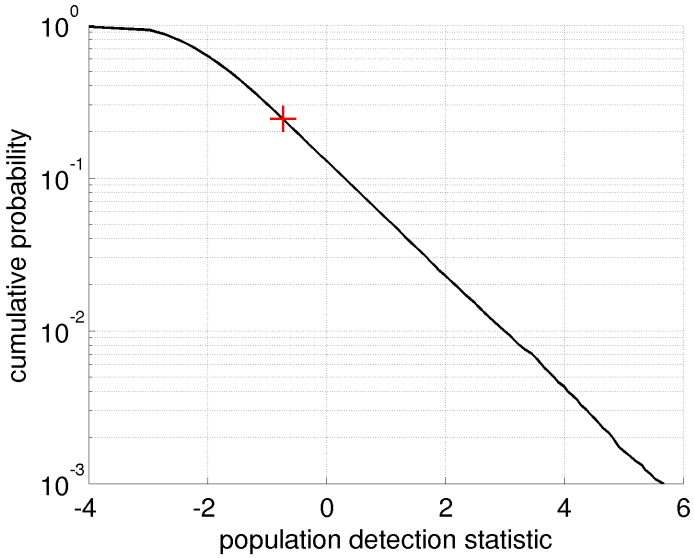

Figure 7.19: The black line shows the cumulative background distribution of the weighted binomial test (7.16), the overlaid red cross is the point resulting from the analyzed sample of GRBs. As can be read from this figure the observed distribution of p-values has a $\simeq 25\%$ probability of being due to the null hypothesis.

- More generally the local population can also be interpreted as the fraction F of analyzed GRBs that emit a large energy in gravitational waves. The remaining GRBs are then interpreted as having effectively a negligible gravitational wave emission instead of an infinite distance.
- Most GRB distance distribution models predict a uniform rate density at close distances and only at cosmological distances a more complex shape. Given that gravitational wave detectors are not sensitive at those large distances a simple information on the fraction of GRBs within a distance where the distribution is uniform is sufficient to parameterize these models.

As in the per GRB case the starting point is the loudest event efficiency curve $e_{\text{loudest}}(r)$. For a single GRB with our model of uniform distribution within volume of radius R the marginalized loudest event efficiency is

$$E(R) = \int_0^R e_{\text{loudest}}(r)\frac{3r^2\mathrm{d}r}{R^3}. \tag{7.18}$$

If we write $M_k(R) = 1 - E_k(R)$ the probability of missing the signal for GRB k, the probability of missing the signal for all GRBs is simply

$$1 - \mathcal{E}_N(R) = \mathcal{M}_N(R) = \prod_{k=1}^{N} M_k(R), \tag{7.19}$$

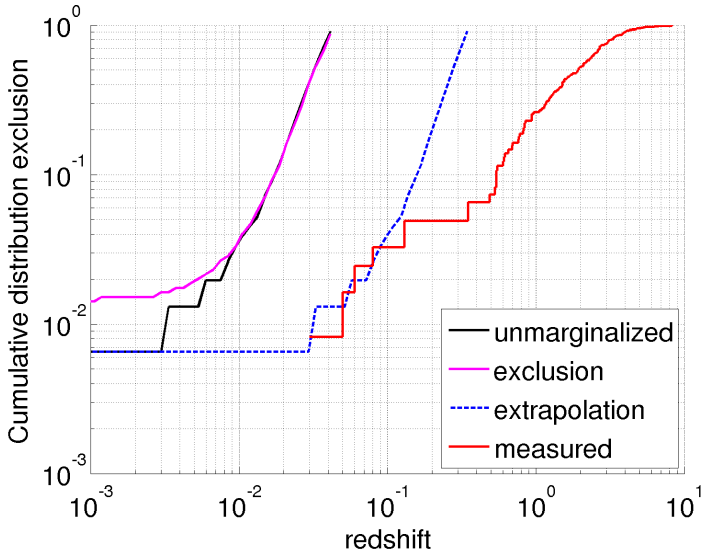

Figure 7.20: The red solid curve shows the observed distribution of redshifts in Swift GRBs [120, 121]. The black solid curve shows the 90% confidence level distribution exclusion limit drawn from the analyzed sample (7.20) of GRBs assuming a sine-Gaussian at 150 Hz signal model with $E_{\mathrm{GW}} = 10^{-2}\,\mathrm{M}_{\odot}\mathrm{c}^2$, and the magenta line shows the 90% confidence level distribution exclusion after marginalizing over the number of close-by GRBs in the analyzed sample (7.22). Finally, the blue dashed curve is the extrapolation of the black curve to advanced LIGO/Virgo, here modeled by simply rescaling the per GRB exclusion distance by a factor 10.

where $\mathcal{E}(R)$ is the population loudest event efficiency. That is the probability that an event louder than the loudest event in any of the analyzed GRB on-source window would be present due to the assumed GRB population. The 90% confidence level exclusion of the population model with radius $R_{90\%}$ and $F = 1$ is then the solution of $\mathcal{E}_N(R) = 0.9$.

This argument can be expanded to the case where only J out of N GRBs are distributed uniformly within the radius R, the probability of missing them is then

$$1 - \mathcal{E}_J(R) = \mathcal{M}_J(R) = \frac{1}{\binom{N}{J}} \sum_{\{k_1,\dots k_J\}\subset[\![1,N]\!]} \prod_{j=1}^{J} M_{k_j}(R), \tag{7.20}$$

where we average over our ignorance of which J GRBs from the whole sample are close-by. For a model with a fraction F of GRBs in the local population the number J of local GRBs in the sample is binomially distributed

$$p(J) = \binom{N}{J} F^J (1-F)^{N-J}, \tag{7.21}$$

and by marginalizing over J we obtain the population efficiency

$$1 - \mathcal{E}_F(R) = \sum_{J=0}^{N} [1 - \mathcal{E}_J(R)]\, p(J) \tag{7.22}$$

$$= \sum_{J=0}^{N} F^J (1-F)^{N-J} \sum_{\{k_1,\dots k_J\} \subset [\![1,N]\!]} \prod_{j=1}^{J} M_{k_j}(R). \tag{7.23}$$

The 90% confidence level exclusion of the population model with radius $R_{90\%}$ and fraction F is the solution of $\mathcal{E}_F(R) = 0.9$.

An example of the obtained fractional exclusion radii in terms of redshift is shown on figure 7.20 along with a sample of 122 GRBs with measured redshifts. To convert our exclusions which are on the luminosity distance into redshift we use a simple flat ΛCDM cosmological evolution [122] with Hubble's constant $H_0 = 70\,\mathrm{km\,s^{-1}Mpc^{-1}}$, a matter fraction $\Omega_m = 0.3$ and dark energy fraction $\Omega_\Lambda = 0.7$. For this cosmological evolution the luminosity distance - redshift relationship is

$$d_L(z) = \frac{c(1+z)}{H_0} \int_0^z \frac{\mathrm{d}z'}{[\Omega_m (1+z')^3 + \Omega_\Lambda]^{1/2}}. \tag{7.24}$$

Unsurprisingly the unmarginalized exclusion (7.20) and the marginalized exclusion (7.22) are very similar for large fractions. Only in the low fraction limit where the binomially distributed number of close-by GRBs can deviate from its expectation value there is a significant deviation. The marginalized exclusion requires that at least a few close-by GRB are expected so that in at least 90% of cases there is one close-by GRB. One should note that these exclusions are on the cumulative distribution under the assumption that the distribution is uniform in volume up to the considered point in the radius vs fraction plane.

As expected the obtained exclusion is quite far from the observed distribution. However the extrapolation to advanced LIGO/Virgo shows a promising overlap between observed GRB redshift and gravitational wave exclusion potential, which will result hopefully into a gravitational wave detection in association with a GRB. This extrapolated exclusion can also be achieved with current detectors if one assumes an overly optimistic $E_{\mathrm{GW}} = 1\,\mathrm{M}_\odot \mathrm{c}^2$ standard siren energy, as increasing the energy by a factor 100 also increases the exclusion distance by a factor 10.

7.5 Comparison with other gravitational wave searches

The search for gravitational wave bursts associated with GRBs we presented here inserts into a broader picture of analyzes performed by the LIGO and Virgo collaborations on the 2009-2010 gravitational wave data. In particular some of these searches are also sensitive to gravitational waves potentially

emitted by GRB progenitors. We briefly present two main analyzes which overlap with the one we presented here: the search for gravitational inspiral waveforms associated with short GRBs, and the all-sky all-time search for generic gravitational wave bursts which is broad in scope. We also discuss how the search we presented here compares with those two searches as far as detection of gravitational waves produced by GRB progenitors is concerned. In particular we try to quantify the gain of the GRB triggered search with respect to the all-sky search.

7.5.1 Dedicated inspiral search

As we have discussed in chapter 4 there are indications that the progenitors of short GRBs are coalescences of compact objects where at least one of the objects is a neutron star. The total mass of the objects involved in the coalescence is thought to be lower than a few dozen solar masses, hence the gravitational wave signal seen by current interferometers would be dominated by the inspiral part as discussed in section 3.3.2.

The gravitational wave signal produced by an inspiral of compact objects is well known, and matched filtering techniques that use a grid of templates in the signal space can be used. These template based techniques are able to recover inspiral signals more efficiently than the general short signals techniques described in this chapter. For this reason a dedicated matched filtered based analysis has been developed for search for inspiral gravitational wave signals in association with short GRBs and short looking GRBs (the distinction between short and long GRBs is not clear as we have seen on figure 4.1).

This analysis has already been performed on the previous 2005-2007 joint LIGO-Virgo run [110], but its application to the latest 2009-2010 run has not been completed at the time of this thesis writing. Beside the specific signal space, this search also uses a tight coincidence window $[-5, 1]$ s between the GRB trigger and the coalescence time estimated from the gravitational wave signal. This window is much shorter than the one we use, as there are no complex precursors and stellar envelopes delaying the emission of γ-rays compared to gravitational waves as in the case of stellar collapses, and the propagation delay is small if one discards the most pessimistic predication of the electromagnetic emission model (see section 4.3.1).

This search and the one presented here are complementary, as one is broad in scope and open to a very wide range of progenitors, and the other is concentrated on a specific emission model to which it is more sensitive. A preliminary assessment was performed on a single GRB and analyzing the same sample of injected inspiral signals, with the two analysis as used for processing the 2009-20101 data. This preliminary comparison indicates that the inspiral specific search is a factor ~ 2 more sensitive for double neutron star system than the more general search presented here. The sensitivity

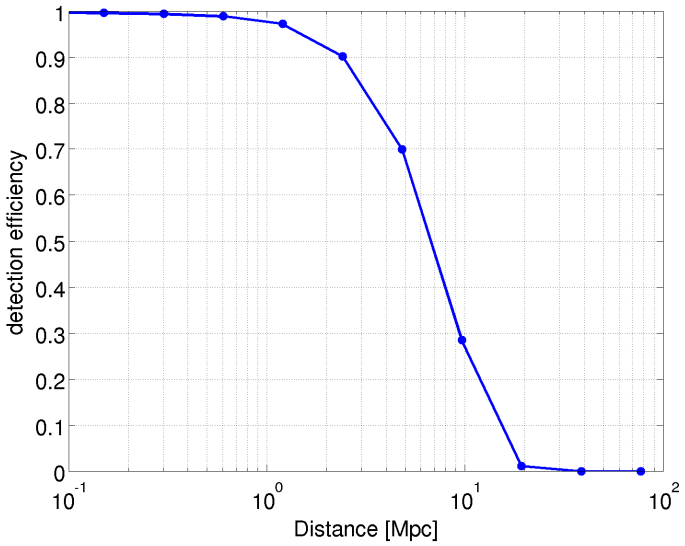

Figure 7.21: Efficiency curve $e^{\text{all-sky}}_{96\%}(r)$ for ~ 96% confidence detection by the all-sky search of elliptical sine-Gaussian waveforms at central frequency f_0 = 150 Hz and quality factor Q = 9 [123]. This efficiency is marginalized over the sky position and orientation of the rotator. To convert injected signal amplitude into distance we assume that an energy $E_{\text{GW}} = 10^{-2}\,\text{M}_\odot\text{c}^2$ is emitted by the rotator.

difference between the two is smaller for higher mass systems, as for higher masses the signals are shorter and the distinction between them and detector glitches performed using the signal shape knowledge is more difficult.

7.5.2 All-sky gravitational wave burst search

As in previous data sets [99, 100, 101] an all-sky all-time search for gravitational wave bursts is being performed on the 2009-2010 data from the LIGO and Virgo detectors. Such an analysis is among others sensitive to gravitational wave bursts emitted by GRB progenitors, and contrarily to the GRB triggered search the all-sky search is sensitive to the emission of gravitational waves even if the gamma-ray emission cone does not include any of the γ-ray spacecrafts. In section 4.6 we used a toy model to discuss how a search triggered by GRB observations is relevant compared to an all-sky search. In this section we perform a similar comparison based on actual results of theses analysis on data from the LIGO-Virgo network.

Comparisons of analyzes are notoriously difficult, especially if their stated goals are different. Here we limit the scope to only the S6C period as there was only one network configuration (H1L1) available during that time. The all-sky search has been performed by collaborators using the coherent Wave-

Burst pipeline [124, 101], and among others they performed an estimation of the sensitivity to elliptical sine-Gaussian waveforms (7.2) with a central frequency $f_0 = 150\,\mathrm{Hz}$ and a quality factor $Q = 9$. The inclination angles for these waveform is distributed uniformly in $\cos(\iota)$. The efficiency was computed for a threshold on false alarm rate $\sim 8 \times 10^{-9}\,\mathrm{Hz}$, which corresponds to a false alarm probability $\sim 4 \times 10^{-2}$ given the ~ 50 days of observational time available in S6C. The obtained efficiency curve $e^{\text{all-sky}}_{96\%}$ is shown on figure 7.21. Following the lines of the discussion in section 4.6 the effective detection volume at 96% confidence for the all-sky search can be obtained from the efficiency curve cast in terms of distance

$$V^{\text{all-sky}}_{\text{eff}} = \int_0^\infty e^{\text{all-sky}}_{96\%}(r) 4\pi r^2 \mathrm{d}r. \tag{7.25}$$

To make a fair comparison we need to estimate efficiency curves for the externally triggered search presented in this chapter with a comparable detection confidence as for the all-sky search. If we use a per GRB detection confidence of 99.9%, we obtain with the 48 GRBs analyzed during S6C a detection confidence of about 95% when taking account the trial factor of analyzing multiple GRBs. This detection confidence level is comparable to the one used for the all-sky search. For each GRB we can compute the effective detection volume to CSG150 waveforms

$$V^{\text{trig}}_{\text{eff}}(\text{circular}) = \int_0^\infty e^{\text{trig}}_{99.9\%}(r) 4\pi r^2 \mathrm{d}r, \tag{7.26}$$

these waveforms correspond to the particular case of $\iota = 0$ for the elliptical sine-Gaussian waveforms used in the all-sky search. For inclination angles ι between 0° and 30° the elliptical sine-Gaussian waveforms stay approximately circularly polarized and are only rescaled in amplitude by the inclination dependent factor $F^{1/2}(\iota)$ shown on figure 7.8. Hence as in section 4.6 we can assume that the effective detection volume to GRB progenitors with rotator gravitational wave emission and gamma-ray emission opening angle θ_c is simply a rescaling of the effective detection volume for face-on rotators. Thus we obtain

$$V^{\text{trig}}_{\text{eff}}(\theta_c) = I(\theta_c) V^{\text{trig}}_{\text{eff}}(\text{circular}) \tag{7.27}$$

where as in section 4.6 we use the integral

$$I(\theta_c) = \int_0^{\theta_c} F(\iota)^{3/2} \sin\iota \mathrm{d}\iota. \tag{7.28}$$

To obtain the effective detection volume averaged over the source sky position we take the average of the effective detection volumes from the sample of 48 GRBs analyzed in S6C. This is not a complete sampling of the distribution of gravitational wave interferometer sensitivity as a function of sky position. To estimate the statistical error of the effective volume

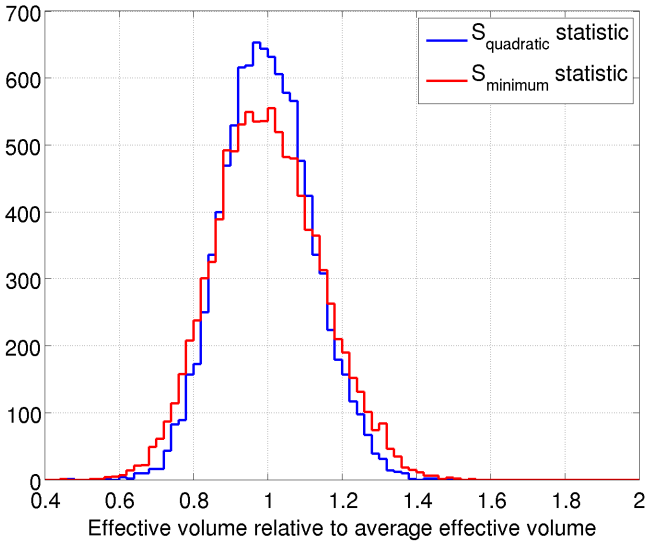

Figure 7.22: Histograms of the effective detection volume which is averaged over 48 random sky position relative to the effective detection volume when averaged over a sample of 5×10^5 sky positions. The blue histogram shows the relative effective volume distribution when the quadratic detection statistic (7.29) is used, and the red histogram shows the relative effective volume distribution when the minimum detection statistic (7.30) is used. This Monte Carlo simulation has been performed using 10^4 trials and the antenna patterns of the H1 and L1 detectors.

computation due to this limited sample of sky positions we perform a Monte Carlo simulation.

For a circularly polarized signal the SNR in a single detector depends on antenna pattern functions as $\mathrm{SNR}^2 \propto (F^+)^2 + (F^\times)^2$. For the two detector case which is of interest here the exact dependence of the analysis sensitivity is more complicated. To estimate the effect on the effective volume we consider two simplified cases: an analysis which uses the quadratic sum of SNRs as a detection statistic, and an analysis which uses the minimum of the two SNRs as a detection statistic. In the first case the dependence of the detection statistic on antenna patterns is

$$S_{\mathrm{quadratic}} \propto \left[(F^+_{\mathrm{H1}})^2 + (F^\times_{\mathrm{H1}})^2 + (F^+_{\mathrm{L1}})^2 + (F^\times_{\mathrm{L1}})^2\right]^{1/2}, \tag{7.29}$$

and in the second case it is

$$S_{\mathrm{minimum}} \propto \min\left[(F^+_{\mathrm{H1}})^2 + (F^\times_{\mathrm{H1}})^2, (F^+_{\mathrm{L1}})^2 + (F^\times_{\mathrm{L1}})^2\right]^{1/2}. \tag{7.30}$$

In both cases the detection statistic is proportional to the gravitational wave amplitude. Hence the effective detection volume for a given sky location

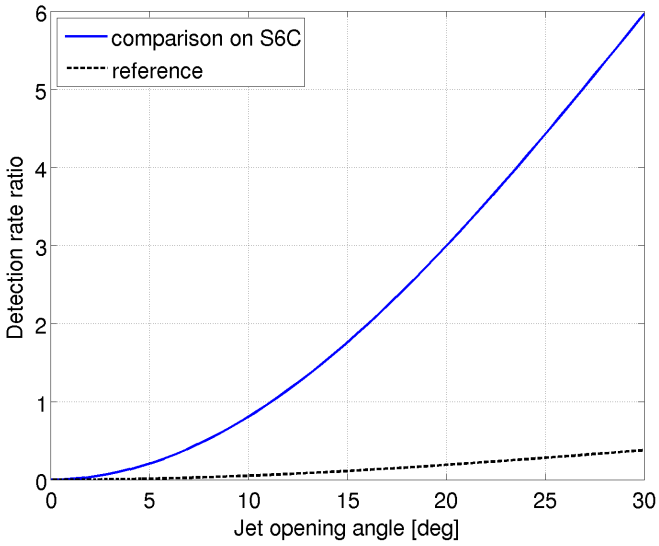

Figure 7.23: Ratio of expected number of detections between the GRB triggered search and the all-sky search in the S6C period as a function of the assumed GRB jet opening angle. The dashed black line shows the fraction $I(\theta_c)/I(\pi/2)$ of the number of expected detections for the all-sky search which have an progenitor inclination angle lower than the opening angle on the x-axis. The difference between the two curves shows the fraction of expected additional detection by the GRB triggered search relative to the total number of expected detections by the all-sky search.

will scale as the cube of the antenna patterns dependence given in either equation (7.29) or (7.30). The scatter of the average effective volume coming from drawing 48 random sky locations is shown on figure 7.22. The width of the distribution depends weakly on which of the two statistic (7.29) or (7.30) is considered, and we conclude that in the comparison performed below a statistical error of $\sim 20\%$ is due to considering only the sky locations of the 48 GRBs analyzed during S6C.

As a result the ratio of the expected numbers of detections between the two searches is

$$R(\theta_c) = \frac{N_{\text{trig}}}{N_{\text{all-sky}}} = I(\theta_c)\frac{V_{\text{eff}}^{\text{trig}}(\text{circular})}{V_{\text{eff}}^{\text{all-sky}}}. \tag{7.31}$$

The value of this ratio for $\theta_c < 30^\circ$ is shown on figure 7.23. The typical measured γ-ray emission opening angles are in the $5 - 30^\circ$ range, thus this comparison shows that the GRB triggered search should detect between 0.1 and 6 times the number of gravitational wave event coming from GRB progenitors detected by the all-sky search. The reference curve shows the

fraction of events detected by the all-sky search that have an inclination angle smaller than the γ-ray emission opening angle, and this reference is much lower than the obtained curve. Hence most of the gravitational wave events found by the GRB triggered search should be new detections that would not be found by the all-sky search.

One should note that in this discussion we assumed, as in section 4.6, that all GRBs whose progenitors are within the horizon of gravitational wave detectors are detected by γ-ray spacecrafts. This assumption is not valid if only GRB observation from Fermi and Swift are considered, as their fields of view do not cover the whole sky. Hence, in practice one should divide the expected detection ratio (7.31) by a factor ~ 1.4 to account for GRBs that are missed by both Fermi and Swift. However, this factor should be recovered by analyzing GRBs found by the Interplanetary Network of spacecrafts which has a roughly isotropic sensitivity.

In conclusion the GRB triggered search is relevant compared to the all-sky search: in the optimistic case it may provide the majority of gravitational wave detections due to GRB progenitors; and in the pessimistic case it may provide the rare but rich in astrophysical interpretations joint observation of γ-rays and gravitational waves of a GRB progenitor, that would most probably be missed otherwise.

Conclusion

We have performed a search for gravitational wave bursts associated with gamma-ray bursts (GRB) in the 2009-2010 data (S6/VSR2-3) from the LIGO and Virgo gravitational wave interferometric detectors. The main content of this thesis is the description and results of this analysis. Similar analyzes had been previously performed by the two collaborations on earlier data sets of LIGO and Virgo, but we have improved all aspects of this search with up-to-date astrophysical inputs and goals.

The first change in paradigm concerns the astrophysical priors, mainly the question of coincidence time window and gravitational waveform models.

On the question of relative time arrivals, only contemporaneous emission or γ-ray emission delayed by at most 100 s by the stellar envelope had been previously considered. We showed with a careful study of the scenarios leading to GRB precursors that a time coincidence window larger by about a factor 5 is actually needed to include all possible cases. To account for this larger coincidence window we developed some flexible segment bookkeeping. As a result our analysis pipeline is currently being adapted to perform a search for gravitational waves in association with optically detected supernovae which requires up to days long time coincidence windows.

On the question of gravitational waveform models, we performed a thorough study of gravitational wave emission scenarios to confirm that any significant emission is approximately circularly polarized. This allowed us to use the circular polarization of gravitational waves associated with GRBs as a search constraint, and to develop new coherent tests which were necessary for analyzing the new gravitational wave interferometer network configurations available in the 2009-2010 data set. Previously, the circular polarization had only been used for the interpretation of results.

The second change in paradigm concerns the search goals. Although the intent of every previous search had been the detection of gravitational waves, the analysis tuning had been geared towards obtaining the best upper limits from null results. On the contrary we have focused on optimizing the analysis towards detection. We changed the figure of merits for the coherent cuts tuning, developed a detection statistic which is robust against noise

transients, and expanded the background estimation.

As a side project related to the focus on gravitational wave detection we have explored the limitations of the time slide method of background estimation, a crucial issue when ascertaining the significance of a gravitational wave candidate. These results should be useful for any gravitational wave transients searches and have already been used when estimating the background of an event candidate coming from the blind gravitational wave injection challenge performed by the collaboration in the 2009-2010 data taking run.

Some improvements were also necessary in the collecting of results across the GRB sample. We improved the population detection statistic to increase the detection sensitivity but also to lessen the arbitrariness of removing some GRBs from the sample, such as cases where only one gravitational wave detector is available. In total we have searched for gravitational waves associated with 153 GRBs in the S6/VSR2-3 data set. We found no gravitational wave candidate for any of the 153 GRBs, and the obtained loudest events are consistent with the expected background distribution in this GRB sample.

From this null result we placed a median exclusion on the GRB progenitor distance between 7 Mpc and 17 Mpc depending on which model is considered. A completely novel aspect that we have developed is the GRB population models exclusion, which finally closes the loop on what we can learn from a non detection of gravitational waves in association with a GRB sample. We were able to exclude GRB distance distributions which are a factor 10 closer than the one currently observed through redshift measurements. Hence the factor 10 improvement in sensitivity expected for advanced LIGO and Virgo should probably lead to first detections of gravitational waves associated with GRBs.

The careful checks of the analysis procedure we performed and the change in focus give us confidence that the analysis and detection procedure will be ready when advanced LIGO and Virgo start taking data anew around 2015, with much improved sensitivity and likely occurrence of detectable gravitational waves associated with GRBs. We should note that in this readiness preparation we have participated during the 2009-2010 run in an effort lead by collaborators to automatically perform the analysis we described here as GRBs are reported through GCN. The typical latency was of $\lesssim 24$ hours after the GRB trigger time for the complete analysis, which included the careful human check of the analysis results. This latency is planned to be reduced in the future so that the result of the gravitational wave data analysis can be used to motivate extensive followup by astronomers, for instance in cases of gravitational wave candidates or relevant distance exclusions. Hopefully, such a program will yield a rich multi-messenger observation of GRB progenitors, and a deep understanding of their nature.

But before this new field of gravitational wave astronomy can be opened

a tremendous amount of work will be necessary over the next few years to construct, commission and operate the required gravitational wave detectors. A good understanding of these detectors will be a stepping-stone for a better understanding of violent phenomenas in the local universe.

Appendix A

Background estimation computations

In this appendix we give the details of the more cumbersome computations which are used in chapter 6.

A.1 Two-detector integral

To compute the integral

$$\begin{aligned} \mathrm{M}_2 &= \int_{x_1} \cdots \int_{x_N} \int_{y_1} \cdots \int_{y_N} \left[\frac{1}{R} \sum_{\pi} \sum_{k} \mathbb{1}(x_k < p) \mathbb{1}(y_{\pi(k)} < q) \right]^2 \\ &= \int \cdots \int \frac{1}{R^2} \sum_{\pi_1} \sum_{\pi_2} \sum_{k} \sum_{l} \mathbb{1}(x_k < p) \mathbb{1}(x_l < p) \mathbb{1}(y_{\pi_1(k)} < q) \mathbb{1}(y_{\pi_2(l)} < q), \end{aligned} \tag{A.1}$$

we move the sums in front of the integrals. When $k \neq l$, the integrals on x_k and x_l are independent, and the integration over $x_1, \ldots, x_N$ gives a p^2 contribution. Otherwise the integration gives a p contribution. Analogously for the y variables we get q^2 or q depending on whether $\pi_1(k) \neq \pi_2(l)$ or not.

Thus we get four types of integrals

	integral × number of such integrals	
$k = l, \pi_2^{-1} \circ \pi_1(k) = l$	$\frac{1}{R^2} pq \times NR$	(A.2a)
$k \neq l, \pi_2^{-1} \circ \pi_1(k) = l$	$\frac{1}{R^2} p^2 q \times NR(R-1)$	(A.2b)
$k = l, \pi_2^{-1} \circ \pi_1(k) \neq l$	$\frac{1}{R^2} pq^2 \times NR(R-1)$	(A.2c)
$k \neq l, \pi_2^{-1} \circ \pi_1(k) \neq l$	$\frac{1}{R^2} p^2 q^2 \times N\left[R(R-1)(N-2) + R(N-1)\right]$	(A.2d)

Here we used the fact that the composition of two circular permutation is a circular permutation, and that the only circular permutation with a fixed point is the identity.

The details of the combinatorics are as follows.

- $k = l, \pi_2^{-1} \circ \pi_1(k) = l$: There are N different k values. For each of them there is only one l that is equal to k. Here $\pi_2^{-1} \circ \pi_1$ is a circular permutation with a fixed point, i.e. the identity. There are R different π_1, and for each of them only $\pi_2 = \pi_1$ gives the identity.

- $k \neq l, \pi_2^{-1} \circ \pi_1(k) = l$: There are N different k values. For every pair $\pi_1 \neq \pi_2$ we get $\pi_1^{-1} \circ \pi_2(k) \neq k$. And the choice of this pair determines a unique l that is not equal to k. There are $R(R-1)$ such pairs.

- $k = l, \pi_2^{-1} \circ \pi_1(k) \neq l$: There are N different k values. The value of l is determined by the equality $k = l$. And there are $R(R-1)$ pairs of π_1, π_2 such that $\pi_1^{-1} \circ \pi_2(k) \neq k$.

- $k \neq l, \pi_2^{-1} \circ \pi_1(k) \neq l$: There are N different k values. In the case where $\pi_1 \neq \pi_2$, we need that $l \neq k$ and $l \neq \pi_2^{-1} \circ \pi_1(k)$, there are $N-2$ such l. In the case where $\pi_1 = \pi_2$ we get $k = \pi_2^{-1} \circ \pi_1(k)$, so there is only one inequality on l, and there are $N-1$ possible l.

By summing the four terms above and subtracting Mean^2 we obtain

$$\text{Var} = \frac{1}{R} Npq\big[1 + p(R-1) + q(R-1) + pq\big((R-1)(N-2) + (N-1)\big)\big] - (Npq)^2 \tag{A.3}$$

$$= Npq\left[\frac{1}{R} + p + q + \frac{pq - (p+q)}{R} - 2pq\right] \tag{A.4}$$

$$\simeq Npq\left[\frac{1}{R} + p + q\right], \tag{A.5}$$

A.2 Three-detector integral

We want to compute the integral

$$\mathrm{M}_2 = \int \cdots \int \frac{1}{R^2} \sum_{\pi_1} \sum_{\pi_2} \sum_{k} \sum_{l} \big[XYX'Y' + XZX'Z' + YZY'Z' + 4XYZX'Y'Z' + 2XYX'Z' + 2XYY'Z' + 2XZY'Z' - 4XYX'Y'Z' - 4XZX'Y'Z' - 4YZX'Y'Z'\big], \tag{A.6}$$

where the $'$ denotes whether the hidden variables are π_1, k or π_2, l.

Similarly to A.1 we have here eight types of integrals.

X	Y	Z	number of such integrals
$k=l,$	$\pi_2^{-1}\circ\pi_1(k)=l,$	$\pi_2\circ\pi_1^{-1}(k)=l,$	NR
$k=l,$	$\pi_2^{-1}\circ\pi_1(k)=l,$	$\pi_2\circ\pi_1^{-1}(k)\neq l,$	0
$k=l,$	$\pi_2^{-1}\circ\pi_1(k)\neq l,$	$\pi_2\circ\pi_1^{-1}(k)=l,$	0
$k=l,$	$\pi_2^{-1}\circ\pi_1(k)\neq l,$	$\pi_2\circ\pi_1^{-1}(k)\neq l,$	$NR(R-1)$
$k\neq l,$	$\pi_2^{-1}\circ\pi_1(k)=l,$	$\pi_2\circ\pi_1^{-1}(k)=l,$	0
$k\neq l,$	$\pi_2^{-1}\circ\pi_1(k)=l,$	$\pi_2\circ\pi_1^{-1}(k)\neq l,$	$NR(R-1)$
$k\neq l,$	$\pi_2^{-1}\circ\pi_1(k)\neq l,$	$\pi_2\circ\pi_1^{-1}(k)=l,$	$NR(R-1)$
$k\neq l,$	$\pi_2^{-1}\circ\pi_1(k)\neq l,$	$\pi_2\circ\pi_1^{-1}(k)\neq l,$	$NR[(R-1)(N-3)+(N-1)]$

In these combinatoric computations we need to assume that all translations are smaller than $N/4$, to ensure that $\pi_2^{-1}\circ\pi_1\circ\pi_2^{-1}\circ\pi_1(k)=k\Rightarrow\pi_1=\pi_2$. This assumption is indeed reasonable, and the final result would not be significantly different without it.

The final result is

$$\begin{aligned}\mathrm{M}_2=\frac{N}{R}\Big\{&(pq+pr+qr-2pqr)\\&+(R-1)\left[pq(p+q+pq)+pr(p+r+pr)+qr(q+r+qr)+6pqr\right.\\&\left.-4pqr(p+q+r)\right]+\left[(R-1)(N-3)+(N-1)\right](pq+pr+qr-2pqr)^2\Big\},\end{aligned}\tag{A.7}$$

A.3 "OR" case for D detectors

Using the same heuristic as in section 6.1.2 and 6.1.3 we compute the variance of the time slide estimation method for D detectors in the "OR" case. This heuristic yielded the same results as the exact computation for the 2 and 3 detector case, thus we may expect it to stay true in the general case.

As in equation (6.16), the variance is the sum of the normal Poisson variance

$$\mathrm{Var}_{\mathrm{Poiss}}=N\left(\sum_{j=1}^{D}\sum_{i=1}^{j-1}p_ip_j\right)\frac{1}{R},\tag{A.8}$$

and the variance due to time slides.

The estimate of the mean rate is

$$\mathrm{Mean}=N\left[\sum_{j=1}^{D}\sum_{i=1}^{j-1}(p_i+\delta p_i)(p_j+\delta p_j)\right]\tag{A.9}$$

$$\simeq N\left[\sum_{j=1}^{D}\sum_{i=1}^{j-1}p_ip_j+\sum_{j=1}^{D}\delta p_j\left(\sum_{\substack{i=1\\i\neq j}}^{D}p_i\right)\right],\tag{A.10}$$

which leads to a variance due to multiple reuse of the data (assuming $\langle \delta p_i^2 \rangle = \frac{p_i}{N}$)

$$\mathrm{Var}_{\mathrm{Slides}}/N = \sum_{j=1}^{D} p_j \left(\sum_{\substack{i=1 \\ i\neq j}}^{D} p_i \right) \left(\sum_{\substack{k=1 \\ k\neq j}}^{D} p_k \right) \tag{A.11}$$

$$= \left(\sum_{j=1}^{D} \sum_{\substack{i=1 \\ i\neq j}}^{D} p_i p_j \right) \left(\sum_{k=1}^{D} p_k \right) - \sum_{j=1}^{D} p_j^2 \sum_{\substack{i=1 \\ i\neq j}}^{D} p_i \tag{A.12}$$

$$= \left(\sum_{j=1}^{D} \sum_{i=1}^{j-1} p_i p_j \right) \left(\sum_{k=1}^{D} p_k \right) + \frac{1}{2} \sum_{j=1}^{D} \sum_{\substack{i=1 \\ i\neq j}}^{D} p_i p_j \left(p_j + p_i + \sum_{\substack{k=1 \\ k\neq i,\, k\neq j}}^{D} p_k \right) - \sum_{j=1}^{D} \sum_{\substack{i=1 \\ i\neq j}}^{D} p_i p_j^2 \tag{A.13}$$

$$= \left(\sum_{j=1}^{D} \sum_{i=1}^{j-1} p_i p_j \right) \left(\sum_{k=1}^{D} p_k \right) + \frac{1}{2} \sum_{j=1}^{D} \sum_{\substack{i=1 \\ i\neq j}}^{D} \sum_{\substack{k=1 \\ k\neq i,\, k\neq j}}^{D} p_i p_j p_k. \tag{A.14}$$

This general formula (A.14) is correctly giving back the extra terms in equations (6.8) and (6.16) for respectively the 2 and 3 detector case.

A.4 Monte Carlo for all-sky background estimation

In section 6.1 we discuss the limitation in the background estimation coming from Poisson distribution of triggers in each detector. However as noted before, this limitation is not valid when the same data are used for background estimation and for the final zero lag results, which is the case for instance of an all-sky all-time search. The reason is that the number of single detector triggers is exactly the same in the zero lag and the time slides used for background estimation, and their is no statistical fluctuations in their number.

As a check of this statement with performed a Monte Carlo simulation in the same condition as the realistic case of section 6.1.4, but with one major difference. For each trial we generate a fixed number of triggers $N_1 = \alpha_1 T$ and $N_2 = \alpha_2 T$ distributed uniformly in time for each detector, instead of generating Poisson distributed triggers with rates α_1 and α_2. The equivalent of figure 6.3 for this Monte Carlo simulation is shown on figure A.1. One can clearly see that in this case the Monte Carlo variance is following the standard deviation coming from the naive variance prediction (6.12), which confirms that in the case of background estimation as used for an all-sky search the single detector Poisson rate error is not a limitation.

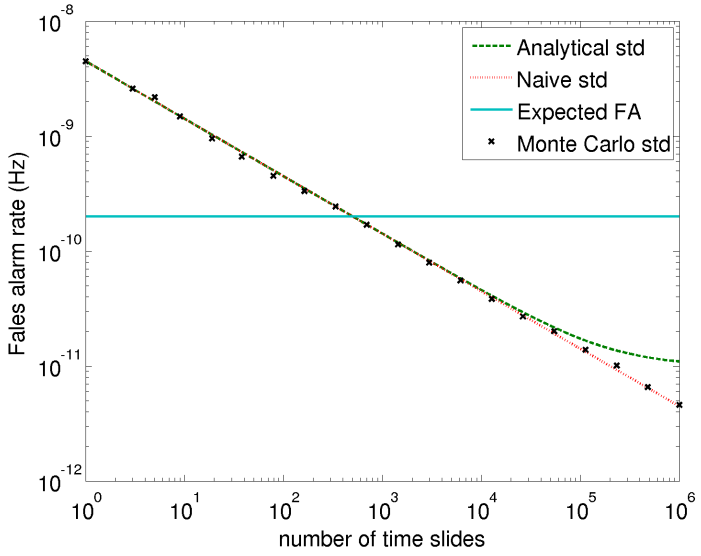

Figure A.1: The cross markers are the standard deviations of the time slide estimator $\widehat{\mathrm{FA}}$ taken from a Monte Carlo simulation, the dashed green line is the standard deviation coming from the exact theoretical formula (6.11), the dotted red line is coming from the naive formula (6.12), and the solid cyan line is the expected false alarm rate. The parameters used are: $N_1 = 2 \times 10^3$, $\alpha_2 = 5 \times 10^2$, $\Delta t = 20\,\mathrm{ms}$, and a $T = 10^7\,\mathrm{s}$. 500 trials are used for the Monte Carlo simulations.

A.5 Estimation error variance computation

We want to compute the variance of

$$\alpha_{\mathrm{Err}} = \frac{1}{RP}\sum_{i=1}^{P}\sum_{\pi}\alpha_1^i\alpha_2^{\pi(i)}\Delta t - \frac{1}{P}\sum_{i=1}^{P}\alpha_1^i\alpha_2^i\Delta t. \tag{A.15}$$

Its mean being zero, the variance is equal to the second moment

$$\mathrm{M}_2 = \left\langle \frac{\Delta t^2}{P^2}\sum_i\sum_j\left[\sum_{\pi_1}\sum_{\pi_2}\frac{1}{R^2}\alpha_1^i\alpha_1^j\alpha_2^{\pi(i)}\alpha_2^{\pi(j)} - \frac{2}{R}\sum_{\pi}\alpha_1^i\alpha_2^{\pi(i)}\alpha_1^j\alpha_2^j + \alpha_1^i\alpha_2^i\alpha_1^j\alpha_2^j\right]\right\rangle. \tag{A.16}$$

Using a method similar to the one used in A.1 and A.2 we obtain the mean values of the three terms in the equation above

$$\frac{\Delta t^2}{P^2}\left\{\frac{P}{R}\alpha_1^2\alpha_2^2 {a_1'}^2 {a_2'}^2 + \frac{P}{R}(R-1)\alpha_1^2\alpha_2^2({a_1'}^2 + {a_2'}^2)\right. \tag{A.17}$$
$$\left. + \frac{P}{R}\left[(R-1)(P-2)+(P-1)\right]\alpha_1^2\alpha_2^2\right\},$$
$$-\frac{\Delta t^2}{P^2}\frac{2}{R}\left[PR\alpha_1^2\alpha_2^2({a_1'}^2 + {a_2'}^2) + P(P-2)R\alpha_1^2\alpha_2^2\right], \tag{A.18}$$
$$\frac{\Delta t^2}{P^2}\left[P(P-1)\alpha_1^2\alpha_2^2 + P\alpha_1^2\alpha_2^2 {a_1'}^2 {a_2'}^2\right], \tag{A.19}$$

where ${a_1'}^2 = 1 + a_1^2$ and ${a_2'}^2 = 1 + a_2^2$. After collecting the terms we obtain

$$\mathrm{M}_2 = \frac{\Delta t^2}{P^2}\left[\frac{P}{R}\alpha_1^2\alpha_2^2({a_1'}^2{a_2'}^2 - {a_1'}^2 - {a_2'}^2 + 1) + \alpha_1^2\alpha_2^2 P({a_1'}^2{a_2'}^2 - {a_1'}^2 - {a_2'}^2 + 1)\right] \tag{A.20}$$
$$= \frac{\Delta t^2}{P}\alpha_1^2\alpha_2^2\left(1 + \frac{1}{R}\right)a_1^2 a_2^2. \tag{A.21}$$

Appendix B

Detailed S6/VSR2-3 GRB analysis results

In this appendix we give the details of the sample of 153 GRBs analyzed by the search for gravitational wave bursts associated with GRBs in the S6/VSR2-3 data which is discussed in chapter 7.

Table B.1 gives the details and limits on associated gravitational wave emission for each of the studied GRBs. The first four columns are: the GRB data in YYMMDD format, the trigger time, and sky position (right ascension and declination). The next two columns are the analysis parameters: the gravitational wave detector network used and the analyzed time window. The remaining columns display the result of the search. The p-value of the loudest on-source event and the number of background trials used to estimate this p-value. A p-value of "–" indicates that no event survived all the consistency cuts. The 90% confidence lower limits on the distance to the GRB for different waveform models are given. For the black hole - neutron star and neutron star - neutron star inspirals the distribution of parameters discussed in section 7.2.3 is assumed. For the three sets of circular sine-Gaussian a standard siren energy emission of $E_{\rm GW} = 10^{-2}\,{\rm M}_\odot{\rm c}^2$ is assumed.

Table B.2 gives some additional details about the analyzed sample of GRBs. The first two columns are: the GRB date in YYMMDD format and the trigger time. The columns three through five give the magnitude of the antenna patterns functions (2.9) for each detector characterized by the value of $\sqrt{F_+^2 + F_\times^2}$ for the sky location of the GRB, a dash "–" means that the given detector was not used in the analysis. The sixth column give the 1-sigma sky location probability coverage radius as used in the analysis, this radius includes both statistical and systematic errors of the given γ-ray detector. The remaining columns provide additional information about the GRB trigger: the duration T_{90} of the γ-ray light curve, the measured redshift if available, and the name of the γ-ray detector providing the sky location used in the analysis.

Table B.1: GRB sample and per GRB search results

Date	UTC time	RA	Dec	network	window	p-value	number of trials	Exclusion distance (Mpc) CSG100	CSG150	NSBH	CSG300	BNS
090709	15:07:42	$6^h14^m05^s$	$64°05'$	L1V1	[-600,60]	0.274	(2455)	12.6	12.4	11.4	6.1	5.1
090717	00:49:32	$5^h47^m19^s$	$-64°11'$	H1V1	[-120,70]	0.301	(7943)	19.6	19.9	15.2	9.7	7.5
090719	01:31:26	$22^h45^m04^s$	$-67°52'$	H1V1	[-600,60]	0.0244	(614)	9.7	10.6	10.3	6.3	4.3
090720	06:38:08	$13^h34^m46^s$	$-10°20'$	L1V1	[-600,60]	0.891	(2314)	13.5	12.5	12.1	6.4	5.8
090720	17:02:56	$13^h31^m59^s$	$-54°48'$	L1V1	[-600,60]	0.731	(2599)	8.0	7.1	7.5	3.8	3.2
090726	05:14:07	$16^h01^m48^s$	$36°45'$	H1L1V1	[-600,60]	0.615	(860)	24.5	20.2	15.7	6.4	8.4
090726	22:42:27	$16^h34^m43^s$	$72°52'$	H1V1	[-600,67]	0.884	(2562)	18.5	17.1	17.2	9.3	8.0
090727	22:42:18	$21^h03^m40^s$	$64°56'$	L1V1	[-600,302]	0.362	(550)	12.1	10.4	11.3	4.9	4.2
090727	23:32:29	$22^h53^m25^s$	$-46°42'$	L1V1	[-600,60]	0.0775	(1780)	3.5	3.3	3.1	1.8	1.5
090802	05:39:03	$3^h24^m07^s$	$37°53'$	H1L1V1	[-600,60]	0.298	(1186)	16.2	15.1	13.2	4.7	6.2
090802	15:58:23	$17^h48^m04^s$	$-71°46'$	H1L1V1	[-600,60]	0.724	(1596)	20.7	20.5	19.4	8.3	8.9
090807	15:00:27	$18^h14^m57^s$	$10°17'$	H1V1	[-600,141]	0.489	(1719)	9.7	9.8	10.0	5.3	4.2
090809	17:31:14	$21^h54^m39^s$	$-0°05'$	H1L1V1	[-600,60]	0.44	(711)	20.0	19.2	18.9	6.4	8.5
090809	23:28:14	$6^h20^m60^s$	$0°10'$	L1V1	[-600,60]	0.731	(2770)	10.0	9.5	9.4	4.9	4.1
090810	15:49:07	$11^h15^m43^s$	$-76°24'$	H1V1	[-600,60]	0.352	(2627)	11.7	14.6	12.1	7.1	5.1
090814	00:52:19	$15^h58^m27^s$	$25°35'$	L1V1	[-600,80]	0.928	(2838)	11.9	9.9	10.1	6.1	4.5
090814	01:21:01	$4^h19^m05^s$	$60°35'$	L1V1	[-600,60]	0.337	(3430)	11.1	10.9	11.3	5.6	4.6
090814	22:47:28	$20^h30^m35^s$	$45°43'$	H1L1V1	[-600,60]	0.815	(1272)	18.4	17.2	15.7	6.3	6.3
090815	07:12:12	$2^h44^m07^s$	$-2°44'$	H1L1V1	[-600,200]	0.466	(986)	6.1	5.4	5.7	1.3	2.4
090815	10:30:41	$1^h25^m40^s$	$53°26'$	H1V1	[-600,60]	0.851	(3504)	10.5	10.6	8.2	5.6	3.3
090815	23:21:39	$4^h17^m57^s$	$-65°57'$	H1L1V1	[-120,60]	0.359	(2804)	31.6	29.8	31.4	12.0	12.5
090815	22:41:46	$16^h45^m02^s$	$52°56'$	L1V1	[-600,60]	0.587	(3052)	16.2	15.7	12.2	6.9	4.9
090820	12:13:16	$21^h13^m02^s$	$-18°35'$	H1V1	[-600,60]	0.751	(1719)	10.2	12.2	7.0	5.8	3.3
090823	03:10:53	$3^h18^m07^s$	$-17°35'$	L1V1	[-600,60]	0.102	(1630)	6.9	5.9	5.9	2.7	2.6
090824	22:02:19	$3^h06^m35^s$	$59°49'$	H1V1	[-600,60]	0.83	(1250)	9.0	9.4	8.9	4.8	4.1
090826	01:37:31	$9^h22^m28^s$	$-0°07'$	H1V1	[-600,60]	0.731	(2900)	2.3	2.7	0.5	0.4	1.2

Table B.1: *continued*

Date	UTC time	RA	Dec	network	window	p-value	number of trials	Exclusion distance (Mpc) CSG100	CSG150	NSBH	CSG300	BNS
090827	19:06:26	$1^h13^m44^s$	$-50°54'$	H1V1	[-600,60]	0.225	(2385)	12.6	15.1	13.4	8.6	6.4
090829	16:50:40	$23^h39^m57^s$	$-9°22'$	H1V1	[-600,100]	0.597	(1637)	7.4	9.0	8.1	4.8	3.4
090831	07:36:36	$9^h40^m23^s$	$50°58'$	H1V1	[-600,70]	0.801	(3483)	6.7	7.2	5.5	2.1	2.4
090926	21:55:48	$3^h05^m14^s$	$-38°60'$	H1L1V1	[-600,110]	0.362	(1594)	21.3	19.1	22.7	7.5	10.2
090927	10:07:16	$22^h55^m42^s$	$-70°58'$	H1L1V1	[-600,60]	0.0913	(1653)	19.8	16.0	17.3	9.0	7.7
090929	04:33:03	$3^h26^m47^s$	$-7°20'$	H1V1	[-600,60]	0.225	(978)	7.0	8.7	7.8	4.4	3.2
091003	04:35:45	$16^h45^m33^s$	$36°35'$	L1V1	[-600,60]	0.126	(3116)	9.8	8.8	8.0	3.2	3.3
091017	20:40:24	$14^h03^m11^s$	$25°29'$	H1V1	[-600,60]	0.913	(3674)	9.9	7.5	7.3	4.9	2.5
091018	22:58:20	$21^h27^m19^s$	$-23°05'$	L1V1	[-600,60]	0.403	(3011)	5.1	3.6	2.8	1.6	1.2
091019	18:00:40	$15^h04^m07^s$	$80°20'$	H1L1V1	[-600,60]	0.306	(1212)	20.8	20.4	19.5	8.2	8.1
091020	21:36:44	$11^h42^m54^s$	$50°59'$	L1V1	[-600,60]	0.398	(3934)	13.1	9.5	10.2	5.2	4.3
091022	18:03:27	$15^h35^m19^s$	$-36°16'$	H1V1	[-600,60]	0.187	(3293)	5.3	4.7	5.4	3.3	2.0
091026	11:38:48	$9^h08^m19^s$	$-23°39'$	H1V1	[-600,60]	0.381	(1970)	5.0	5.1	3.3	3.0	1.0
091030	19:52:26	$2^h46^m40^s$	$21°32'$	H1V1	[-600,160]	0.16	(854)	10.0	11.5	9.1	4.9	4.3
091031	12:00:28	$4^h46^m47^s$	$-57°30'$	H1V1	[-600,100]	0.668	(2437)	13.5	14.2	14.5	6.2	6.0
091103	21:53:51	$11^h22^m24^s$	$11°18'$	L1V1	[-600,60]	–	(3178)	4.5	5.1	4.5	2.2	1.9
091109	04:57:43	$20^h37^m00^s$	$-44°11'$	H1V1	[-600,60]	0.291	(2693)	13.1	13.0	12.5	7.3	5.9
091109	21:49:03	$7^h31^m00^s$	$-54°06'$	H1V1	[-600,60]	0.997	(4200)	12.6	14.2	15.0	8.7	6.5
091115	04:14:50	$20^h31^m02^s$	$71°28'$	H1L1V1	[-120,60]	0.0115	(5303)	14.7	14.1	14.1	7.2	5.9
091122	03:54:20	$7^h23^m26^s$	$0°34'$	H1V1	[-600,60]	0.0963	(3726)	11.2	11.9	9.6	5.5	3.9
091123	01:55:59	$22^h31^m16^s$	$13°21'$	L1V1	[-120,60]	0.933	(3288)	13.1	9.8	10.3	5.4	4.5
091127	23:25:45	$2^h26^m19^s$	$-18°57'$	L1V1	[-120,60]	0.862	(10011)	5.7	5.9	4.9	2.3	2.4
091128	06:50:34	$8^h30^m45^s$	$1°44'$	H1V1	[-600,60]	0.202	(3304)	6.6	6.7	5.9	3.1	2.5
091202	01:44:06	$17^h09^m59^s$	$-1°54'$	H1V1	[-600,60]	0.3	(2593)	9.7	10.5	8.6	4.6	3.5
091202	05:15:42	$0^h55^m26^s$	$9°05'$	H1V1	[-600,60]	0.519	(1367)	13.1	12.6	11.4	6.2	4.7
091202	23:10:04	$9^h15^m18^s$	$62°33'$	H1V1	[-600,60]	0.931	(2261)	13.2	14.4	12.5	6.5	6.0

Table B.1: *continued*

Date	UTC time	RA	Dec	network	window	p-value	number of trials	Exclusion distance (Mpc) CSG100	CSG150	NSBH	CSG300	BNS
091215	05:37:26	$18^h52^m59^s$	$17°33'$	H1L1	[-120,60]	0.537	(12499)	18.6	18.5	17.3	8.1	7.9
091219	11:04:45	$19^h37^m57^s$	$71°55'$	H1L1V1	[-600,60]	0.815	(1333)	11.1	12.4	11.6	6.1	5.7
091220	10:36:50	$11^h07^m04^s$	$4°49'$	H1L1V1	[-600,60]	0.56	(2146)	18.8	21.0	18.1	8.6	8.2
091223	12:15:53	$15^h25^m04^s$	$54°44'$	H1L1	[-600,60]	0.798	(2691)	19.3	24.3	22.1	9.9	9.5
091224	08:57:36	$22^h04^m40^s$	$18°16'$	H1L1	[-600,60]	0.158	(1086)	13.5	16.4	14.8	6.4	6.4
091227	07:03:13	$19^h47^m45^s$	$2°36'$	H1L1V1	[-600,60]	0.837	(2668)	18.8	19.7	17.5	8.6	8.5
100101	00:39:49	$20^h29^m16^s$	$-27°00'$	H1L1	[-120,60]	0.118	(6776)	6.4	9.1	7.1	4.5	3.4
100103	17:42:32	$7^h29^m28^s$	$-34°29'$	H1L1V1	[-600,60]	0.943	(2083)	24.6	26.0	27.3	12.1	11.7
100111	04:12:49	$16^h28^m06^s$	$15°32'$	H1L1	[-600,60]	0.68	(2811)	16.8	18.8	17.8	8.6	8.3
100112	10:01:17	$16^h00^m33^s$	$-75°06'$	H1L1	[-600,60]	0.398	(2358)	13.4	15.7	16.3	7.5	6.5
100201	14:06:17	$8^h52^m24^s$	$-37°17'$	H1L1	[-120,60]	0.889	(7023)	26.2	25.9	24.0	10.8	10.5
100206	13:30:05	$3^h08^m40^s$	$13°10'$	H1L1	[-600,60]	0.549	(2830)	18.6	21.0	18.2	8.8	8.4
100212	13:11:45	$8^h57^m04^s$	$32°13'$	H1L1	[-120,60]	0.544	(2100)	8.2	6.8	7.1	3.7	3.4
100213	22:27:48	$23^h17^m30^s$	$43°22'$	H1L1	[-600,60]	0.0359	(3978)	26.6	22.4	23.1	10.0	10.8
100213	22:58:34	$8^h17^m16^s$	$43°28'$	H1L1	[-600,60]	0.487	(3980)	15.9	15.6	14.6	7.1	6.5
100216	10:07:00	$10^h17^m03^s$	$35°31'$	H1L1	[-600,60]	0.735	(3972)	31.0	29.1	28.1	13.0	12.2
100219	15:15:46	$10^h16^m48^s$	$-12°33'$	H1L1	[-600,60]	0.406	(3876)	14.1	17.3	15.1	6.7	6.9
100221	08:50:26	$1^h48^m28^s$	$-17°25'$	H1L1	[-600,60]	0.638	(2272)	26.4	29.1	25.2	12.5	11.4
100225	05:59:05	$23^h31^m24^s$	$15°02'$	H1L1	[-600,60]	0.123	(1322)	16.7	20.0	19.1	8.3	8.3
100225	13:55:31	$20^h57^m04^s$	$0°13'$	H1L1	[-120,60]	0.999	(839)	11.9	13.7	14.2	5.8	5.7
100228	20:57:47	$7^h51^m57^s$	$18°38'$	H1L1	[-600,60]	0.0826	(3282)	13.6	13.8	13.5	6.8	6.2
100301	05:21:46	$13^h27^m24^s$	$19°50'$	H1L1	[-600,60]	0.902	(2603)	19.1	24.0	18.5	9.1	8.7
100315	08:39:12	$13^h55^m35^s$	$30°08'$	H1L1	[-600,60]	0.802	(1974)	36.9	43.5	36.6	16.9	16.5
100316	02:23:00	$16^h47^m48^s$	$71°49'$	H1L1	[-600,60]	0.0202	(544)	16.2	18.2	16.2	6.9	6.9
100316	08:57:59	$2^h09^m14^s$	$-67°60'$	H1L1	[-600,60]	0.764	(1219)	37.4	39.4	35.6	16.5	15.9
100322	07:06:18	$5^h05^m57^s$	$42°41'$	H1L1	[-600,60]	0.0645	(3331)	18.3	18.5	17.7	7.4	8.0

Table B.1: *continued*

Date	UTC time	RA	Dec	network	window	p-value	number of trials	Exclusion distance (Mpc) CSG100	CSG150	NSBH	CSG300	BNS
100324	00:21:27	$6^h34^m26^s$	$-9°44'$	H1L1	[-600,60]	0.686	(1438)	28.0	34.3	31.1	12.6	12.4
100324	04:07:36	$2^h38^m41^s$	$-19°17'$	H1L1	[-600,60]	0.835	(3675)	19.2	20.2	18.1	7.3	8.1
100325	05:54:43	$13^h56^m33^s$	$-79°06'$	H1L1	[-600,60]	0.37	(3973)	19.1	21.8	20.6	8.7	8.2
100325	06:36:08	$22^h00^m57^s$	$-26°28'$	H1L1	[-600,60]	0.679	(3821)	35.5	36.7	33.6	14.1	13.8
100326	07:03:05	$8^h44^m57^s$	$-28°11'$	H1L1	[-600,60]	0.499	(3658)	12.9	13.1	11.8	5.6	4.9
100327	09:43:15	$22^h19^m43^s$	$-5°50'$	H1L1	[-600,60]	0.883	(2496)	18.5	18.4	16.6	7.1	7.1
100328	03:22:44	$10^h23^m45^s$	$47°02'$	H1L1	[-600,60]	–	(3133)	28.0	28.9	31.5	12.4	13.5
100331	21:08:38	$20^h11^m56^s$	$-11°04'$	H1L1	[-600,60]	0.448	(2482)	13.1	14.1	13.4	6.1	6.1
100401	07:07:31	$19^h23^m15^s$	$-8°15'$	H1L1	[-600,100]	0.518	(3672)	14.2	17.6	15.1	6.2	6.4
100401	18:34:10	$4^h41^m02^s$	$44°31'$	H1L1	[-120,60]	0.792	(5005)	21.2	25.0	24.2	10.8	11.4
100410	08:31:57	$8^h40^m04^s$	$21°29'$	H1L1	[-120,60]	0.276	(12510)	3.0	3.6	3.2	1.5	1.2
100410	17:45:46	$21^h16^m59^s$	$37°26'$	H1L1	[-600,60]	0.669	(1772)	24.8	28.3	26.0	12.7	12.1
100418	21:10:08	$17^h05^m25^s$	$11°27'$	H1L1	[-600,60]	0.297	(2121)	27.7	26.5	28.3	11.8	11.4
100420	00:12:06	$8^h02^m11^s$	$-5°49'$	H1L1	[-600,60]	0.183	(3158)	29.9	32.6	27.9	12.5	11.9
100420	05:22:42	$19^h44^m21^s$	$55°45'$	H1L1	[-600,60]	0.92	(2107)	19.9	19.1	17.1	7.5	8.2
100423	05:51:25	$7^h58^m40^s$	$5°47'$	H1L1	[-600,60]	0.478	(3700)	19.3	18.6	17.0	6.4	7.1
100425	02:50:45	$19^h56^m38^s$	$-26°28'$	H1L1	[-600,60]	0.849	(2834)	38.5	41.4	36.4	15.6	15.8
100427	08:31:55	$5^h56^m41^s$	$-3°28'$	H1L1	[-600,60]	0.621	(2200)	27.2	25.5	24.7	11.2	11.3
100502	08:33:02	$8^h44^m02^s$	$18°23'$	H1L1	[-600,60]	0.104	(2802)	2.2	4.0	6.2	2.6	2.4
100507	13:51:15	$0^h11^m36^s$	$-79°01'$	H1L1	[-600,60]	0.107	(2658)	21.6	23.9	20.1	7.8	8.9
100508	09:20:42	$5^h05^m03^s$	$-20°45'$	H1L1	[-120,60]	0.361	(10725)	46.5	47.3	45.2	18.2	18.0
100515	11:13:09	$18^h21^m52^s$	$27°01'$	H1L1	[-600,60]	0.177	(2176)	35.9	38.2	36.8	17.1	16.2
100516	08:50:41	$18^h17^m38^s$	$-8°12'$	H1L1	[-600,60]	0.274	(2188)	27.0	28.9	27.3	11.1	11.9
100516	09:30:38	$19^h50^m43^s$	$18°40'$	H1L1	[-600,60]	0.205	(2177)	36.3	35.0	31.5	14.3	13.8
100517	01:43:08	$6^h43^m43^s$	$-28°59'$	H1L1	[-600,60]	0.849	(3960)	18.5	18.6	17.2	7.0	8.0
100517	03:42:08	$16^h14^m21^s$	$-10°22'$	H1L1	[-600,60]	0.939	(3105)	1.9	3.4	3.1	2.7	2.9

Table B.1: *continued*

Date	UTC time	RA	Dec	network	window	p-value	number of trials	Exclusion distance (Mpc) CSG100	CSG150	NSBH	CSG300	BNS
100517	05:49:52	$0^h41^m45^s$	$4°26'$	H1L1	[-600,60]	0.446	(3863)	22.7	26.8	26.6	10.5	11.5
100517	15:19:58	$3^h30^m55^s$	$-71°52'$	H1L1	[-600,60]	0.282	(2763)	19.2	23.9	22.1	10.2	9.7
100517	03:09:50	$2^h42^m31^s$	$-44°19'$	H1L1	[-600,60]	0.931	(3367)	30.2	35.9	33.3	13.6	16.1
100526	19:00:38	$0^h03^m06^s$	$-37°55'$	H1L1	[-600,64]	0.772	(646)	8.3	12.5	10.8	5.4	5.0
100604	06:53:34	$16^h33^m12^s$	$-73°11'$	H1L1	[-600,60]	0.5	(3475)	18.8	19.3	19.3	9.0	8.4
100608	09:10:06	$2^h02^m09^s$	$20°27'$	H1L1	[-600,60]	0.905	(2469)	21.3	24.9	21.7	10.4	9.5
100628	08:16:40	$15^h03^m46^s$	$-31°39'$	H1L1	[-600,60]	0.333	(1585)	18.7	20.6	19.7	8.3	8.6
100701	11:45:23	$2^h52^m26^s$	$-2°13'$	H1L1	[-600,60]	0.0923	(2697)	13.3	14.1	12.9	6.3	6.0
100709	14:27:32	$9^h30^m07^s$	$17°23'$	H1L1	[-600,60]	0.249	(3149)	13.2	16.9	13.1	6.5	6.2
100717	08:55:06	$19^h08^m14^s$	$-0°40'$	H1L1	[-600,60]	0.907	(3954)	26.3	27.3	25.2	10.7	11.4
100717	10:41:47	$20^h17^m14^s$	$19°32'$	H1L1	[-600,60]	0.67	(3644)	28.5	31.3	31.3	13.2	12.5
100719	23:44:04	$7^h33^m12^s$	$5°24'$	H1L1	[-600,60]	0.0329	(2281)	13.8	15.3	12.5	5.9	5.9
100722	06:58:24	$2^h07^m14^s$	$56°14'$	H1L1	[-120,60]	0.776	(2989)	15.2	17.7	16.2	6.7	7.1
100725	07:12:52	$11^h05^m52^s$	$-26°40'$	H1L1	[-600,141]	0.824	(3924)	31.9	35.5	33.6	14.0	13.7
100725	11:24:34	$19^h20^m06^s$	$76°57'$	H1L1	[-600,200]	0.0397	(1462)	26.0	25.9	23.5	10.8	10.1
100727	05:42:17	$10^h16^m44^s$	$-21°25'$	H1L1	[-600,84]	0.41	(3721)	26.9	31.3	29.2	12.6	12.4
100802	05:45:36	$0^h09^m55^s$	$47°45'$	H1L1	[-600,487]	0.673	(1181)	34.5	36.4	32.9	16.3	14.7
100804	02:29:26	$16^h35^m52^s$	$27°27'$	H1L1	[-600,60]	0.244	(3746)	36.7	40.4	37.4	18.0	16.6
100814	03:50:11	$1^h29^m54^s$	$-17°59'$	H1L1V1	[-600,175]	0.282	(1456)	15.5	17.3	17.1	7.3	7.7
100814	08:25:25	$8^h11^m16^s$	$18°29'$	L1V1	[-120,60]	0.611	(9426)	6.9	14.1	12.4	8.0	5.0
100816	00:12:41	$6^h48^m28^s$	$-26°40'$	L1V1	[-120,60]	–	(10328)	3.5	6.6	3.8	3.5	2.1
100816	00:37:51	$23^h26^m57^s$	$26°34'$	L1V1	[-600,60]	0.9	(2199)	6.8	9.5	8.9	5.8	4.5
100819	11:56:35	$18^h38^m23^s$	$-50°02'$	H1L1V1	[-600,60]	0.8	(2057)	25.2	30.1	25.7	12.5	12.1
100820	08:56:58	$17^h15^m09^s$	$-18°31'$	H1L1V1	[-600,60]	0.0304	(1807)	13.5	18.2	16.6	7.2	7.5
100823	17:25:35	$1^h22^m49^s$	$5°51'$	H1L1V1	[-120,60]	0.0681	(5625)	6.8	8.7	8.4	4.0	3.6
100825	06:53:48	$16^h53^m45^s$	$-56°34'$	H1L1V1	[-600,60]	0.993	(1999)	18.4	18.7	16.0	7.3	7.3

Table B.1: *continued*

Date	UTC time	RA	Dec	network	window	p-value	number of trials	Exclusion distance (Mpc) CSG100	CSG150	NSBH	CSG300	BNS
100826	22:58:22	$19^h05^m43^s$	$-32°38'$	L1V1	[-600,60]	0.9	(1454)	4.9	4.8	4.3	2.3	1.6
100829	21:02:08	$6^h06^m52^s$	$29°43'$	H1L1V1	[-600,60]	0.115	(1034)	9.5	12.3	9.0	4.7	4.3
100904	01:33:43	$11^h31^m37^s$	$-16°11'$	L1V1	[-600,60]	0.408	(576)	9.1	13.1	12.1	7.3	5.8
100905	15:08:14	$2^h06^m10^s$	$14°55'$	H1L1	[-600,60]	0.898	(2802)	17.6	17.3	16.5	6.3	7.1
100905	21:46:22	$17^h30^m36^s$	$13°05'$	H1L1V1	[-600,60]	0.27	(1712)	12.5	17.8	14.8	7.5	6.4
100906	13:49:27	$1^h54^m47^s$	$55°38'$	H1L1	[-120,115]	0.701	(5759)	26.6	30.5	29.4	12.2	12.5
100916	18:41:12	$10^h07^m50^s$	$-59°23'$	H1L1V1	[-600,60]	–	(1735)	5.5	8.3	8.0	3.6	3.3
100917	05:03:25	$19^h16^m59^s$	$-17°07'$	H1L1V1	[-600,66]	0.00158	(19032)	15.5	18.2	16.9	8.0	8.1
100918	20:42:18	$20^h33^m38^s$	$-45°58'$	H1L1V1	[-600,60]	0.85	(968)	18.9	19.4	16.8	7.8	7.0
100919	21:12:16	$10^h52^m57^s$	$6°01'$	H1L1V1	[-600,60]	0.223	(1390)	20.7	19.9	22.7	10.3	9.3
100922	14:59:43	$23^h47^m55^s$	$-25°11'$	H1V1	[-600,60]	0.666	(1782)	7.1	9.2	6.6	4.7	2.2
100924	03:58:08	$0^h02^m41^s$	$7°00'$	H1L1	[-600,96]	0.341	(2937)	27.1	29.2	26.5	12.0	11.8
100926	14:17:03	$14^h50^m59^s$	$-72°21'$	H1L1	[-600,60]	0.486	(2260)	26.1	29.5	27.8	13.1	12.3
100926	16:39:54	$2^h54^m19^s$	$-11°06'$	H1L1V1	[-600,60]	0.591	(1206)	6.1	12.2	12.2	5.1	5.8
100928	02:19:52	$14^h52^m08^s$	$-28°33'$	H1L1	[-600,60]	0.408	(2564)	22.8	26.1	22.9	10.1	10.0
100929	21:59:45	$12^h12^m07^s$	$-24°56'$	H1V1	[-600,60]	0.783	(1771)	8.7	10.1	9.0	6.0	4.2
101002	06:41:26	$21^h33^m23^s$	$-27°28'$	H1V1	[-600,60]	0.0497	(3601)	6.8	9.5	7.2	4.6	3.4
101003	05:51:08	$11^h43^m24^s$	$2°29'$	H1L1V1	[-600,60]	0.837	(2378)	26.7	34.1	30.1	13.1	12.7
101004	10:13:49	$15^h28^m52^s$	$-43°59'$	H1L1	[-600,60]	0.303	(3142)	40.5	46.8	39.5	17.5	17.4
101010	04:33:46	$3^h08^m45^s$	$43°34'$	L1V1	[-600,60]	0.626	(1668)	9.7	9.0	8.0	4.7	3.3
101013	09:52:42	$19^h28^m19^s$	$-49°38'$	H1L1V1	[-600,60]	0.796	(2480)	28.3	35.8	33.0	15.0	15.4
101015	13:24:02	$4^h52^m38^s$	$15°28'$	H1L1	[-600,60]	0.845	(633)	27.9	29.9	30.8	12.4	12.5
101016	05:50:16	$8^h52^m09^s$	$-4°37'$	L1V1	[-600,60]	0.721	(2841)	7.6	9.4	8.6	4.7	3.8

Table B.2: Additional information on the GRB sample

Date	UTC time	antenna response H1	L1	V1	error (deg)	T_{90} (sec)	redshift	γ-ray detector
090709	15:07:42	–	0.78	0.74	0.021	27.2	–	Swift
090717	00:49:32	0.74	–	0.82	7.6	70	–	Fermi
090719	01:31:26	0.89	–	0.47	7.6	16	–	Fermi
090720	06:38:08	–	0.48	0.80	0.036	7	–	Swift
090720	17:02:56	–	0.57	0.41	8	20	–	Fermi
090726	05:14:07	0.95	0.75	0.10	10	n/a	–	Fermi
090726	22:42:27	0.72	–	0.81	0.02	67.0	2.7	Swift
090727	22:42:18	–	0.28	0.92	0.026	302	–	Swift
090727	23:32:29	–	0.81	0.10	0.72	25	–	IPN
090802	05:39:03	0.37	0.35	0.99	9	0.128	–	Fermi
090802	15:58:23	0.89	0.77	0.57	13	n/a	–	Fermi
090807	15:00:27	0.59	–	0.39	0.021	140.8	–	Swift
090809	17:31:14	0.54	0.82	0.33	0.024	5.4	2.7	Swift
090809	23:28:14	–	0.48	0.53	7.6	15	–	Fermi
090810	15:49:07	0.74	–	0.63	9.3	n/a	–	Fermi
090814	00:52:19	–	1.00	0.49	0.024	80	0.7-2.2	Swift
090814	01:21:01	–	0.38	0.73	0.035	50	–	Integral
090814	22:47:28	0.46	0.42	1.00	7.8	n/a	–	Fermi
090815	07:12:12	0.14	0.41	0.56	11	200	–	Fermi
090815	10:30:41	0.97	–	0.45	9.4	30	–	Fermi
090815	23:21:39	0.85	0.80	0.68	0.032	0.6	–	Swift
090815	22:41:46	–	0.81	0.78	7.9	n/a	–	Fermi
090820	12:13:16	0.47	–	0.86	12	11.2	–	Fermi
090823	03:10:53	–	0.66	0.43	13	n/a	–	Fermi
090824	22:02:19	0.54	–	0.63	14	n/a	–	Fermi
090826	01:37:31	0.11	–	0.51	12	8.5	–	Fermi
090827	19:06:26	0.82	–	0.71	0.033	7	–	Swift
090829	16:50:40	0.40	–	0.47	8.2	100	–	Fermi
090831	07:36:36	0.15	–	0.87	7.7	69.1	–	Fermi
090926	21:55:48	0.98	0.96	0.35	0.012	109.7	1.2	Swift
090927	10:07:16	0.56	0.45	0.89	0.019	2.2	1.4	Swift
090929	04:33:03	0.23	–	0.59	7.6	8.5	–	Fermi
091003	04:35:45	–	0.26	0.50	0.15	21.1	0.9	FermiLAT
091017	20:40:24	0.93	–	0.29	11	n/a	–	Fermi
091018	22:58:20	–	0.48	0.22	15	n/a	–	Fermi
091019	18:00:40	0.79	0.67	0.71	15	n/a	–	Fermi
091020	21:36:44	–	0.50	0.43	0.012	34.6	<2.1	Swift
091022	18:03:27	0.50	–	0.32	15	n/a	–	Fermi
091026	11:38:48	0.49	–	0.18	11	n/a	–	Fermi
091030	19:52:26	0.43	–	0.69	7.6	160	–	Fermi
091031	12:00:28	0.30	–	0.94	0.17	100	–	FermiLAT
091103	21:53:51	–	0.21	0.59	7.9	n/a	–	Fermi
091109	04:57:43	0.43	–	1.00	0.025	48	3.1	Swift
091109	21:49:03	0.91	–	0.58	0.014	0.3	–	Swift
091115	04:14:50	0.84	0.64	0.53	11	n/a	–	Fermi

Table B.2: *continued*

Date	UTC time	antenna response H1	L1	V1	error (deg)	T_{90} (sec)	redshift	γ-ray detector
091122	03:54:20	0.45	–	0.74	19	n/a	–	Fermi
091123	01:55:59	–	0.90	0.48	9.6	n/a	–	Fermi
091127	23:25:45	–	0.13	0.53	0.014	7.1	0.5	Swift
091128	06:50:34	0.16	–	0.48	7.6	n/a	–	Fermi
091202	01:44:06	0.32	–	0.70	14	n/a	–	Fermi
091202	05:15:42	0.78	–	0.51	9.5	n/a	–	Fermi
091202	23:10:04	0.44	–	0.75	0.03	45	–	Integral
091215	05:37:26	0.45	0.66	–	12	n/a	–	Fermi
091219	11:04:45	0.49	0.36	0.86	9.3	n/a	–	Fermi
091220	10:36:50	0.65	0.89	0.43	7.7	n/a	–	Fermi
091223	12:15:53	0.73	0.75	–	7.9	n/a	–	Fermi
091224	08:57:36	0.51	0.69	–	17	n/a	–	Fermi
091227	07:03:13	0.63	0.84	0.40	8.3	n/a	–	Fermi
100101	00:39:49	0.44	0.44	–	19	n/a	–	Fermi
100103	17:42:32	0.81	0.97	0.59	0.019	40	–	Integral
100111	04:12:49	0.54	0.67	–	0.014	12.9	–	Swift
100112	10:01:17	0.76	0.59	–	17	n/a	–	Fermi
100201	14:06:17	0.59	0.70	–	8.7	n/a	–	Fermi
100206	13:30:05	0.55	0.68	–	0.018	0.12	–	Swift
100212	13:11:45	0.45	0.22	–	7.6	n/a	–	Fermi
100213	22:27:48	0.99	0.84	–	0.017	2.4	–	Swift
100213	22:58:34	0.50	0.49	–	0.017	48.0	–	Swift
100216	10:07:00	0.94	0.74	–	0.036	0.3	–	Swift
100219	15:15:46	0.33	0.68	–	0.03	18.8	4.7	Swift
100221	08:50:26	0.69	0.94	–	11	n/a	–	Fermi
100225	05:59:05	0.49	0.70	–	20	n/a	–	Fermi
100225	13:55:31	0.26	0.65	–	7.6	n/a	–	Fermi
100228	20:57:47	0.51	0.50	–	13	n/a	–	Fermi
100301	05:21:46	0.42	0.68	–	9	n/a	–	Fermi
100315	08:39:12	0.89	1.00	–	9.3	n/a	–	Fermi
100316	02:23:00	0.48	0.36	–	0.02	7.0	–	Swift
100316	08:57:59	0.91	0.81	–	0.024	9.3	–	Swift
100322	07:06:18	0.57	0.35	–	0.048	1.5	–	Swift
100324	00:21:27	0.60	0.79	–	0.03	6	–	Swift
100324	04:07:36	0.43	0.59	–	0.1	15	–	IPN
100325	05:54:43	0.68	0.54	–	10	n/a	–	Fermi
100325	06:36:08	0.93	0.84	–	0.44	9	–	FermiLAT
100326	07:03:05	0.38	0.40	–	15	n/a	–	Fermi
100327	09:43:15	0.59	0.41	–	16	n/a	–	Fermi
100328	03:22:44	0.89	0.94	–	8.9	n/a	–	Fermi
100331	21:08:38	0.35	0.52	–	0.1	30	–	AGILE
100401	07:07:31	0.50	0.31	–	0.024	100	–	Swift
100401	18:34:10	0.67	0.76	–	0.036	n/a	–	Swift
100410	08:31:57	0.41	0.03	–	13	n/a	–	Fermi
100410	17:45:46	0.94	0.72	–	14	n/a	–	Fermi

Table B.2: *continued*

Date	UTC time	antenna response H1	L1	V1	error (deg)	T_{90} (sec)	redshift	γ-ray detector
100418	21:10:08	0.59	0.77	–	0.023	7.0	0.62	Swift
100420	00:12:06	0.63	0.82	–	8	n/a	–	Fermi
100420	05:22:42	0.45	0.36	–	0.055	48	–	Swift
100423	05:51:25	0.56	0.38	–	7.6	21.6	–	Fermi
100425	02:50:45	0.92	0.79	–	0.029	37.0	1.8	Swift
100427	08:31:55	0.57	0.85	–	0.03	26	–	Swift
100502	08:33:02	0.21	0.33	–	7.8	n/a	–	Fermi
100507	13:51:15	0.66	0.52	–	7.9	n/a	–	Fermi
100508	09:20:42	0.90	0.94	–	0.036	52	–	Swift
100515	11:13:09	0.94	0.88	–	7.8	n/a	–	Fermi
100516	08:50:41	0.62	0.80	–	20	n/a	–	Fermi
100516	09:30:38	0.72	0.96	–	16	n/a	–	Fermi
100517	01:43:08	0.39	0.40	–	8.4	n/a	–	Fermi
100517	03:42:08	0.16	0.51	–	8.6	n/a	–	Fermi
100517	05:49:52	0.62	0.67	–	14	n/a	–	Fermi
100517	15:19:58	0.67	0.53	–	7.8	n/a	–	Fermi
100517	03:09:50	0.78	0.89	–	9.1	n/a	–	Fermi
100526	19:00:38	0.40	0.39	–	0.036	64.0	–	Swift
100604	06:53:34	0.53	0.42	–	8.3	n/a	–	Fermi
100608	09:10:06	0.50	0.52	–	9.2	n/a	–	Fermi
100628	08:16:40	0.46	0.46	–	0.036	0.036	–	Swift
100701	11:45:23	0.26	0.64	–	7.5	27.5	–	Fermi
100709	14:27:32	0.50	0.51	–	8.7	n/a	–	Fermi
100717	08:55:06	0.66	0.65	–	12	n/a	–	Fermi
100717	10:41:47	0.82	0.64	–	12	n/a	–	Fermi
100719	23:44:04	0.55	0.38	–	7.6	n/a	–	Fermi
100722	06:58:24	0.59	0.54	–	11	n/a	–	Fermi
100725	07:12:52	0.66	0.91	–	0.036	141	–	Swift
100725	11:24:34	0.79	0.62	–	0.036	200	–	Swift
100727	05:42:17	0.54	0.84	–	0.036	84	–	Swift
100802	05:45:36	0.66	0.71	–	0.036	487	–	Swift
100804	02:29:26	0.91	0.99	–	7.6	n/a	–	Fermi
100814	03:50:11	0.63	0.32	0.59	0.036	174.5	–	Swift
100814	08:25:25	–	0.48	0.85	7.9	6.4	–	Fermi
100816	00:12:41	–	0.79	0.70	7.6	n/a	–	Fermi
100816	00:37:51	–	0.43	0.95	0.036	2.9	0.8	Swift
100819	11:56:35	0.73	0.79	0.81	8.4	n/a	–	Fermi
100820	08:56:58	0.42	0.59	0.80	7.8	n/a	–	Fermi
100823	17:25:35	0.06	0.41	0.49	0.036	16.9	–	Swift
100825	06:53:48	0.52	0.45	0.97	9.8	n/a	–	Fermi
100826	22:58:22	–	0.28	0.44	8.4	n/a	–	Fermi
100829	21:02:08	0.47	0.13	0.51	7.6	n/a	–	Fermi
100904	01:33:43	–	0.53	0.84	0.036	31.3	–	Swift
100905	15:08:14	0.59	0.30	–	0.036	3.4	–	Swift
100905	21:46:22	0.37	0.73	0.56	8.5	n/a	–	Fermi

Table B.2: *continued*

Date	UTC time	antenna response H1	L1	V1	error (deg)	T_{90} (sec)	redshift	γ-ray detector
100906	13:49:27	0.88	0.61	–	0.036	114.4	1.7	Swift
100916	18:41:12	0.30	0.21	0.85	8.3	20	–	Fermi
100917	05:03:25	0.44	0.50	0.82	0.036	66	–	Swift
100918	20:42:18	0.78	0.44	0.44	7.6	n/a	–	Fermi
100919	21:12:16	0.71	0.60	0.61	7.7	n/a	–	Fermi
100922	14:59:43	0.53	–	0.68	17	n/a	–	Fermi
100924	03:58:08	0.45	0.80	–	0.036	96.0	–	Swift
100926	14:17:03	0.83	0.63	–	8.4	n/a	–	Fermi
100926	16:39:54	0.30	0.57	0.68	14	n/a	–	Fermi
100928	02:19:52	0.49	0.50	–	0.036	3.3	–	Swift
100929	21:59:45	0.40	–	0.92	11	n/a	–	Fermi
101002	06:41:26	0.32	–	0.91	18	n/a	–	Fermi
101003	05:51:08	0.68	0.82	0.54	11	n/a	–	Fermi
101004	10:13:49	1.00	0.93	–	10	n/a	–	Fermi
101010	04:33:46	–	0.76	0.84	20	n/a	–	Fermi
101013	09:52:42	0.78	0.85	0.75	7.7	n/a	–	Fermi
101015	13:24:02	0.79	0.63	–	9.6	n/a	–	Fermi
101016	05:50:16	–	0.56	0.66	8	n/a	–	Fermi

Bibliography

[1] S. Weinberg. *Gravitation and Cosmology*. John Wiley & Sons, 1972.

[2] E. Gourgoulhon. *Relativité générale*. Cours du Master Astronomie et Astrophysique, 2010.

[3] C. W. Misner, K. S. Thorne, and J. A. Wheeler. *Gravitation*. W. H. Freeman and company, 1973.

[4] R. M. Wald. *General Relativity*. The University of Chicago Press, 1984.

[5] Philippe Tourrenc. *Relativité et Gravitation*. Collection S. Armand Colin, 1992.

[6] H. Beltrami and W. Y. Chau. Analytic results for the properties of gravitational waves emitted by a large class of model sources. *Astrophys. & Space Sci.*, **111**(2):335–341, 1985.

[7] J. Weber. Detection and generation of gravitational waves. *Phys. Rev.*, **117**:306, 1960.

[8] Z. A. Allen *et al.* First search for gravitational wave bursts with a network of detectors. *Phys. Rev. Lett.*, **85**:5046, 2000.

[9] G. E. Moss, L. R. Miller, and R. L. Forward. Photon-noise-limited laser transducer for gravitational antenna. *Appl. Opt.*, **10**:2495, 1971.

[10] P. R. Saulson. *Fundamentals of interferometric gravitational wave detectors*. World Scientific, 1994.

[11] T. Accadia *et al.* Calibration and sensitivity of the Virgo detector during its second science run. *Class. Quantum. Grav.*, **28**:025005, 2011.

[12] B. F. Schutz and M. Tinto. Antenna patterns of interferometric detectors of gravitational waves. *Mon. Not. R. Astron. Soc.*, **224**:131, 1987.

[13] P. R. Saulson. Thermal noise in mechanical experiments. *Phys. Rev. D*, **42**:2437, 1990.

[14] F. Acernese *et al.* Measurements of Superattenuator seismic isolation by Virgo interferometer. *Astropart. Phys.*, **33**:182, 2010.

[15] G. Ballardin *et al.* Measurement of the virgo superattenuator performance for seismic noise suppression. *Rev. Sci. Instrum.*, **72**:3643, 2001.

[16] J.-Y. Vinet. Recycling interferometric antennas for peridodic gravitational waves. *J. Physique*, **47**:639, 1986.

[17] R. Kubo. The fluctuation-dissipation theorem. *Rep. Prog. Phys*, **29**:255, 1966.

[18] E. Tournefier for the Virgo Collaboration. Noise budget and noise hunting in Virgo. In *42nd Rencontres de Moriond Gravitational Waves and Experimental Gravity*, 2007.

[19] M. Punturo. The virgo sensitivity curve. Technical report, 2004. VIR-NOT-PER-1390-51.

[20] B. P. Abbott *et al.* Searches for gravitational waves from known pulsars with science run 5 LIGO data. *Astrophys. J.*, **713**:671, 2010.

[21] R. N. Manchester, G. B. Hobbs, A. Teoh, and M. Hobbs. The australia telescope national facility pulsar catalogue. *Astron. J.*, **129**:1993, 2005.

[22] `http://www.atnf.csiro.au/people/pulsar/psrcat/` , Dec 2008.

[23] J. M. Weisberg, D. J. Nice, and J. H. Taylor. Timing measurements of the relativistic binary pulsar PSR B1913+16. *Astrophys. J.*, **722**:1030, 2010.

[24] A. Hulse and J. Taylor. Discovery of a pulsar in a binary system. *Astrophys. J. Lett.*, **195**, 1975.

[25] I. H. Stairs. Pulsars in binary systems: probing binary stellar evolution and general relativity. *Science*, **304**:547, 2004.

[26] B. P. Abbott *et al.* An upper limit on the stochastic gravitational-wave background of cosmological origin. *Nature*, **460**(7258):990, 2009.

[27] W. H. Lee and E. Ramirez-Ruiz. The progenitors of short gamma-ray bursts. *New J. Phys.*, **9**:17, 2007.

[28] J. E. McClintock and R. A. Remillard. *Compact Stellar X-ray Sources*, chapter 4. Cambridge University Press, 2003.

[29] R. A. Remillard and J. E. McClintock. X-ray properties of black-hole binaries. *Annu. Rev. Astron. Astrophys.*, **44**:49, 2006.

[30] J. B. Hartle. *Gravity.* Addison Wesley, 2003.

[31] K. Thorne. Disk-accretion onto a blackhole. II. Evolution of the hole. *Astrophys. J.*, **191**:507, 1974.

[32] M. Kesden, G. Lockhart, and E. S. Phinney. Maximum black-hole spin from quasi-circular binary mergers. *Phys. Rev. D*, **82**:124045, 2010.

[33] F. Echievera. Gravitational-wave measurements of the mass and angular momentum of a black hole. *Phys. Rev. D*, **40**:3194–3202, 1989.

[34] S. Fabrika, P. Abolmasov, and S. Karpov. The supercritical accretion disk in SS433 and ultraluminous X-ray sources. In V. Karas and G. Matt, editors, *Black Holes From Stars to Galaxies — Across the Range of Masses*, page 225. Cambridge University Press, 2007.

[35] A. R. King. *Compact Stellar X-ray Sources*, chapter Accretion in Compact Binaries. Cambridge University Press, 2006.

[36] R. Fender and T. Belloni. GRS 1915+105 and the disc-jet coupling in accreting black hole systems. *Annu. Rev. Astron. Astrophys.*, **42**(1):317, 2004.

[37] J.-P. Lasota. The disc instability model of dwarf-novae and low-mass X-ray binary transients. *New Astron. Rev.*, **45**:449, 2001.

[38] S. Hild *et al.* A xylophone configuration for a third generation gravitational wave detector. *Class. Quantum Grav.*, **27**:015003, 2010.

[39] S. W. Hawking and W. Israel. *300 years of gravitation.* Cambridge University Press, 1989.

[40] J. Abadie *et al.* Predictions for the rates of compact binary coalescences observable by ground-based gravitational-wave detectors. *Class. Quantum Grav.*, **27**:173001, 2010.

[41] P. C. Peters. Gravitational radiation and the motion of two point masses. *Phys. Rev. B*, **136**:1224, 1964.

[42] K. Belczynski, V. Kalogera, and T. Bulik. A Comprehensive Study of Binary Compact Objects as Gravitational Wave Sources: Evolutionary Channels, Rates, and Physical Properties. *Astrophys. J*, **572**:407, 2002.

[43] L. Blanchet, B. R. Iyer, C. M. Will, and A. G. Wiseman. Gravitational waveforms from inspiralling compact binaries to second-post-newtonian order. *Class. Quantum Grav.*, **13**:575, 1996.

[44] J. G. Baker, M. Campanelli, F. Pretorius, and Y. Zlochower. Comparisons of binary black hole merger waveforms. *Class. Quantum Grav.*, **24**:S25, 2007.

[45] I. Mandel and R. O'Shaughnessy. Compact binary coalescences in the band of ground-based gravitational-wave detectors. *Class. Quantum Grav.*, **27**:114007, 2010.

[46] Estimating the spins of stellar-mass black holes by fitting their continuum spectra. *AIP Conf. Proc.*, **968**:265, 2007.

[47] G. B. Cook, S. L. Shapiro, and S. A. Teukolsky. Rapidly rotating neutron stars in general relativity: Realistic equations of state. *Astrophys. J.*, **424**:823, 1994.

[48] L. E. Kidder. Coalescing binary systems of compact objects to $(\text{post})^{5/2}$-Newtonian order. V. Spin effects. *Phys. Rev. D*, **52**:821, 1995.

[49] S. E. Woosley and J. S. Bloom. The supernova–gamma-ray burst connection. *Annu. Rev. Astron. Astrophys.*, **44**:507, 2006.

[50] L. Scheck, H.-Th. Janka, T. Foglizzo, and K. Kifondis. Multidimensional supernova simulations with approximative neutrino transport. *Astron. Astrophys.*, **477**:931, 2007.

[51] G. Vedrenne and J.-L. Atteia. *Gamma-Ray Bursts.* Springer, 2009.

[52] B. D. Metzger *et al.* The proto-magnetar model for gamma-ray bursts. *Mon. Not. R. Astron. Soc.*, **413**:2031, 2011.

[53] A. I. MacFadyen, S. E. Woosley, and A. Heger. Supernovae, jets, and collapsars. *Astrophys. J.*, **550**:410, 2001.

[54] C. D. Ott. The gravitational-wave signature of core-collapse supernovae. *Class. Quantum Grav.*, **26**(6):063001, 2009.

[55] H. Dimmelmeier, C. Ott, A. Marek, and H.-T. Janka. Gravitational wave burst signal from core collapse of rotating stars. *Phys. Rev. D*, **78**:0654056, 2008.

[56] C. D. Ott *et al.* 3D collapse of rotating stellar iron cores in general relativity including deleptonization and a nuclear equation of state. *Phys. Rev. Lett.*, **98**:261101, 2007.

[57] M. Shibata, K. Shigeyuki, and E. Yoshiharu. Dynamical bar-mode instability of differentially rotating stars: effects of equations of state and velocity profiles. *Mon. Not. R. Astron. Soc.*, **343**:619, 2003.

[58] P. N. McDermott, H. M. van Horn, and C. J. Hansen. Nonradial oscillations of neutron stars. *Astrophys. J.*, **325**:725, 1988.

[59] C. D. Ott, A. Burrows, L. Dessart, and E. Livne. A new mechanism for gravitational-wave emission in core-collapse supernovae. *Phys. Rev. Lett.*, **96**:201102, 2006.

[60] M. B. Davies, A. King, S. Rosswog, and G. Wynn. Gamma-ray bursts, supernova kicks, and gravitational radiation. *Astrophys. J. Lett.*, **579**:L63, 2002.

[61] A. L. Prio and E. Pfahl. Fragmentation of collapsar disks and the production of gravitational waves. *Astrophys. J.*, **658**:1173, 2007.

[62] G. E. Romero, M. M. Reynoso, and H. R. Christiansen. Gravitational radiation from precessing accretion disks in gamma-ray bursts. *Astron. Astrophys.*, **524**:A4, 2010.

[63] W. S. Paciesas *et al.* The fourth batse gamma-ray burst catalog (revised). *Astrophys. J. Suppl. Ser.*, **122**:465, 1999.

[64] R. D. Blandford and R. L. Znajek. Electromagnetic extraction of energy from Kerr black holes. *Mon. Not. R. Astron. Soc.*, **179**:433, 1977.

[65] M. Lyutikov. The electromagnetic model of gamma-ray bursts. *New J. Phys.*, **8**:119, 2006.

[66] C. Meegan *et al.* The Fermi gamma-ray burst monitor. *Astrophys. J.*, **702**:791, 2009.

[67] S. D. Barthelmy *et al.* The Burst Alert Telescope (BAT) on the Swift MIDEX mission. *Space Sci. Rev.*, **120**:143, 2005.

[68] K. Hurley *et al.* The status and future of the third interplanetary network. *AIP Conf. Proc*, **1133**:55, 2009.

[69] S. Barthelmy. `http://gcn.gsfc.nasa.gov/`.

[70] M. Briggs *et al.* The error distribution of batse gamma-ray burst locations. *Astrophys. J. Suppl. Ser.*, **122**:503–518, 1999.

[71] M. Briggs *et al.* The accuracy of GBM GRB locations. *AIP Conf. Proc.*, **1133**:40, 2009.

[72] V. Connaughton. GCN circular 11574. 2011.

[73] E. Nakar. Short-hard gamma-ray bursts. *Phys. Rep.*, **442**:166, 2007.

[74] D. Burlon, G. Ghirlanda, G. Ghisellini, J. Greiner, and A. Celotti. Time resolved spectral behavior of bright batse precursors. *Astron. Astrophys.*, **505**:569, 2009.

[75] L.-X. Li. Gamma-ray burst precursors as the remnant of the thermal radiation initially trapped in the fireball. *Mon. Not. R. Astron. Soc.*, **380**(2):621, 2007.

[76] D. Lazzati and M. C. Begelman. Universal grb jets from jet-cocoon interaction in massive stars. *Astrophys. J.*, **629**:903, 2005.

[77] X.-Y. Wang and P. Meszaros. GRB precursors in the fallback collapsar scenario. *Astrophys. J.*, **670**:1247, 2007.

[78] J. L. Racusin *et al.* Jet breaks and energetics of Swift gamma-ray burst x-ray afterglows. *Astrophys. J.*, **698**:43, 2009.

[79] A. Goldstein *et al.* A new derivation of grb jet opening angles from the prompt gamma-ray emission. arxiv:1101.2458, 2011.

[80] K. Belczynski, R. E. Taam, E. Rantsiou, and M. van der Sluys. Black hole spin evolution: Implications for short-hard gamma-ray bursts and gravitational wave detection. *Astrophys. J*, **682**:474, 2008.

[81] E. Rantsiou, S. Kobayashi, P. Laguna, and F. A. Rasio. Mergers of black hole–neutron star binaries. i. methods and first results. *Astrophys. J.*, **680**:1326, 2008.

[82] I Leonor *et al.* Estimating detection rates for the LIGO–Virgo search for gravitational-wave burst counterparts to gamma-ray bursts using inferred local GRB rates. *Class. Quantum. Grav*, **26**:204017, 2009.

[83] R Chapman, N. R. Tanvir, R. S. Priddey, and A. J. Levan. How common are long gamma-ray bursts in the local Universe? *Mon. Not. R. Astron. Soc.*, **382**:L21, 2007.

[84] F. J. Virgili, E.-W. Liang, and B. Zhang. Low-luminosity gamma-ray bursts as a distinct GRB population: a firmer case from multiple criteria constraints. *Mon. Not. R. Astron. Soc.*, **392**:91, 2009.

[85] B. P. Abbott *et al.* Search for gravitational-wave bursts associated with gamma-ray bursts using data from LIGO Science Run 5 and Virgo Science Run 1. *Astrophys. J.*, **715**:1438, 2010.

[86] L. Scharf. Topics in satistical signal processing. In *Les Houches, Session XLV, Signal Processing*. 1985.

[87] S. Kay. *Fundamentals of Statistical Signal Processing*, chapter 6. Prentice Hall - PTR, 1998.

[88] L. A. Wainstein and V. D. Zubakov. *Extraction of signals from noise*, chapter 3. Prentice-Hall, 1962.

[89] P. Flandrin. *Temps-Fréquence*. Hermès, 1993.

[90] D. A. Klarner. Cell growth problems. *Can. J. Math*, **19**:851, 1967.

[91] M. F. Sykes and M. Glen. Percolation processes in two dimensions. I. Low-density series expansions. *J. Phys. A: Math. Gen*, **9**:87, 1976.

[92] S. Martens. Lattice animals: A fast enumeration algorithm and new perimeter polynomials. *J. Stat. Phys.*, **58**:1095, 1990.

[93] A. C. Searle, P. J. Sutton, M. Tinto, and G. Woan. Robust bayesian detection of unmodelled bursts. *Class. Quantum Grav.*, **25**:114038, 2008.

[94] B. Allen. χ^2 time-frequency discriminator for gravitational wave detection. *Phys. Rev. D*, **71**(6):062001, 2005.

[95] S. Chatterji *et al.* Coherent network analysis technique for discriminating gravitational-wave bursts from instrumental noise. *Phys. Rev. D*, **74**(8):082005, 2006.

[96] P. J. Sutton *et al.* X-pipeline: an analysis package for autonomous gravitational-wave burst searches. *New J. Phys.*, **12**(5):053034, 2010.

[97] J. Weber *et al.* New gravitational radiation experiments. *Phys. Rev. Lett.*, **31**:779, 1973.

[98] B. P. Abbott *et al.* Search for Gravitational Waves from Low Mass Binary Coalescences in the First Year of LIGO's S5 Data. *Phys. Rev. D*, **79**(12):122001, 2009.

[99] B. P. Abbott *et al.* Search for gravitational-wave bursts in the first year of the fifth ligo science run. *Phys. Rev. D*, **80**(10):102001, 2009.

[100] B. P. Abbott *et al.* Search for high frequency gravitational-wave bursts in the first calendar year of LIGO's fifth science run. *Phys. Rev. D*, **80**:102002, 2009.

[101] J. Abadie *et al.* All-sky search for gravitational-wave bursts in the first joint LIGO-GEO-Virgo run. *Phys. Rev. D*, **81**:102001, 2010.

[102] B. P. Abbott *et al.* Search for gravitational waves from low mass compact binary coalescence in 186 days of LIGO's fifth science run. *Phys. Rev. D*, **80**(4):047101, 2009.

[103] M. Wąs *et al.* On the background estimation by time slides in a network of gravitational wave detectors. *Class. Quantum Grav.*, **27**(1):015005, 2010.

[104] M. Wąs *et al.* Limitations of the time slide method of background estimation. *Class. Quantum Grav.*, **27**:194014, 2010.

[105] F. Beauville *et al.* A comparison of methods for gravitational wave burst searches from LIGO and Virgo. *Class. Quantum Grav.*, **25**:045002, 2008.

[106] T. Accadia *et al.* Noise from scattered light in Virgo's second science run data. *Class. Quantum Grav*, **27**:194011, 2010.

[107] B. Abbott *et al.* Search for gravitational waves associated with the gamma ray burst GRB030329 using the LIGO detectors. *Phys. Rev. D*, **72**(4):042002, 2005.

[108] F. Acernese *et al.* Search for gravitational waves associated with GRB 050915a using the Virgo detector. *Class. Quantum Grav.*, **25**:225001, 2008.

[109] B. Abbott *et al.* Search for gravitational waves associated with 39 gamma-ray bursts using data from the second, third, and fourth LIGO runs. *Phys. Rev. D*, **77**:062004, 2008.

[110] B. P. Abbott *et al.* Search for gravitational-wave inspiral signals associated with short Gamma-Ray Bursts during LIGO's fifth and Virgo's first science run. *Astrophys. J*, **715**:1453, 2010.

[111] B. Mours and L. Rolland. h(t) reconstruction for VSR2. Technical report, 2010. VIR-0340A-10.

[112] L. Rolland. `https://wwwcascina.virgo.infn.it/DataAnalysis/Calibration/Reconstruction/Runs/VSR3/index.html`.

[113] I. Bartos and others. Frequency domain calibration error budget for LIGO in S6. Technical report, 2011. LIGO-T1100071.

[114] F. Robinet *et al.* Data quality in gravitational wave bursts and inspiral searches in the second Virgo Science Run. *Class. Quantum. Grav*, **27**:194012, 2010.

[115] K. Strobel and M. K. Weigel. On the minimum and maximum mass of neutron stars and the delayed collapse. *Astron. Astrophys.*, **367**:582, 2001.

[116] K. Belczynski *et al.* On the rarity of double black hole binaries: Consequences for gravitational wave detection. *Astrophys. J.*, **662**:504, 2007.

[117] `https://www.lsc-group.phys.uwm.edu/daswg/projects/lalsuite.html`.

[118] A. Buonanno, Y. Chen, and M. Vallisneri. Detecting gravitational waves from precessing binaries of spinning compact objects: Adiabatic limit. *Phys. Rev. D*, **67**:104025, 2003. Erratum-ibid. 74:029904, 2006.

[119] H. B. Mann and D. R. Whitney. On a test of whether one of two random variables is stochastically larger than the other. *Ann. Math. Stat.*, **18**:50, 1947.

[120] P. Jakobsson *et al.* A mean redshift of 2.8 for Swift gamma-ray bursts. *Astron. Astrophys.*, **447**:897, 2006.

[121] `http://raunvis.hi.is/~pja/GRBsample.html`, Mar 2011.

[122] E. J. Copeland, M. Sami, and S. Tsujikawa. Dynamics of dark energy. *Int. J. Mod. Phys. D*, **15**:1753, 2006.

[123] coherent WaveBurst team, private communications.

[124] S. Klimenko, I Yakushin, A. Mercer, and G Mitselmakher. A coherent method for detection of gravitational wave bursts. *Class. Quantum Grav.*, **25**:114029, 2008.